Light hole ground state in anisotropic nanowire - quantum dots: numerical calculations and magneto-optical spectroscopy

Kimon Moratis

Communauté UNIVERSITÉ Grenoble Alpes

THÈSE

Pour obtenir le grade de

DOCTEUR DE LA COMMUNAUTÉ UNIVERSITÉ GRENOBLE ALPES

Spécialité : **NANOPHYSIQUE**

Arrêté ministériel : 25 mai 2016

Présentée par

Kimon MORATIS

Thèse dirigée par **David FERRAND**
et codirigée par **Yann-Michel NIQUET, CEA**

préparée au sein du **CNRS au Laboratoire Institut Néel**
dans l'**École Doctorale de Physique**

Etat fondamental de trous légers dans des boîtes quantiques en nanofils: Calculs numériques et spectroscopie magnéto-optique

Light hole ground state in anisotropic nanowire - quantum dots: Numerical calculations and magneto-optical spectroscopy

Thèse soutenue publiquement le **7 novembre 2019**,
devant le jury composé de :

Monsieur David FERRAND
Professeur, Université Grenoble-Alpes, Chercheur à l'Institut Néel CNRS, Directeur de thèse
Monsieur Yann-Michel NIQUET
Chercheur CEA, Interdisciplinary Research Institute of Grenoble, CEA Grenoble, Co-Directeur de thèse
Monsieur Denis SCALBERT
Directeur de Recherche, UMR5221 Laboratoire Charles Coulomb (L2C), Rapporteur
Monsieur Nicolas CHAUVIN
Chargé de Recherche, Institut des Nanotechnologies de Lyon - UMR CNRS 5270, Rapporteur
Madame Fabienne MICHELINI
Maître de Conférences, UMR7334 Institut des Matériaux, de Microélectronique et des Nanosciences de Provence (IM2NP), Examinatrice
Monsieur Julien PERNOT
Professeur, Université Grenoble-Alpes, Examinateur, Président

Dark is the sea: raging waves
endless the sky above me
mighty is the wind that fills our sail
many of us will follow: our journey brave

The day when ice would break and sun was high
we sailed with wind of fate across the seas
we followed the stars bright in the night

Bathory, Blooded Shores

Acknowledgments

From an external point of view, for an achievement such as a PhD defense all credits are usually given to a single person, the one who is awarded the title. And indeed hard work, devotion, stubbornness and "virtues" as such are considered essential for the fulfillment of a research project. What really determines the quality of results and the degree of efficiency though, is the interaction with other people. I believe that this assessment reflects on every aspect of human activity, as without cooperation any progress would be anemic, if non-existent at all. This section is dedicated to the people with whom I collaborated during these three years and contributed to the successful completion of my doctoral studies.

Supervisors

First I want to thank my supervisor David Ferrand who coordinated the ANR-ESPADON project, in the context of which, I prepared my PhD thesis. David supervised mostly the optical spectroscopy measurements presented in this work and his involvement in the lab, both scientifically and technically, was crucial for conducting properly the experiments and interpreting meaningfully their results. Without David's suggestions and assistance, my comprehension as well as the analysis of the experimental results presented in Chapter 4 would be poorer and incomplete.

Alongside experiments, my PhD thesis had an equal share of theory. For this part I want to thank Yann-Michel Niquet, my coo-supervisor, who provided me with the TB_Sim package of codes and the required computational power by gaining me access to the cluster at CEA-Grenoble, in order to run the numerical calculations. Without the optimization of codes and the development of additional modules by Yann-Michel as required for this project, large part of the results presented in Chapters 2 and 3 would be impossible.

Last but not least, I want to thank Jöel Cibert, who was my third, "unofficial" supervisor. Joel's vast knowledge in the field of semiconductor physics and his ability to combine with integrity the results obtained from both numerical calculations and experiments, in combination with analytical models initially proposed by him, led to the demonstration of the original and extraordinary results which constitute the backbone of this PhD thesis.

Colleagues

Apart from those who directly supervised my thesis, the final shape and quality of this work was influenced by the discussions and collaboration with other permanent and non-permanent researchers who participated in the ANR-ESPADON project. Special thanks go to Edith Bellet-Amalric who supervised the growth of all samples I used for the optical spectroscopy measurements. This project required high quality nanowire quantum dots with very specific structural properties. I think it is needless to say that without the proper samples this work in general would be impossible.

Another collaboration which enriched the results of this thesis was the one I had with Gilles Nogues. I want to thank Gilles for giving me access to his optical setup and assisting me with

the emission diagram measurements and their analysis. Additionally, I want to thank Fabrice Donatini, with whom I carried out the cathodoluminescence measurements.

Finally I want to thank Regis André, Kuntheak Kheng, Eric Robin, Martien Den Hertog, Marta Orrú and Saransh Gosain for our excellent collaboration and their scientific feedback during the group meetings of the project.

During my work at Institut Néel, I had the opportunity to interact also with other members of the NPSC group, which made every day life in the laboratory much easier and productive. I want to thank Lucien Besombes, Jacek Kasprzak, Dang Le-Si, Jean-Philippe Poizat, Maxime Richard, Petr Stepanov, Alberto Artioli, Thibault Cremel, Mathieu Jeannin, Nitika Vaish, Vivekanand Tiwari, Alban Lafuente-Sampietro and Valentin Delmonte for their assistance in the lab and the fruitful scientific discussions.

The fact that I was given the opportunity to come in Grenoble and complete my doctoral studies was not by chance or random. For this, I want to thank Nikos Pelekanos from University of Crete, who introduced me to NPSC group and encouraged me to apply for this position in summer 2016.

At this point, I have to underline that the determining factor for someone to be awarded a doctoral degree, is of course the decision of the jury. For this I want to thank Denis Scalbert, Nicolas Chauvin, Fabienne Michelini and Julien Pernot who accepted to review my manuscript, provide me with suggestions for improvements and be the members of my jury.

and the Social Terrain...

Scientific collaboration and interaction with colleagues, are of course essential for the completion of a PhD. What makes life rich however, while giving strength and motivation, is one's social environment. Nietzsche put it in an elaborate way: *A good writer possesses not only his own spirit, but also the spirit of his friends...* During these three years I met a lot of wonderful people in Grenoble with whom we had a great time while engaging in activities involving a lot of food, a lot of drinks and some sports... occasionally at least... In particular, I want to thank Hugo, Francesco, Maria, Roberto, Joachim, Simone, Angel, Alvaro, Ana, Juliette, Jorge, Stefano, Lucas, Pavel, Martin, Vladimir and Thanasis... Now, this list should be much much bigger as I omitted a lot off people, I apologize, but you know who you are and I thank you all for the nice moments we shared together!

To conclude this section I want to thank my family in Greece for their constant support all these years, as well as my friends there who regardless the distance, they are always present in my life.

Abstract

In this work we investigated the valence band ground state properties of nanowire quantum dots based on the II-VI materials. The main objective was to prove experimentally the stabilization of a light hole ground state in the nanowire quantum dot and understand which parameters influence the purity of the valence band ground state. The two main factors which determine the switching between heavy and light holes and their mixing, is confinement and mismatch induced strain. These parameters can be tuned by modifying the length to diameter aspect ratio of the quantum dot and by choosing properly the material which surrounds it in order to maintain confinement of the hole inside the quantum dot.

The effect of strain and confinement was studied extensively by $\vec{k} \cdot \vec{p}$ theory on nanowire quantum dots similar to those we studied with optical measurements. More specifically we investigated the hole ground state properties of both compressive CdTe quantum dots in ZnTe nanowire and tensile ZnTe quantum dots surrounded by ZnMgTe. Strain was tuned by modifying the aspect ratio of the quantum dot and by depositing an external ZnMgTe shell to the ZnTe core. The effect of confinement was investigated by changing the valence band offset between the core and the dot and switching from a strong type I to a strong type II. Additionally, for the CdTe quantum dots we carried out calculations also under the presence of an exchange field, in order to study the spin properties of the ground state through the giant Zeeman shift. These calculations revealed a strong renormalization of the light hole Landé factor due to a combined effect of elastic strain and spin-orbit coupling.

The nanowires were grown by molecular beam epitaxy in our group and the electronic properties of the quantum dots inserted in them, were studied by low temperature micro-photoluminescence spectroscopy. The study of the excitonic properties (identification of confined excitons, cathodoluminescence, autocorrelation) and the degree of polarization, allowed us to identify without ambiguity the presence of light holes in the valence band ground state, in agreement to what is expected from theoretical predictions.

In order to investigate the spin properties of a light hole ground state, we carried out measurements on magnetic quantum dots containing Mn atoms (concentration in the order of 10%). These quantum dots were characterized by magneto-optical spectroscopy under strong magnetic fields, up to 11 T. This study was carried out for different magnetic field configurations, using both a uniaxial and a vectorial magnet (magnetic fields applied parallel and perpendicular to the nanowire axis, rotating magnetic fields). The presence of a light hole ground state was confirmed through a quantitative study of the excitonic giant Zeeman shift. Light hole presence was manifested through the formation of an exciton magnetic polaron characterized by anisotropic magnetic properties, which were observed for the first time. The experimental data were fitted in very good agreement with a quantitative model which was developed, using the results obtained from numerical calculations.

Résumé

Dans ce travail, nous avons étudié les propriétés électroniques d'états de trous confinés dans des boites quantiques en nanofils. L'objectif principal était de déterminer les conditions permettant de stabiliser un état fondamental de trou léger et de mettre en évidence expérimentalement cet état de trou à l'aide de mesures de spectroscopie optique. Les deux principaux facteurs qui déterminent la nature de l'état de trou (trou lourd ou trou léger) et les mélanges entre états sont le confinement et les déformations élastiques. Ces paramètres peuvent être ajustés en modifiant le rapport entre la hauteur et la largeur des boites quantiques et en choisissant correctement le matériau qui l'entoure afin de maintenir le confinement du trou à l'intérieur de la boite quantique.

D'un point de vue théorique, l'effet des déformations élastiques et du confinement a été étudié de manière approfondie par la mise en œuvre de calculs numériques $\vec{k} \cdot \vec{p}$. Ces calculs ont été menés avec des boites quantiques en nanofils ayant une structure identique aux échantillons étudiés expérimentalement. Plus spécifiquement, nous avons étudié les propriétés de boites quantiques en compression (boites quantique de CdTe insérées dans des nanofils de ZnTe) et des boites quantiques en tension (boites quantiques de ZnTe entourées de coquilles de ZnMgTe). Les déformations élastiques et le confinement ont été ajustés en modifiant le rapport d'aspect des boites quantiques. Différents types de confinement ont été étudiés en modifiant le décalage de bande de valence entre la boite quantique et le nanofil (configurations de type I et de type II). De plus, une étude détaillée des propriétés de spin des états de trous légers a été menée en intégrant l'effet d'un champ d'échange dans les calculs $\vec{k} \cdot \vec{p}$. Cette étude révèle une forte renormalisation du facteur de Landé des trous légers sous l'effet combiné des contraintes élastiques et du couplage spin-orbite.

D'un point de vue expérimental, nous avons étudié des nanofils II-VI élaborés dans l'équipe par croissance par épitaxie par jets moléculaires. Des mesures de micro-photoluminescence à basse température ont été mises en œuvre avec des nanofils isolés afin d'étudier les propriétés électroniques de boites quantiques insérées dans les nanofils. L'étude des propriétés excitoniques (identification des excitons confinés, cathodoluminescence, autocorrélation) et du taux de polarisation a permis d'identifier sans ambigüité la présence de trous légers dans l'état fondamental en accord avec les prédictions théoriques. Afin de caractériser les états de trous légers à l'aide de leurs propriétés de spin, des études ont été menées avec des boites quantiques magnétiques contenant des atomes de manganèse (concentration de l'ordre de 10%). Ces boites quantiques ont été caractérisées par spectroscopie magnéto-optique sous fort champ magnétique (champ magnétique jusqu'à 11T). Différentes configurations de champs magnétiques ont été étudiées à l'aide de bobines de champs uni-axes et vectorielles (champs magnétiques parallèles ou perpendiculaires à l'axe des nanofils, champs magnétiques tournants). Une étude quantitative de l'effet Zeeman géant excitonique a permis de confirmer la présence d'état fondamental de trou léger dans les boites. Celle-ci se manifeste par la formation de polarons magnétiques excitoniques ayant des propriétés magnétiques anisotropes très originales. Un modèle quantitatif complet s'appuyant sur les modélisations numériques a été développé en très bon accord avec les résultats expérimentaux.

Contents

Introduction

Spintronics

The work carried out in this thesis is attached to wider area of spintronics. Research in this field begun through the observation of certain phenomena which were dependent on the electronic spin. A very important discovery was that of tunnel magneto-resistance, discovered through experiments on Fe-Ge-Co thin films in 1975 [1]. Further research on different materials to better understand these phenomena, continued during 1980s and in 1988, spin injection from a ferromagnetic material to a paramagnetic one was first demonstrated [2]. Another major advancement in this field was the discovery of giant magneto-resistance in 1988, which opened the way of controlling the motion of electrons by acting on their spin via the orientation of a magnetization [3]. The potential of semiconductor devices for spintronics technology was first suggested in 1990 through a theoretical model predicting a transistor operating directly on electron spin [4].

Quantum technologies

In this work we studied theoretically and experimentally semiconductor nanowire quantum dots. The reason that we are interested in quantum dots, is due to their excellent optical properties, as they are characterized by very bright lines with narrow linewidths and as they can act as single photon and entangled photon pair emitters [5], [6], [7]. Also by incorporating a quantum dot in a heterostructure and through post-growth processing techniques, we are able to tailor its electronic properties and control the photonic modes with which the dot interacts [8]. A carrier trapped inside a quantum dot can be used for applications in spintronics, irrespective to fast spin dephasing, as single spins can by manipulated optically in sub-nanosecond scale. Probing a qubit in a semiconductor heterostructure can have applications in quantum communication, quantum information and metrology. A qubit is a two level system which can be initialized and manipulated. A major limitation is the decoherence time and it imposes that the manipulation of qubit must be carried out in a time shorter than that where the qubit loses information encoded to its phase [8]. A qubit in a semiconductor can be achieved by taking advantage of the quantum superposition of electron spin states. Electrons interact strongly with experimental probes (opposite to nuclear spins), while the interaction with phonons, which is the main parameter influencing decoherence time is weak. An excellent candidate for the implementation of an electronic spin superposition is through a light hole ground state in a quantum dot.

An example of how we could exploit the properties of a light hole ground state and the advantages over heavy hole, is demonstrated in Fig. 1. The idea is to excite the quantum dot in resonance with the charged exciton line. Then by applying at the same time σ and π polarized optical pulses we can address to $|1/2\rangle$ and $|-1/2\rangle$ electron spin states through stimulated emission. By repeating this procedure we can stabilize a λ type system as shown in Fig. 1 b) and manipulate a quantum superposition of spins. For the case of a heavy hole however, a superposition like that is not feasible, as we can not address simultaneously to $|1/2\rangle$ and $|-1/2\rangle$ states. Probing a light hole ground state is of particular interest as they exhibit a Zeeman shift irrespective of the orientation of the applied field, leading to applications in quantum infor-
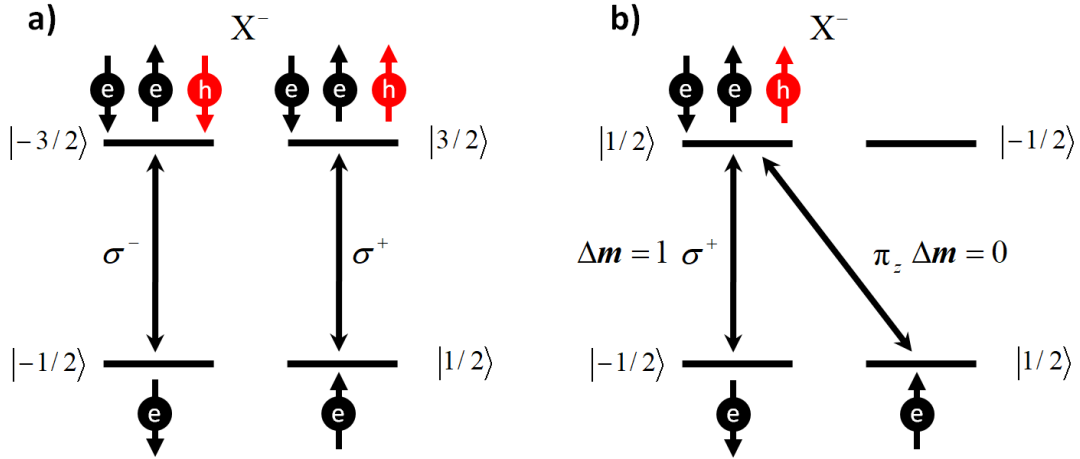
Figure 1 – A heavy hole - charged exciton where the two electron states can be addressed separately through σ^+ or σ^- polarized light a). Probing a λ type system through a charged exciton exploiting a light hole ground state b).

mation protocols as for instance the direct manipulation of the spin state using RF fields [9], the control of a spin introduced by a magnetic impurity and electron-spin state tomography [10]. Additionally, light holes can be subject to spin-flip transitions among up and down states induced by phonons, something which is not allowed for heavy hole states, resulting to a more versatile spin relaxation process [11]. From the perspective of this work, light holes confined in a nanowire - quantum dot, could be exploited in order to manipulate optically a quantum superposition of spins.

The objective of this work is to investigate in detail the parameters which influence the properties and purity of the valence band ground state in a semiconductor nanowire quantum dot and promote a light hole over a heavy hole.

Outline of this thesis

In Chapter 1 we begin with a general introduction on semiconductors based on II - VI materials and we describe their electronic and optical properties. Then we discuss the properties of semiconductor quantum dots, which are typically characterized by a heavy hole ground state. Following that we describe the parameters which govern the switching from heavy to light hole and we present the results of some important works carried out on semiconductor quantum dots with a light hole ground state. The chapter concludes with a description of the giant Zeeman effect in Diluted Magnetic Semiconductors (DMS) and the magnetic polaron formation, which can be observed in magneto-optical measurements.

In Chapter 2 we present the numerical calculation results based on $\vec{k} \cdot \vec{p}$ theory for CdTe quantum embedded in ZnTe nanowires with and without an external ZnMgTe shell. The purpose of this chapter is to investigate the parameters which influence the valence ground state. The most important parameters which affect the switching from heavy to light hole and the mixing of the two states, are the quantum dot aspect ratio, the axial shear strain and the valence band offset. The results obtained from these calculations are very important for the analysis of the experimental data.

In Chapter 3 we extend our theoretical study on the nanowire quantum dots by applying an exchange field to investigate the Zeeman shift. The objective of these calculations is to study the spin properties and the effect of the exchange field on the valence band ground state. The knowledge acquired from these calculations is of great importance as we will use it to under-

stand and explain the experimental data obtained through magneto-optical spectroscopy.

In Chapter 4 we present the experimental results obtained mostly by photoluminescence spectroscopy but also other techniques for three different systems. We begin by discussing the optical properties of a flat ZnTe quantum dot in a ZnTe-ZnMgTe core-shell nanowire. Then we present the results as regards an attempted strong type II system consisting of a ZnSe inclusion in a ZnTe nanowire. In the last part of this chapter we present the complete study and analysis of the optical and electronic properties of Cd(Mn)Te quantum dots in ZnTe nanowires. For this we use a combination of analytical models and the results obtained from the numerical calculations. We demonstrate that the factors which strongly influence the Zeeman shift, is the renormalization of spin due to the coupling of light hole with split-off, the field induced reconfinement of the hole ground state and the formation of magnetic polaron.

In Chapter 5 we give a summary of the main results and knowledge acquired during the elaboration of this work.

Chapter 1

Light holes in II-VI nanostructures

We begin this chapter by discussing the properties of semiconductors based on II-VI materials. Then we explain the advantages of light holes over heavy holes and the methods to stabilize them as a ground state and characterize them. We conclude this chapter by discussing the giant Zeeman effect in diluted magnetic semiconductors and the formation of an exciton magnetic polaron, which it strongly influences the optical properties of the nanowire - quantum dots under magnetic field.

1.1   Properties of semiconductors based on II-VI materials

In this work, we studied nanowire - quantum dots, based on the II-VI family of materials. These compounds are formed by elements from column II of the periodic element, like Zn, Cd, Mg, Mn and from column VI like Te and Se. The crystal structure of CdTe and ZnTe as well as of the ternary alloys $Zn_xMg_{1-x}Te$ and $Cd_xMn_{1-x}Te$ is zinc blende, as shown in Fig. 1.1.
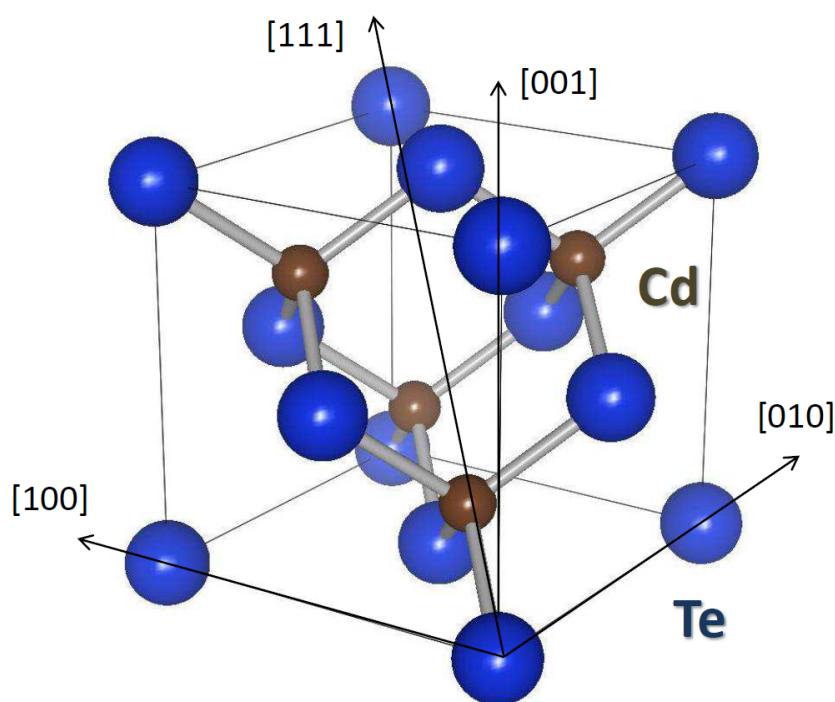

Figure 1.1 – The zinc blende crystal structure with different crystallographic orientations indicated by the corresponding arrows. Image taken from [12]

Zinc blende structure consists of two interpenetrating FCC (face centered) lattices where along

1

(111) direction, one lattice is shifted by 1/4 of the distance in respect to the other. One lattice is filled with elements from the column II of the periodic table, while the other with elements from column VI and the compounds are formed by covalent bonds. The elements which constitute a II-VI compound are characterized by 1 type s external level and three type p. Hybridization of these orbital states results in the formation of 4 bonding and 4 antibonding orbitals. Material II contributes its 2 external electrons to the bonding state, while material VI, contributes 4. Antibonding orbitals are initially empty. Valence band is formed by the 4 bonding orbitals, while conduction band is formed by the lowest s-like state of the 4 antibonding. One method for the calculation of the electronic band structure is through $\vec{k} \cdot \vec{p}$ perturbation theory which will be explained in detail in Chapter 2.

The II-VI materials we studied in this work are characterized by a direct band gap. This means that the maximum of valence band and the minimum of conduction band are both in the center of the first Brillouin zone where $\vec{k} = 0$, consequently the band symmetry at this point determines the optical properties of the semiconductors.
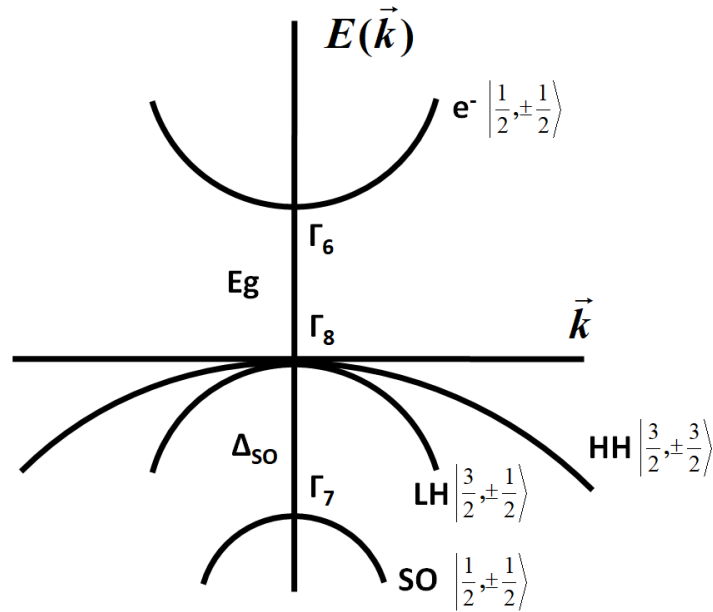
Figure 1.2 – Schematic representation of the band structure near $\vec{k} = 0$ for a direct gap cubic semiconductor

In Fig. 1.2 we present the band structure of a direct gap cubic semiconductor, similar to those studied in this work. The electronic and optical properties of semiconductors, are determined mostly by the behaviour of electrons near the band gap. For a direct gap semiconductor, like ZnTe this region is near $\vec{k} = 0$ and the energy dispersion $E_n(\vec{k})$ in the vicinity of this point is parabolic. The bottom of conduction band at Γ_6, for which the orbital angular momentum component is zero, is occupied by electrons. The total angular momentum of conduction band states is $J = \frac{1}{2}$ and the secondary total angular momentum number $m_j = \pm\frac{1}{2}$. These states are characterized by an s-like symmetry and they are isotropic in space [13]. In order to take into account the effect of the crystal lattice, the free electron mass m_0, gets replaced by an *effective electron mass*, given by

$$m_n = \hbar^2 \left(\frac{d^2 E_n}{dk^2} \right)^{-1} \tag{1.1}$$

The so called effective mass approximation simplifies significantly the theoretical study of semiconductors and is used systematically in modeling structures based on these materials.

The states at the top of valence band (Γ_8 point) where orbital angular momentum is non vanishing, adopt a p-like symmetry. For that reason these states are not isotropic in space. The spin-orbit coupling gives rise to a total angular momentum $J = \frac{3}{2}$, where heavy holes are characterized by a secondary total angular momentum quantum number $m_j = \pm\frac{3}{2}$ and light holes by $m_j = \pm\frac{1}{2}$ for $\vec{k}//z$. For a bulk semiconductor the two bands, corresponding to heavy $|3/2, \pm 3/2\rangle$ and light holes $|3/2, \pm 1/2\rangle$ are degenerate at $\vec{k} = 0$. The total angular momentum of split-off band at Γ_7 which is energetically separated by Δ_{SO} from heavy and light holes, is $J = \frac{1}{2}$ with secondary total angular momentum quantum numbers $m_j = \pm\frac{1}{2}$. Although it is commonly mentioned that split-off band is of less significance, we will demonstrate in Chapter 3 that it plays an important role in the spin properties of a quantum dot valence band ground state. Returning to the two types of holes of the Γ_8 manifold, these are also treated as free particles. In the context of $\vec{k} \cdot \vec{p}$ theory and along (111) direction, the longitudinal effective masses for heavy and light holes, are respectively

$$m_{hh}^{(111)} = \frac{m_0}{\gamma_1 - 2\gamma_3} \quad m_{lh}^{(111)} = \frac{m_0}{\gamma_1 + 2\gamma_3} \tag{1.2}$$

where γ_1 and γ_3 are the Luttinger parameters [14]. For the materials studied in this work these parameters are given in Appendix A. The longitudinal component of the effective mass tensor of a heavy hole is always larger than that of a light hole. Effective mass determines confinement and the properties of the valence band ground state, which in a quantum well for instance is typically a heavy hole.

For the characterization of the valence band ground state of a semiconductor heterostructure we can use different optical spectroscopy techniques. The optically bright transitions between conduction band electrons and valence band holes, are characterized by specific *opticalselectionrules*.

a)

HH: $\left|\frac{3}{2}, \pm\frac{3}{2}\right\rangle = \mp\frac{1}{\sqrt{2}}(P_x \pm iP_y)|\pm\rangle$

$|1/2\rangle \qquad |-1/2\rangle$

$\sigma^- \qquad \sigma^+$

$|-3/2\rangle \qquad |3/2\rangle$

Polarization $\perp$ to NW axis

b)

LH: $\left|\frac{3}{2}, \pm\frac{1}{2}\right\rangle = \mp\frac{1}{\sqrt{6}}[(P_x \pm iP_y)|\mp\rangle \mp 2P_z|\pm\rangle]$

$|1/2\rangle \qquad |-1/2\rangle$

$\frac{\sigma}{\sqrt{3}}$

$\pi\sqrt{\frac{2}{3}} \qquad \pi\sqrt{\frac{2}{3}}$

$\frac{-\sigma^-}{\sqrt{3}}$

$|-1/2\rangle \qquad |1/2\rangle$

Polarization predominantly // to NW axis
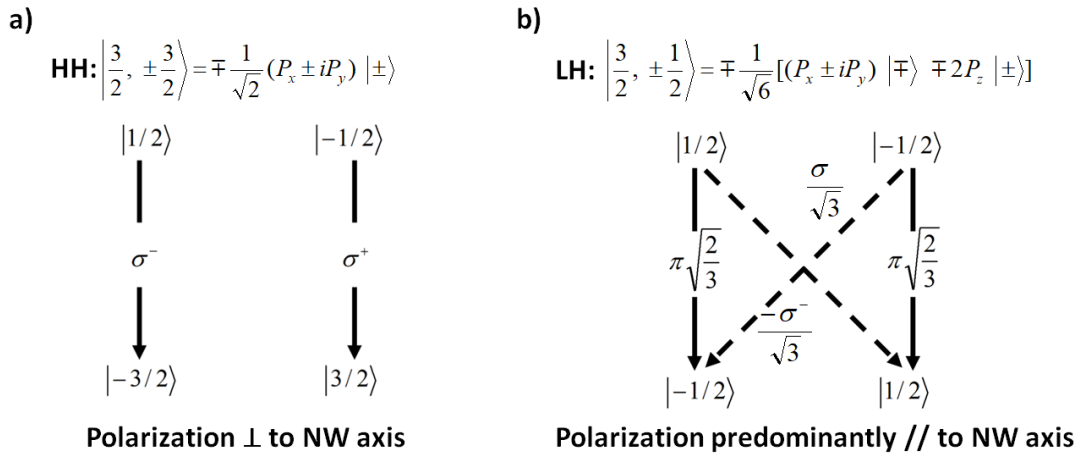
Figure 1.3 – Heavy hole states for a bulk semiconductor written on the orbital and spin basis and the corresponding optical selection rules with conduction band a). The light hole state in the same basis with the optical selection rules b). In this scheme we use the hole convention

In Fig. 1.3 a) we present the optical selection rules for a heavy hole and in Fig. 1.3 b) for a light hole for a bulk semiconductor. Heavy holes recombine optically bright only with electrons of opposite total angular momentum sign. In this case, carrier recombination is characterized by σ^+ or σ^- polarized light where the electric field components are perpendicular to z axis and they rotate on xy plane. On the contrary, light holes are characterized by both $\sigma^\pm$ and π transitions, for which the electric field oscillates parallel to z axis. From the scheme of Fig. 1.3 we confirm that light holes are characterized by more versatile optical selection rules than heavy holes, as from the same electron state we can address both light hole spin states. We

notify the reader, that throughout this text we use the hole convention for the optical selection rules.

In this work, we investigated the optical properties of different nanowire heterostructures, incorporating ZnTe and Cd(Mn)Te quantum dots surrounded by either ZnTe or ZnMgTe. By using different combinations of materials we are able to tune the elastic strain and the valence band offset, which are critical parameters, affecting the hole ground state. The variation of band gap of these alloys at low temperatures is given by the relations ([15] and Appendix E)

$$
\begin{aligned}
E_g^{Zn_xMg_{1-x}Te} &= 2391 + 959x + 250x^2 \quad \text{(meV)} \\
E_g^{Cd_xMn_{1-x}Te} &= 1606 + 1592x \quad \text{(meV)}
\end{aligned}
\tag{1.3}
$$

where the energy gaps of ZnTe and CdTe, are respectively $E_g^{ZnTe} = 2391$ meV and $E_g^{CdTe} = 1606$ meV. The strain in the nanowire quantum dot, is introduced through the lattice mismatch. The lattice parameter of a ternary alloy can be calculated through Vegard's linear interpolation law, where the lattice constants of the binary alloys on which the studied heterostructures are based, are

$$
\begin{aligned}
a_{ZnTe} &= 6.104 \text{Å} \\
a_{CdTe} &= 6.481 \text{Å} \\
a_{MgTe} &= 6.42 \text{Å} \\
a_{MnTe} &= 6.337 \text{Å}
\end{aligned}
\tag{1.4}
$$

Mismatch induced strain affects the position of conduction band and the position and splitting of the valence band. As regards ZnTe and CdTe there are different reports according to which the valence band offset between the two unstrained materials varies in the range of ± 50 meV which means that the band alignment is either weak type I or type II [16], [17]. As we will see in the following chapters, valence band offset is a very important parameter, as it determines the hole confinement inside the dot, which in turn governs the purity and spin properties of the ground state.

What makes II-VI materials very interesting is the fact that they can be doped with magnetic ions [15]. More specifically the lattice cations can be substituted with Mn atoms where the $sp-d$ exchange interaction between the carriers and the spin of Mn gives rise to the giant Zeeman effect, through which an energy shift in the order of $\sim 50 meV$ can be achieved for magnetic fields near 10 T. Without this effect a magnetic field in the order of 10^2 T would be required to achieve the same Zeeman shift. The $sp-d$ exchange interaction and the giant Zeeman effect in diluted magnetic semiconductors are discussed in detail later in this chapter.

It is important to point out, that Mn doping further reduces the valence band offset, resulting to a type II band alignment between Cd(Mn)Te and ZnTe. For that reason and in order to restore confinement, Cd(Mn)Te quantum dots were embedded in ZnMgTe.

1.2 Heavy holes confined in quantum dots

In this work we were interested to confine the carriers in quantum dots and further manipulate their electronic and optical properties through the induced strain and piezoelectric effects. Quantum dots are ideal systems, as 3D confinement of carriers in an inclusion of dimensions comparable to exciton Bohr radius results in the discretization of the energy levels. We can imagine a quantum dot as an artificial atom where by taking advantage of the fermionic nature of electrons and holes and Pauli's exclusion principle, a maximum of two carriers can be on the same energy level. This effect gives rise to different excitonic complexes, as shown in Fig. 1.4.
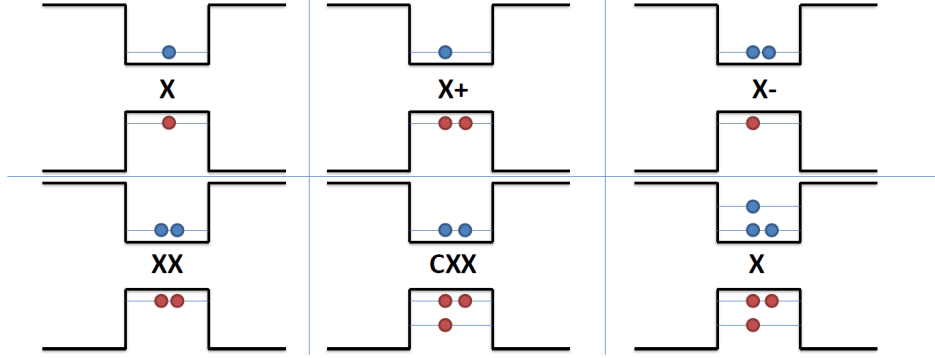
Figure 1.4 – Different excitonic complexes in a quantum dot. Image taken from [12]

Excitonic transitions in a quantum dot are characterized by the effect of radiative cascade, where a multi-excitonic complex X_n, decays to a X_{n-1} by emitting a photon of energy hf_n. This process continues until all excitonic complexes up to X decay and the quantum dot either becomes empty or contains a single carrier. The number of occupied states increases with excitation power.

Hole spins confined in semiconductor quantum dots are particularly attractive for applications in the field of quantum information. The main reason for that, is the weak hyperfine coupling of hole spin to the surrounding spin bath in comparison to electrons [18], [19], [20] which results an increase to decoherence time in the order of hundreds microseconds [21]. The majority of works reported in literature focus on the study of heavy holes, as strain and confinement promote them as the dominant ground state component. This is the case for self assembled quantum dots grown by the Stranski–Krastanov method. As mentioned in the previous section, heavy hole effective mass m^* for $\vec{k}//z$ is larger than the one of light hole along, as a result for a flat quantum dot where confinement is stronger along z axis, valence band ground state is heavy hole. Both experimental and theoretical studies confirm the heavy hole nature of the valence band ground state in a self assembled quantum dot [22].

In a very interesting work however, the authors demonstrated a method to promote a light hole exciton by applying externally an elastic stress to an unstrained flat quantum dot [23]. In that case a GaAs quantum dot was incorporated in AlGaAs and the strain was induced by two InAlGaAs layers grown on top and bottom of AlGaAs.
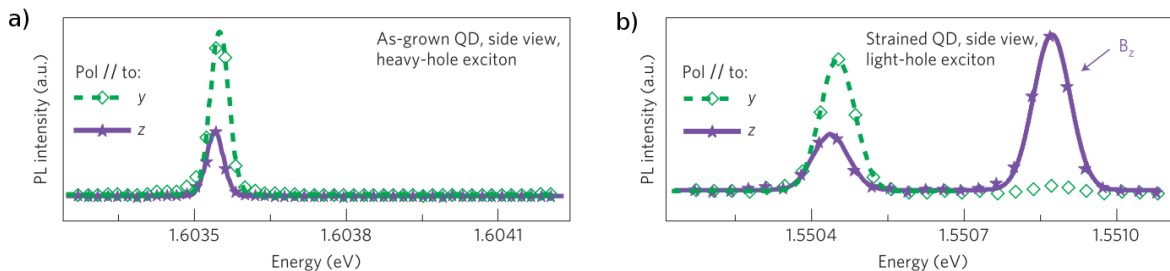
Figure 1.5 – Polarization dependent spectra obtained from a cleaved edge parallel to x axis for an unstrained quantum dot with a heavy hole ground state a) and a strained dot with a light hole ground state b). Image taken from [23].

An important method to analyze the hole ground state is through polarization dependent measurements. The authors of this work investigated an unstrained quantum dot with a heavy hole ground state and a strained one where light hole gets promoted over heavy hole. By measuring the degree of polarization from the cleaved edge of the two samples containing the quantum

dots, they showed that for a light hole there is a strongly linearly polarized component associated to a π transition. The polarization dependent spectra for a heavy and light hole ground state are shown in Fig. 1.5 a) and Fig. 1.5 b) respectively.

From this work it becomes evident, that alongside confinement, strain also plays a crucial role to the nature of the hole ground state. Our objective is to probe a light hole exciton and this can be achieved through a combined effect of confinement and the variation of axial shear strain along z axis. A method to achieve that, is by tuning for instance the dimensions of a nanowire quantum dot [24].

1.3 Heavy hole - light hole switching in a quantum dot

In this section we describe the parameters which govern the switching from a heavy hole ground state to a light hole one and the signature of the valence band ground state according to the results obtained by optical spectroscopy. In the context of our discussion we will review indicatively some very interesting works where the authors present methods to probe light hole as the dominant ground state component and the different theoretical models or spectroscopic techniques through which they investigate the valence band.

As already discussed, the first parameter which determines the hole ground state in a semiconductor is confinement. The longitudinal component of the heavy hole effective mass tensor is larger than that of the light hole one, $m_{z,hh}^* > m_{z,lh}^*$ while the in-plane one is the smallest, $m_{xy,hh}^* < m_{xy,lh}^*$. This means that heavy holes have lower confinement energy along the z axis and light holes have lower confinement energy along the xy plane. For a flat dot the confinement is stronger along z axis and for an elongated dot is stronger along x and y. As a consequence the ground state of flat dot with aspect ratio $L_{QD}/D_{QD} < 1$ is heavy hole type, while the ground state of an elongated dot with aspect ratio $L_{QD}/D_{QD} > 1$ is light hole type.

The second factor which determines the valence band ground state, is the axial shear strain, induced in the quantum dot due to lattice mismatch with the nanowire core. The strain problem can be solved analytically by considering that the quantum dot is in fact an ellipsoidal inclusion in an infinite matrix as described by Eshelby in [25].
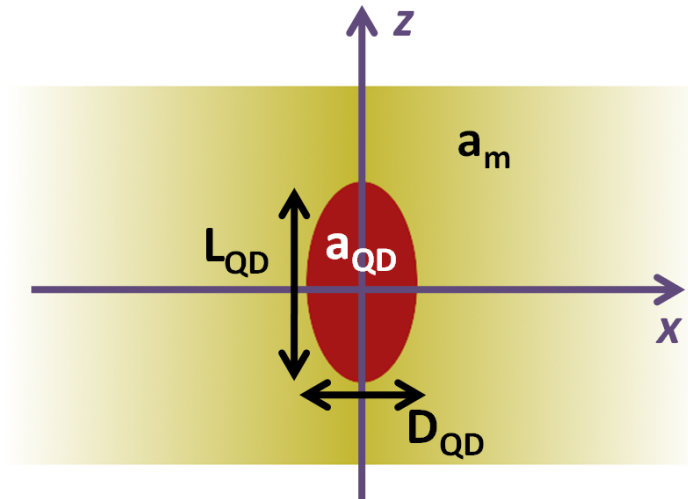

Figure 1.6 – A quantum dot in the form of an ellipsoidal inclusion in an infinite matrix. With a_{QD} we denote the lattice parameter of the quantum dot and with a_m that of the infinite medium.

The strain is uniform in the inclusion and from the analytical solutions of the model, we obtain the diagonal components of the strain tensor

$$\frac{\varepsilon_{zz}}{f} = \left(\frac{1+\nu}{1-\nu}\right)\left[\phi\left(\frac{L_{QD}}{D_{QD}}\right) - 1\right]$$
$$\frac{\varepsilon_{xx}}{f} = \frac{\varepsilon_{yy}}{f} = \left(\frac{1+\nu}{1-\nu}\right)\frac{1}{2}\phi\left(\frac{L_{QD}}{D_{QD}}\right)$$

(1.5)

where f the lattice mismatch and ν Poisson's ratio between the two materials. Functions ϕ are given by

$$\phi(x) = 1 - \left[1 - \frac{x\arccos(x)}{\sqrt{1-x^2}}\right]\frac{1}{1-x^2}, \quad x < 1$$

$$\phi(x) = 1 - \left[1 - \frac{x\ln\left(x + \sqrt{x^2-1}\right)}{\sqrt{x^2-1}}\right]\frac{1}{1-x^2}, \quad x > 1$$

(1.6)

From these expressions, we can calculate the hydrostatic ε_{hyd} and axial shear ε_{shear} strain given by

$$\varepsilon_{hyd} = \varepsilon_{xx} + \varepsilon_{yy} + \varepsilon_{zz} \quad \text{and} \quad \varepsilon_{shear} = \varepsilon_{zz} - \frac{(\varepsilon_{xx} + \varepsilon_{yy})}{2}$$

(1.7)

Hydrostatic strain is responsible for the shift of the band edges, while axial shear strain lifts the degeneracy of valence band. We give more details about Bir and Pikus mechanism in Chapter 2, section 2.2.4.
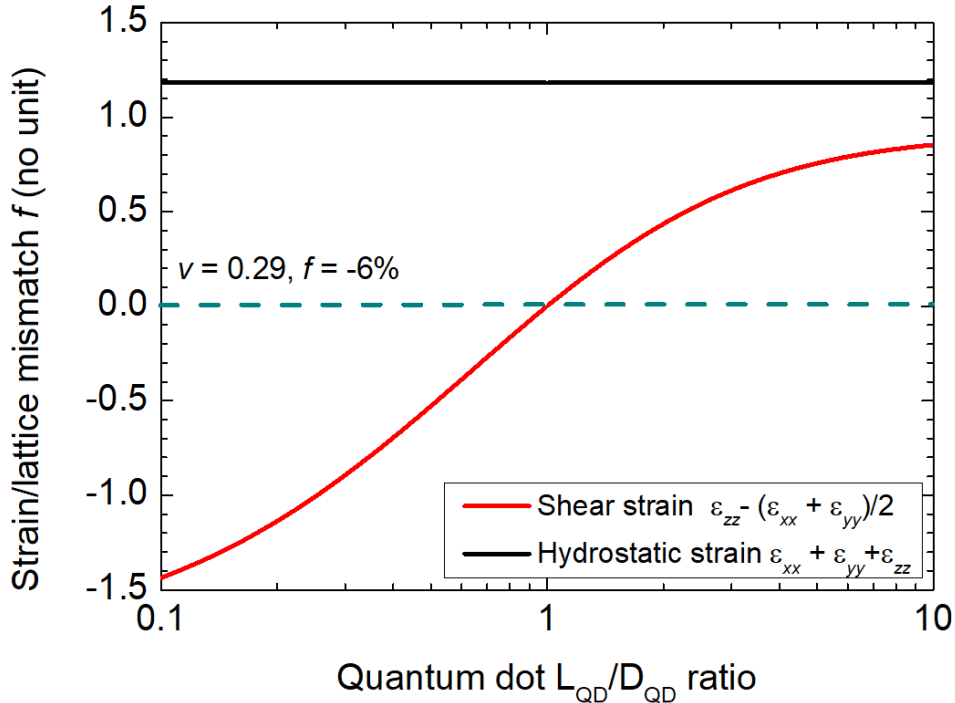

Figure 1.7 – Hydrostatic and axial shear strain divided by the lattice mismatch of an ellipsoidal inclusion inside an infinite matrix as a function of L_{QD}/D_{QD}.

In Fig. 1.7 we present the hydrostatic and axial shear strain of an ellipsoidal inclusion divided by the lattice mismatch as a function of the L_{QD}/D_{QD} aspect ratio as calculated from Eshelby's

model [25]. Hydrostatic strain remains constant for all values of L_{QD}/D_{QD}, meaning that it is independent of the shape and size of the quantum dot. On the contrary, axial shear strain normalized by the lattice mismatch, is monotonously decreasing and for $L_{QD}/D_{QD} < 1$ is positive, while for $L_{QD}/D_{QD} > 1$ it becomes negative. Of course the sign of axial shear strain is determined by the sign of the lattice mismatch. For a compressive mismatch it is $a_{QD} > a_m$ ($f_{\text{¡}}0$) and for a tensile one $a_{QD} < a_m$ ($f_{\text{¿}}0$). In the case of a tensile mismatch, we expect that for $L_{QD}/D_{QD} < 1$, shear strain will promote a light hole ground state. One has to keep in mind, that as L_{QD}/D_{QD} increases, the sign of axial shear strain changes and this governs the switching between heavy and light hole. In the convention we follow throughout this text, positive shear strain promotes a heavy hole and vice versa.
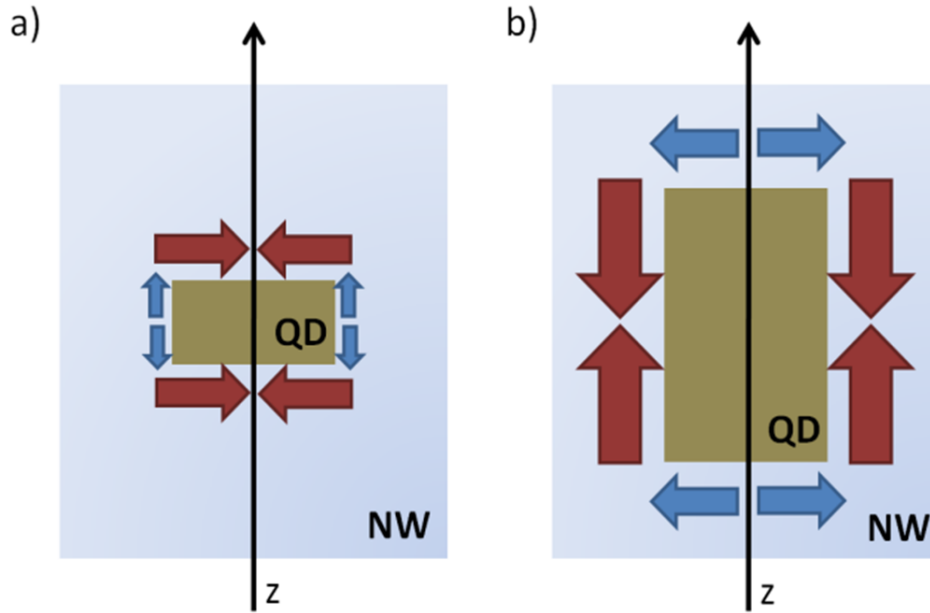
Figure 1.8 – A flat quantum dot in a nanowire where axial shear strain is compressive along xy plane a). An elongated quantum dot in a nanowire where axial shear strain becomes compressive along z axis b). For both cases it is $a_{QD} > a_{NW}$.

In Fig. 1.8 we present a scheme of the axial shear strain induced in a quantum dot from a nanowire core, assuming that the lattice parameter of the dot is larger than the lattice parameter of the nanowire ($a_{QD} > a_{NW}$). For a flat quantum dot, as shown in Fig. 1.8 a), strain is compressive in plane, while for an elongated quantum dot, similar to that shown in Fig. 1.8 b) strain becomes compressive along z axis. This in turn and in combination with confinement determines the valence band ground state.

For a bulk semiconductor under vanishing strain, similar to that shown in Fig. 1.9 a), heavy and light hole bands are degenerate, as a result we cannot discriminate between the two states. When axial shear strain is compressive in plane, then degeneracy gets lifted and heavy hole gets promoted as the valence band ground state. This is shown in Fig. 1.9 b). When the strain becomes compressive along z axis, a switching between the two valence band states occurs and light hole becomes the dominant ground state component over heavy hole. This is illustrated in Fig. 1.9 c).

By changing the sign of lattice mismatch, axial shear strain becomes negative for flat quantum dots with $L_{QD}/D_{QD} < 1$. This means that another way to probe a light hole ground state is through a flat tensile quantum dot in a nanowire [23]. This case will be investigated extensively in Chapter 4, where we will demonstrate that for this system, switching from heavy to light hole is not that straightforward.

No strain $\varepsilon_{zz} > \dfrac{\varepsilon_{xx} + \varepsilon_{yy}}{2}$ $\varepsilon_{zz} < \dfrac{\varepsilon_{xx} + \varepsilon_{yy}}{2}$

CB   CB   CB

HH   HH

LH   LH   LH

HH

a)   b)   c)

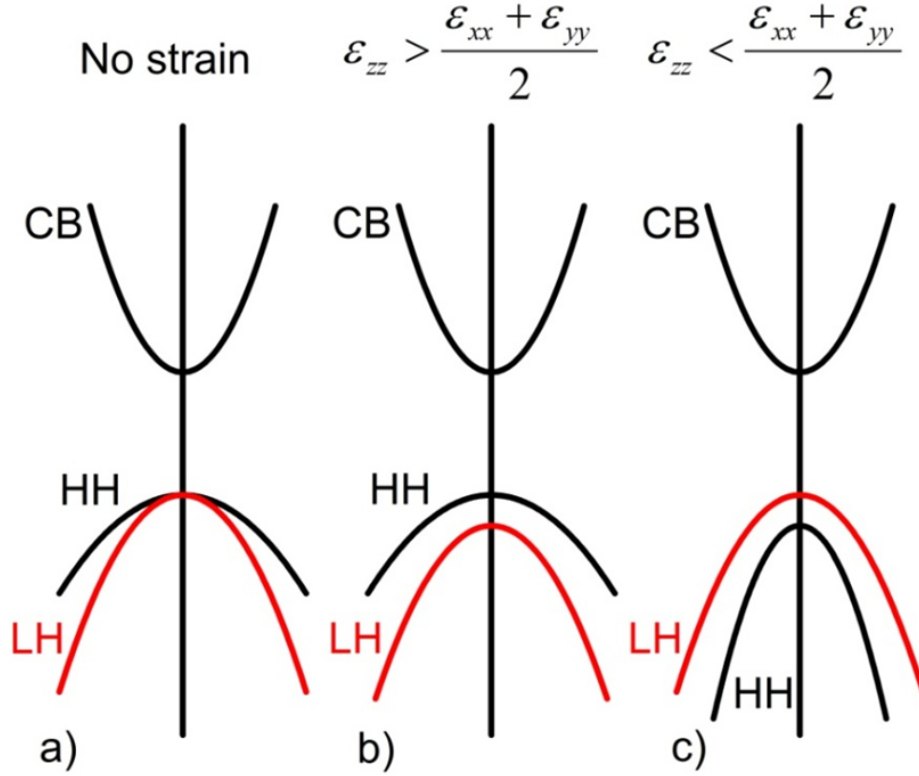Figure 1.9 – Schematic representation of the band structure, for a semiconductor without strain a), under compressive strain along *xyplane* b) and under compressive strain along z axis c)

From a theoretical point of view, in a very interesting article, the switching from heavy to light hole has been demonstrated by numerical calculations based on a tight binding method [26]. The author carried out the calculations on InAs cylindrical quantum dots embedded in InP nanowires along (001) direction.

In this work the diameter of the quantum dot is kept constant at $D_{QD} = 9.6$ nm and the height varied from $L_{QD} = 1.8$ nm to 18 nm. For $L_{QD}/D_{QD} < 1$ the ground state is predominantly of heavy hole type ($J_z = 3/2$). This is depicted in Fig. 1.10. When $L_{QD}/D_{QD} >= 1$, there is a sharp switching and light hole ($J_z = 1/2$) becomes the dominant ground state component. Since the nanowire axis is along (001) direction, the author neglects the piezoelectric effect. In our case we perform a similar study using $\vec{k} \cdot \vec{p}$ perturbation theory. The nanowire axis is along the (111) direction, consequently we take into account the piezoelectric effects. In addition we investigate the effect of an external shell around the nanowire core. The results are demonstrated in Chapter 2.

Incorporating a quantum dot in a nanowire and manipulating the valence band ground state by tuning the axial shear strain through its dimensions is an attractive alternative to multi-step procedures which involve both growth and sample processing as reported in [23]. The optical characterization of a Cd(Mn)Te-ZnTe nanowire quantum dot is reported in [27], where the emission of a light hole exciton is identified.

A powerful method to characterize the hole ground state is through polarization resolved Fourier spectroscopy. In this study, the as grown sample was introduced in the cryostat and the emission diagram was recorded for different polarization angles using a Fourier lens. The results are shown in Fig. 1.11. The emission diagram associated to the electric field of a dipole oscillating parallel to the nanowire axis is characterized by two rotating lobes for different polarization angles. This is also a direct evidence of a ground state with strong light hole contribution, as the dipole which contributes to π polarization is oriented parallel to the quantization axis
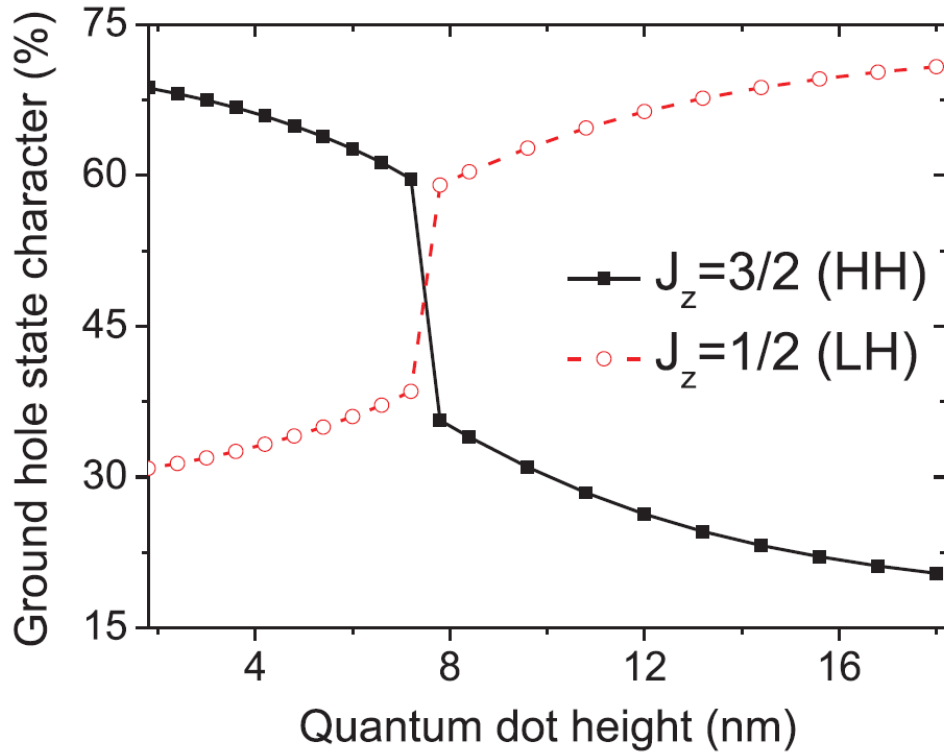
Figure 1.10 – Evolution of the hole ground state type in an InAs/InP nanowire quantum dot of diameter $D_{QD} = 9.6$ nm, as a function of dot height. Image taken from [26].
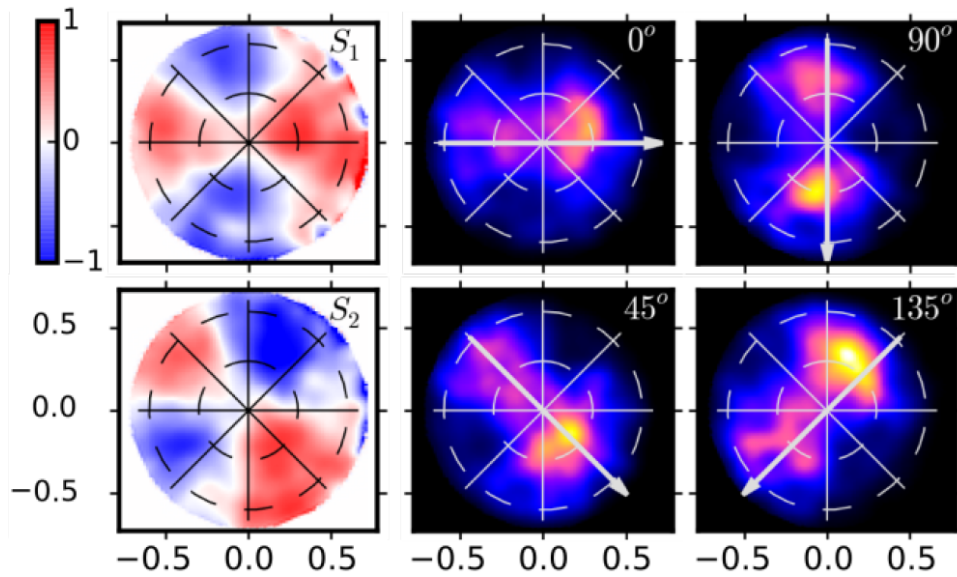
Figure 1.11 – Polarization resolved far field emission and the corresponding Stokes parameter colormaps of a Cd(Mn)Te quantum dot in a ZnTe nanowire as recorded from the as-grown sample. Image taken from [27].

of the dot. One limitation, is that Fourier spectroscopy provides conclusive results mostly for nanowires measured in vacuum, i.e. directly from the as-grown sample. When the objects are dispersed on a substrate, then the dielectric environment influences the far field emission and the analysis of recorded images is not straightforward. The authors of this work clarify that measurement results varied among different nanowires and that in many cases the valence band

ground state was strongly mixed. This is attributed to the weak valence band offset between CdTe and ZnTe. One of the objectives of present work is to tackle this issue and restore a stronger confinement of the hole ground state.

Experimentally we will employ two main techniques for characterizing the valence band ground state. As a first step we will investigate the optical properties of nanowire quantum dots by polarization resolved spectroscopy. Then we will study the hole properties of a diluted magnetic semiconductor nanowire quantum dot, by measuring the giant Zeeman shift for different orientations of an applied magnetic field.

1.4 Diluted Magnetic Semiconductors

For the magneto-optical measurements, CdTe quantum dots were doped with Mn in order to take advantage of the giant Zeeman effect, induced by $sp - d$ exchange interaction in magnetic alloys such as $Cd_{(1-x)}Mn_xTe$. The spin of Mn is $S_{Mn} = \frac{5}{2}$. The measurements are carried out in low temperatures, where Mn ions in diluted semiconductor alloys behave like paramagnetic spins, consequently the magnetization in the volume of a quantum dot can be expressed through a modified Brillouin function as

$$m = m_{sat}B_{5/2}\left[\frac{5\mu_B B}{k_B(T + T_0)}\right] \tag{1.8}$$

where T_0 is an effective temperature which takes into account the residual anti-ferromagnetic interaction between the non-nearest neighbor Mn ions [28].The expression of Brillouin function is

$$B_{\frac{5}{2}}(x) = \frac{6}{5}\coth\left(\frac{6}{5}x\right) - \frac{1}{5}\coth\left(\frac{1}{5}x\right) \tag{1.9}$$

The magnetization at saturation is given by

$$m_{sat} = g_{Mn}\mu_B S_{Mn}N_0 x_{eff} \tag{1.10}$$

where g_{Mn} and S_{Mn} the Landé factor and spin for Mn, N_0 the volume density of cation sites and x_{eff} the effective Mn concentration corresponding to magnetic ions which do not get blocked by anti-ferromagnetic interactions (essentially between the nearest neighbors). The Landé factor expression for Mn is

$$g_{Mn} = 1 + \frac{J(J + 1) + S_{Mn}(S_{Mn} + 1) - L(L - 1)}{2J(J + 1)} \tag{1.11}$$

where for $L = 0$ and $S_{Mn} = \frac{5}{2}$ it is $g_{Mn} = 2$.
In Fig. 1.12 a) we present x_{eff} as a function of total Mn content. For a Mn content of about 10%, which will be our target during the quantum dot growth, it is $x_{eff} \approx 4\%$. The effective Mn concentration as a function of the actual Mn content was investigated both experimentally and theoretically through numerical simulations in different works [29], [28]. The effective temperature T_0 increases with Mn content, as depicted in Fig. 1.12 b).

Giant Zeeman effect arises from the $sp - d$ exchange interaction between the photo generated carriers and the spin of magnetic atoms. The ferromagnetic sd exchange interaction is a direct consequence of Pauli's exclusion principle. When two electrons have the same spin, they can not be at the same energy level, as a result the repulsive Coulomb interaction energy decreases. On the other hand, electrons with opposite spins can occupy the same energy level, thus the repulsive interaction energy increases. This leads to an exchange constant $\alpha > 0$ between
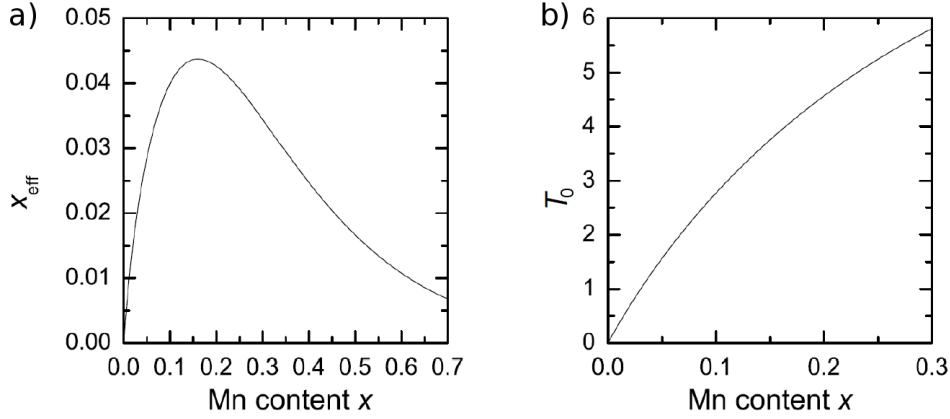
Figure 1.12 – Effective Mn concentration x_{eff} as a function of Mn content a). Effective temperature T_0 as a function of Mn content b). Images taken from [12]

electrons and Mn as shown in Eq. 1.13. $3d$ orbitals contribute to the valence band states of DMS based on the II-VI family of materials, consequently pd hybridization gives rise to an antiferromagnetic exchange interaction named *kinetic exchange* [12]. The exchange interaction Hamiltonian between carriers and Mn ions is

$$\mathcal{H}_{carriers-Mn} = -\alpha \sum_i \vec{S}_i \cdot \vec{\sigma}_e \delta(\vec{r} - \vec{r}_e) - \beta \sum_i \vec{S}_i \vec{\sigma}_h \delta(\vec{r} - \vec{r}_h) \tag{1.12}$$

where $\vec{\sigma}_e$, $\vec{\sigma}_h$ the electron and hole spin. With α we denote the exchange integral between s-like Γ_6 electrons and Mn spins, while β corresponds to the exchange integral for the p-like states of Γ_8 band, describing the interaction between holes and Mn spins. The exchange constant β is negative ($\beta < 0$). The values of α and β are given by

$$\begin{aligned} \alpha &= \langle S| J^{sp-d} |S\rangle \ \Omega_0 \\ \beta &= \langle X| J^{sp-d} |X\rangle \ \Omega_0 \end{aligned} \tag{1.13}$$

where $|S\rangle$ and $|X\rangle$ the orbital part of conduction band electrons and valence band holes, J^{sp-d} the electron - ion $sp-d$ exchange term and Ω_0 the volume of an elementary cell [15]. From mean field and virtual crystal approximation we replace $\vec{S}_i$ with the average value $< \vec{S} >$ at thermal equilibrium. This means that we treat all cations as equivalent, restoring the translational invariance of the crystal. By summing over all Mn atoms the Hamiltonian expression becomes

$$\mathcal{H}_{carriers-Mn} = \alpha \frac{\vec{m}}{g_{Mn}\mu_B} \cdot \vec{\sigma}_e + \beta \frac{\vec{m}}{g_{Mn}\mu_B} \cdot \vec{\sigma}_h \tag{1.14}$$

where

$$\vec{m} = -g_{Mn}\mu_B N_0 x_{eff} < \vec{S} > \tag{1.15}$$

In Fig. 1.13 a), b) we present a sketch of the Zeeman splitting for a heavy hole ground state in a quantum dot and in Fig. 1.13 c), d) for a light hole ground state. When the applied field is parallel to x axis, we expect vanishing splitting for a pure heavy hole, while for strong magnetic fields the two components of the Kramer's doublet could begin to shift weakly due to field
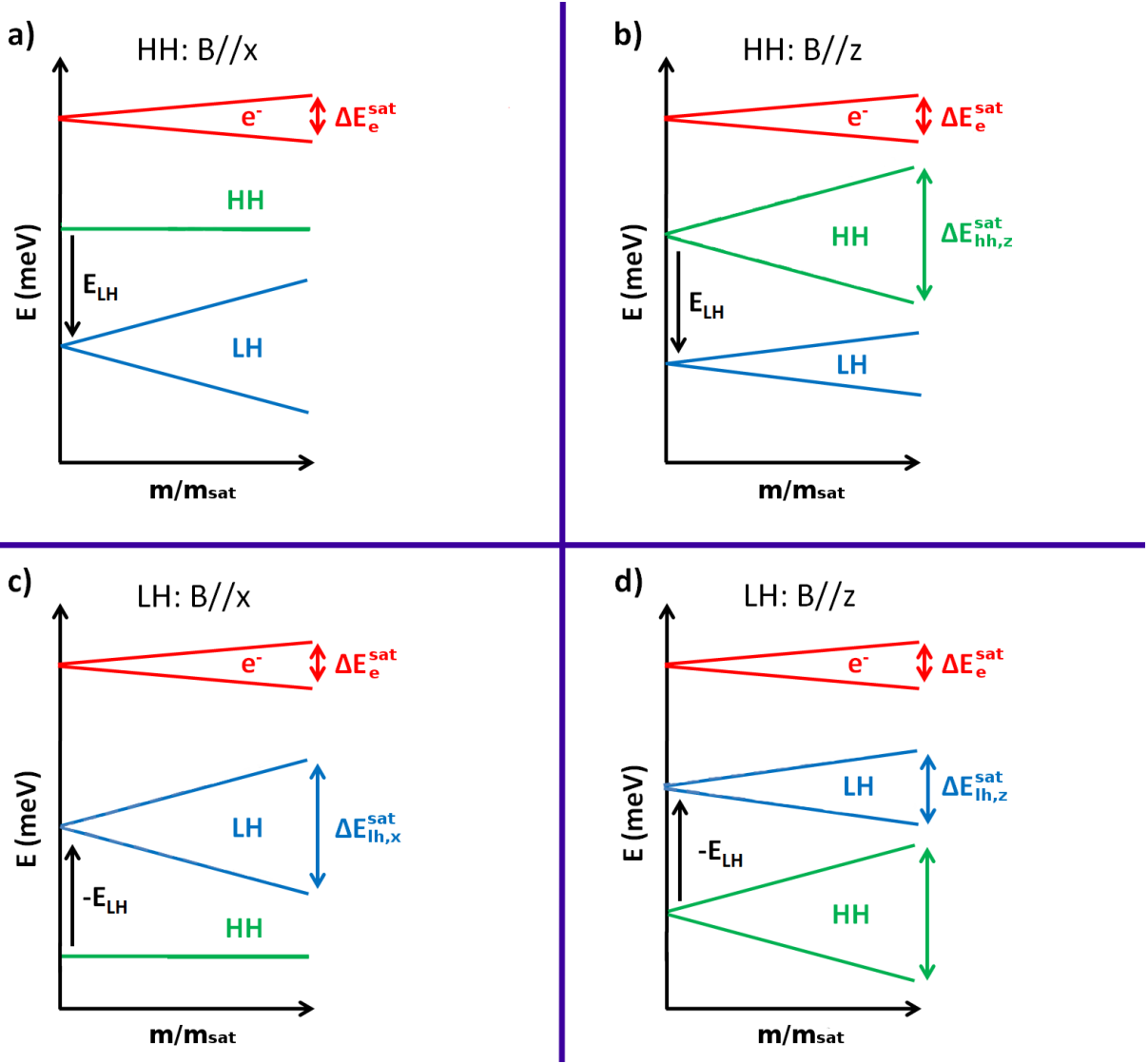
Figure 1.13 – Schematic representation of Zeeman splitting for a quantum dot with a heavy hole as aground state, for a magnetization perpendicular a) and parallel b) to the quantum dot quantization axis and for a light hole ground state with magnetization perpendicular c) and parallel d) to the quantum dot axis.

induced mixing with excited states. First we describe the results for valence and conduction band and then we present analytically how they are calculated.

- When the field is applied along z axis, the Zeeman splitting of heavy hole at saturation is $\Delta E_{hh,z}^{sat}$. For a light hole ground state, (and for a field applied perpendicular to the dot quantization axis) we expect a splitting of $\Delta E_{lh,x}^{sat} = \frac{2}{3}\Delta E_{hh,z}^{sat}$.

- For a field applied parallel to the dot quantization axis, we expect a splitting of $\Delta E_{lh,z}^{sat} = \frac{1}{3}\Delta E_{hh,z}^{sat}$. These results are obtained from Eq. 1.14, where the spin for heavy and light holes is given in Eq. 1.21 and Eq. 1.26 respectively. We notify the reader in advance, that The Zeeman shift, might get affected by the anticrossing of excited states. This is discussed thoroughly in Chapter 3.

- Concerning conduction band electrons, Zeeman shift is isotropic and regardless the direction of field, splitting at saturation is always equal to ΔE_e^{sat}. This is attributed to the fact that spin is also isotropic in space. Spin matrices for electrons are shown in Eq. 1.17.

In the following paragraphs we will develop the formalism describing the Zeeman splitting

for electrons, heavy holes and light holes.

Electron Zeeman splitting

For the electrons in conduction band, the Hamiltonian is written

$$\mathcal{H}_{e-Mn} = \alpha \frac{\vec{m}}{g_{Mn}\mu_B} \cdot \vec{\sigma}_e = \frac{\alpha}{g_{Mn}\mu_B} \begin{pmatrix} \frac{m_z}{2} & \frac{m_x - m_y i}{2} \\ \frac{m_x + m_y i}{2} & -\frac{m_z}{2} \end{pmatrix} \tag{1.16}$$

where $\vec{\sigma}_{e,(x,y,z)}$ the electron spin matrices, given by

$$\sigma_{e,z} = \begin{pmatrix} 1/2 & 0 \\ 0 & -1/2 \end{pmatrix}, \qquad \sigma_{e,x} = \begin{pmatrix} 0 & 1/2 \\ 1/2 & 0 \end{pmatrix}, \qquad \sigma_{e,y} = \begin{pmatrix} 0 & -i/2 \\ i/2 & 0 \end{pmatrix} \tag{1.17}$$

From the above Hamiltonian expression we calculate the Zeeman splitting for electrons which is isotropic for any direction of $\vec{m}$

$$\Delta E_e = \frac{\alpha m}{g_{Mn}\mu_B} = \Delta E_e^{sat} \frac{m}{m_{sat}} \tag{1.18}$$

where ΔE_e^{sat}, the saturation energy for electrons, given by

$$\Delta E_e^{sat} = N_0 x_{eff} \alpha S_{Mn} \tag{1.19}$$

For $\alpha > 0$, $|-1/2\rangle$ state moves towards lower energies. Assuming an effective Mn concentration $x_{eff} \approx 4\%$, the $sp - d$ exchange constants for electrons is $N_0\alpha = 0.22$ [15], resulting a Zeeman splitting at saturation $\Delta E_e^{sat} = 22$meV.

Heavy hole Zeeman splitting

The exchange interaction Hamiltonian between heavy holes and Mn ions is

$$\mathcal{H}_{hh-Mn} = \beta \frac{\vec{m}}{g_{Mn}\mu_B} \cdot \vec{\sigma}_{hh} = \frac{\beta}{g_{Mn}\mu_B} \begin{pmatrix} \frac{m_z}{2} & 0 \\ 0 & -\frac{m_z}{2} \end{pmatrix} \tag{1.20}$$

as the spin matrices in that case are

$$\sigma_{hh,z} = \begin{pmatrix} 1/2 & 0 \\ 0 & -1/2 \end{pmatrix} \quad \text{and} \quad \sigma_{hh,x} = \sigma_{hh,y} = 0 \tag{1.21}$$

Along x, y and z axis, the spin expectation values for heavy hole are $< S_x >=< S_y >= 0$ and $< S_z >= \frac{1}{2}$ respectively. As a result, the energy splits only for a field applied along z as for the other two directions, Zeeman shift vanishes. From the Hamiltonian of Eq. 1.20, we calculate the Zeeman shift for heavy holes along x, y and z axis

$$\Delta E_{hh,x} = \Delta E_{hh,y} = 0 \quad \Delta E_{hh,z} = \frac{|\beta|}{g_{Mn}\mu_B} m_z = \Delta E_{hh,z}^{sat} \frac{m_z}{m_{sat}} \tag{1.22}$$

with

$$\Delta E_{hh,z}^{sat} = N_0 |\beta| S_{Mn} x_{eff} \tag{1.23}$$

From the operations above, we confirm that the Zeeman shift for heavy holes is anisotropic

for $\beta < 0$, $|3/2, +3/2\rangle$ moves to lower energies. As regards a field applied along z axis, the $sp - d$ exchange constant for heavy holes, is $N_0\beta = 0.88$ [15], [30]. As a result the giant Zeeman splitting of heavy holes at saturation is $\Delta E_{hh}^{sat} = 88$ meV [30], [31]. Experimentally, from magneto-optical spectroscopy, we measure the Zeeman shift of the exciton and in order to calculate it, we must take into account the splitting of both electrons and holes. The Zeeman shift for a heavy hole exciton is given by

$$\Delta E_{X-hh,z} = \frac{(\Delta E_e^{sat} + \Delta E_{hh,z}^{sat})}{2} \frac{m}{m_{sat}}$$

$$\Delta E_{X-hh,x} = \Delta E_{X-hh,y} = \frac{\Delta E_e^{sat}}{2} \frac{m}{m_{sat}} \tag{1.24}$$

For $x_{eff} \approx 4\%$, at saturation, we expect $\Delta E_{X-hh,z} = 50$ meV and $\Delta E_{X-hh,x} = 11$ meV. As mentioned earlier, this is what we expect for a pure heavy hole state, strongly isolated from excited states. In a real system however and in particular for a magnetization along x or y, we anticipate that field induced mixing between heavy and light holes will result a non-linear giant Zeeman effect.

Light hole Zeeman splitting

The exchange interaction Hamiltonian between light holes and Mn ions is

$$\mathcal{H}_{lh-Mn} = \beta \frac{\vec{m}}{g_{Mn}\mu_B} \cdot \vec{\sigma}_{lh} = \frac{\beta}{g_{Mn}\mu_B} \begin{pmatrix} \frac{m_z}{6} & \frac{m_x - m_y i}{3} \\ \frac{m_x + m_y i}{3} & -\frac{m_z}{6} \end{pmatrix} \tag{1.25}$$

where the spin matrices in that case, they are

$$\sigma_{lh,z} = \begin{pmatrix} 1/6 & 0 \\ 0 & -1/6 \end{pmatrix}, \quad \sigma_{lh,x} = \begin{pmatrix} 0 & 1/3 \\ 1/3 & 0 \end{pmatrix}, \quad \sigma_{lh,y} = \begin{pmatrix} 0 & -i/3 \\ i/3 & 0 \end{pmatrix} \tag{1.26}$$

For the light hole states, the spin expectation values along x, y and z axis are $< S_x >=< S_y >= \frac{1}{3}$ and $< S_z >= \frac{1}{6}$, consequently we expect a Zeeman shift for any direction of the applied field. By diagonalizing the exchange interaction Hamiltonian, we calculate the Zeeman splitting for light holes

$$\Delta E_{lh} = \frac{2|\beta|}{g_{Mn}\mu_B} \sqrt{\frac{m_z^2}{6^2} + \frac{(m_x^2 + m_y^2)}{3^2}} = 2\Delta E_{hh,z}^{sat} \frac{\sqrt{\frac{m_z^2}{6^2} + \frac{(m_x^2 + m_y^2)}{3^2}}}{m_{sat}} \tag{1.27}$$

Similarly to heavy holes, Zeeman shift for light holes is also anisotropic, depending on the direction of magnetization vector and for $\beta < 0$, $|+3/2, 1/2\rangle$ component moves to lower energies. Assuming $\Delta E_{hh,z}^{sat} = 88$ meV for heavy holes, the giant Zeeman splitting at saturation for light holes along z axis and x axis is respectively $\Delta E_{lh,z}^{sat} \approx 29$ meV and $\Delta E_{lh,x}^{sat} \approx 59$ meV [32]. Including the energy shift of the electrons, we calculate the Zeeman shift of a light hole exciton, through the relations

$$\Delta E_{X-lh,z} = \frac{[\Delta E_e^{sat} + \frac{\Delta E_{hh,z}^{sat}}{3}]}{2} \frac{m_z}{m_{sat}}$$

$$\Delta E_{X-lh,x} = \Delta E_{X-lh,y} = \frac{[\Delta E_e^{sat} + \frac{2\Delta E_{hh,z}^{sat}}{3}]}{2} \frac{m_{(x,y)}}{m_{sat}} \tag{1.28}$$

For $x_{eff} \approx 4\%$, at saturation, we expect $\Delta E_{X-lh,z} = 26$ meV and $\Delta E_{X-lh,x} = 40$ meV.

Exchange field induced by Mn to the carriers

In this paragraph we calculate the exchange field acting on the carriers due to the presence of Mn spins. The Hamiltonian describing the exchange interaction between Mn spins and electrons can be rewritten as

$$\mathcal{H}_{e-Mn} = g_e \mu_B \vec{B}_{exc,e}^{Mn} \cdot \vec{\sigma}_e \tag{1.29}$$

and the exchange field acting on electrons

$$\vec{B}_{exc,e}^{Mn} = \frac{\alpha \vec{m}}{(g_e \mu_B)(g_{Mn} \mu_B)} = \frac{\Delta E_e^{sat}}{g_e \mu_B} \left(\frac{\vec{m}}{m_{sat}} \right) \tag{1.30}$$

The Hamiltonian describing the exchange interaction between Mn spins and heavy holes can be rewritten as

$$\mathcal{H}_{hh-Mn} = g_e \mu_B \vec{B}_{exc,hh}^{Mn} \cdot \vec{\sigma}_h \tag{1.31}$$

From this Hamiltonian we calculate the exchange field acting on the spin of the holes

$$\vec{B}_{exc,hh}^{Mn} = \frac{|\beta| \vec{m}}{(g_e \mu_B)(g_{Mn} \mu_B)} = \frac{\Delta E_{hh}^{sat}}{g_0 \mu_B} \frac{\vec{m}}{m_{sat}} \tag{1.32}$$

This results an exchange field $0 \leq \vec{B}_{exc,hh}^{Mn} \leq 759.4$ T for $0 \leq m \leq m_{sat}$. We inform the reader in advance that the numerical calculations discussed in Chapter 3 are carried out under this exchange field.

In a very interesting report, the authors identified the light hole character of excitonic emission in CdMnTe - CdMgTe core - shell nanowires [33]. In this work they investigated the hole properties by recording the micro-photoluminescence spectra of individual nanowires under magnetic field. In order to perform these measurements, CdTe was doped with Mn ions. Through magnetic doping, the energy splitting gets enhanced due to giant Zeeman effect induced by the $sp - d$ exchange interaction between the generated carriers and localized Mn spins.
For their measurements they used a vectorial magnet through which they were able to apply the magnetic field along different directions on zx plane. They observed that the Zeeman shift was larger when the magnetic field was applied perpendicular to the nanowire axis and by applying a numerical model to fit their results, they confirmed a ground state of predominantly light hole type. The energy shift for the two orientations of magnetic field and the anisotropic shift for a rotating field in plane, are shown in Fig. 1.14 a) and Fig. 1.14 b) respectively. For a light hole ground state we expect a larger Zeeman shift for a field applied perpendicular to the nanowire axis due to the fact that along this direction, spin expectation value $< S_x >= 1/3$ is larger than the value along z, $< S_z >= 1/6$.

In this section, we described the giant Zeeman effect in a diluted magnetic semiconductor, induced by doping it with magnetic ions. In the following section, we will describe the effect of carriers on the spin of magnetic impurities.

1.5   Magnetic polaron formation

In this subsection, we discuss the effect of magnetic polaron and its influence on Zeeman shift, as recorded through magneto-optical measurements. In Fig. 1.15 is presented schematically the mechanism of magnetic polaron formation.
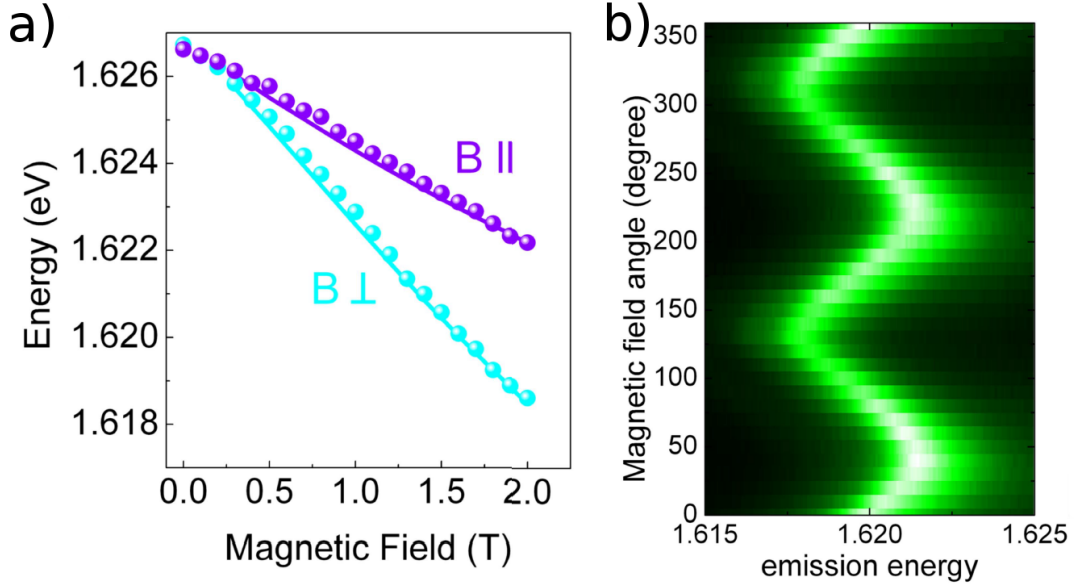
Figure 1.14 – Energy shift for different orientations of magnetic field as recorded for a dispersed nanowire a). Field applied along zx plane demonstrating the anisotropic Zeeman shift. Images taken from [33].

The spin of an exciton in a DMS can polarize the spins of magnetic ions which are localized within its presence probability through the $sp-d$ exchange interaction [15]. This polarization of spins leads to the decrease of exciton energy by a quantity E_{MP} which is defined as the magnetic polaron energy. This simultaneous polarization of spins, introduces a total magnetic moment to the system which at low temperatures takes values in the order of $10^2 \mu_B$ [35]. The magnetic polaron effect was first revealed experimentally by transport measurements carried out on EuO [36]. More detailed studies based on diluted magnetic semiconductors quantifying the polaron energy E_{MP} and spin were published in later years [37], [38]. The focus of these studies was bound magnetic polaron states, with conduction band electrons in CdMnSe. This effect was revealed by measuring the Stokes shift under magnetic field. In another work, a bound magnetic polaron state formed by the exchange field introduced by holes, was reported for p-type CdMnTe structures [39].

The first study of localized exciton magnetic polaron in $Cd_{1-x}Mn_xTe$ bulk epilayers is reported in [40], where localized excitons were probed through selective excitation using a tunable dye laser. The authors measured the Stokes shift through which they determined the energy of the localized exciton magnetic polarons.

The most direct evidence of an exciton magnetic polaron formation in a self assembled quantum dot is by plotting the emission energy as a function of temperature.
In Fig. 1.16 a) is presented the energy shift of a flat $Cd_{1-x}Mn_xTe$ quantum dot with different Mn concentrations, varying from 4-10%. From these plots, it becomes clear that as Mn concentration increases, Zeeman shift is larger, further confirming the giant Zeeman effect induced by the $sp-d$ exchange interaction. In Fig. 1.16 b) are depicted the temperature dependent measurements of the same samples. From these plots we clearly see that the energy shift as a function of temperature is not monotonous. The fact that emission energy decreases by decreasing temperature is an indication of the magnetic polaron formation. This effect becomes stronger by increasing Mn concentration and it is attributed to the polarization of Mn spins due to the exchange field induced by the carriers. As shown in In Fig. 1.16 b), from 50 K to 30 K the blueshift in emission energy corresponds to the increase of the band gap. Below 20 K we observe a redshift resulting from the exchange coupling between the carriers and Mn ions which at low
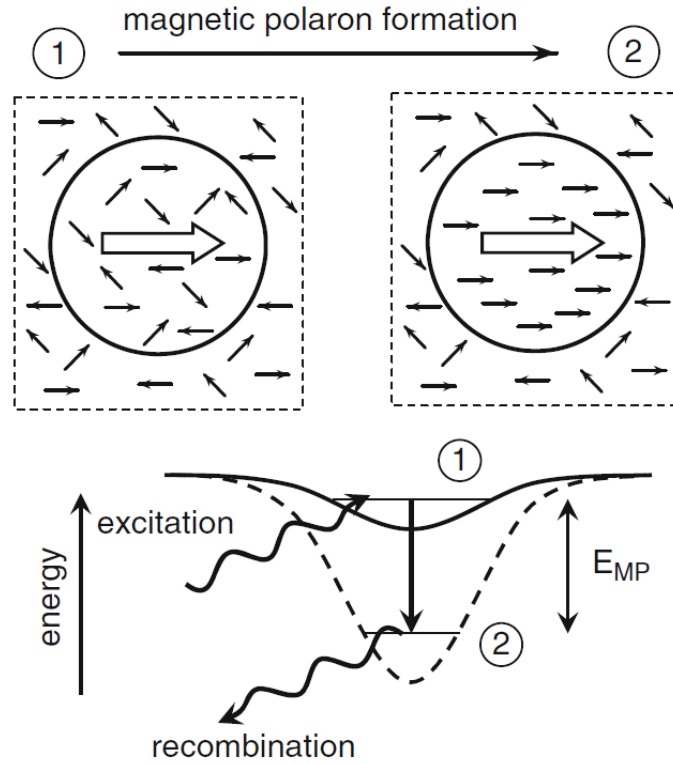
Figure 1.15 – Schematic representation of magnetic polaron formation in a diluted magnetic semiconductor (DMS). The spin of the photogenerated exciton is depicted with the large arrow where the surrounding circle designates the orbit determined by the exciton Bohr radius. With small black arrows we denote the spin introduced by the magnetic ions, which initially are randomly oriented (state 1). Within the Bohr radius, the magnetic ion spins are aligned ferromagnetically while exciton energy decreases by the magnetic polaron formation (state 2). With E_{MP} we denote the magnetic polaron energy. Figure taken from [34]
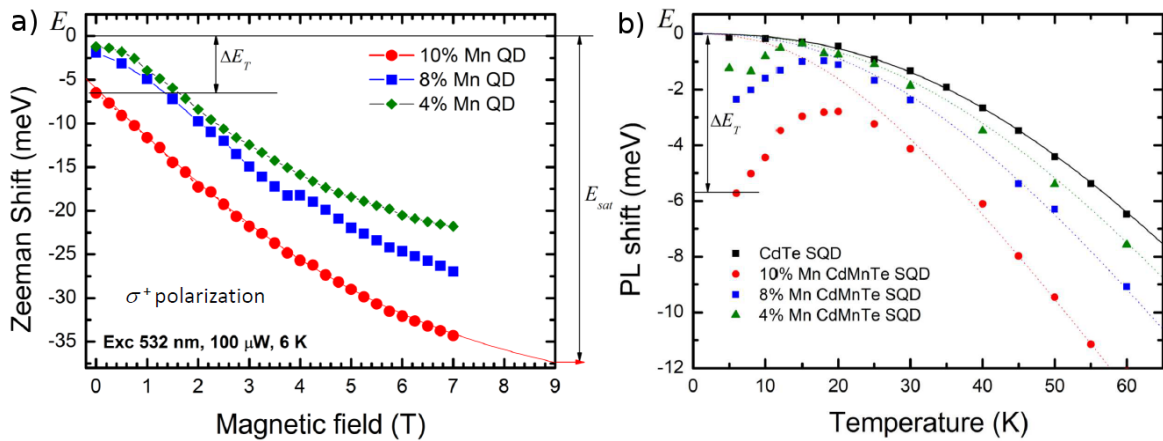
Figure 1.16 – Zeeman shift of a flat $Cd_{1-x}Mn_xTe$ quantum dot emission with different Mn content a). Energy position as a function of temperature for the same samples. Images taken from [12].

temperatures they align their spins. This alignment induces a Zeeman shift of the emission energy. As a first step, we describe this exchange interaction for electrons and hole separately and then we will calculate the exchange field induced by the exciton.

Electron exchange field

In this paragraph we consider a quantum dot occupied by one electron. As we will see, the presence of the electron, induces an exchange field which acts on Mn spins. Starting from the Hamiltonian describing the exchange field of electrons acting on the Mn spin, we calculate

$$\mathcal{H}_{e-Mn} = \frac{\alpha \vec{m}}{g_{Mn}\mu_B} \cdot \vec{\sigma}_e = -\vec{M} \cdot \vec{B}^e_{exc} \tag{1.33}$$

where $\vec{M} = V_{QD}\vec{m}$ the total magnetic moment in the volume V_{QD} of the quantum dot. In that case, the exchange field induced by the electron is given by

$$\vec{B}^e_{exc} = -\frac{a\vec{\sigma}_e}{g_{Mn}\mu_B V_{QD}} \tag{1.34}$$

and it is isotropic towards every direction. For a quantum dot of volume $V_{QD} = 100$ nm^3 for instance, conduction band $|+1/2\rangle$ component, will induce an exchange field $B^e_{exc} \approx 0.5$ T.

Heavy hole field

For a heavy hole, the exchange Hamiltonian is

$$\mathcal{H}_{hh-Mn} = \frac{\beta \vec{m} \cdot \vec{\sigma}_{hh}}{g_{Mn}\mu_B} = -\vec{M} \cdot \vec{B}^{hh}_{exc} \tag{1.35}$$

Then the exchange field along x, y and z axis is

$$B^{hh}_{exc,x} = B^{hh}_{exc,y} = 0 \quad \text{and} \quad B^{hh}_{exc,z} = \frac{|\beta|\sigma_{hh,z}}{g_{Mn}\mu_B V_{QD}} \tag{1.36}$$

where again for quantum dot with volume $V_{QD} \approx 100$ nm^3, the exchange field along z axis, is $B^{hh}_{exc,x} = 2.5$ T.

Light hole exchange field

By carrying out similar calculations, the exchange field induced by a light hole is

$$\begin{aligned} B^{lh}_{exc,z} &= \frac{|\beta|\sigma_{lh,z}}{g_{Mn}\mu_B V_{QD}} = \frac{B^{hh}_{exc,z}}{3} \\ B^{lh}_{exc,x} &= \frac{|\beta|\sigma_{lh,x}}{g_{Mn}\mu_B V_{QD}} = \frac{2B^{hh}_{exc,z}}{3} \end{aligned} \tag{1.37}$$

This exchange field is non zero in all directions and it becomes maximum when it is along x axis.

To summarize, the exchange fields B^e_{exc}, B^{hh}_{exc} and B^{lh}_{exc} are responsible for a carrier induced ferromagnetism in doped diluted magnetic semiconductors and for the formation of an exciton magnetic polaron in a quantum dot.

Exciton exchange field

In the presence of an exciton we have to sum the exchange fields induced by both electrons and holes. An optically bright heavy hole exciton can be formed by the $|-1/2\rangle$ electron and $|+3/2\rangle$ hole state and is characterized by a σ^+ transition, or by the $|+1/2\rangle$ and $|-3/2\rangle$ where in that case the transition is a σ^-. The exchange field induced by a heavy hole exciton is

$$B_{exc,z}^{X-hh} = \pm(B_{exc}^e + B_{exc}^{hh})$$
$$B_{exc,x}^{X-hh} = B_{exc,y}^{X-hh} = 0$$

$$(1.38)$$

For a light hole, the picture is more complicated as the exciton is also characterized by a π state, formed either by a $|+1/2\rangle$ electron and a $|-1/2\rangle$ hole, or by a $|-1/2\rangle$ electron and a $|+1/2\rangle$ hole. In that case the exchange field is non zero everywhere and it depends on the polar angle θ in respect to z axis

$$B_{exc}^{X-lh}(\theta) = \pm\left[B_{exc}^e + 2B_{exc}^{hh}\sqrt{\frac{cos^2(\theta)}{6^2} + \frac{sin^2(\theta)}{3^2}}\right]$$

$$(1.39)$$

For a light hole exciton, it is always $B_{exc}^{X-lh} \neq 0$ for different spin orientations and the exchange field takes its maximum absolute value for $\theta = \pm 90^o$, parallel to x axis

$$B_{exc,x}^{X-lh} = \pm\left(B_{exc}^e + \frac{2}{3}B_{exc}^{hh}\right)$$

$$(1.40)$$

For a more detailed and complete description of the magnetic polaron effect in semiconductor nanowire quantum dots we prompt the reader in reference [32].

1.6   Conclusions

In this chapter we presented the properties of diluted magnetic semiconductors based on II-VI materials and we discussed the benefits of stabilizing a light hole over a heavy hole in a semiconductor nanowire quantum dot. In Chapters 2 and 3 we present the results obtained from numerical calculations by $\vec{k} \cdot \vec{p}$ theory and in Chapter 4 the results from optical spectroscopy.

Chapter 2

Parameters governing the heavy hole - light hole switching and mixing

2.1 Introduction

The valence band ground state of a quantum dot is influenced by strains and the valence band offset between the dot and the nanowire core. Also the piezoelectric effects induced by shear strain affect the optical properties of the heterostructure as they enhance the electron-hole separation thus reducing the oscillator strengths. In this chapter we first develop the theory and methods used for the electronic structure calculation. We begin by describing continuum elasticity and piezoelectric effects and then the valence and conduction band calculation by $\vec{k} \cdot \vec{p}$ theory. Finally we present the numerical calculations results, on anisotropic nanowire quantum-dots based on the II-VI materials and their analysis.

2.2 The theoretical framework for calculating the electronic structure

In this section we present a summary of the theory upon which the computational models are developed. Initially we discuss strains in the context of continuum elasticity theory. Then we will describe the piezoelectric effects which emerge due to strains. Finally we develop the 6 band $k \cdot p$ Hamiltonian, taking into account both strain and piezoelectric potentials.

2.2.1 Continuum elasticity

Strain in a semiconductor heterostructure is induced by the crystal deformation due to the lattice mismatch of the materials comprising it. The strain introduced to a material of lattice constant a' from a material with lattice constant a due to mismatch at their interface is

$$\varepsilon_{||} = \frac{a - a'}{a'} \tag{2.1}$$

An unstrained lattice can be represented by three unit vectors $\hat{x}$, $\hat{y}$ and $\hat{z}$ [41]. As shown in Figure 2.1, a deformation of the lattice alters both the orientation and magnitude of these vectors which are written as follows:

$$\begin{aligned}
\hat{x}' &= (1 + \varepsilon_{xx})\hat{x} + \varepsilon_{xy}\hat{y} + \varepsilon_{xz}\hat{z} \\
\hat{y}' &= \varepsilon_{yx}\hat{x} + (1 + \varepsilon_{yy})\hat{y} + \varepsilon_{yz}\hat{z} \\
\hat{z}' &= \varepsilon_{zx}\hat{x} + \varepsilon_{zy}\hat{y} + (1 + \varepsilon_{zz})\hat{z}
\end{aligned} \tag{2.2}$$

The deformation of the lattice is defined by the components of the transformation matrix

$$\varepsilon = \begin{pmatrix} \varepsilon_{xx} & \varepsilon_{xy} & \varepsilon_{xz} \\ \varepsilon_{yx} & \varepsilon_{yy} & \varepsilon_{yz} \\ \varepsilon_{zx} & \varepsilon_{zy} & \varepsilon_{zz} \end{pmatrix} \tag{2.3}$$

After a deformation, the new position of a lattice point being initially at $\boldsymbol{r}{=}x\hat{\boldsymbol{x}}{+}y\hat{\boldsymbol{y}}{+}z\hat{\boldsymbol{z}}$ will be $\boldsymbol{r}' = x\hat{\boldsymbol{x}}' + y\hat{\boldsymbol{y}}' + z\hat{\boldsymbol{z}}'$. The displacement field $\boldsymbol{R}$ due to deformation is defined as follows

$$\boldsymbol{R} = \boldsymbol{r}' - \boldsymbol{r} = x(\boldsymbol{x}' - \hat{\boldsymbol{x}}) + y(\boldsymbol{y}' - \hat{\boldsymbol{y}}) + z(\boldsymbol{z}' - \hat{\boldsymbol{z}}) \tag{2.4}$$

or by taking into account Eq. 2.2

$$\boldsymbol{R}(\boldsymbol{r}) = (x\epsilon_{xx} + y\epsilon_{yx} + z\epsilon_{zx})\hat{\boldsymbol{x}} + (x\epsilon_{xy} + y\epsilon_{yy} + z\epsilon_{zy})\hat{\boldsymbol{y}} + (x\epsilon_{xx} + y\epsilon_{yz} + z\epsilon_{zz})\hat{\boldsymbol{z}} \tag{2.5}$$

The equation above can be written in a more simplified form by using the vectors u, v, w

$$\boldsymbol{R}(\boldsymbol{r}) = u(\boldsymbol{r})\hat{\boldsymbol{x}} + v(\boldsymbol{r})\hat{\boldsymbol{y}} + w(\boldsymbol{r})\hat{\boldsymbol{z}} \tag{2.6}$$
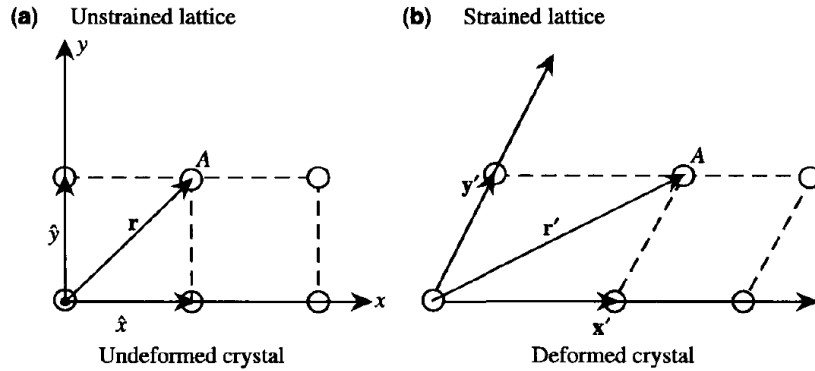
Figure 2.1 – Schematic representation of the position vector **r** for (a) a deformed lattice and (b) an undiformed one. Image taken from [42]

For convenience, the strain components which describe the infinitesimal distortions due to change of length can be written as

$$\begin{aligned} e_{xx} &= \varepsilon_{xx} = \frac{\partial u}{\partial x} \\ e_{yy} &= \varepsilon_{yy} = \frac{\partial v}{\partial y} \\ e_{zz} &= \varepsilon_{zz} = \frac{\partial w}{\partial z} \end{aligned} \tag{2.7}$$

and the remaining components defined in terms of the angle change between the axis as

$$\varepsilon_{xy} = \hat{x}' \cdot \hat{y}' = \frac{1}{2}(e_{xy} + e_{yx}) = \frac{1}{2}\left(\frac{\partial u}{\partial y} + \frac{\partial v}{\partial x}\right)$$

$$\varepsilon_{yz} = \hat{y}' \cdot \hat{z}' = \frac{1}{2}(e_{yz} + e_{zy}) = \frac{1}{2}\left(\frac{\partial v}{\partial z} + \frac{\partial w}{\partial y}\right) \qquad (2.8)$$

$$\varepsilon_{zx} = \hat{z}' \cdot \hat{x}' = \frac{1}{2}(e_{zx} + e_{xz}) = \frac{1}{2}\left(\frac{\partial u}{\partial z} + \frac{\partial w}{\partial x}\right)$$

The fractional increase of the volume crystal is called the *dilation* [43] and it is given by the relation

$$\frac{V + \delta V}{V} = x' \cdot y' \times z' = 1 + (\varepsilon_{xx} + \varepsilon_{yy} + \varepsilon_{zz}) \qquad (2.9)$$

When strain is induced to a crystal, its response is manifested through the force of *stress* τ_{ij}. The first index of stress component represents the direction of the applied force, while the second one the direction parallel to the normal of the plane on which the force is applied (Figure 2.2). Since strain components are only ratios of lengths, they are dimensionless. On the other hand stress has dimensions of force per unit area, or energy per unit volume [43] .
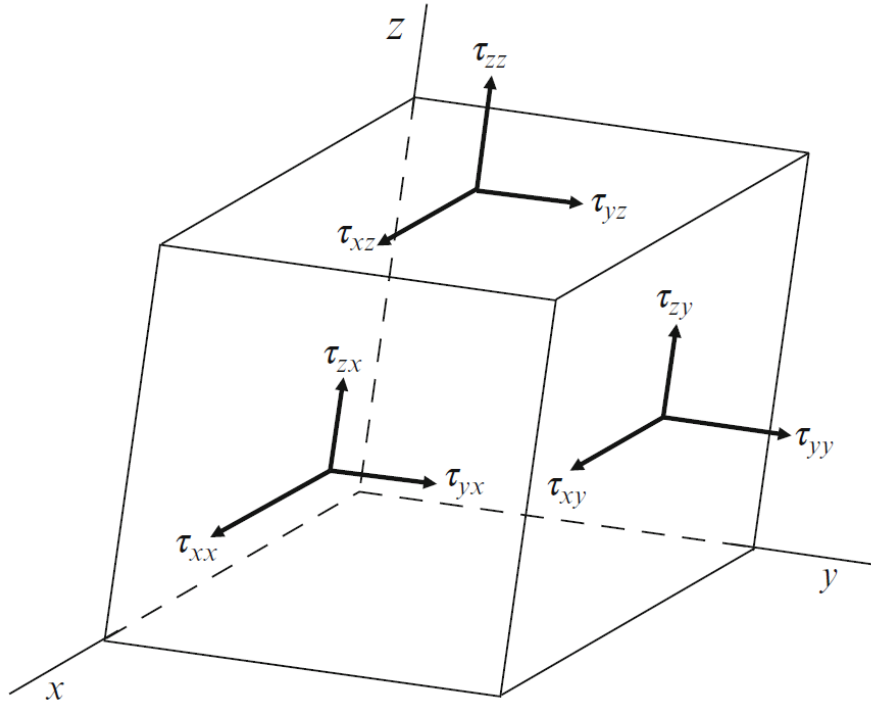
Figure 2.2 – Different stress components on the planes of an infinitesimal cube. Image taken from [41]

For sufficiently small deformations, stress is linearly connected to strain through Hooke's law by the relation

$$\tau_{ij} = \sum_{uv} C_{ijuv} e_{uv}, \quad i, j, u, v = x, y, z \qquad (2.10)$$

where C_{ijum} are the components of the elastic stiffness tensor which describes the linear elastic behavior of a material. By excluding rotations, we impose that both tensors of stress and strain

are symmetric. As a result we have $C_{ijuv} = C_{jiuv} = C_{ijvu}$, thus we can define their respective tensors through a six component array by sum

$$\tau_{ij} = \sum_m C_{im} e_m \tag{2.11}$$

where in the so-called Voigt notation, $e_1 = \varepsilon_{xx}$, $e_2 = \varepsilon_{yy}$, $e_3 = \varepsilon_{zz}$, $e_4 = 2\varepsilon_{zy}$, $e_5 = 2\varepsilon_{xz}$ and $e_6 = 2\varepsilon_{xy}$. In matrix form the above expression is written

$$\begin{pmatrix} \tau_{xx} \\ \tau_{yy} \\ \tau_{zz} \\ \tau_{xy} \\ \tau_{xz} \\ \tau_{yz} \end{pmatrix} = \begin{pmatrix} C_{11} & C_{12} & C_{12} & 0 & 0 & 0 \\ C_{12} & C_{11} & C_{12} & 0 & 0 & 0 \\ C_{12} & C_{12} & C_{11} & 0 & 0 & 0 \\ 0 & 0 & 0 & 2C_{44} & 0 & 0 \\ 0 & 0 & 0 & 0 & 2C_{44} & 0 \\ 0 & 0 & 0 & 0 & 0 & 2C_{44} \end{pmatrix} \begin{pmatrix} e_{xx} \\ e_{yy} \\ e_{zz} \\ e_{xy} \\ e_{xz} \\ e_{yz} \end{pmatrix} \tag{2.12}$$

In order to calculate the strain in a heterostructure we have to minimize the elastic energy of the system which in the context of Hooke's approximation is

$$E = \int U(\vec{r}) d^3\vec{r} \quad \text{where} \quad U = \frac{1}{2} \sum_i \sum_j e_i C_{ij} e_j, \tag{2.13}$$

For the case of cubic crystals and due to symmetry the elastic energy becomes

$$U = \frac{1}{2} C_{11}(\varepsilon_{xx}^2 + \varepsilon_{yy}^2 + \varepsilon_{zz}^2) + 2C_{44}(\varepsilon_{yz}^2 + \varepsilon_{zx}^2 + \varepsilon_{xy}^2) + C_{12}(\varepsilon_{xx}\varepsilon_{yy} + \varepsilon_{yy}\varepsilon_{zz} + \varepsilon_{zz}\varepsilon_{xx}) \tag{2.14}$$

In a nanostructure, strain can be found by minimizing the elastic energy given in Eq. 2.13 with respect to the displacement field $\vec{u}$

2.2.2   Piezoelectric effects

For a crystal which does not have a center of inversion like zinc-blende compound semiconductors the strains induce a dielectric polarization given by

$$\vec{P} = \bar{\bar{e}} \vec{e}_{strain} \tag{2.15}$$

where $\vec{P}$ is the polarization vector, $\vec{e}_{strain}$ the six component strain vector and $\bar{\bar{e}}$ the piezoelectric tensor which is a 3×6 matrix[41]. For materials with the zinc-blende structure, the piezoelectric tensor has only one non zero element, e_{14} and the polarization vector is given by

$$\begin{pmatrix} P_x \\ P_y \\ P_z \end{pmatrix} = \begin{pmatrix} 0 & 0 & 0 & 2e_{14} & 0 & 0 \\ 0 & 0 & 0 & 0 & 2e_{14} & 0 \\ 0 & 0 & 0 & 0 & 0 & 2e_{14} \end{pmatrix} \begin{pmatrix} \varepsilon_{xx} \\ \varepsilon_{yy} \\ \varepsilon_{zz} \\ \varepsilon_{yz} \\ \varepsilon_{zx} \\ \varepsilon_{xy} \end{pmatrix} \tag{2.16}$$

For the III-V materials, values of e_{14} are negative because the A-faces (cation faces) become negatively charged. For the II-VI materials the cation faces are positively charged, so e_{14} takes positive values. The anions and cations of the alloy are stacked in the (111) planes of the crystal, thus shear strain applied towards $< 111 >$ direction results in their relative displacement. As

a consequence piezoelectric effects become stronger for structures grown towards the $< 111 >$ direction, while they vanish towards $< 100 >$. The piezoelectric potential $V_p(\vec{r})$ is calculated from Poisson's equation

$$\vec{\nabla} \varepsilon_0 \varepsilon_r(\vec{r}) \vec{\nabla} V_p(\vec{r}) = -\rho_p(\vec{r}) \tag{2.17}$$

where $\varepsilon_r(\vec{r})$ is the static dielectric constant of each material and $\rho_p(\vec{r}) = -\nabla \cdot \vec{P}$ the volumetric bound charge density.

2.2.3 The $\vec{k} \cdot \vec{p}$ theory

The most basic model for the band structure calculation of a direct gap semiconductor is an isotropic parabolic dispersion [44] for both valence (E_v) and conduction (E_c) band

$$E_{c/v}(\vec{k}) = \pm \left(\frac{E_g}{2} + \frac{\hbar^2 k^2}{2m^*_{e/h}} \right) \tag{2.18}$$

where E_g is the energy gap and m^*_e, m^*_h the effective masses for the conduction and valence band respectively. A drawback of this model is that it does not take into account nonparabolicity of the bands, anisotropy and the mixing between heavy and light holes. A more rigorous method for calculating the electronic structure is through the application of $k \cdot p$ perturbation theory for more than one band. This method is very effective for any arbitrary point of k space and in particular for $\vec{k} = 0$ i.e. in the vicinity of the fundamental gap. For the development of $\vec{k} \cdot \vec{p}$ theory we have to introduce Bloch's theorem. The ion positions of an ideal crystal form a periodic structure. As a consequence, the crystal potential $V(\vec{r})$ maintains the periodicity of the Bravais lattice

$$V(\vec{r}) = V(\vec{r} + \vec{R}) \tag{2.19}$$

where $\vec{R} = m_1 \vec{a_1} + m_2 \vec{a_2} + m_3 \vec{a_3}$ is a vector of the Bravais lattice, $\vec{a_1}, \vec{a_2}, \vec{a_3}$ the lattice vectors and m_1, m_2, m_3 integers. The wavefunction of electrons moving in this potential should satisfy Schrodinger's equation

$$\mathcal{H} \psi_{n\vec{k}}(\vec{r}) = \left(\frac{\hbar^2}{2m_0} \nabla^2 + V(\vec{r}) \right) \psi_{n\vec{k}}(\vec{r}) = E_n(\vec{k}) \psi_{n\vec{k}}(\vec{r}) \tag{2.20}$$

where m_0 is the free electron mass, $\vec{k}$ the wave vector of the electron and n the band index. Due to translational symmetry of the crystal and through Bloch's theorem, the eigenstates of Eq. 2.20 have the form

$$\psi_{n\vec{k}}(\vec{r}) = e^{i\vec{k}\vec{r}} u_{n\vec{k}}(\vec{r}) \tag{2.21}$$

where $u_{n\vec{k}}(\vec{r}) = u_{n\vec{k}}(\vec{r} + \vec{R})$ is also a periodic function. Schrodinger's equation for the periodic part is

$$\left[\frac{p^2}{2m_0} + \frac{\hbar^2}{m_0} \vec{k} \cdot \vec{p} + V(\vec{r}) \right] u_{n\vec{k}}(\vec{r}) = \left[E_n(\vec{k}) - \frac{\hbar^2 k^2}{2m_0} \right] u_{n\vec{k}}(\vec{r}) \tag{2.22}$$

We rewrite the above equation by separating the perturbed and unperturbed part as

$$\left[\mathcal{H}_0 + \frac{\hbar^2}{m_0} \vec{k} \cdot \vec{p} \right] u_{n\vec{k}}(\vec{r}) = \left[E_n(\vec{k}) - \frac{\hbar^2 k^2}{2m_0} \right] u_{n\vec{k}}(\vec{r}) \tag{2.23}$$

where

$$\mathcal{H}_0 = \frac{p^2}{2m_0} + V(\vec{r}) \tag{2.24}$$

and

$$\mathcal{H}_0 u_{n0}(\vec{r}) = E_n(0) u_{n0}(\vec{r}) \tag{2.25}$$

is the unperturbed Schrodinger's equation near $\vec{k} = 0$. In our calculations we consider that the conduction band is weakly coupled to the other bands and we ignore any spin orbit effects. In order to calculate the structure of a single band we apply time independent perturbation theory. A simple approach is to divide the bands of interest in two classes. The first class contains the band of interest n and the second the rest of the bands $n' \neq n$ [42] . The energy up to second order perturbation is

$$E_n(\vec{k}) = E_n(0) + \frac{\hbar^2 k^2}{2m_0} + \frac{\hbar}{m_0}\vec{k} \cdot \vec{p}_{nn} + \frac{\hbar^2}{m_0^2} \sum_{n' \neq n} \frac{|\vec{k} \cdot \vec{p}_{nn'}|^2}{E_n(0) - E_{n'}(0)} \tag{2.26}$$

and the corresponding wavefunction up to first order

$$u_{n\vec{k}}(\vec{r}) = u_{n0}(\vec{r}) + \sum_{n' \neq n} \left(\frac{\hbar}{m_0} \frac{\vec{k} \cdot \vec{p}_{n'n}}{E_n(0) - E_{n'}(0)} \right) u_{n'0}(\vec{r}) \tag{2.27}$$

The momentum matrix elements in the above equations are

$$\vec{p}_{nn'} = \int u_{n0}^*(\vec{r}) \vec{p} u_{n'0}(\vec{r}) d^3\vec{r} \tag{2.28}$$

By using second order perturbations for the energy, the dependence of $E_n(\vec{k})$ near $\vec{k} = 0$ becomes quadratic for $p_{nn} = 0$. From Eq. 2.26 we can define the effective mass for one band

$$\left(\frac{1}{m^*} \right)_{ij} = \frac{1}{m_0}\delta_{ij} + \frac{2}{m_0^2} \sum_{n' \neq n} \frac{p_{nn'}^i p_{n'n}^j + p_{nn'}^j p_{n'n}^i}{E_n(0) - E_{n'}(0)} \tag{2.29}$$

where $i, j = x, y, z$. Therefore in order to calculate the band dispersion we need only the energy gap and the momentum matrix elements [45].

The single band equation is sufficient to calculate the conduction band, but for the description of valence band we must include multiple bands and more precisely those which correspond to heavy hole, light hole and split-off. Also we must take into account the fact that heavy holes are quasi degenerate with light holes. As we will see later the contribution of split-off band is important as it significantly affects the spin properties of the ground state. A schematic representation for the band structure of a semiconductor is shown in Fig. 2.3
By taking into account spin orbit interaction, Eq. 2.22 becomes

$$\left[\mathcal{H}_0 + \frac{\hbar^2 k^2}{2m_0} + \frac{\hbar}{4m_0^2 c^2}(\nabla V \times \vec{p}) \cdot \vec{\sigma} + \mathcal{H}' \right] u_{n\vec{k}}(\vec{r}) = E_n(\vec{k}) u_{n\vec{k}}(\vec{r}) \tag{2.30}$$

where

$$\mathcal{H}_0 = \frac{p^2}{2m_0} + V(\vec{r}) \ , \ \ \mathcal{H}' = \frac{\hbar}{m_0}\vec{k} \cdot \vec{\Pi} \tag{2.31}$$
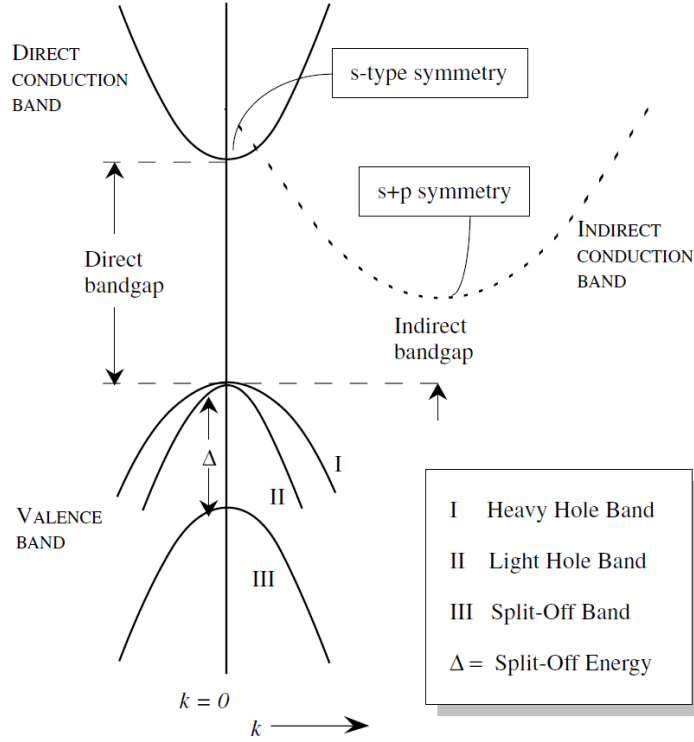
Figure 2.3 – The band structure for a direct and an indirect gap bulk semiconductor. The valence band is described by two degenerate bands for heavy and light holes and one band for the split-off states separated by Δ_{SO} . Image taken from [46]

is the unperturbed and perturbed Hamiltonian components and

$$\vec{\Pi} = \vec{p} + \frac{\hbar}{4m_0c^2}\vec{\sigma} \times \nabla V \tag{2.32}$$

At the edge of the valence band, the Bloch waves have a p like symmetry and without taking into account spin they exhibit a three fold degeneracy. We denote these states as $|X\rangle, |Y\rangle$ and $|Z\rangle$. These functions are written as periodic representations of the corresponding atomic orbitals with periodicity similar to that of the Bravais lattice. The Bloch functions of the valence band in presence of spin-orbit coupling are

$$u_{10}(\vec{r}) = \left|\frac{3}{2}, \frac{3}{2}\right\rangle = -\frac{1}{\sqrt{2}}|(X + iY)\uparrow\rangle$$

$$u_{20}(\vec{r}) = \left|\frac{3}{2}, \frac{1}{2}\right\rangle = -\frac{1}{\sqrt{6}}|(X + iY)\downarrow\rangle + \sqrt{\frac{2}{3}}|Z\uparrow\rangle$$

$$u_{30}(\vec{r}) = \left|\frac{3}{2}, -\frac{1}{2}\right\rangle = \frac{1}{\sqrt{6}}|(X - iY)\uparrow\rangle + \sqrt{\frac{2}{3}}|Z\downarrow\rangle$$

$$u_{40}(\vec{r}) = \left|\frac{3}{2}, -\frac{3}{2}\right\rangle = \frac{1}{\sqrt{2}}|(X - iY)\downarrow\rangle \tag{2.33}$$

$$u_{50}(\vec{r}) = \left|\frac{1}{2}, \frac{1}{2}\right\rangle = \frac{1}{\sqrt{3}}|(X + iY)\downarrow\rangle + \sqrt{\frac{1}{3}}|Z\uparrow\rangle$$

$$u_{60}(\vec{r}) = \left|\frac{1}{2}, -\frac{1}{2}\right\rangle = \frac{1}{\sqrt{3}}|(X - iY)\uparrow\rangle - \sqrt{\frac{1}{3}}|Z\downarrow\rangle$$

Where $u_{10}(\vec{r})$, $u_{40}(\vec{r})$ are the Bloch functions for the heavy hole band, $u_{20}(\vec{r})$, $u_{30}(\vec{r})$ for the light hole band and $u_{50}(\vec{r})$, $u_{60}(\vec{r})$ for the split-off band. The expansion of Bloch function in two sets is

$$u_{n\vec{k}}(\vec{r}) = \sum_{j'}^{A} a_{j'}(\vec{k})u_{j'0}(\vec{r}) + \sum_{\gamma}^{B} a_{\gamma}(\vec{k})u_{\gamma 0}(\vec{r}) \tag{2.34}$$

where i are the valence band components belonging in class A and i' the conduction band components which belong in class B. In other words, class A contains all bands belonging to Γ_8 and Γ_7 manifolds and class B all other including conduction band at Γ_6 which also has the strongest contribution. The eigenvalue problem we have to solve is

$$\sum_{j'}^{A}(\mathcal{H}_{jj'} - E\delta_{jj'})a_{j'}(\vec{k}) = 0 \tag{2.35}$$

and by applying Löwdin's perturbation theory, we can write it as

$$\sum_{j'}^{A}(U_{jj'}^{A} - E\delta_{jj'})a_{j'}(\vec{k}) = 0 \tag{2.36}$$

where

$$U_{jj'}^{A} = \mathcal{H}_{jj'} + \sum_{\gamma \neq j,j'}^{B} \frac{\mathcal{H}_{j\gamma}\mathcal{H}_{\gamma j'}}{E_0 - E_\gamma} = \mathcal{H}_{jj'} + \sum_{\gamma \neq j,j'}^{B} \frac{\mathcal{H}'_{j\gamma}\mathcal{H}'_{\gamma j'}}{E_0 - E_\gamma} \tag{2.37}$$

and

$$\mathcal{H}_{jj'} = \langle u_{j0}| \mathcal{H} |u_{j'0}\rangle = \left[E_j(0) + \frac{\hbar^2 k^2}{2m_0}\right]\delta_{jj'} \quad (j,j' \in A)$$
$$\mathcal{H}'_{j\gamma} = \langle u_{j0}| \frac{\hbar}{m_0}\vec{k} \cdot \vec{\Pi} |u_{\gamma 0}\rangle \approx \sum_{\alpha} \frac{\hbar k_\alpha}{m_0}p_{j\gamma}^{\alpha} \quad (j \in A, \gamma \notin A) \tag{2.38}$$

When $j,j' \in A$ and $\gamma \notin A$ then $\Pi_{jj'} = 0$ and $\Pi_{j\gamma}^{\alpha} \approx p_{j\gamma}^{\alpha}$ [42]. Consequently we obtain

$$U_{jj'}^{A} = \left[E_j(0) + \frac{\hbar^2 k^2}{2m_0}\right]\delta_{jj'} + \frac{\hbar^2}{m_0^2}\sum_{\gamma \neq j,j'}^{B}\sum_{\alpha,\beta} \frac{k_\alpha k_\beta \, p_{j\gamma}^{\alpha} p_{\gamma j'}^{\beta}}{E_0 - E_\gamma} = E_j(0)\delta_{jj'} + \sum_{\alpha\beta} D_{jj'}^{\alpha\beta}k_\alpha k_\beta \tag{2.39}$$

where $D_{jj'}^{\alpha\beta}$ is the matrix given by

$$D_{jj'}^{\alpha\beta} = \frac{\hbar^2}{2m_0}\left\{\delta_{jj'}\delta_{\alpha\beta} + \sum_{\gamma}^{B} \frac{p_{j\gamma}^{\alpha}p_{\gamma j'}^{\beta} + p_{j\gamma}^{\beta}p_{\gamma j'}^{\alpha}}{m_0(E_0 - \gamma)}\right\} \tag{2.40}$$

The above equation is a general expression of the single band case 2.29 in which we take into account the degenerate bands. In order to construct the matrix elements $D_{jj'}$ we define the following components

$$A_0 = \frac{\hbar^2}{2m_0} + \frac{\hbar^2}{m_0^2} \sum_\gamma^B \frac{p_{x\gamma}^x p_{\gamma x}^x}{E_0 - E_\gamma}$$

$$B_0 = \frac{\hbar^2}{2m_0} + \frac{\hbar^2}{m_0^2} \sum_\gamma^B \frac{p_{x\gamma}^y p_{\gamma x}^y}{E_0 - E_\gamma} \tag{2.41}$$

$$C_0 = \frac{\hbar^2}{m_0^2} \sum_\gamma^B \frac{p_{x\gamma}^x p_{\gamma y}^y + p_{x\gamma}^y p_{\gamma y}^x}{E_0 - E_\gamma}$$

through which we can write the expressions for the Luttinger-Kohn parameters $\gamma_1, \gamma_2, \gamma_3$

$$-\frac{\hbar^2}{2m_0}\gamma_1 = \frac{1}{3}(A_0 + 2B_0)$$

$$-\frac{\hbar^2}{2m_0}\gamma_2 = \frac{1}{6}(A_0 - B_0) \tag{2.42}$$

$$-\frac{\hbar^2}{2m_0}\gamma_3 = \frac{C_0}{6}$$

Using Eq. 2.39, we construct the 6 band Luttinger-Kohn Hamiltonian $\mathcal{H}_{LK}$ in the total angular momentum basis (Eq. 2.33)

$$\mathcal{H}_{LK} = - \begin{pmatrix} P+Q & -S & R & 0 & -\frac{1}{\sqrt{2}}S & \sqrt{2}R \\ -S^\dagger & P-Q & 0 & R & -\sqrt{2}Q & \sqrt{\frac{3}{2}}S \\ R^\dagger & 0 & P-Q & S & \sqrt{\frac{3}{2}}S^\dagger & \sqrt{2}Q \\ 0 & R^\dagger & S^\dagger & P+Q & -\sqrt{2}R^\dagger & -\frac{1}{\sqrt{2}}S^\dagger \\ -\frac{1}{\sqrt{2}}S^\dagger & -\sqrt{2}Q^\dagger & \sqrt{\frac{3}{2}}S & -\sqrt{2}R & P+\Delta_{SO} & 0 \\ \sqrt{2}R^\dagger & \sqrt{\frac{3}{2}}S^\dagger & \sqrt{2}Q^\dagger & -\frac{1}{\sqrt{2}}S & 0 & P+\Delta_{SO} \end{pmatrix} \tag{2.43}$$

where

$$P = \frac{\hbar^2\gamma_1}{2m_0}(k_x^2 + k_y^2 + k_z^2), \quad Q = \frac{\hbar^2\gamma_2}{2m_0}(k_x^2 + k_y^2 - 2k_z^2),$$

$$R = \frac{\hbar^2}{2m_0}[-\sqrt{3}\gamma_2(k_x^2 - k_y^2) + i2\sqrt{3}\gamma_3 k_x k_y], \quad S = \frac{\hbar^2\gamma_3}{2m_0}\sqrt{3}(k_x - ik_y)k_z \tag{2.44}$$

and Δ_{SO} the spin-orbit splitting which is the energy difference between the heavy or light hole band and the split off band at $k = 0$. The expressions for the P, Q, R, S terms of Eq. 2.44, are valid provided that x, y, z coordinates are parallel to the cubic axis and specifically z parallel to $< 001 >$ direction. For x, y, z parallel to the cubic axis and z parallel to $< 111 >$ direction we have to rotate the Hamiltonian by applying the proper transformation matrices on both the coordinate system and the Bloch basis functions [45], [47]. In that case the terms of the 6 band $k \cdot p$ Hamiltonian are written

$$P = \frac{\hbar^2 \gamma_1}{2m_0}(k_x^2 + k_y^2 + k_z^2), \quad Q = \frac{\hbar^2 \gamma_3}{2m_0}(k_x^2 + k_y^2 - 2k_z^2),$$

$$R = \frac{\hbar^2}{2m_0}\left[-\frac{1}{\sqrt{3}}(\gamma_2 + 2\gamma_3)(k_x - ik_y)^2 + \frac{2\sqrt{2}}{3}(\gamma_2 - \gamma_3)(k_x + ik_y)k_z\right],$$

$$S = \frac{\hbar^2}{2m_0}\left[\sqrt{\frac{2}{3}}(\gamma_2 - \gamma_3)(k_x + ik_y)^2 - \frac{2}{\sqrt{3}}(2\gamma_2 + \gamma_3)(k_x - ik_y)k_z\right]$$

$$(2.45)$$

2.2.4 The effect of strain on the electronic band structure: Bir-Pikus components

The mismatch among comprising materials of a semiconductor heterostructure due to different values of their lattice constants, induces a strain field which alters the band structure. In this section we discuss how strain affects both conduction and valence band. We will begin by first discussing the more simple case of conduction band which is calculated by solving the single band equation. For the isotropic case, strain is introduced to the energy parabolic dispersion through the product of conduction band deformation potential a_c and the hydrostatic strain, given by the sum of the diagonal elements of strain tensor ϵ [42]. In that case, the conduction band energy dispersion is near $\vec{k} = 0$ written

$$E(k) = E_c(0) + \frac{\hbar^2}{2m_e^*}(k_x^2 + k_y^2 + k_z^2) + a_c(\varepsilon_{xx} + \varepsilon_{yy} + \varepsilon_{zz}) \tag{2.46}$$

where m_e^* the electron effective mass. Hydrostatic strain affects the shift of the energy band gap as it modifies the distance between atoms. For a compressive hydrostatic strain the band gap increases, while for a tensile one it decreases. For the discussion of strain effects on the valence band, axial shear strain has to be taken also into account. Shear strain lowers the crystal symmetry which results in the lift of valence band degeneracy and the splitting of heavy hole and light hole bands. By adding the strain dependent contributions [48] and for z axis parallel to $< 111 >$ direction the Hamiltonian terms become

$$P \rightarrow P + P_\varepsilon, \quad P_\varepsilon = -a_v(\varepsilon_{xx} + \varepsilon_{yy} + \varepsilon_{zz})$$

$$Q \rightarrow Q + Q_\varepsilon, \quad Q_\varepsilon = \frac{d}{2\sqrt{3}}(\varepsilon_{xx} + \varepsilon_{yy} - 2\varepsilon_{zz})$$

$$R \rightarrow R + R_\varepsilon, \quad R_\varepsilon = -\frac{\sqrt{3}}{6}\left(b + \frac{2d}{\sqrt{3}}\right)(\varepsilon_{xx} - \varepsilon_{yy} - 2i\varepsilon_{xy}) + \frac{2}{\sqrt{6}}\left(b - \frac{d}{\sqrt{3}}\right)(\varepsilon_{xz} + i\varepsilon_{yz})$$

$$S \rightarrow S + S_\varepsilon, \quad S_\varepsilon = \frac{\sqrt{3}}{3}\left(2b + \frac{d}{\sqrt{3}}\right)(\varepsilon_{xz} - i\varepsilon_{yz}) - \frac{1}{\sqrt{6}}\left(b - \frac{d}{\sqrt{3}}\right)(\varepsilon_{xx} - \varepsilon_{yy} + 2i\varepsilon_{xy})$$

$$(2.47)$$

where a_v, b_v and d_v are the Bir-Pikus deformation potentials which define the effect of hydrostatic, uniaxial and shear strain in the heterostructure. The term P_ε appears in every diagonal component of the Hamiltonian matrix, and corresponds to the hydrostatic strain which is responsible for the uniform shift of the entire valence band. Under strain, the bands containing the diagonal terms $-P - Q$ are the heavy hole bands and those containing the $-P + Q$ are the light hole bands. Q becomes positive for tensile strain and negative for compressive. For the simple case of biaxial strain, where $R_\varepsilon = S_\varepsilon = 0$, the zone center energies for the HH, LH and SO are respectively [41]

$$E_{HH}(k=0) = -P_\varepsilon - Q_\varepsilon$$

$$E_{LH}(k=0) = -P_\varepsilon + \frac{1}{2}(Q_\varepsilon - \Delta_{SO} + \sqrt{9Q_\varepsilon^2 + 2\Delta_{SO}Q_\varepsilon + \Delta_{SO}^2})$$

$$E_{SO}(k=0) = -P_\varepsilon + \frac{1}{2}(Q_\varepsilon - \Delta_{SO} - \sqrt{9Q_\varepsilon^2 + 2\Delta_{SO}Q_\varepsilon + \Delta_{SO}^2})$$

(2.48)

2.2.5 The envelope function approximation

We consider a set of degenerate bands which satisfy the Hamiltonian

$$\left[\frac{p^2}{2m_0} + V(\vec{r}) + \frac{\hbar}{4m_0^2c^2}\nabla V \times \vec{p} \cdot \vec{\sigma}\right]\psi_{n\vec{k}}(\vec{r}) = E(\vec{k})\psi_{n\vec{k}}(\vec{r}) \tag{2.49}$$

The energy dispersion relation near $k=0$ is given by

$$\sum_{j'=1}^{6} \mathcal{H}_{jj'}^{LK} a_{j'}(\vec{k}) = \sum_{j'=1}^{6}\left[E_j(0)\delta_{jj'} + \sum_{\alpha,\beta} D_{jj'}^{\alpha\beta}k_\alpha k_\beta\right] a_{j'}(\vec{k}) = E(\vec{k})a_j(\vec{k}) \tag{2.50}$$

For a perturbation $U(\vec{r})$ which describes the potential of a defect or a heterostructure, we look for solutions $\psi(\vec{r})$ of the Hamiltonian

$$[H + U(\vec{r})]\psi(\vec{r}) = E\psi(\vec{r}) \tag{2.51}$$

in the form

$$\psi(\vec{r}) = \sum_{j=1}^{6} F_j(\vec{r})u_{j0}(\vec{r}) \tag{2.52}$$

In the equation above, $F_j(\vec{r})$ represents the envelope function, which must satisfy the relation

$$\sum_{j'=1}^{6}\left[E_j(0)\delta_{jj'} + \sum_{\alpha,\beta} D_{jj'}^{\alpha\beta}\left(-i\frac{\partial}{\partial x_\alpha}\right)\left(-i\frac{\partial}{\partial x_\beta}\right) + U(\vec{r})\delta_{jj'}\right] F_{j'}(\vec{r}) = EF_j(\vec{r}) \tag{2.53}$$

Here we have to underline that this approximation is valid, provided that the potential $V(\vec{r})$ is slowly varying at the scale of crystal unit cell. For its application to heterostructures caution should be taken on how continuity is treated in sharply varying potentials.

2.2.6 Calculation of oscillator strengths

Absorption and emission processes can be described with time-dependent perturbation theory [49]. The transition probability from an initial state i to a final f is given by Fermi's golden rule

$$w_{fi}(\hbar\omega) = \frac{2\pi}{\hbar}|\mathcal{H}_{fi}|^2\delta(E_f - E_i - \hbar\omega) \tag{2.54}$$

where E_i and E_f the energies of the initial and final state, $\hbar\omega$ is the energy of the the photon and $\mathcal{H}_{fi}$ is the matrix element

$$\mathcal{H}_{fi} = \langle\psi_f|\mathcal{H}_{em}|\psi_i\rangle \tag{2.55}$$

with ψ_i and ψ_f the wavefunctions of the initial and final states, and $\mathcal{H}_{em}$ the light-matter interaction Hamiltonian. When the light can be described as a transverse electro-magnetic plane wave, the electric field $\vec{E} = -\dot{\vec{A}}$ and magnetic field $\vec{B} = \nabla \times \vec{A}$ both derive from a vector potential $\vec{A} = \vec{A}_0 \exp\left[i(\vec{k} \cdot \vec{r} - \omega t)\right]$ that enters in the kinetic Hamiltonian:

$$\mathcal{H}_{kin} = \frac{1}{2m}(\vec{p} - q\vec{A})^2 = \frac{p^2}{2m} - \frac{q}{m}\vec{A} \cdot \vec{p} + \frac{q^2}{2m}\vec{A}^2 \tag{2.56}$$

Neglecting corrections in $\vec{A}^2$ (dipole approximation),

$$\mathcal{H}_{em} = -\frac{q}{m}\vec{A}_0 \cdot \vec{p} = \frac{iq\hbar}{m}\vec{A}_0 \cdot \vec{\nabla} \tag{2.57}$$

Therefore,

$$|\langle\psi_f| \mathcal{H}_{em} |\psi_i\rangle|^2 = \frac{q^2|\vec{A}_0|^2}{m^2}|\langle\psi_f| \vec{e} \cdot \vec{p}|\psi_i\rangle|^2 \tag{2.58}$$

where $\vec{e}$ is the unit polarization vector along the electric field $\vec{E}$ (or vector potential $\vec{A}$).

For inter-band transitions (between valence and conduction bands), we may assume without loss of generality that ψ_i is a conduction band state and ψ_f a valence band state. Then, in the effective mass approximation,

$$\psi_i(\vec{r}) = \sum_{\sigma=\uparrow,\downarrow} F_{c,\sigma}(\vec{r})u_{c,\sigma}(\vec{r}) \tag{2.59}$$

where $F_{c,\sigma}(\vec{r})$ is the envelope function with spin σ and $u_{c,\sigma}(\vec{r})$ the associated conduction band Bloch function. Likewise, in the six bands $\vec{k} \cdot \vec{p}$ model,

$$\psi_f(\vec{r}) = \sum_{n=1}^{6} F_{v,n}(\vec{r})u_{v,n}(\vec{r}) \tag{2.60}$$

where $F_{v,n}(\vec{r})$ are the envelope functions associated with the valence band Bloch functions $u_{v,n}(\vec{r})$. Since the envelope functions are slowly varying with respect to the Bloch functions, we may neglect the action of the $\vec{p}$ operator onto the former, and factorize the matrix elements of $\vec{p}$ as follows:

$$\langle\psi_f| \vec{p} |\psi_i\rangle = \sum_{n=1}^{6} \sum_{\sigma=\uparrow,\downarrow} \langle F_{v,n}|F_{c,\sigma}\rangle \langle u_{v,n}| \vec{p}|u_{c,\sigma}\rangle_{\Omega_0} \tag{2.61}$$

where Ω_0 is the unit cell. We can next define:

$$p_{\alpha,n\sigma} = \langle u_{v,n}| p_\alpha |u_{c,\sigma}\rangle_{\Omega_0} \tag{2.62}$$

where $\alpha \in \{x, y, z\}$, so that:

$$\langle\psi_f| p_\alpha |\psi_i\rangle = \sum_{n=1}^{6} \sum_{\sigma=\uparrow,\downarrow} \langle F_{v,n}|F_{c,\sigma}\rangle p_{\alpha,n\sigma} \tag{2.63}$$

The values of the $p_{\alpha,n\sigma}$ for the six bands $\vec{k} \cdot \vec{p}$ model follow strict selection rules and can be found, e.g., in Ref. [50] [51] . The matrix elements of $\vec{p}$ hence appear as linear combinations of the $p_{\alpha,n\sigma}$ weighted by the overlap of the envelope functions $F_{v,n}$ and $F_{c,\sigma}$, which must therefore have same symmetries to contribute. The absorption/emission rates for an electric field parallel to $\alpha \in \{x, y, z\}$ are proportional to $|\langle\psi_f| p_\alpha |\psi_i\rangle|^2$.

2.3 Description of simulated structures and methods

The nanowires studied experimentally have a diameter $D_{NW} \approx 140$ nm and a length $L_{NW} \approx 1$ μm. The quantum dot diameter is $D_{QD} \approx 10$ nm and its length $L_{QD} \approx 90$ nm. The nanowire dimensions are large and it is impossible to use them in calculations without compromising accuracy.
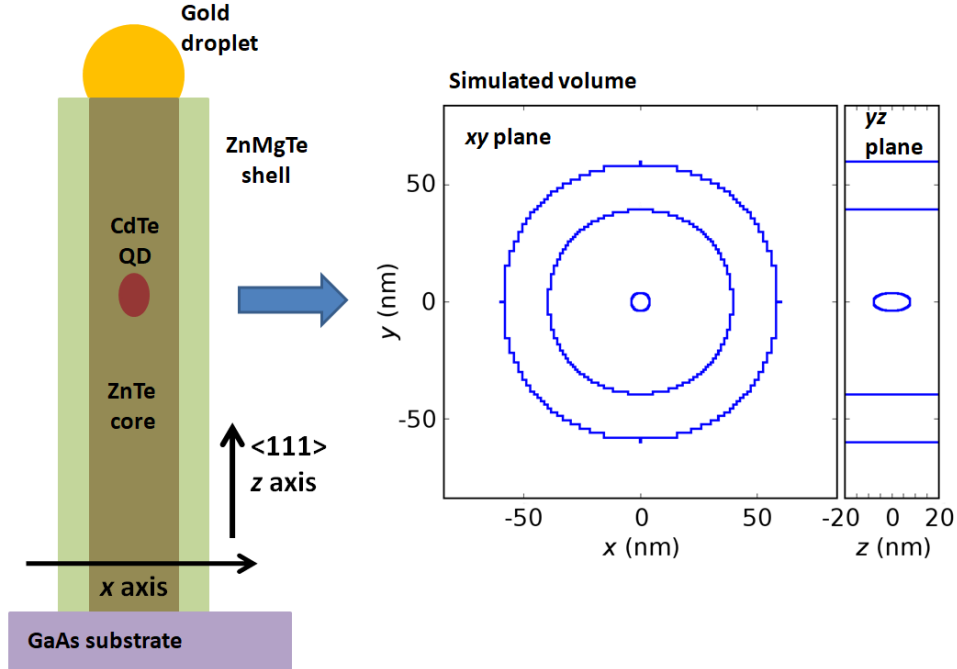

Figure 2.4 – Schematic representation of the actual nanowire quantum dot structure (left) and the section we define for the numerical calculation (right).

As regards the quantum dot, we are interested to study the switching from heavy to light hole which is in the vicinity of $L_{QD}/D_{QD} \approx 1$. It is thus unnecessary to look at a dot with $L_{QD}/D_{QD} \approx 9$, similar to that we have for the experimental measurements. Due to the fact that we can not simulate the full structure, we carry out the calculations in a slab of length $L_{NW} = 40$ nm which contains an ellipsoidal quantum dot of varying length $L_{QD} = 1 - 20$ nm and constant diameter $D_{QD} =8$ nm.In Fig. 2.4 we present a sketch of the nanowire quantum dot and two cross sections of the volume we simulate along xy and yz plane. In order to calculate accurately the piezoelectric potential by solving Poisson's equation, we have to define a vacuum volume surrounding the nanowire.

The objective of these simulations is to calculate the ground and excited states for conduction band electrons and valence band holes. The volume of the simulated structure, as shown to the right of Fig. 2.4 is defined through a non-uniform mesh which is necessary for the finite element and finite difference calculations. For the electronic structure calculations, we use the TB_Sim [1] package of codes developed by Yann-Michel Niquet. The core of TB_Sim/ is implemented in FORTRAN and for data post processing we use scripts written in Python and Bash. The program can run efficiently only in UNIX based environments while part of post processing can be realized on different operating systems. The codes are optimized to run parallel on multiple CPUs using the Open MPI library. The management of calculations, takes place completely in command line environment since there is no graphical user interface. This facilitates significantly the process as for the calculations we use computer clusters to which we have to connect remotely.

---

[1]http://inac.cea.fr/L_Sim/TB_Sim/

In order to launch a calculation we have first to prepare two input files. The first one contains the parameters of materials which constitute the nanostructure. These are for each material the electron effective mass, the conduction and valence bad offsets, the elastic constants C_{11}, C_{12}, C_{44}, the Bir-Pikus deformation potentials for conduction a_c and valence band a_v, b_v, d_v, the piezoelectric constant e_{14}, the Luttinger parameters $\gamma_1, \gamma_2, \gamma_3$ and the dielectric constant. The parameters used for different materials are listed in Appendix A. In the second one we define the materials, dimensions and geometry of the structure we want to simulate. Another important parameter we optimize in the second file is the size of the calculation mesh. More specifically, we have to choose the mesh step size carefully in order to converge with a certain accuracy in a cost effective computational time. Along z direction the algorithm uses periodic boundary conditions. This means that we carry out the calculations for an infinitely long nanowire with multiple quantum dots inserted in it in a periodic pattern. In order to avoid interference effects we have run several test calculations for the optimization of the nanowire length according to quantum dot dimensions. On the xy plane, the boundary conditions impose that both stress components and wavefunctions are vanishing outside the nanowire.
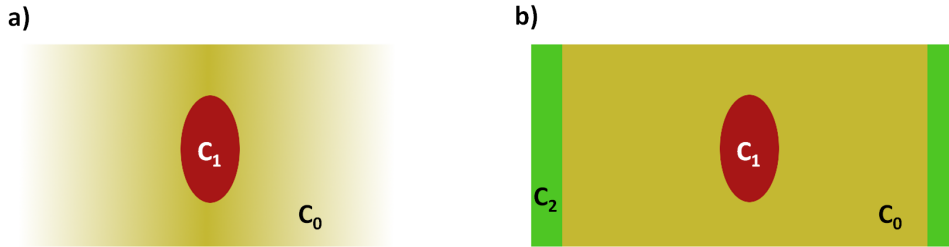

Figure 2.5 – Schematic representation of an ellipsoidal inclusion in an infinite matrix a) and inside a medium with a defined geometry b). With C_1, C_0, C_2 we denote the stiffness matrices for the different lattice mismatched materials

Considering an ellipsoidal inclusion in an infinite matrix as shown in Fig. 2.5 a) we can calculate analytically the strain field by using the method developed by Eshelby [52], [25], as discussed in the introduction. For the case of an infinite core-shell nanowire, similar to that shown in Fig. 2.5 b), one way to calculate the strain field is by solving analytically the Navier-Clapeyron-Lamé equation

$$\sum_{jkl} c_{ijkl} \frac{\partial}{\partial x_j} \left(\frac{\partial u_k}{\partial x_l} + \frac{\partial u_l}{\partial x_k} \right) = 0 \qquad (2.64)$$

where $u(\vec{r})$ the displacement field and c_{ijkl} the components of stiffness tensor which relates the stress to strain tensor through Hooke's law [53]. A very important parameter for the calculation is the boundary conditions. At the sidewall of the nanowire we have to impose that the stress component of the shell material $\sigma^s(r_s) = 0$. At the interface of the shell and nanowire core we have to impose $\sigma_{rr}^c(r_c) - \sigma_{rr}^s(r_c) = 0$ and at the interface of the core and the quantum dot inclusion $\sigma_{rr}^i(r_c) - \sigma_{rr}^c(r_c) = 0$. Another way to calculate the strain field, for an ellipsoidal inclusion in a core-shell nanowire as shown in Fig. 2.5 b), is by minimizing the elastic energy. This is also what the codes we use for the numerical calculations do. Initially, the program calculates the displacement field due to lattice mismatch. Then from the displacement field it calculates the elastic energy, which is subsequently minimized iteratively through the finite element method. When the elastic energy becomes minimum the system reaches an equilibrium with respect to mechanical forces and the boundary conditions discussed above are automatically fulfilled. After the calculation of strain field, the program calculates the piezoelectric potential by solving Poisson's equation. Finally the potentials generated by strain and due to piezoelectric effects enter the 6 band $\vec{k} \cdot \vec{p}$ Hamiltonian for the calculation of the electronic structure.
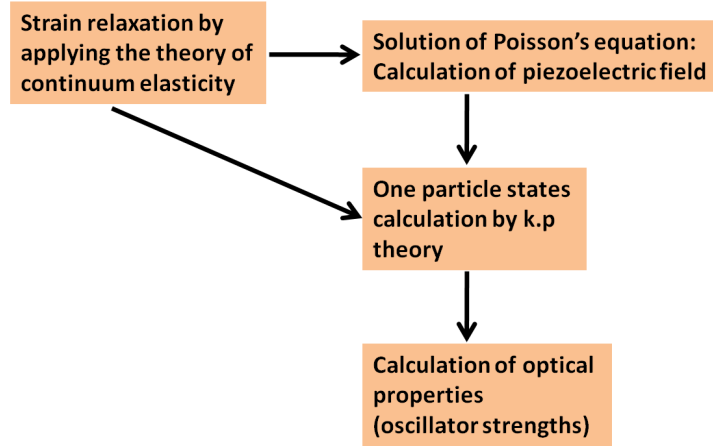
Figure 2.6 – The flow chart of numerical calculations as implemented by the TB_Sim package

A qualitative description of the Hamiltonian is

$$\mathcal{H}_{6\times6} = H' + H_{BP} + V(\vec{r}) \tag{2.65}$$

where H' contains the kinetic term, H_{BP} is the Bir-Pikus Hamiltonian and $V(\vec{r})$ includes the piezoelectric potential and the chemical valence band offset. By diagonalizing the Hamiltonian we calculate the energy level and envelope components of the single particle states, the total wavefunction of which is given by the Kramers doublet

$$
\begin{aligned}
|\psi_+\rangle = {} & F_{3/2,3/2}(\vec{r})\,|3/2,3/2\rangle + F_{3/2,1/2}(\vec{r})\,|3/2,1/2\rangle + F_{3/2,-1/2}(\vec{r})\,|3/2,-1/2\rangle \\
& + F_{3/2,-3/2}(\vec{r})\,|3/2,-3/2\rangle + F_{1/2,1/2}(\vec{r})\,|1/2,1/2\rangle + F_{1/2,-1/2}(\vec{r})\,|1/2,-1/2\rangle
\end{aligned}
$$
$$
\begin{aligned}
|\psi_-\rangle = {} & -F^*_{3/2,3/2}(\vec{r})\,|3/2,3/2\rangle + F^*_{3/2,1/2}(\vec{r})\,|3/2,1/2\rangle - F^*_{3/2,-1/2}(\vec{r})\,|3/2,-1/2\rangle \\
& + F^*_{3/2,-3/2}(\vec{r})\,|3/2,-3/2\rangle - F^*_{1/2,1/2}(\vec{r})\,|1/2,1/2\rangle + F^*_{1/2,-1/2}(\vec{r})\,|1/2,-1/2\rangle
\end{aligned}
\tag{2.66}
$$

Each component of the wavefunction is written as a product of the envelope component $F(\vec{r})$ and the corresponding Bloch component in the total angular momentum basis. The spin of calculated valence band states is half-integer, therefore from Kramers degeneracy theorem [54] there is at least another eigenstate with the same energy. For a state with total angular momentum j and secondary quantum number m_j the two Kramers conjugates are related [50] through the operation

$$\hat{K}\,|jm_j\rangle = (-1)^{j-m_j}\,|j,-m_j\rangle \tag{2.67}$$

In our simulations, we calculate twelve levels for the valence band (the first six Kramers doublets). For the conduction band the program uses the single band approximation thus it does not take into account the electron spin. The Kramers degeneracy however, due to spin for conduction band states is accounted manually afterwards. The simulation steps are shown in Fig. 2.6.

In this work we are interested to investigate the properties of the valence band ground state and the switching from heavy hole to light hole in a nanowire quantum dot.
More specifically we studied two different heterostructures as shown in Fig. 2.7. The first structure studied consisted of an ellipsoidal CdTe quantum dot inserted in a ZnTe nanowire.
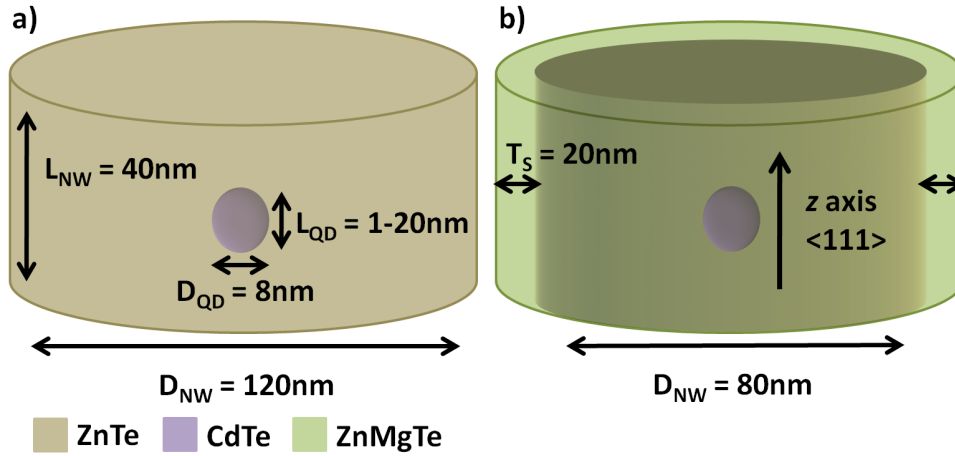
Figure 2.7 – The configuration of the two different nanowire quantum dots studied. A CdTe quantum dot inserted in a ZnTe nanowire a) and a CdTe quantum dot inserted in a ZnTe nanowire passivated by a ZnMgTe shell
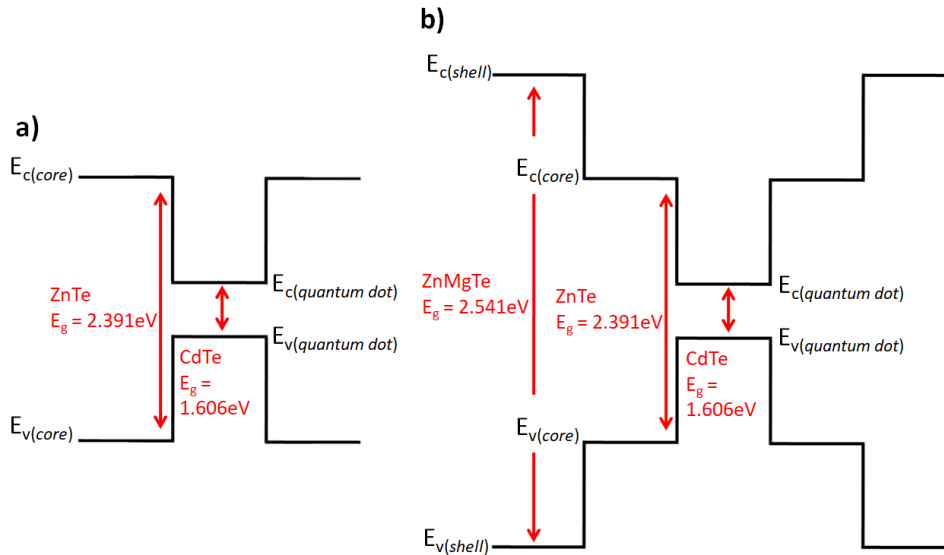

Figure 2.8 – Schematic representation of a type I band alignment for a CdTe quantum dot in a ZnTe nanowire a) and for a CdTe quantum dot in a ZnTe-ZnMgTe core-shell nanowire b)

The length and diameter of the ZnTe nanowire were kept constant and equal to $L_{NW} = 40$ nm and $D_{NW} = 120$ nm respectively. The diameter of the CdTe quantum dot was also kept constant and equal to $D_{QD} = 8$ nm and in order to investigate the valence band ground state as a function of the length to diameter ratio, we varied the quantum dot length L_{QD} from 1 to 20 nm.

For the second structure, we reduced the diameter of the core at $D_{NW} = 80$ nm and we introduced a ZnMgTe shell of thickness $T_S = 20$ nm. Experimentally, ZnMgTe shell acts as a higher gap passivation layer for the ZnTe nanowire core. The calculation parameters for ZnMgTe were extrapolated from those of ZnTe and they correspond to a Mg content of 15%. We adapted the geometry and Mg content in order to carry out the calculations for a structure similar to the nanowires studied experimentally. In this case again we kept constant the quantum dot diameter and we varied the length from 1-20nm. Band profiles for a type I configuration for the two different simulated heterostructures are presented in Fig. 2.8. As reported in [26] we expect that for an elongated quantum dot with a length to diameter ratio $L_{QD}/D_{QD} \geq 1$ we

switch from a heavy hole to a light hole ground state.

Another important parameter which influences the valence band ground state is the valence band offset between the core and the dot. From different experimental studies, it is known that the valence band offset between CdTe and ZnTe is small. From photoelectron spectroscopy studies a valence band offset between 50 meV (type I) and -100 meV (type II) is reported [55]. From optical spectroscopy measurements on CdTe - (Zn,Cd)Te quantum wells values between +50meV (type I) and -50meV (type II) are reported [56] which are strongly affected by mismatch induced strain. Considering the values in literature we concluded that we had to carry out calculations for different valence band offsets switching from a type I to type II band alignment as shown in Fig. 2.9.
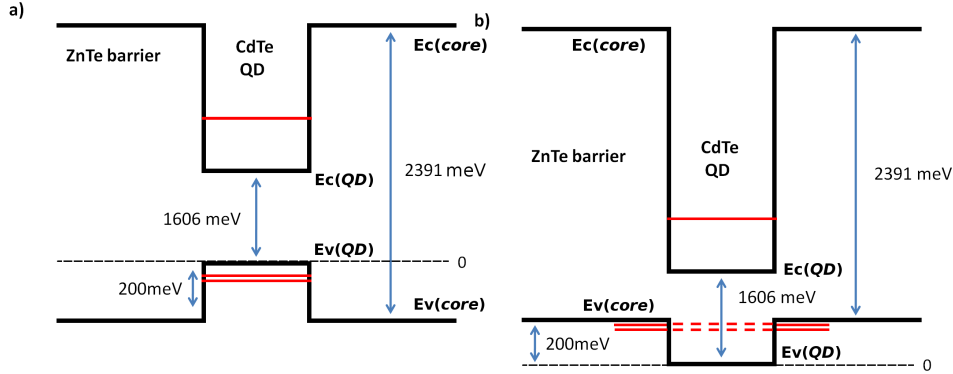

Figure 2.9 – Schematic representation of a type I band alignment a) and type II b). For demonstration purposes, in both pictures we present the first calculated conduction band state and the first Kramers degenerate valence band state.

In our convention, for constructing different band alignments we always set the top of the quantum dot valence band at $E_{v(QD)} = 0$ eV and the bottom at $E_{c(QD)} = E_{g(QD)}$. As an example for a CdTe quantum dot it will be $E_c = 1.606$ eV. For a type I configuration the chemical valence band offset for the material of the barrier is always $E_{v(core)} < 0$ and the value of conduction band $E_{c(core)}$ is selected accordingly so that $E_{c(core)} - E_{v(core)} = E_{g(core)}$. As we switch from type I to type II we gradually increase both $E_{c(core)}$ and $E_{v(core)}$ by the same value. For a type II configuration the chemical band offset of the barrier is always $E_{v(core)} > 0$.

At this point we underline the fact that the chemical valence band offset itself does not stipulate the band alignment, since lattice mismatch induced strain shifts the band edges. For instance for a weak type II chemical valence band offset in the order a few meV, strain effects can reverse the band alignment and switch to a type I. Studying the effect of different band alignments is very important because as we switch from type I to type II confinement gets reduced therefore the presence probability of holes start to leak in ZnTe barrier [57]. In particular, for the core-shell structures we expect that additional strain induced by the outer ZnMgTe shell to ZnTe core will further influence the valence band ground state.

Weak confinement in combination with the emerging piezoelectric potential which further enhances electron-hole spatial separation [58], both affect the optical properties of the quantum dot by reducing oscillator strengths.
As an illustration we present in Fig. 2.10 the piezoelectric potential along xy and yz planes (left and right respectively) for a quantum dot with $L_{QD} = 4$ nm and $D_{QD} = 8$ nm. From the colormap on yz plane we observe that along the equator of the quantum dot, the piezoelectric potential $V_p = 0$. At the poles of the quantum dot, piezoelectric potential exhibits local maxima and minima. It is thus expected that the electron envelope will shift towards the pole where V_p becomes positive while the hole envelope will localize towards the opposite direction where V_p is negative. This of course is the case for a state well confined inside the dot. For a weakly
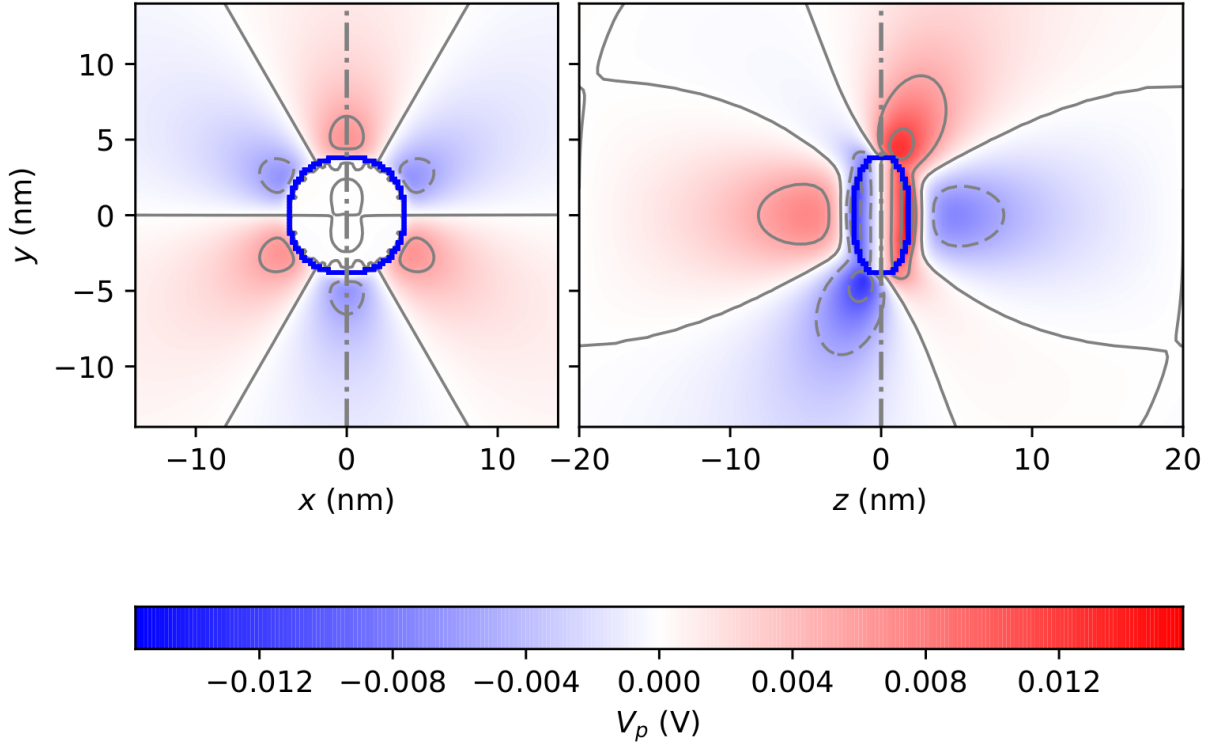
Figure 2.10 – The piezoelectric potential for a flat quantum dot with $L_{QD} = 4$nm along the xy plane (left) and yz plane (right)

confined hole which leaks towards the ZnTe barrier, s-like symmetry will break and the envelope will be localized to the three pockets of local minima as shown in Fig. 2.10.

In Fig. 2.11 we present the colormap of the piezoelectric potential for an elongated quantum dot with $L_{QD} = 18$ nm and $D_{QD} = 8$ nm. For a flat dot with $L_{QD}/D_{QD} = 0.125$ ($L = 1$nm) the magnitude of piezoelectric potential is 0.01 V while for a long dot with with $L_{QD}/D_{QD} = 2.5$ ($L = 20$nm) the magnitude is 0.025 V. The piezoelectric potential becomes stronger as we get closer to the poles of the dot and it takes its maximum values outside the dot, near to the interface with ZnTe where the effect of lattice mismatch is stronger. The values of the piezoelectric potential both inside the dot and outside near the interface with ZnTe do not get affected by the ZnMgTe shell.

There are two ways through which we can analyze the valence band ground state properties. The first one is to calculate the presence probability of light and heavy holes for each value of L_{QD}/D_{QD} by integrating the envelope function in space. The second one is to investigate hole mixing by calculating the oscillator strengths. There is a module in the *TB_Sim* package through which we can calculate the different momentum matrix elements for an interband transition from conduction to valence band. From these calculations we obtain the probability to have an optically bright transition for the electric field of light $\vec{E}//x$, $\vec{E}//y$ and $\vec{E}//z$.

2.4   Numerical calculations results of ZnTe-CdTe nanowire quantum dots

As discussed in the introduction, both confinement and axial shear strain determine the hole ground state. For a flat quantum dot ($L_{QD}/D_{QD} < 1$), shear strain becomes compressive along the xy plane, while for an elongate quantum dot ($L_{QD}/D_{QD} \geqslant 1$) shear strain becomes compressive along z axis which is parallel to $< 111 >$ direction. In Fig. 2.12 we plot the axial
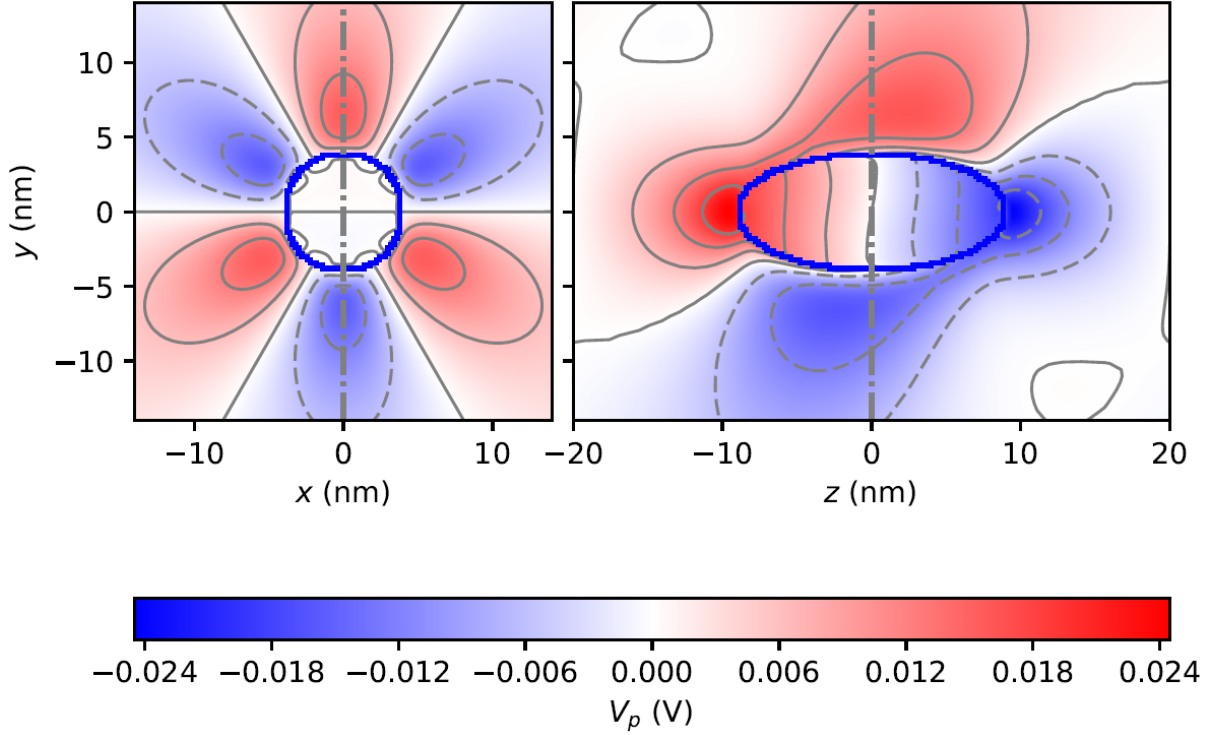
Figure 2.11 – The piezoelectric potential for an elongated CdTe quantum dot in a ZnTe nanowire with $L_{QD} = 18nm$ and $L_{QD}/D_{QD} = 2.25$ along the xy plane (left) and yz plane (right)

shear strain profile for a flat dot with $L_{QD}/D_{QD} = 0.5$. In this case we observe that inside the quantum dot $\varepsilon_{zz} > (\varepsilon_{xx} + \varepsilon_{yy})/2$ which means that shear strain is compressive along xy plane and the valence band will split promoting heavy hole as the ground state. What we also observe from Fig. 2.12 is that strain is not uniform inside the dot, as predicted from analytical models like the one developed by Eshelby [25]. This is attributed to the fact that the ellipsoidal inclusion i.e. the quantum dot, is incorporated in a cylinder with finite dimensions along x and y axis and not inside an infinite matrix.
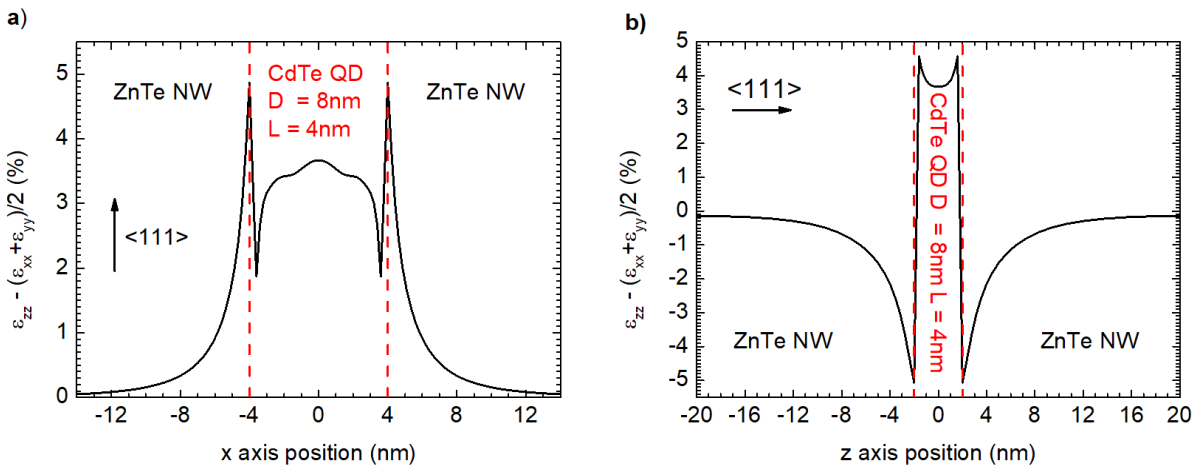

Figure 2.12 – Axial shear strain profile of a flat quantum dot along the xy plane a) and yz plane b).

As explained at the introduction of this chapter, the Q component of Luttinger-Kohn Hamiltonian influences the degeneracy of valence band and the splitting between hole states. Axial

shear strain influences Q through the Bir-Pikus component

$$Q_\varepsilon = \frac{d_v}{2\sqrt{3}}(\varepsilon_{xx} + \varepsilon_{yy} - 2\varepsilon_{zz}) \tag{2.68}$$

where d_v the deformation potential. For a flat dot where shear strain is compressive along xy plane it is $Q > 0$.
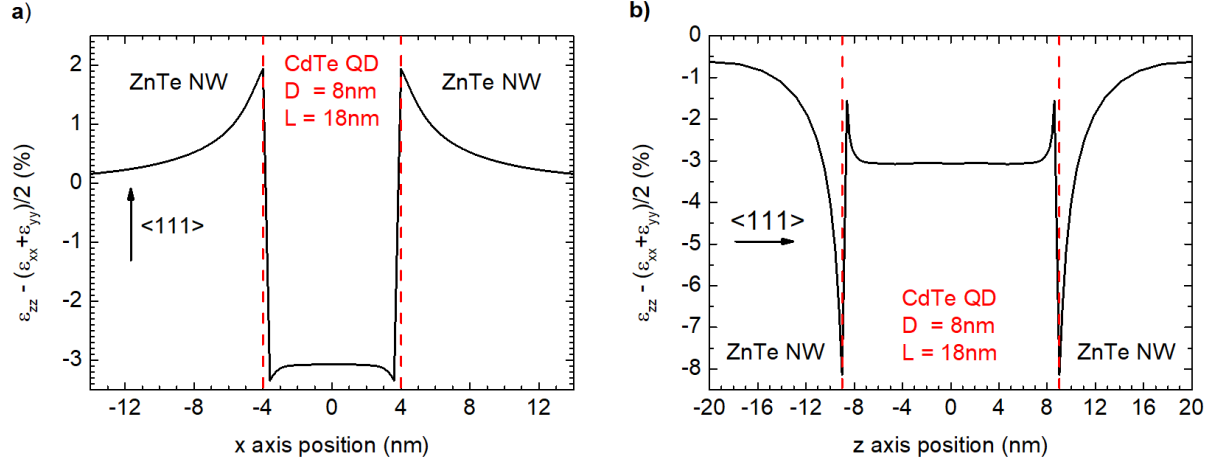

Figure 2.13 – Axial shear strain profile of an elongated quantum dot on the xy plane a) and yz plane b).

The R_ε and S_ε terms which influence the mixing of heavy and light holes are vanishing inside the dot and they take non-zero values in the ZnTe barrier outside. We will discuss their influence to the valence band ground state in the following subsections.

In Fig. 2.13 we plot the axial shear strain on xy plane for an elongated dot with $L_D/D_D = 2.25$. For this geometry it is $\varepsilon_{zz} < (\varepsilon_{xx} + \varepsilon_{yy})/2$ inside the quantum dot, consequently axial shear strain is compressive along z axis. For the elongated quantum dot it is $Q < 0$, as a result we expect a light hole ground state. In the next subsections we discuss the numerical calculation results for a flat ($L_D/D_D = 0.5$) and an elongated ($L_D/D_D = 2.25$) quantum dot for a strong type I and type II band alignment and a weak type II. By examining these cases for the two nanowire quantum dots depicted at Fig. 2.7 we can draw useful conclusions through which we can interpret experimental results.

2.4.1 Strongly confined type I nanowire quantum dot

The first structure we examined was a CdTe quantum dot in a ZnTe nanowire assuming a strong type I CdTe/ZnTe valence band offset equal to 200 meV. We carried out calculations for a nanowire quantum dot with and without the presence of a ZnMgTe shell. Before analyzing the valence band we will discuss the properties of electrons which are similar for all three cases since the conduction band offset between ZnTe and CdTe remains almost the same.
In Fig. 2.14 we plot the envelope presence probability $|F_e|^2$ for electrons on two planes for a flat dot with $L_{QD}/D_{QD} = 0.5$ a), b) and for an elongated dot with $L_{QD}/D_{QD} = 2.25$ c), d). The variation of envelope presence probability for conduction and valence band changes along the three directions. For this reason in order to reveal the shape and symmetry, we introduced the projection of each component on xy and yz planes, otherwise information as regards the wavefunction will be incomplete. The projections along xy and yz planes are calculated from the integrals

$$P_{F_i}^{(xy)} = \int F_i(x,y,z)F_i^*(x,y,z)dz \qquad P_{F_i}^{(yz)} = \int F_i(x,y,z)F_i^*(x,y,z)dx \tag{2.69}$$
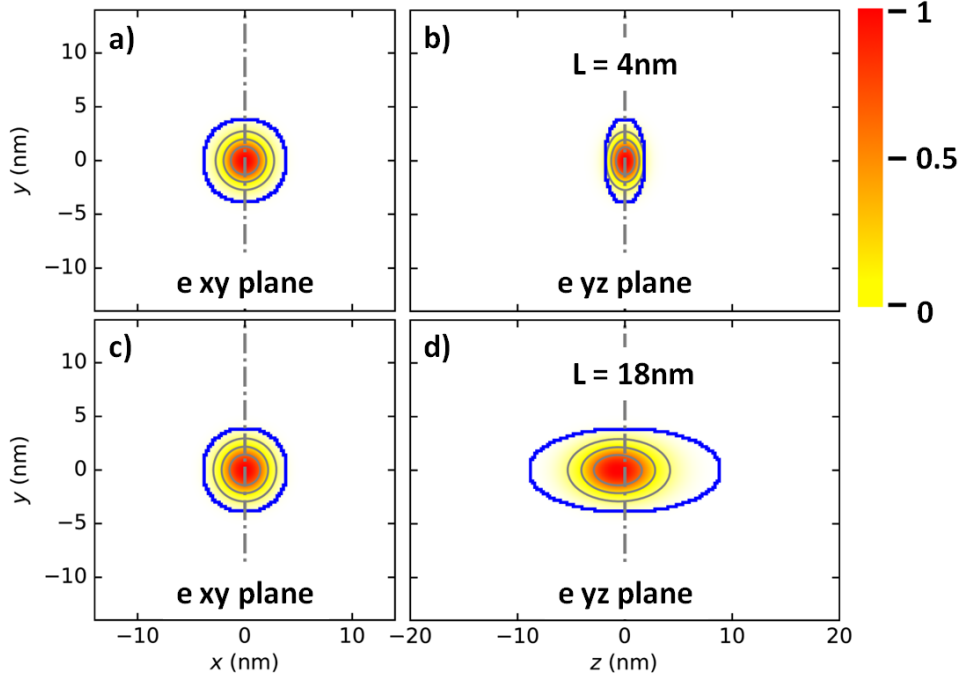
Figure 2.14 – The electron envelope functions for a flat a) on xy plane b) on yz plane and an elongated quantum dot c) on xy plane d) on yz plane.

where i the index which represents the corresponding envelope, i.e. $i = e$ for electrons, $i = 3/2, \pm 3/2$ for heavy holes, $i = 3/2, \pm 1/2$ for light holes and $i = 1/2, \pm 1/2$ for split-off. The envelope for electrons has an s-like symmetry, as expected for the ground state. The presence of an external ZnMgTe shell does not affect significantly the electrons since they are strongly confined inside the dot.

For the elongated dot we observe a shift of the envelope towards the quantum dot pole, attributed to the piezoelectric potential. As we switch from a flat to an elongated quantum dot, we induce more strain and as consequence we increase the magnitude of piezoelectric potential.

In Fig. 2.15 we plot the eigenvalues of the electrons for the first two calculated energy levels as a function of the quantum dot aspect ratio. From the plot we confirm that electrons are strongly confined inside the dot, as the conduction band offset between CdTe and ZnTe is 785 meV. Also, the ground state is well separated from the first excited state for $L_{QD} > 1$ nm. For the case where $L_{QD} = 1$ nm ground state is almost degenerate with the excited state. This is due to the fact that electrons are weakly bound and they become resonant with the barrier. This is something we observe systematically, as ground state and excited states are well separated, with the exception of small dots, where states become weakly bound and they merge with the barrier. This case however is not of interest in the context of this study. As regards the excited state, for $L_{QD} = 1$ - 3 nm the energy level is pinned at 2.19 eV. This is attributed to the strong leaking of the electron envelope in the ZnTe core. For $L_{QD} > 3$ nm, confinement gets restored.

By looking at the properties of valence band, we observe that for this structure the presence of an external ZnMgTe shell does not affect significantly the properties of the hole ground state since the confinement is strong inside the dot. This becomes clear from the energy curve plots of Fig. 2.16. Our results are in agreement with those discussed in [26] for a III-V based heterostructure.

In Fig. 2.17 we plot the integrated presence probability for the two hole components given by
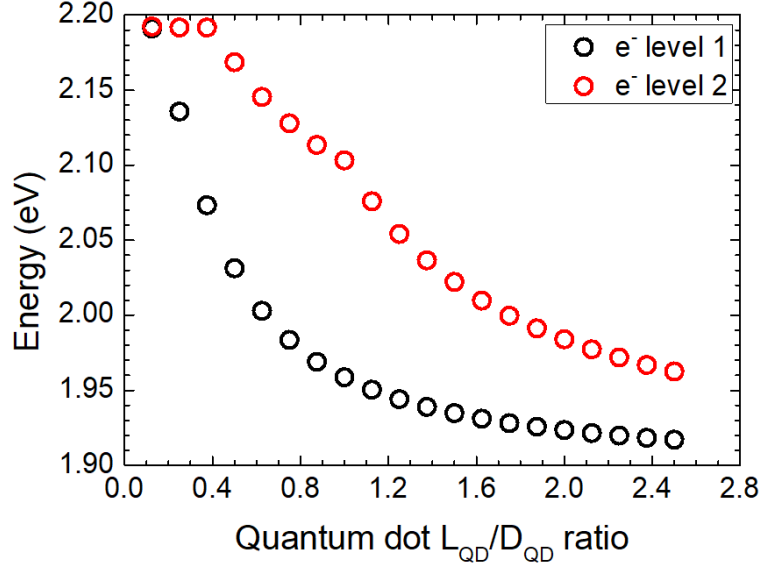
Figure 2.15 – The evolution of conduction band electrons energy for the two first calculated levels as a function of L_{QD}/D_{QD} ratio.
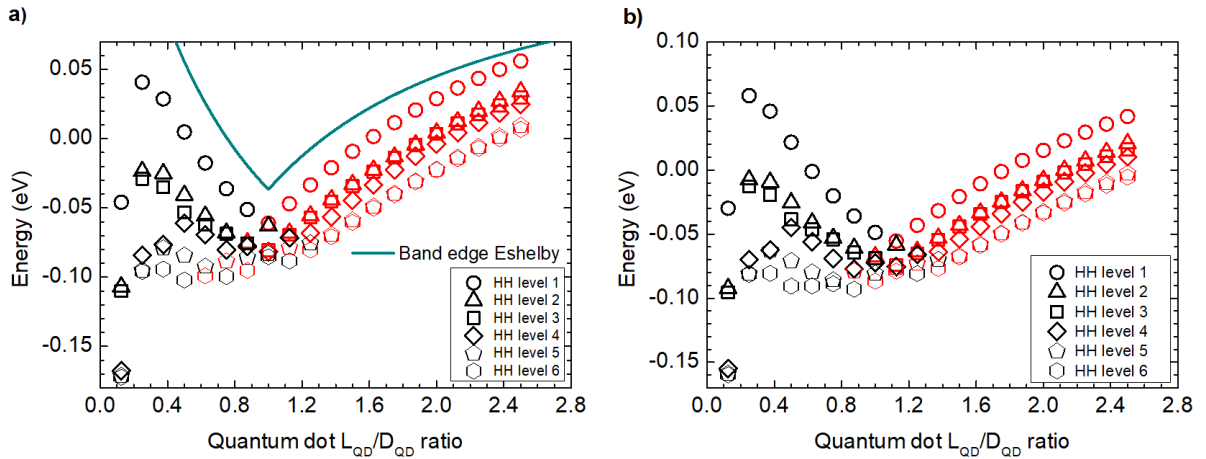

Figure 2.16 – The energy of the first six Kramers doublets as a function of the aspect ratio for a CdTe quantum dot in a ZnTe nanowire including the analytical calculation of the valence band edge a) and for a CdTe quantum dot in a ZnTe-ZnMgTe core-shell nanowire b). Black color corresponds to a predominantly heavy hole component and red color to a light hole.

$$P_{HH} = \int \sum_{m=\pm\frac{3}{2}} |F_{3/2,m}(\vec{r})|^2 d^3\vec{r}, \qquad P_{LH} = \int \sum_{m=\pm\frac{1}{2}} |F_{3/2,m}(\vec{r})|^2 d^3\vec{r} \qquad (2.70)$$

For an aspect ratio $L_{QD}/D_{QD} \geq 1$ the valence band ground state switches from heavy hole to light hole. In the vicinity of $L_{QD}/D_{QD} \approx 1$ we observe a weak mixing between the two hole state. Later we will show that this mixing is optically dark. What we observe by plotting the valence band energies for the first six calculated Kramers doublets, is that the ground state is well separated from the excited states for all different aspect ratios.

For $L_{QD}/D_{QD} = 1$ where we observe the switching, the separation between light and heavy hole is 2 meV for a CdTe quantum dot in a ZnTe nanowire and 3 meV for a CdTe quantum dot in a ZnTe-ZnMgTe core-shell nanowire (Fig. 2.16). Normally we would expect for a spherical
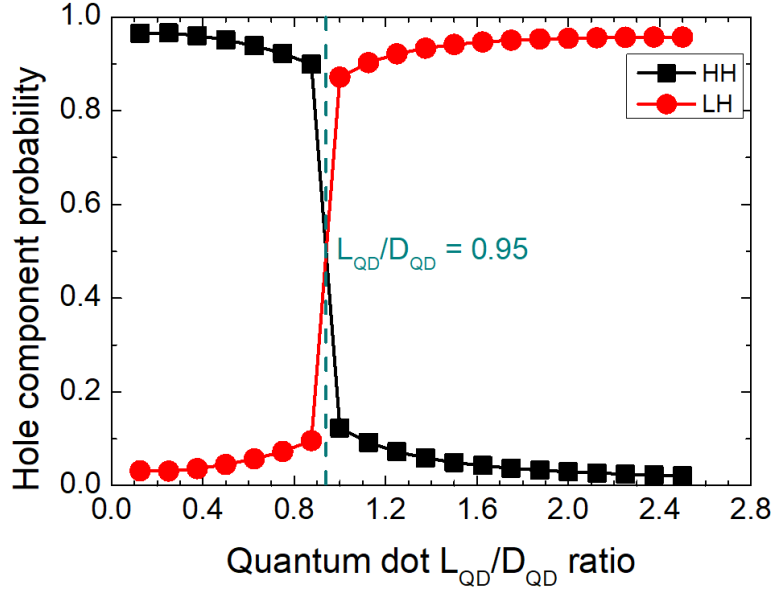
Figure 2.17 – The switching curve from heavy hole to light ground state as a function of the quantum dot length to diameter aspect ratio.

inclusion the two states to be degenerate since strain inside the dot vanishes. This indeed would be true for an inclusion in a infinite matrix where the strain would be isotropic. This is not our case, since the dot is inside an infinite nanowire along z with finite dimensions along x and y axis, consequently, induced axial shear strain is anisotropic. Energy separation becomes stronger for the core-shell nanowire due to additional anisotropic strain introduced by the shell. Nevertheless, we expect that in the vicinity of $L_{QD}/D_{QD} \approx 1$ there is a certain value of aspect ratio for which the levels become degenerate. In Fig. 2.16 a) we plot the energy of confined states as a function of the L_{QD}/D_{QD} aspect ratio and the valence band edge as derived from the model of Eshelby including the Bir-Pikus deformation potential for an ellipsoidal inclusion in an infinite matrix [25]. We observe that the slope of confined states is in good agreement with the slope of valence band edge calculated analytically and any differences are attributed to non-uniformity of strain inside the dot as shown in Fig. 2.12.

To investigate the valence band ground state in terms of allowed optical transitions we calculated the oscillator strengths.

The momentum operator discussed in subsection 4.2.6 changes the parity of the state and for a bright optical transition, the momentum matrix element should be non zero. The Bloch components of conduction and valence band have different parity. Conduction band Bloch function is a linear combination of s-like atomic orbitals while valence band is a linear combination of p-like atomic orbitals. On the other hand, the envelope components of both conduction and valence band ground state are s-type thus they have the same parity. For this reason the allowed optical transitions are only among states which share the same envelope function symmetry, as is the case for the ground states characterized by s-like envelopes.

The direction of dipole transition and by extent the polarization of emitted light are determined only by the Bloch function symmetry of the valence band. The conduction band - valence band transitions where $\Delta J_z = \pm 1$ generate light where the electric field components are polarized along the xy plane, while transition where $\Delta J_z = 0$ generates light with the electric field polarized along z axis. In Fig. 2.18 we plot the normalized oscillator strength probability amplitudes in xy plane and along z as a function of the quantum dot aspect ratio.
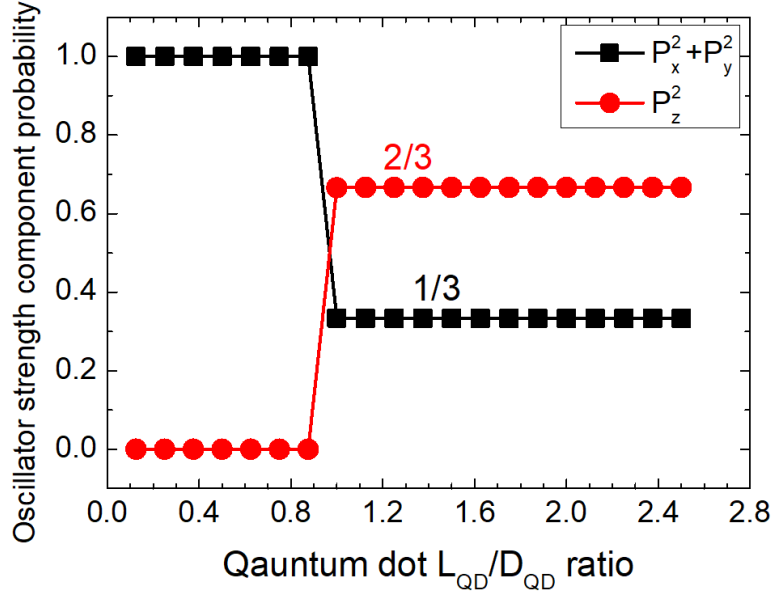
Each component is given by

Figure 2.18 – Oscillator strength components P_x^2 and P_y^2 in plane and P_z^2 along the nanowire axis, associated with transitions polarized on xy plane and along z respectively, as a function of the quantum dot aspect ratio, for a CdTe quantum dot in a ZnTe nanowire. For the oscillator strength calculations we consider only the ground state of electron, for which the transition energy is minimum.

$$|P_x|^2 + |P_x|^2 = \frac{|p_x|^2 + |p_y|^2}{\sum_{j=x,y,z} |p_j|^2}, \qquad |P_z|^2 = \frac{|p_z|^2}{\sum_{j=x,y,z} |p_j|^2} \qquad (2.71)$$

where p_x, p_y, p_z are the complex dipole matrix elements along the three directions x, y, z. From these calculations we always confirm that $|P_x|^2 = |P_y|^2$ as expected for the transitions associated to emitting dipoles along x and y axis. For $L_{QD}/D_{QD} < 1$, $|P_z|^2$ vanishes and there is contribution only from $|P_x|^2$ and $|P_y|^2$, which is in agreement with a pure heavy hole ground state. When $L_{QD}/D_{QD} \geq 1$ there is a sharp switch from heavy to light hole where $|P_x|^2$ and $|P_y|^2$ account for the 1/3 of total probability and $|P_z|^2$ for 2/3. This is in perfect agreement with the optical selection rules for a light hole ground state in a bulk semiconductor. At the same time we confirm that mixing for L_{QD}/D_{QD} values near 1, as shown in Fig. 2.17, is optically dark. An explanation for this effect is due to the fact that light and heavy hole envelope symmetries before and after the switching respectively, are not compatible with a dipole transition. Another significant quantity is the phase of the envelope, but it was beyond the scope of this work to study in detail its effect on the oscillator strengths.

The projections of envelope components for heavy hole, light hole and split-off band for the flat dot are shown in Fig. 2.19. In this case, we have a heavy hole ground state -Fig. 2.19 a), b)- with a very small contribution of light hole -Fig. 2.19 c), d)- and split-off band -Fig. 2.19 e), f). Heavy hole component has an s-like symmetry and it is strongly confined inside the dot. On the other hand, light hole and split-off have a symmetry resembling a torus like shape and they leak towards the CdTe-ZnTe interface and outside the dot. Light hole leaks towards the poles of quantum dot and its shape is distorted due to the abrupt switching from compressive strain along xy inside the dot to compressive along z outside. Split-off projection is more symmetric because it mostly leaks towards the equator where axial shear strain is compressive along xy and follows a smooth gradient from the dot to the barrier. By plotting the total presence probability -Fig. 2.19 g), h)- we retrieve the strongly confined s-like shell of heavy hole, while the contribution of light hole and split-off is vanishing and as we showed previously they do not
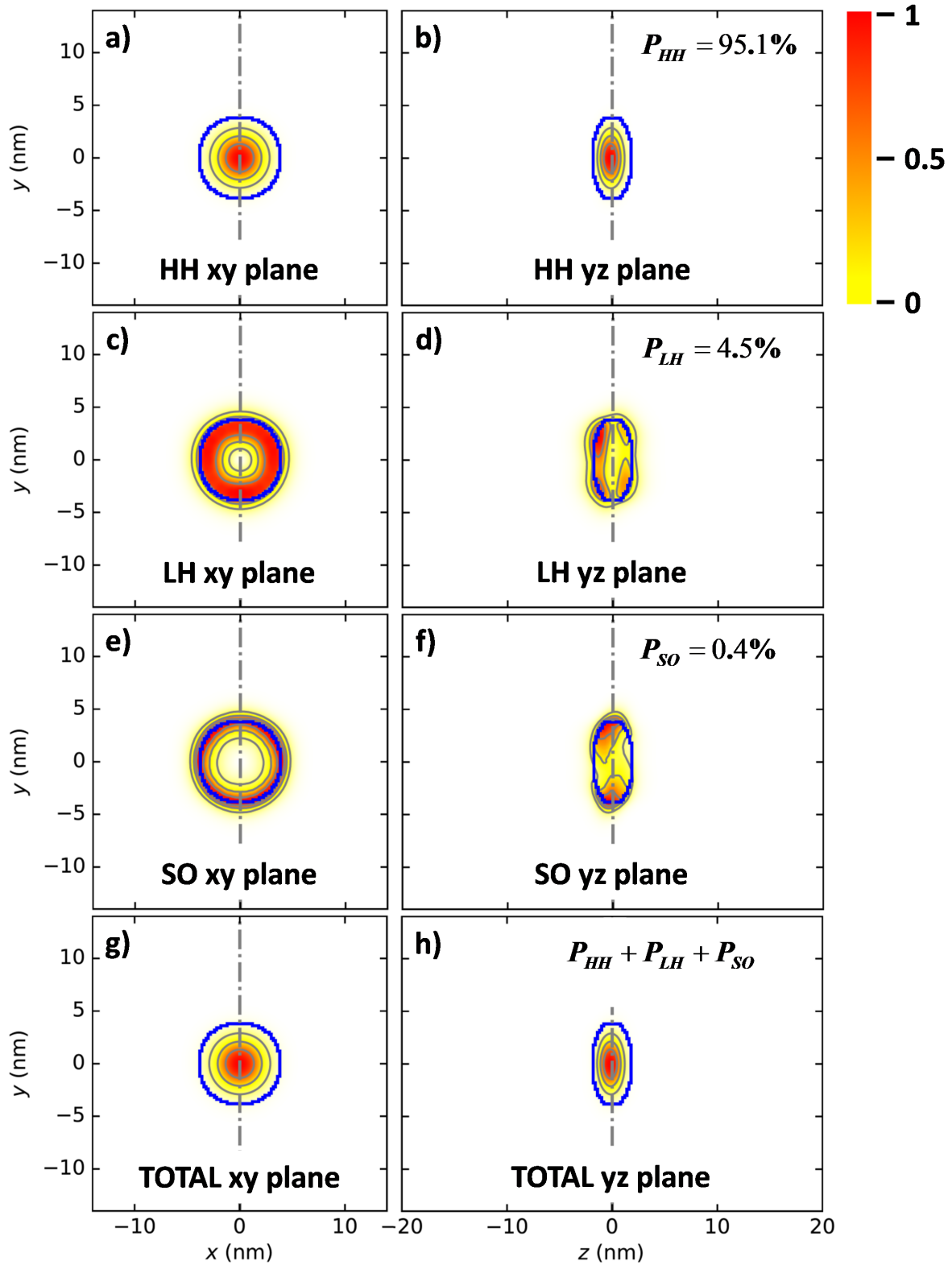
Figure 2.19 – **200 meV type I flat dot in a ZnTe nanowire:** The projections of presence probability components for a 200 meV type I flat CdTe quantum in a ZnTe nanowire with $L_D/D_D = 0.5$. Heavy hole component on xy a) and yz b) plane. Light hole component on xy c) and yz d) plane. Split-off component on xy e) and yz f) plane. The sum of the three envelope components on xy g) and yz h) plane

Figure 2.20 – **200 meV type I elongated dot in a ZnTe nanowire:** The projections of presence probability components for a 200 meV type I elongated CdTe quantum dot in a ZnTe nanowire with $L_D/D_D = 2.25$. Heavy hole component on xy a) and yz b) plane. Light hole component on xy c) and yz d) plane. Split-off component on xy e) and yz f) plane. The sum of the three envelope components on xy g) and yz h) plane
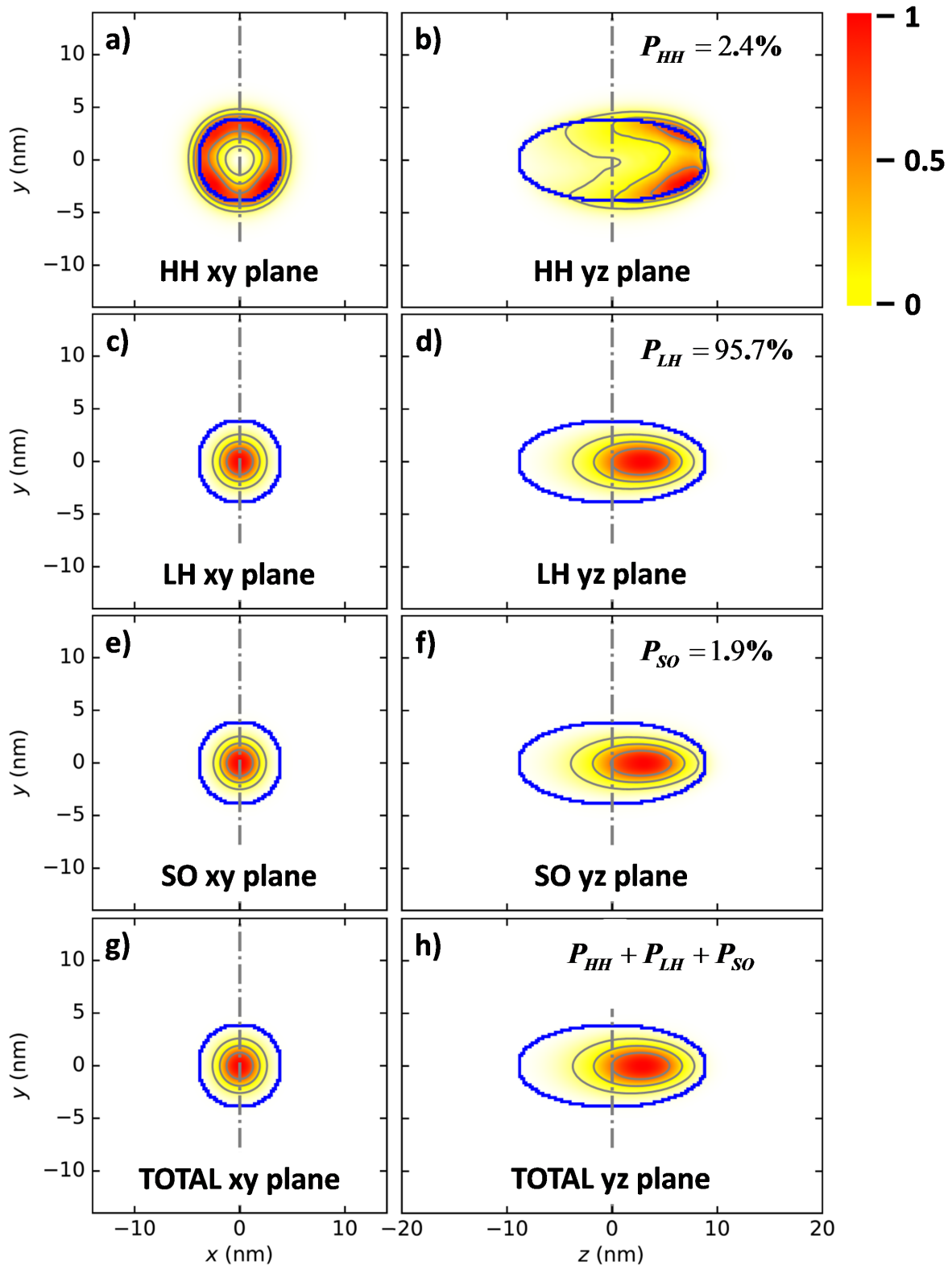
contribute to optically bright transitions at all.

In Fig. 2.20 we present the valence band envelope components for an elongated quantum dot. In this case, ground state is a light hole -Fig. 2.20 c), d)- mixed very weakly with heavy hole which leaks towards the barriers and split-off. What we observe here is that the contribution of split-off state is slightly stronger and that its symmetry is identical to the light hole. This was not the case for the flat dot where split-off was strongly pushed towards the barrier. The effect of piezoelectric potential becomes obvious as the hole envelope is shifted towards the opposite direction of that of the electron. This separation affects the values of oscillator strengths which become weaker for an L_{QD}/D_{QD} taking values larger than 1.

2.4.2 Reducing the valence band offset: Properties of a weak type I quantum dot

In this section we will investigate the properties of the valence band ground state in a quantum dot with a reduced chemical valence band offset of 20 meV type I. We expect that this band alignment is similar to that of a batch of samples studied experimentally which will be discussed in a following chapter. In a same way as in the previous section we will discuss the effect of reducing the valence band offset in a flat and an elongated CdTe quantum dot in a ZnTe nanowire with and without the presence of an external ZnMgTe shell.
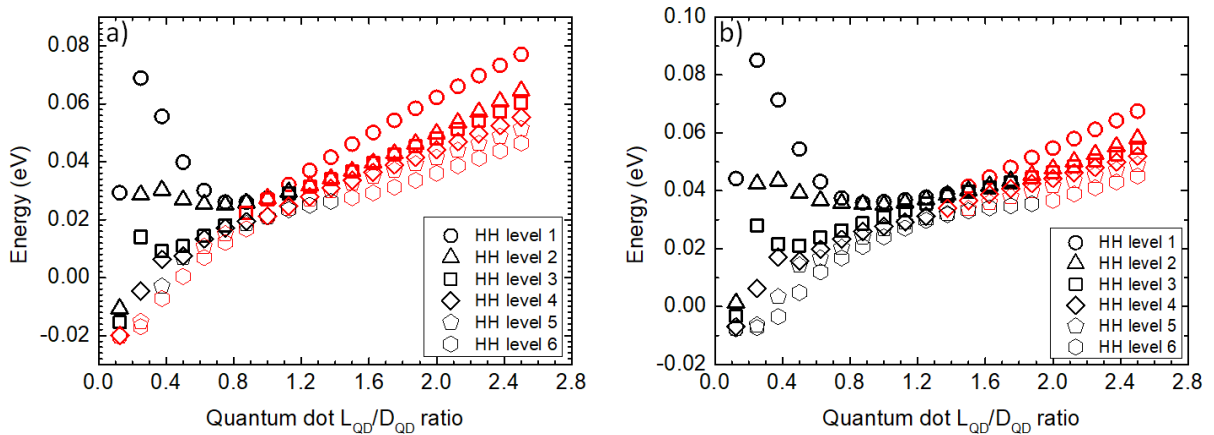

Figure 2.21 – Valence band energy levels of the first six Kramers doublets as a function of the quantum dot L_{QD}/D_{QD} ratio. For a CdTe - ZnTe nanowire quantum dot a) and for a CdTe dot in a core shell ZnTe - ZnMgTe nanowire b). Black color corresponds to a predominantly heavy hole component and red color to a light hole.

In Fig. 2.21 a) we present the evolution of the first 6 calculated valence band energy levels for a CdTe quantum dot in a ZnTe nanowire and in Fig. 2.21 b) for a CdTe quantum dot in a ZnTe-ZnMgTe core-shell nanowire. The first thing we notice is the effect of reduced confinement, as the energy difference between the levels becomes smaller. This effect is stronger for the core-shell nanowire and it is a direct evidence that the strain induced from the external ZnMgTe shell, further reduces the valence band offset and thus confinement. For the CdTe-ZnTe quantum dot without the external shell, we observe as expected, that for $L_{QD}/D_{QD} > 1$, light holes are the predominant components of the calculated states. By introducing the external ZnMgTe shell however, heavy hole contribution becomes stronger and even at $L_{QD}/D_{QD} = 1.4$ they are the predominant components of the ground state. In order of course to understand the purity of the ground state and quantify the mixing between heavy and light holes, we have to plot the switching curves and calculate the oscillator strengths. In order to do that though, we have also to take into account the excited states which are degenerate or quasi-degenerate with the first calculated state. This is attributed to the fact that symmetries break, because we use a

square mesh, which is not compatible with the three fold symmetry of $< 111 >$ axis. As a results, states which should be completely degenerate, they are not. In general states separated by up to 1 meV can be considered degenerate and in order to calculate the overall contribution of each hole component we just take the average value of each, over the states we consider degenerate. It is important to underline that we didn't choose this value of 1 meV arbitrarily. We concluded to this assessment by a thorough study of the symmetry of the total envelope function. Initially we plotted the projections of all envelope components of all calculated states for all L_{QD}/Q_{QD} aspect ratios where there was evidence of degeneracy. Then we calculated in steps their sums by starting from the first excited state and then gradually adding the rest of them. We observed that by summing all states which are within 1 meV difference, we restored a three fold symmetry which is what we expect for a system with weak confinement where the envelope starts to leak outside the dot.
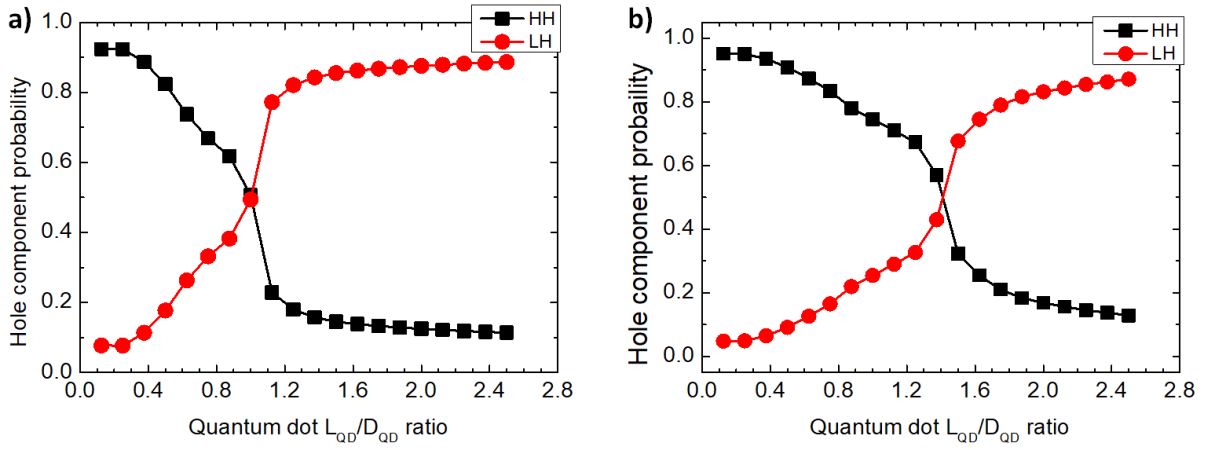

Figure 2.22 – Heavy hole - light hole switching as a function of L_{QD}/D_{QD} ratio for a CdTe - ZnTe nanowire quantum dot with a weak type I chemical valence band offset of 20 meV, without a shell a) and passivated by a ZnMgTe shell b).

In Fig. 2.22 a), we present the switching curve between heavy and light holes for a CdTe quantum dot in a ZnTe nanowire. The main difference in comparison to the strong type I case, is that for aspect ratios $L_{QD}/D_{QD} > 0.3$, we start to mix heavy with light holes. For $L_{QD}/D_{QD} > 1$ we restore light hole as the predominant component of the ground state, though mixed by 20% with a heavy hole. By increasing the quantum dot aspect ratio, the percentage of light hole also increases and at $L_{QD}/D_{QD} = 2.5$ it becomes 90%.

In Fig. 2.22 b), we present the switching curve between heavy and light holes for a CdTe quantum dot in a ZnTe-ZnMgTe core-shell nanowire. Similar to the nanowire quantum dot without the shell, for increasing L_{QD}/D_{QD} aspect ratio, heavy holes mix with light holes. The most important observation though is that the switching from light hole to heavy hole takes place at $L_{QD}/D_{QD} \geq 1.5$. From that, we confirm that there is a mechanism which delays the switching between heavy and light hole for values of the quantum dot aspect ratio significantly larger than one. Also, even when ground state becomes predominantly light hole, the mixing with heavy hole is arround 20%.

For both heterostructures, with and without the shell, the results obtained from the switching curves are very interesting and it remains to be further confirmed from the calculation of oscillator strengths.

In Fig. 2.23 a) we present the oscillator strength probabilities $|P_x|^2 + |P_y|^2$ and $|P_z|^2$ for a CdTe quantum dot in a ZnTe nanowire. Contrary to our observation from the switching curve, from the oscillator strength probabilities we confirm that for $L_{QD}/D_{QD} < 1$ optically bright transitions are associated only to heavy holes and for $L_{QD}/D_{QD} > 1$ to light holes. For
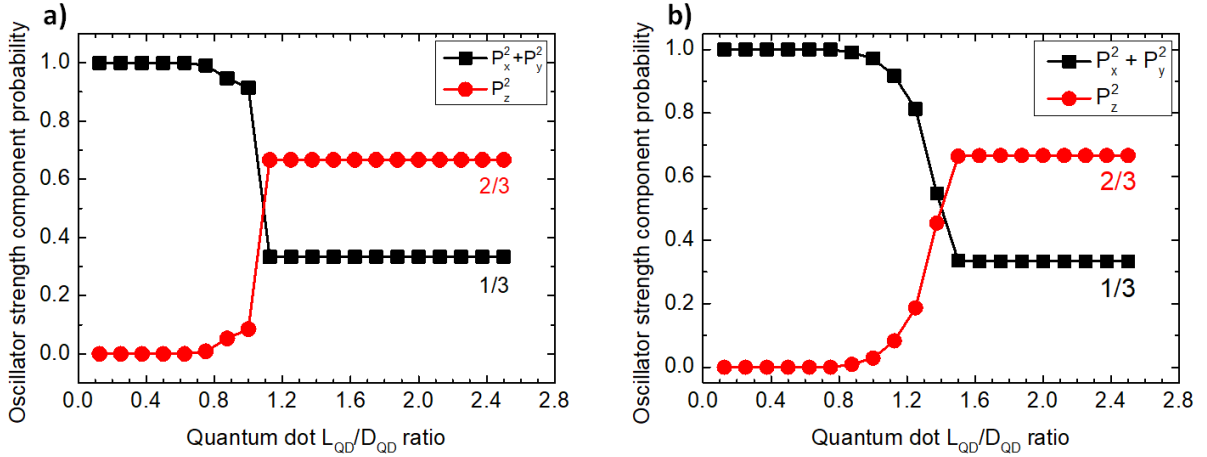
Figure 2.23 – The probability of oscillator strength components $|P_x|^2$ and $|P_y|^2$ in plane and $|P_z|^2$ along the nanowire axis, associated with transitions polarized on xy plane and along z respectively, as a function of the quantum dot aspect ratio, for a CdTe quantum dot in a ZnTe nanowire a) and for a CdTe quantum dot in a ZnTe-ZnMgTe core-shell nanowire b)

$0.9 < L_{QD}/D_{QD} < 1$ there is a weak mixing between the two hole states. From the oscillator strengths plot we understand that the mixing between heavy and light holes as shown in the switching curve of integrated presence probabilities of Fig. 2.22 a), is mostly optically dark.

The picture becomes different when we introduce the ZnMgTe shell, as shown in Fig. 2.23 b). For $L_{QD}/D_{QD} < 0.9$, only heavy holes contribute to optically bright transitions, then for $0.9 < L_{QD}/D_{QD} < 1.5$ heavy holes become mixed with light holes and for $L_{QD}/D_{QD} > 1.5$, oscillator strengths probabilities are in agreement with a pure light hole ground state. Again in this case the mixing obtained from the integrated presence probability switching curve for small values of L_{QD}/D_{QD} is optically dark. What we confirm however, is that switching from heavy to light hole, takes place at $L_{QD}/D_{QD} > 1.5$.

So far, it has become clear that the valence band offset plays an important role to the hole type and purity of the valence band ground state. In Fig. 2.24 we present the envelope projections for the different hole states for a flat quantum dot in a ZnTe nanowire. For both structures with and without the shell, the symmetry and envelope presence probability of each hole state are similar. Comparing with the strong type I case, we see that although the envelope is still well confined inside the dot, it begins to leak towards the ZnTe core. The mixing obtained from the switching curves is attributed to the fact that off-diagonal strain components start to mix light hole with heavy hole near the CdTe-ZnTe interface and outside the dot. On the other hand, the envelope of electrons is strongly confined inside the dot as with the strong type I case, because the conduction band offset does not change. As a result, there is a very strong overlap with the envelope of heavy holes and an almost vanishing one with that of light holes. This is why at small L_{QD}/D_{QD}, optically bright transitions are almost exclusively along xy plane.

The situation for small aspect ratios is straightforward. We now want to investigate the envelope shape and presence probability for quantum dot aspect ratios where from both the switching curves and oscillator strengths we see that heavy holes are strongly mixed with light holes.

In Fig. 2.25 we present the envelope presence projections for the different hole states for a CdTe dot in a ZnTe-ZnMgTe core-shell nanowire for $L_{QD} = 9$nm. The integrated presence probability of heavy hole is $P_{HH} = 70.4\%$ and that of light hole $P_{LH} = 28.7\%$. Also, according to Fig. 2.23 b) the oscillator strength probabilities are $|P_x|^2 + |P_y|^2 = 0.91$ and $|P_z|^2 = 0.09$. In this case, heavy hole leaks outside the dot, thus reducing the overlap between its envelope and that of the electron. Light hole on the other begins to enter the quantum and its overlap

Figure 2.24 – **20 meV type I flat dot in a ZnTe nanowire:** The projections of presence probability components for a 20 meV weak type I flat CdTe quantum in a ZnTe core nanowire with $L_{QD}/D_{QD} = 0.5$. Heavy hole component on xy a) and yz b) plane. Light hole component on xy c) and yz d) plane. Split-off component on xy e) and yz f) plane. The sum of the three envelope components on xy g) and yz h) plane

Figure 2.25 – **20 meV type I elongated dot in a ZnTe-ZnMgTe core-shell nanowire:** The projections of presence probability components for a 20 meV weak type I elongated CdTe quantum in a ZnTe-ZnMgTe core-shell nanowire with $L_{QD}/D_{QD} = 1.125$. Heavy hole component on xy a) and yz b) plane. Light hole component on xy c) and yz d) plane. Split-off component on xy e) and yz f) plane. The sum of the three envelope components on xy g) and yz h) plane

with the electron becomes comparable to that of the heavy hole. Of course, still the integrated presence probability of heavy hole is stronger, as a result oscillator strengths associated to it are also stronger. Gradually however, by increasing L_{QD}/D_{QD}, we increase both the integrated presence probability and confinement of light hole, ultimately stabilizing it as the predominant valence band ground state component.

In Fig. 2.26 we present the envelope projections for an elongated CdTe quantum in a ZnTe nanowire with $L_{QD}/D_{QD} = 2.25$. Similar to the flat quantum dot case, for both heterostructures with and without the ZnMgTe external shell, the envelope symmetry and presence probability is almost the same. In this case a light hole is stabilized as a ground state. The effect of weak confinement due to reduced valence band offset is clearly visible, as the envelopes of all hole states are localized near the pole of the quantum dot and they start to leak towards the ZnTe shell. This is attributed to the piezoelectric potential which is negative in this region and just outside the dot it exhibits a minimum of 25 mV. Finally, as with the strong type I one, the presence probability of split-off also increases by increasing the L_{QD}/D_{QD} aspect ratio, indicating a coupling with the light hole state.

2.4.3   The effect of a strong type II offset on the valence band ground state

So far we have discussed the properties of the valence band ground state for a type I band alignment and we saw that its properties are strongly affected as we reduce it. As a consequence it is important to investigate the effect of switching from a type I to a type II band alignment which could be the case of the nanowire quantum dots we studied experimentally.

In this section we discuss the effect of a large type II chemical band offset of 200 meV on the valence band ground state. This value is larger in comparison to what is reported in literature and it was selected on purpose because we wanted to study the hole ground state when its wavefunction leaks strongly towards the ZnTe core.

As we see in Fig. 2.27 for both cases the first calculated energy level is always quasi-degenerate with excited states. As a consequence, for the calculation of the ground state and mixing between heavy and light holes we have to take degeneracy into account. For a nanowire quantum dot without the external ZnMgTe shell, we observe that for all values of L_{QD}/D_{QD}, heavy holes are strongly mixed with light holes. At this point we do not know if for larger L_{QD}/D_{QD} ratios, a pure light hole as a ground state gets restored. Also for $L_{QD} = 1$ nm we observe the same effect as we did for electrons. Holes get bound to the barrier, as a result the states become degenerate, but again this is beyond the scope of this work.

From the plot of integrated presence probabilities as a function of the quantum dot aspect ratio for a CdTe dot in a ZnTe nanowire, shown in Fig. 2.28 a), we confirm the strong mixing between heavy and light holes. For $L_{QD}/D_{QD} < 2$ the integrated presence probability of heavy hole component is always smaller than that of light holes. In particular, for $1.4 < L_{QD}/D_{QD} < 1.9$ light hole becomes significantly stronger with a contribution ranging from 60% - 70%. Then for $L_{QD}/D_{QD} > 2$ the probability of heavy hole becomes larger than that of light hole and up to the calculated value for $L_{QD} = 20$ nm it increases constantly.

The switching curve shape is strange and it raises again the question about how accurate it is to just rely on the integrated presence probability of each envelope component, in order to investigate the mixing and switching between heavy and light holes for a type II band alignment. We have already shown in the previous subsections that for both strong and weak type I band alignment, near $L_{QD}/D_{QD} \approx 1$ light holes get darkly mixed with heavy holes. Dark mixing becomes stronger for the weak type I valence band offset, where leaking of the envelope outside the dot is also larger. As a conclusion there is a strong connection between leaking and dark mixing. Another factor which might have a small effect on the shape of the switching curve is the method we use to average upon states which are degenerate. A more accurate method would be to take a thermal average using exponential functions, but we do not expect a significant change on the shape.
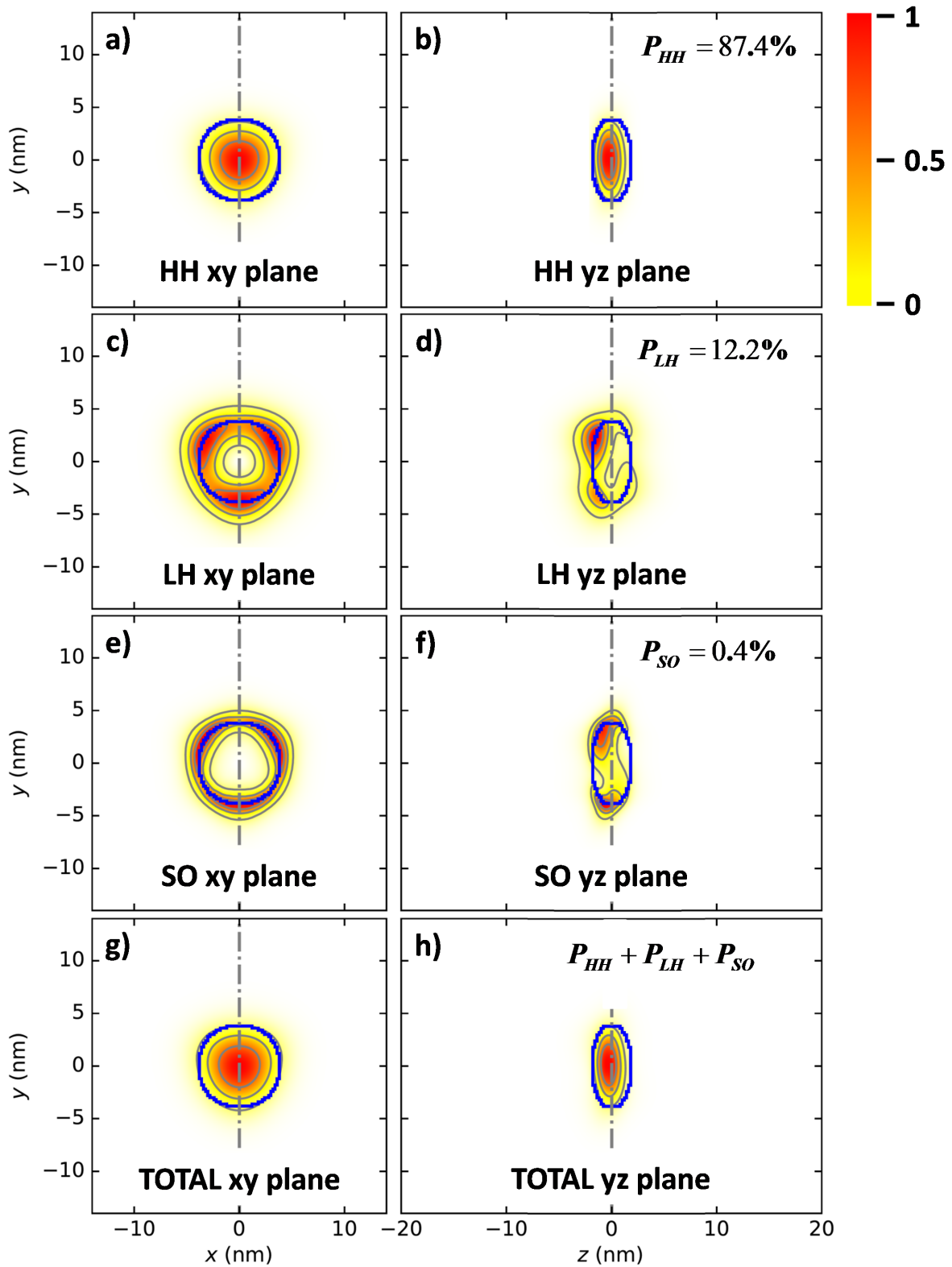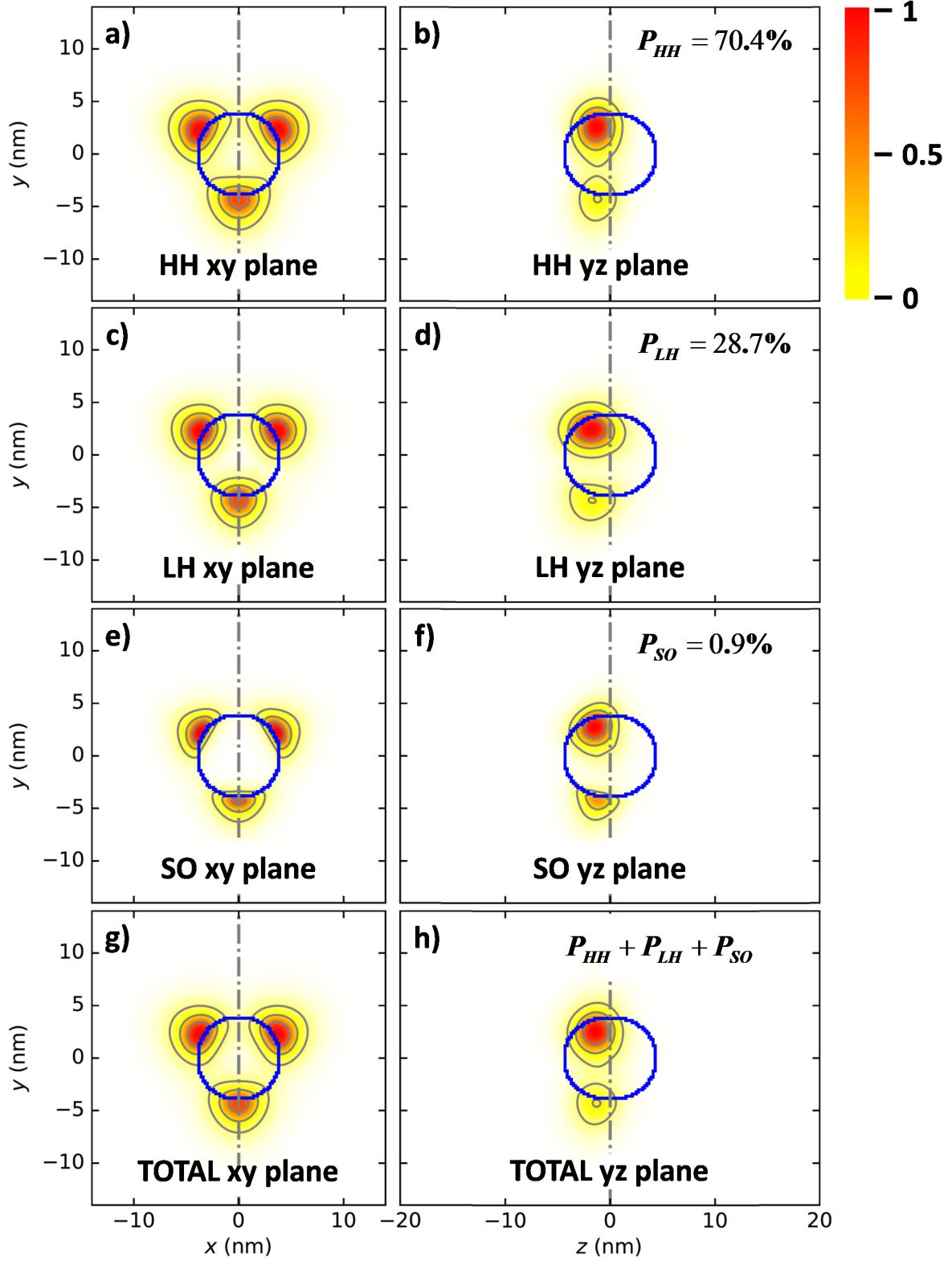
Figure 2.26 – **20 meV type I elongated dot in a ZnTe nanowire:** The projections of presence probability components for a 20 meV weak type I elongated CdTe quantum in a ZnTe core nanowire with $L_{QD}/D_{QD} = 2.25$. Heavy hole component on xy a) and yz b) plane. Light hole component on xy c) and yz d) plane. Split-off component on xy e) and yz f) plane. The sum of the three envelope components on xy g) and yz h) plane
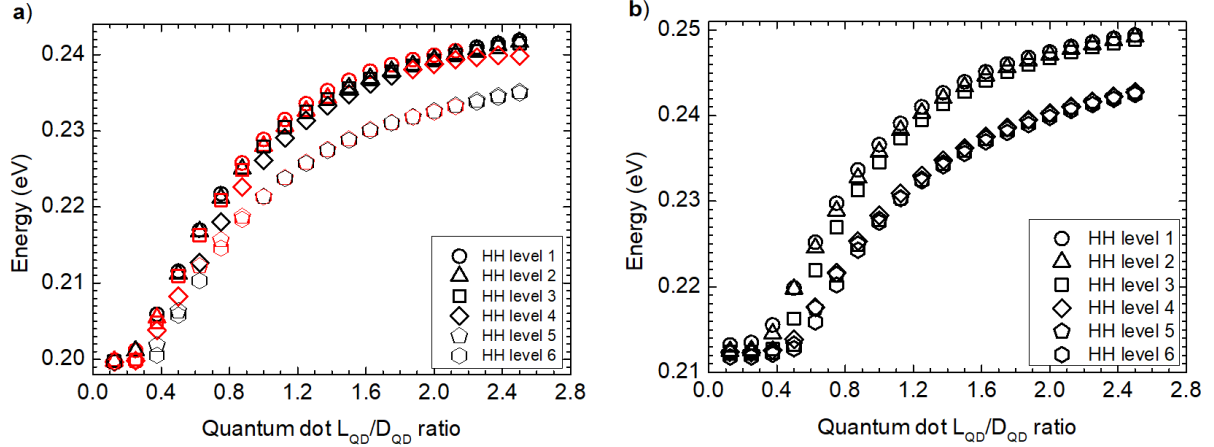
Figure 2.27 – Valence band energy levels of the first six Kramers doublets as a function of the quantum dot L_{QD}/D_{QD} ratio. For a CdTe - ZnTe nanowire quantum dot a) and for a CdTe dot in a core shell ZnTe - ZnMgTe nanowire b). Black color corresponds to a predominantly heavy hole component and red color to a light hole.
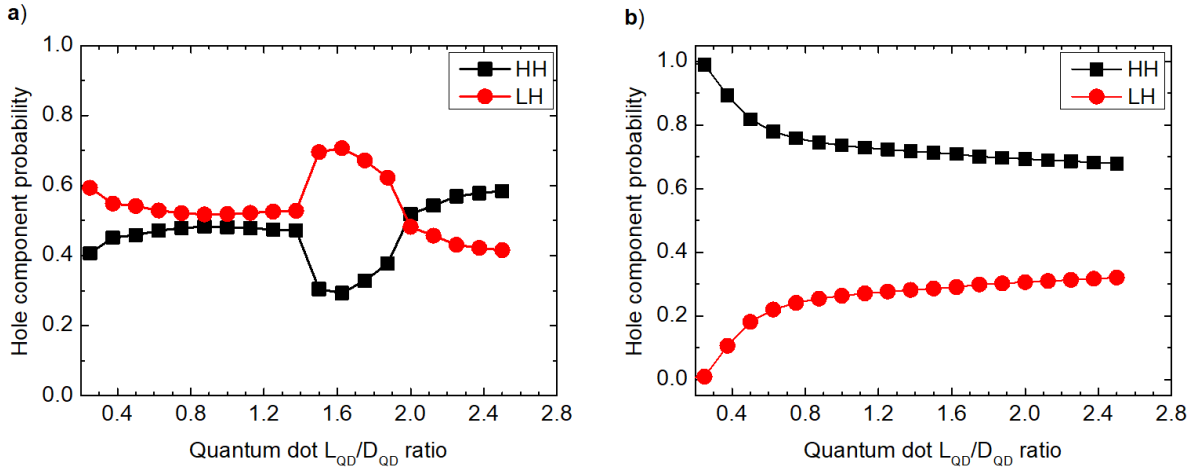
Figure 2.28 – Heavy hole - light hole switching as a function of L_{QD}/D_{QD} ratio for a CdTe - ZnTe nanowire quantum dot with a strong type II chemical valence band offset of 200 meV. Without a shell a), passivated by a ZnMgTe shell b).

For a flat quantum dot with $L_{QD}/D_{QD} = 0.5$, the integrated presence probabilities for heavy and light hole are respectively $P_{HH} = 45.3\%$ and $P_{LH} = 54.5\%$. From the presence probability projection colormaps of each envelope component as shown in Fig. 2.29, we see that all envelope components leak strongly outside the dot. Heavy hole leaks from the equator of the quantum dot, thus adopting a three-fold symmetry imposed by the strain and piezoelectric potential outside the dot. On the other hand, light hole leaks mostly from the pole of the quantum dot, with a small part leaking from the equator.

Heavy hole confinement is still stronger inside the dot, while that of light hole is almost vanishing. As a result, mixing between hole states is dark and that is confirmed from the graphs of oscillator strengths. This again is attributed to the fact that light hole envelope symmetry is different to the electron one, as a result the oscillator strength vanishes.

In Fig. 2.30 a) we present the oscillator strengths probabilities $|P_x|^2 + |P_y|^2$ and $|P_z|^2$ for a CdTe quantum dot in a ZnTe nanowire. For $L_{QD}/D_{QD} < 0.6$ there are only optically bright transitions associated to p_x and p_y matrix elements. In other words, the oscillator strength for
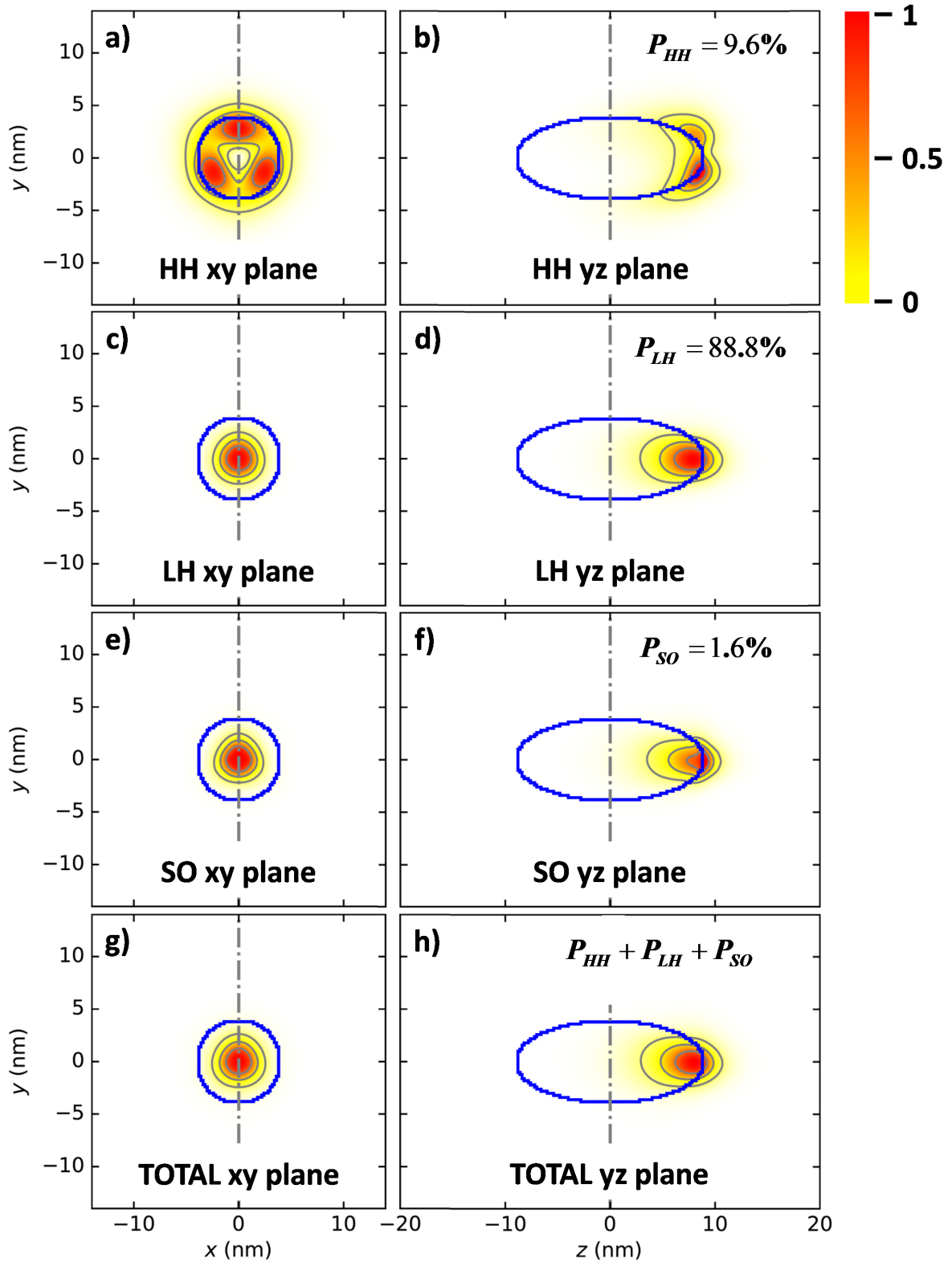
Figure 2.29 – **200 meV type II flat dot in a ZnTe nanowire:** The projections of presence probability components for a 200 meV strong type II flat CdTe quantum in a ZnTe core nanowire with $L_{QD}/D_{QD} = 0.5$. Heavy hole component on xy a) and yz b) plane. Light hole component on xy c) and yz d) plane. Split-off component on xy e) and yz f) plane. The sum of the three envelope components on xy g) and yz h) plane
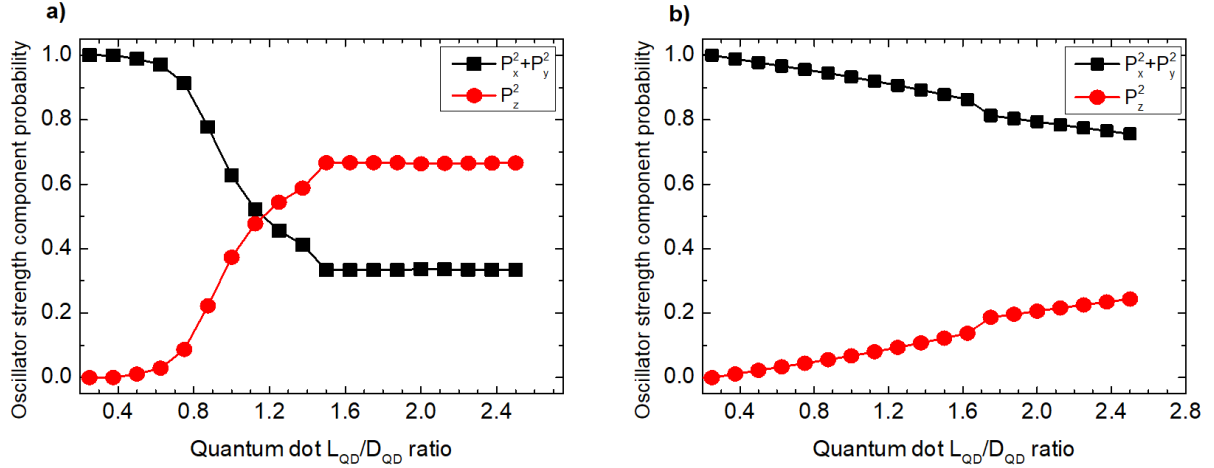
Figure 2.30 – The probability of oscillator strength components $|P_x|^2 + |P_y|^2$ in plane and $|P_z|^2$ along the nanowire axis, associated with transitions polarized on xy plane and along z respectively, as a function of the quantum dot aspect ratio, for a CdTe quantum dot in a ZnTe nanowire a) and for a CdTe quantum dot in a ZnTe-ZnMgTe core-shell nanowire b)

heavy holes is much stronger than that for light holes. For $0.75 < L_{QD}/D_{QD} < 1.4$ heavy hole starts to mix with light hole and at $L_{QD}/D_{QD} > 1.2$ the contribution of $|P_z|^2$ becomes larger than the contribution of $|P_x|^2 + |P_y|^2$. At $L_{QD}/D_{QD} > 1.5$ the probabilities $|P_x|^2 + |P_y|^2 = 1/3$ and $|P_z|^2 = 2/3$ are restored which is an indication of a light hole ground state.

From the envelope projection colormaps for $L_{QD}/D_{QD} \geq 1.5$ we observe that heavy hole leaks completely outside the dot, while a small part for light hole is still inside. This is depicted in Fig 2.31 c) for a quantum dot with $L_{QD}/L_{QD} = 2.25$. At the same time the absolute values of oscillator strengths become smaller due to weak overlap between electron and hole envelopes. For instance, oscillator strength values for the 200 meV type I elongated quantum dot with L_{QD}/D_{QD} are $|p_x|^2 + |p_y|^2 = 0.51$ a.u. and $|p_z|^2 = 1.02$ a.u. while for the strong type II they are $|p_x|^2 + |p_y|^2 = 0.21$ a.u. and $|p_z|^2 = 0.42$ a.u. This also confirms that light hole is restored as a ground state.

At the interface of CdTe - ZnTe, shear strain near the quantum dot equator is 1.7% compressive along xy plane as shown in Fig. 2.13 a). The strain affects the envelope which also leaks towards the equator and promotes a heavy hole as the predominant envelope component. This is the reason why heavy holes and light holes are strongly mixed also for large L_{QD}/D_{QD}. The contribution of heavy hole to the oscillator strengths however is vanishing, since the electron envelope which is still confined inside the dot overlaps with the small percentage of light hole which is also still inside mostly from the side of equator.

For the quantum dot in a core-shell nanowire, as shown in Fig. 2.28 b) and further confirmed from oscillator strength calculation in Fig. 2.27 b), any contribution from light holes vanishes and for all values of L_{QD}/D_{QD} both ground and excited states are predominantly of heavy hole type. From the oscillator strengths calculation we confirm that the order of magnitude of $|p_z|^2$ is 10^{-3} a.u. and it remains almost constant as a function of L_{QD}/D_{QD}. The sum $|p_x|^2 + |p_y|^2$ is decreasing from 0.1 a.u. at $L_{QD}/D_{QD} = 0.25$ to 0.01 a.u. at $L_{QD}/D_{QD} = 2.5$. This is the reason why in Fig. 2.30 we see that as we increase L_{QD}/D_{QD} aspect ratio, $|P_z|^2$ increases. This is expected, since already for small aspect ratios the envelope function leaks outside the quantum dot as shown in Fig. 2.32 and by increasing L_{QD}/D_{QD} aspect ratio, envelope leaking becomes stronger.

In Fig. 2.33 we present the envelope presence probability projection for an elongated quantum dot in a ZnTe-ZnMgTe core-shell nanowire. Similar to the heterostructure case without the ZnMgTe shell, for all envelope components s-like symmetry of the ground state breaks. Instead,
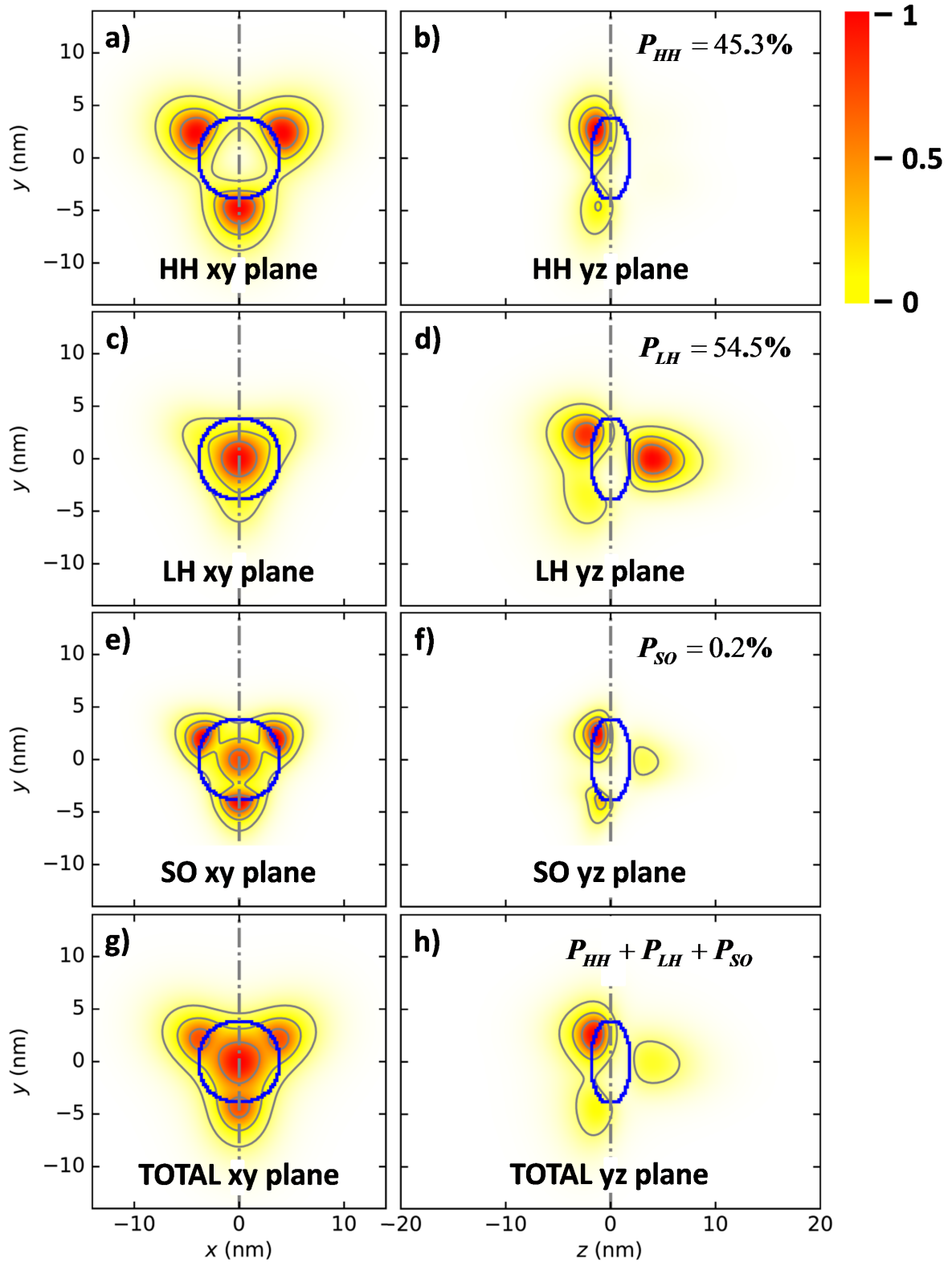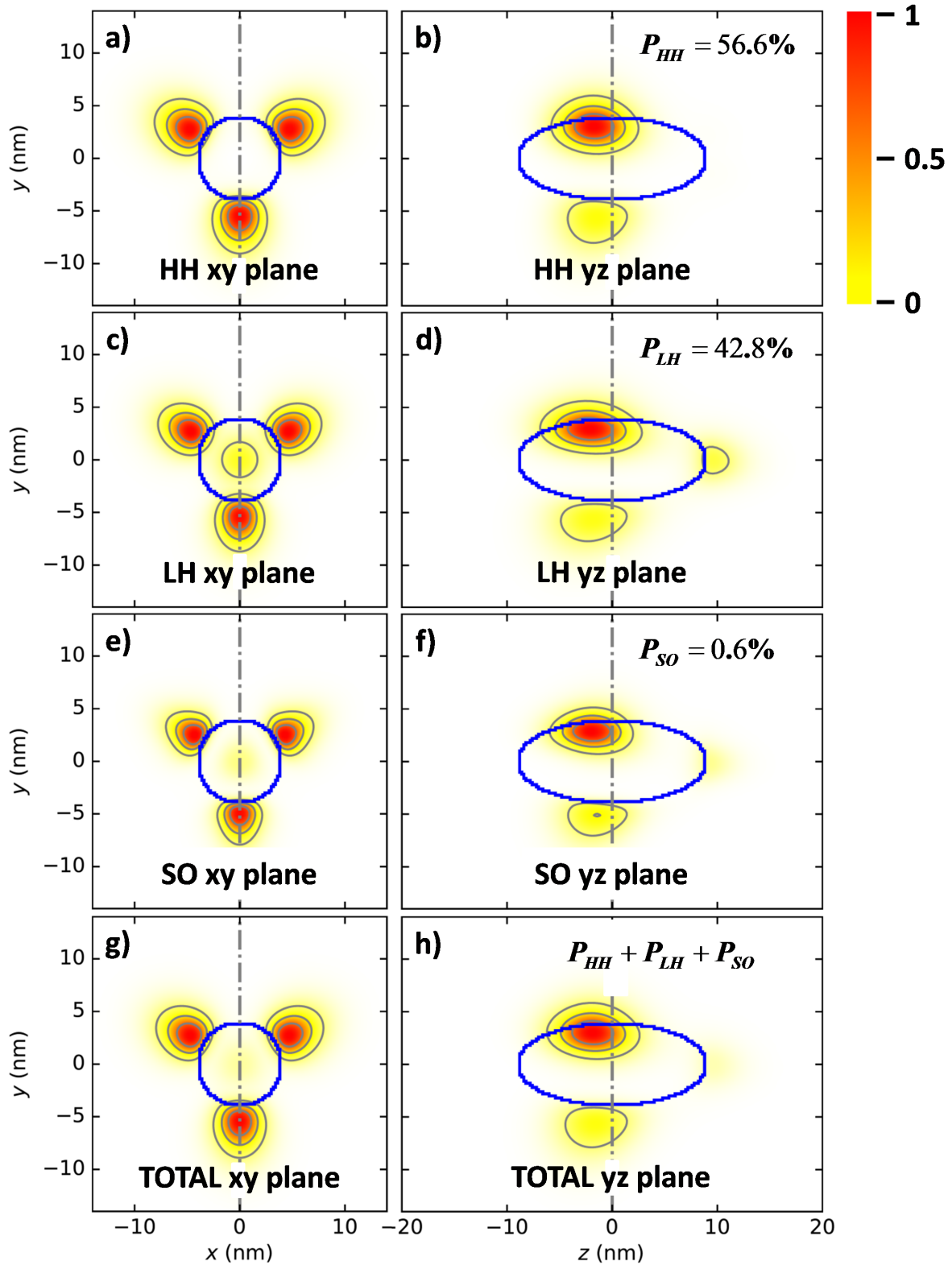
Figure 2.31 – **200 meV type II elongated dot in a ZnTe nanowire:** The projections of presence probability components for a 200 meV strong type II elongated CdTe quantum in a ZnTe core nanowire with $L_{QD}/D_{QD} = 2.25$. Heavy hole component on xy a) and yz b) plane. Light hole component on xy c) and yz d) plane. Split-off component on xy e) and yz f) plane. The sum of the three envelope components on xy g) and yz h) plane
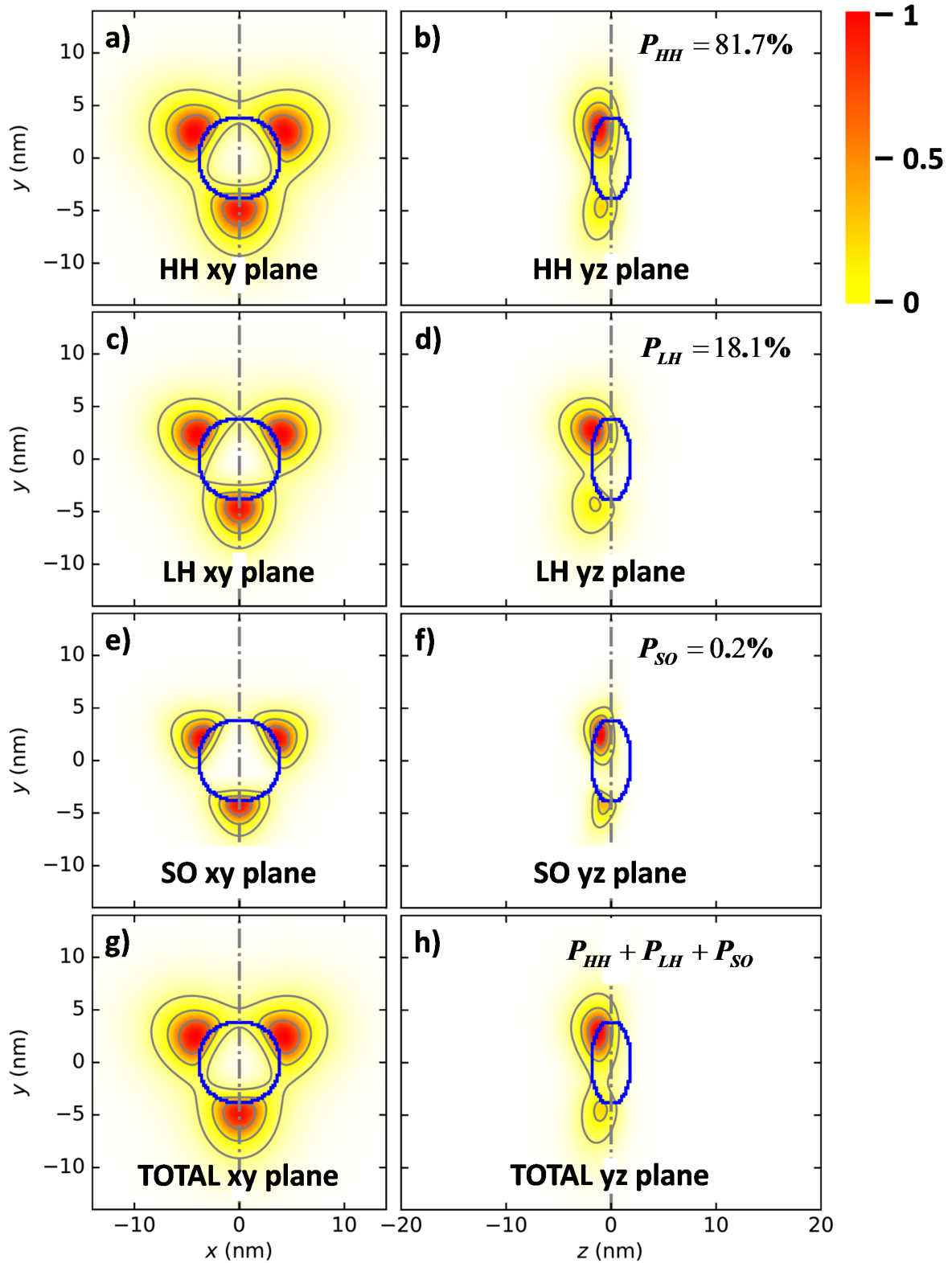
Figure 2.32 – **200 meV type II flat dot in a core-shell ZnTe-ZnMgTe nanowire:** The projections of presence probability components for a 200 meV strong type II flat CdTe quantum in a ZnTe-ZnMgTe core-shell nanowire with $L_{QD}/D_{QD} = 0.5$. Heavy hole component on xy a) and yz b) plane. Light hole component on xy c) and yz d) plane. Split-off component on xy e) and yz f) plane. The sum of the three envelope components on xy g) and yz h) plane

Figure 2.33 – **200 meV type II elongated dot in a core-shell ZnTe-ZnMgTe nanowire:** The projections of presence probability components for a strong type II elongated CdTe quantum in a ZnTe-ZnMgTe core-shell nanowire with $L_{QD}/D_{QD} = 0.5$. Heavy hole component on xy a) and yz b) plane. Light hole component on xy c) and yz d) plane. Split-off component on xy e) and yz f) plane. The sum of the three envelope components on xy g) and yz h) plane
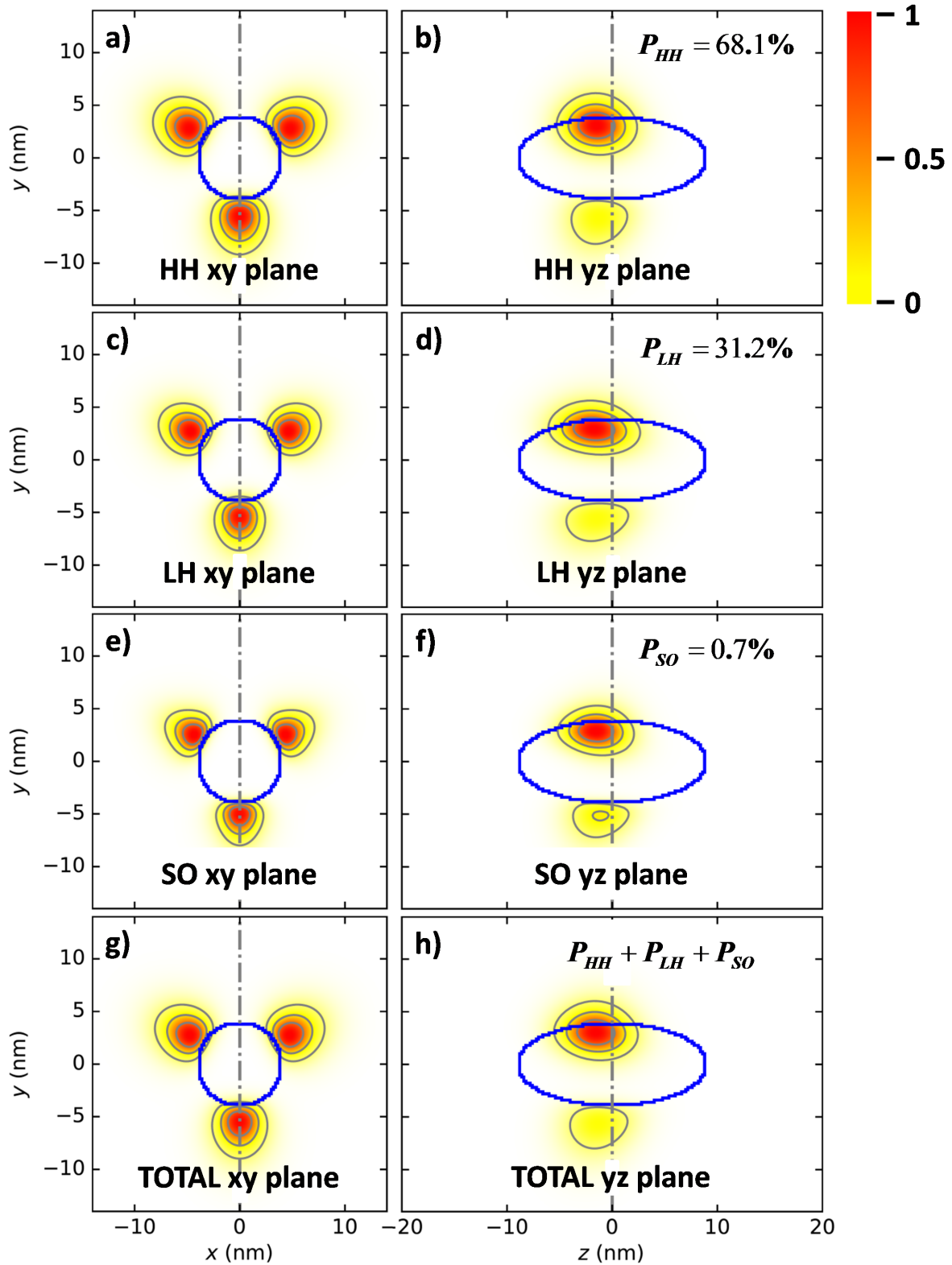
we retrieve a three-fold symmetry on xy plane outside the dot. This is because of the effect of Q term and due to the fact that outside the dot, axial shear strain also imposes a three fold symmetry to the piezoelectric potential as we see in Fig. 2.34). The difference here is that the envelopes for heavy hole, light hole and split-off have all the same three-fold symmetry on xy plane and they all leak around the equator of the quantum dot. For the structure without the shell, a small part of both light hole and split-off leaked also from the quantum dot pole.

Comparing the symmetry texture of both Fig. 2.34 and Fig. 2.33, we observe that the envelope function presence probability localizes near the points where the piezoelectric potential takes its minimum values. This is expected for a positively charged hole.
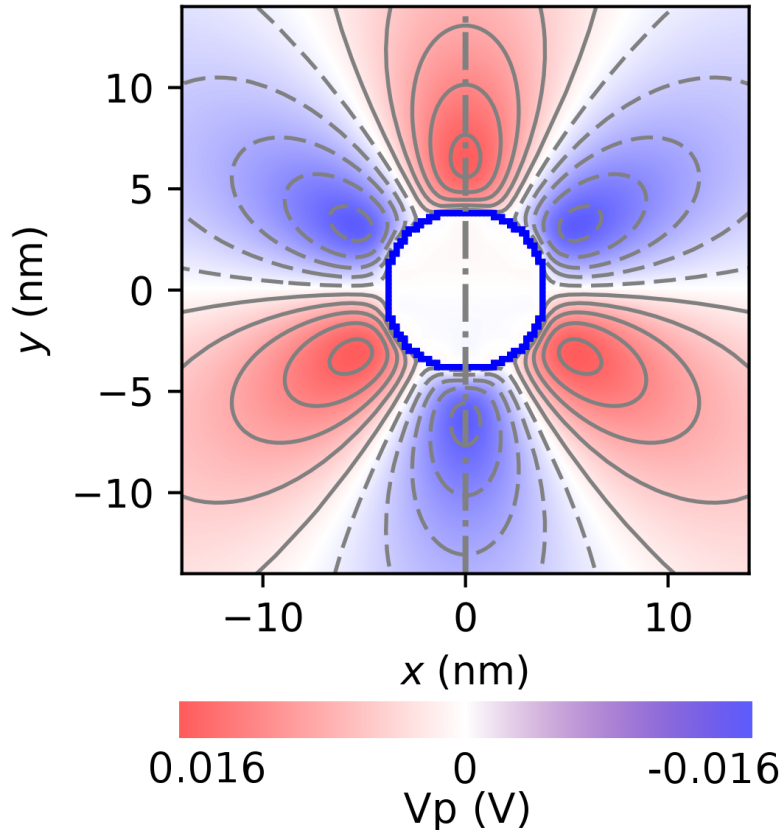
Figure 2.34 – The piezoelectric potential profile for an elongated quantum dot on xy plane. The distribution of presence probability for a weakly confined valence band state is defined by the local minima.

As L_{QD}/D_{QD} increases, the presence probability vanishes inside the dot. We can already see that in Fig. 2.33 where we plot the envelope functions for $L_{QD}/D_{QD} = 2.25$. The profile of envelope components on xy plane is similar to that of the nanowire quantum dot without the shell. What makes the difference and affects also the oscillator strength values is that without the shell there is still part of the envelope inside the dot. This is revealed by comparing Fig. 2.31 c), d) with Fig. 2.33 c), d). By including an outer ZnMgTe shell, all components leak outside and the presence probability of light hole inside the quantum dot is vanishing. This also explains why oscillator strengths are stronger on the xy plane and they vanish along z. Leaking envelope suffers the additional in plane compressive strain of 2.1% imposed by the shell and as result ground state gets dominated by the heavy hole component. Understanding the effect of valence band offset in combination with strain environment is very important as it explains why although the quantum dot is elongated, experimental measurements reveal still a ground state of heavy hole character or a mixture between heavy and light holes.

2.4.4 Reduced valence band offset: The weak type II case

In this final part we discuss the case of a nanowire quantum dot with a weak type II chemical valence band offset between CdTe and ZnTe barrier equal to 20meV. This case, like the weak type I, is less trivial that is why it was useful to discuss first the structure with the strong type II band offset.
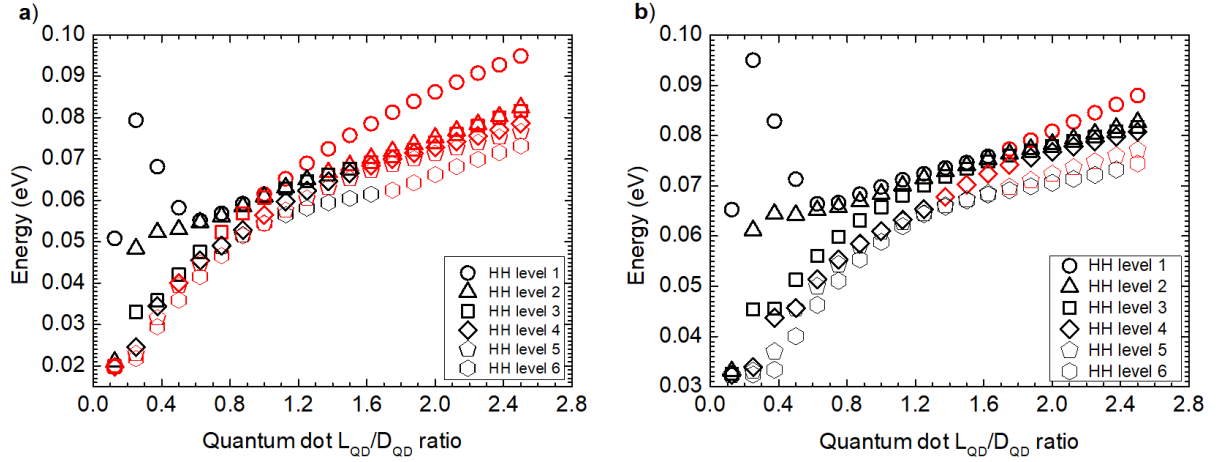

Figure 2.35 – Valence band energy levels of the first six Kramers doublets as a function of the quantum dot L_{QD}/D_{QD} ratio for a CdTe quantum dot in a ZnTe nanowire a) and for a CdTe dot in a core-shell ZnTe-ZnMgTe nanowire b). Black color corresponds to a predominantly heavy hole component and red color to a light hole.

In Fig. 2.35 a) we present the evolution of valence band energy levels for a CdTe quantum dot in a ZnTe nanowire as a function of the quantum dot aspect ratio. For $L_{QD}/D_{QD} < 0.6$, the first calculated energy level is well separated from the excited states and it is predominantly of heavy hole type. As we increase L_{QD}/D_{QD}, we start to reduce the energy difference among the levels and near $L_{QD}/D_{QD} = 1$ states which are predominantly heavy hole type, become degenerate with states dominated by the light hole component. This is an indication that near this region, heavy holes will be strongly mixed with light holes. For $L_{QD}/D_{QD} > 1.25$. The first energy level becomes again isolated, stabilizing a predominantly light hole component.

In Fig. 2.35 b) we plot the energy of the first six valence band Kramers doublet as a function of L_{QD}/D_{QD} for a CdTe quantum dot in a ZnTe-ZnMgTe core-shell nanowire. For $L_{QD}/D_{QD} \leq 0.5$, the first calculated level is well isolated from other states and it is predominantly of heavy hole type. Opposite to the structure without the ZnMgTe shell, here the first calculated level remains degenerate or quasi degenerate with excited states for large values of L_{QD}/D_{QD} which exhibit a strong heavy hole character. For $L_{QD}/D_{QD} > 2$, the first energy level gets separated from the excited states and the hole component becomes predominantly of light hole type.

In order to quantify the purity of valence band ground state and the switching from heavy to light hole, we have to plot the integrated presence probability as a function of L_{QD}/D_{QD} and to calculate of course the oscillator strengths. Similar to all different valence band offsets discussed so far, for certain L_{QD}/D_{QD} the first calculated level becomes degenerate with excited states. These have to be taken into account for the calculation of integrated presence probability and oscillator strengths of the ground state.

What we understand immediately from Fig. 2.36 is that the presence of the external shell affects heavily the mixing and switching from heavy to light hole. This has been already seen in the section discussing the weak type I quantum dot. The effect however here is stronger. In Fig. 2.36 a) we observe that for $L_{QD}/D_{QD} < 0.4$ the mixing between heavy and light hole is small, similarly to the strong and weak type I case. As we increase the quantum dot aspect ratio we begin to mix the hole states and for an $L_{QD}/D_{QD} = 1$, heavy and light hole are almost equally
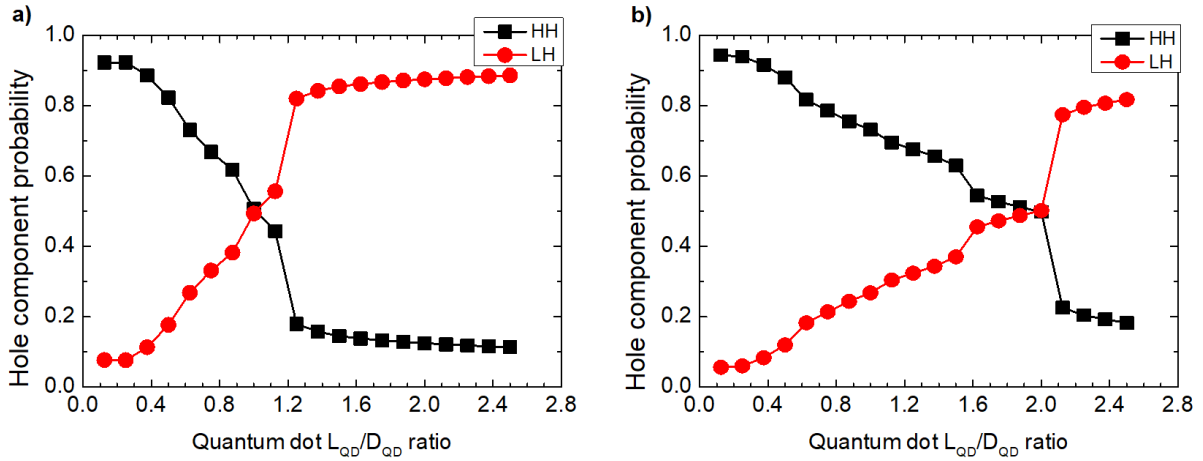
Figure 2.36 – Switching between heavy hole and light hole as a function of L_{QD}/D_{QD} ratio for a CdTe - ZnTe nanowire quantum dot with a weak type II chemical valence band offset of 20meV, without an external shell a) and passivated by a ZnMgTe shell b).

mixed with an integrated presence probability of 50%. For $L_{QD}/D_{QD} > 1.2$ we stabilize a light hole as a ground state mixed by around 10% with heavy hole. In that region the mixing between heavy and light hole is similar to that of the weak type I case.
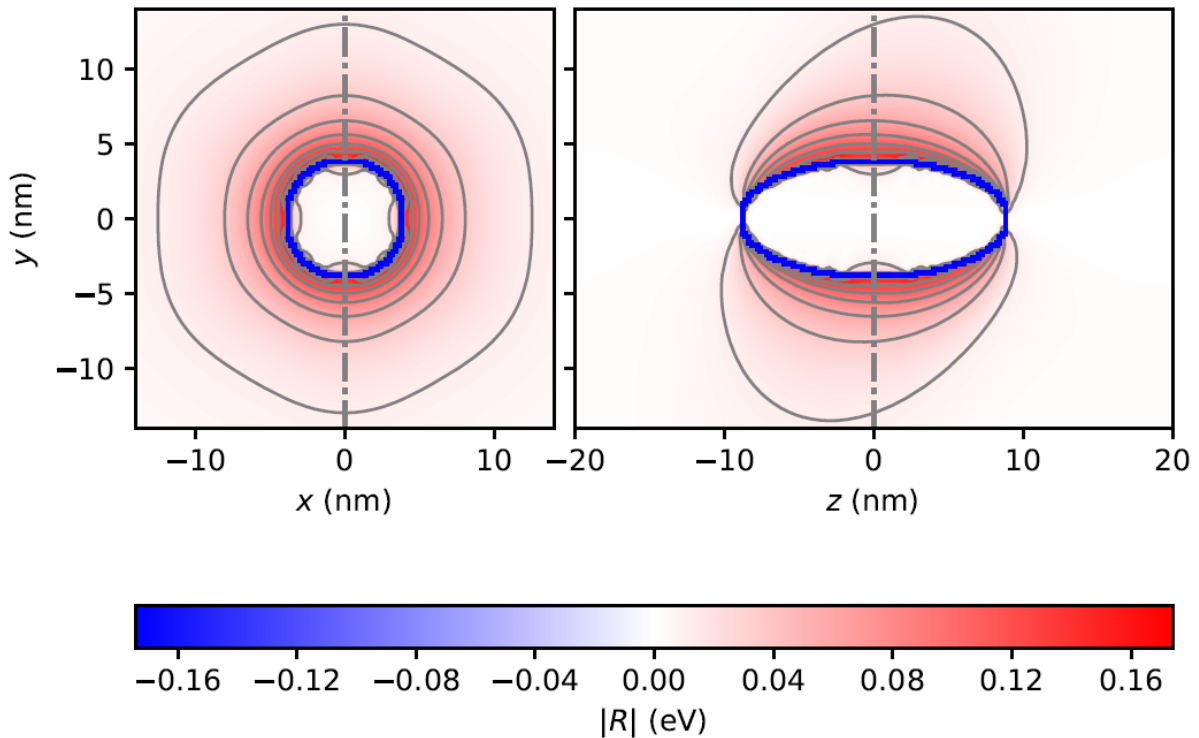
Figure 2.37 – Colormap of the $|R|$ component of Bir-Pikus Hamiltonian for an elongated CdTe quantum dot with $L_{QD} = 18nm$ and $D_{QD} = 8nm$ in a ZnTe nanowire. Left figure corresponds to the cross section on xy plane and the right one to the cross section on yz plane.

The fact that mixing between heavy and light holes becomes stronger, is attributed to the envelope leaking towards the CdTe-ZnTe interface and outside the quantum dot. By looking at the $|R|$ and $|S|$ components of the Hamiltonian, shown in Fig. 2.37 and Fig. 2.38 respectively, which govern the mixing between light and heavy holes, we observe that they are vanishing

inside the dot.
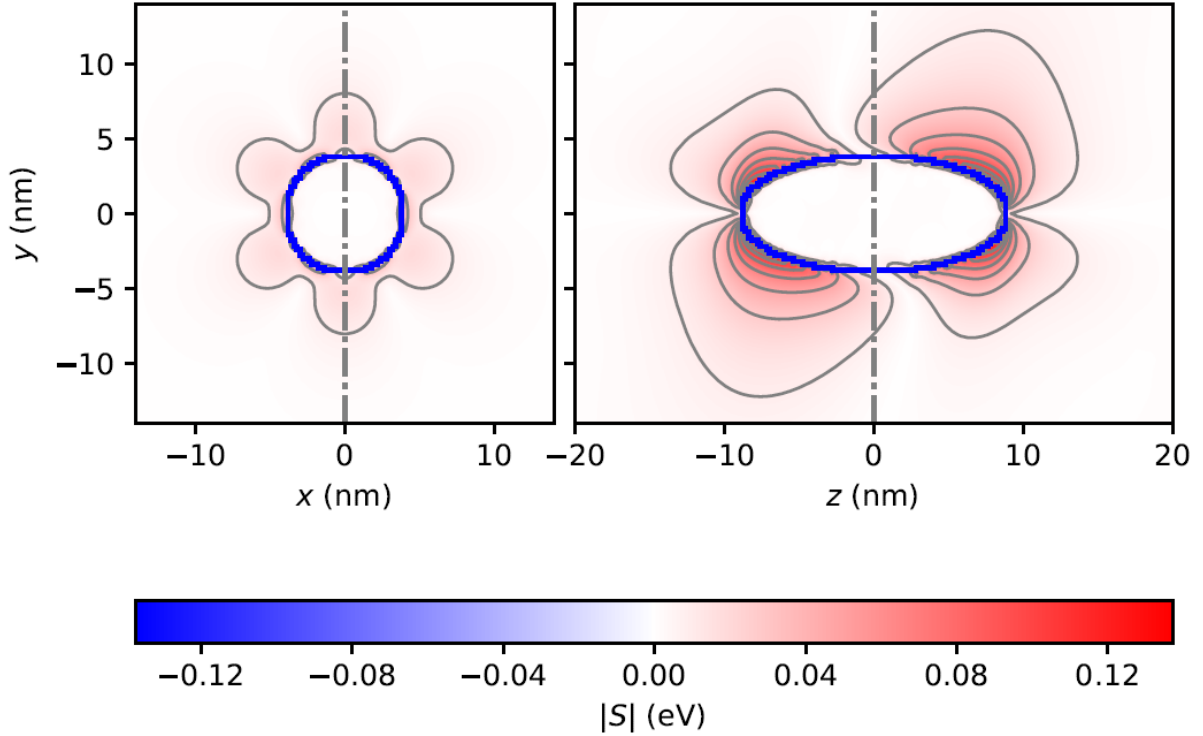
Figure 2.38 – Colormap of the $|S|$ component of Bir-Pikus Hamiltonian for an elongated CdTe quantum dot with $L_{QD} = 18nm$ and $D_{QD} = 8nm$ in a ZnTe nanowire. Left figure corresponds to the cross section on xy plane and the right one to the cross section on yz plane.

On the contrary, values of R_e and S_e are non-zero outside the dot, consequently as the envelope leaks towards ZnTe barrier and particularly from the quantum dot equator, mixing between heavy and light holes becomes stronger. The presence of an external ZnMgTe shell does not modify R_e and S_e terms but its addition around the ZnTe core, strongly affects the switching and mixing of valence band ground state through the Q_e term.

In Fig. 2.36 b) we present the integrated presence probability for heavy and light holes as a function of L_{QD}/D_{QD} for a CdTe quantum dot in a ZnTe-ZnMgTe core-shell nanowire. In this case, light hole becomes the dominant ground state component at $L_{QD}/D_{QD} > 2$, being mixed however by 20% with heavy hole. For $1.5 < L_{QD}/D_{QD} < 2$ the two hole states are strongly mixed with almost 50% contribution each.

In Fig. 2.39 we plot the presence probability projections of the different hole states for a flat CdTe quantum dot in a ZnTe nanowire. In this configuration, the dominant heavy hole envelope component is still confined inside the quantum dot but leaking towards ZnTe barrier is stronger. Presence probability of both light hole and split-off is vanishing inside the dot, as both components are localized near the CdTe-ZnTe interface and outside. Due to leaking all envelope component start to adopt a three-fold symmetry. As we increase L_{QD}/D_{QD} ratio, envelope leaking also increases. We can see that in Fig. 2.40, where we present the presence probabilities projections of the hole states for an elongated CdTe quantum dot.

For both heterostructures, with and without the external ZnMgTe shell, the shape and localization of the envelope projections are similar. The envelope presence probability distribution is not very different in comparison to the weak type I case. We observe that the dominant light hole component of the envelope is pushed towards the pole of the quantum dot, where large part of it leaks outside due to a combined effect of weak confinement and piezoelectric potential. However, regardless of the fact that we impose a chemical band offset type II, for both flat and

Figure 2.39 – **20 meV type II flat dot in a ZnTe nanowire:** The projections of presence probability components for a 20 meV weak type II flat CdTe quantum dot in a ZnTe nanowire with $L_{QD}/D_{QD} = 0.5$. Heavy hole component on xy a) and yz b) plane. Light hole component on xy c) and yz d) plane. Split-off component on xy e) and yz f) plane. The sum of the three envelope components on xy g) and yz h) plane

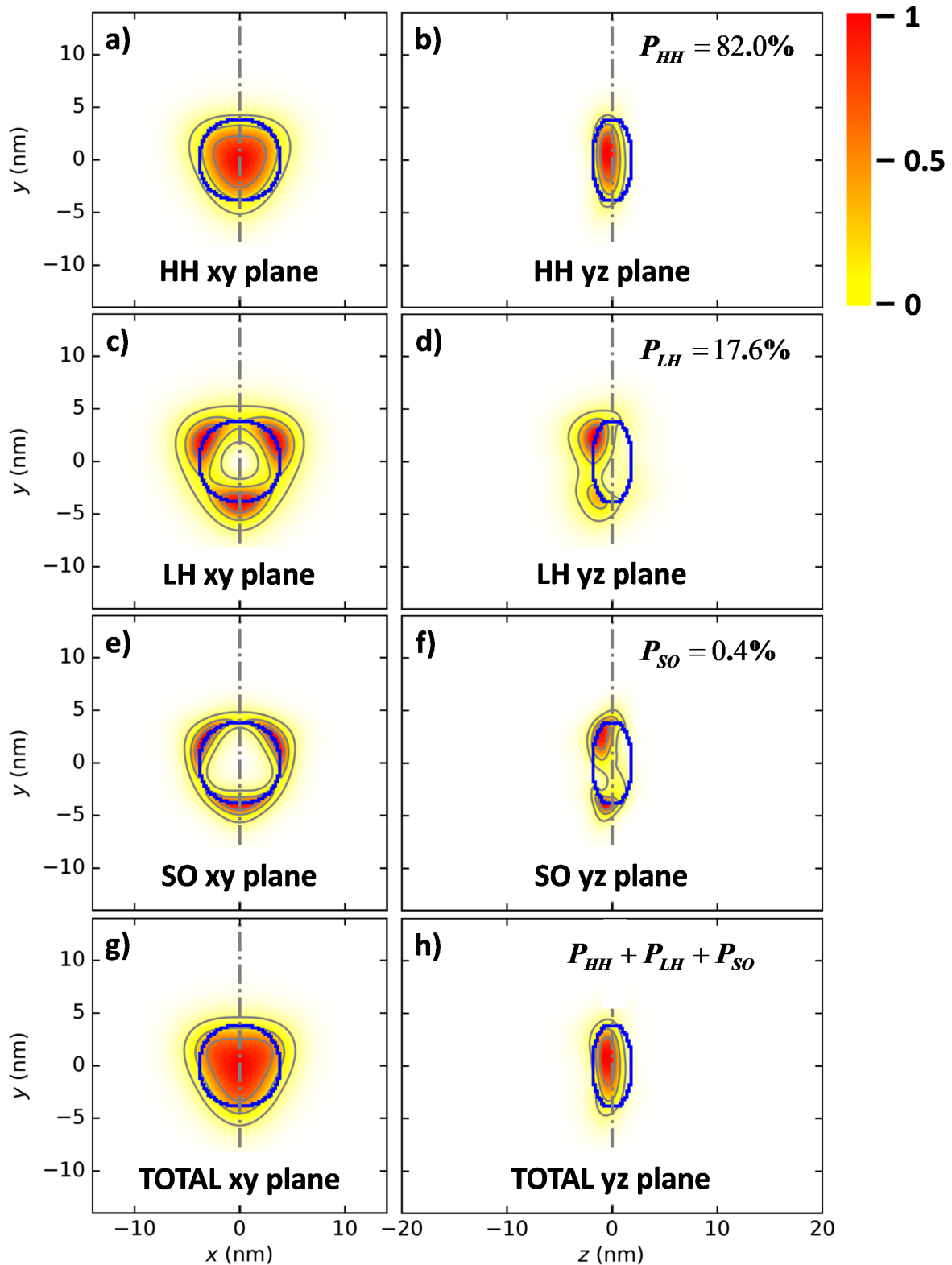Figure 2.40 – **200 meV type II elongated dot in a ZnTe nanowire:** The projections of presence probability components for a 20 meV weak type II elongated CdTe quantum dot in a ZnTe nanowire with $L_D/D_D = 2.25$. Heavy hole component on xy a) and yz b) plane. Light hole component on xy c) and yz d) plane. Split-off component on xy e) and yz f) plane. The sum of the three envelope components on xy g) and yz h) plane
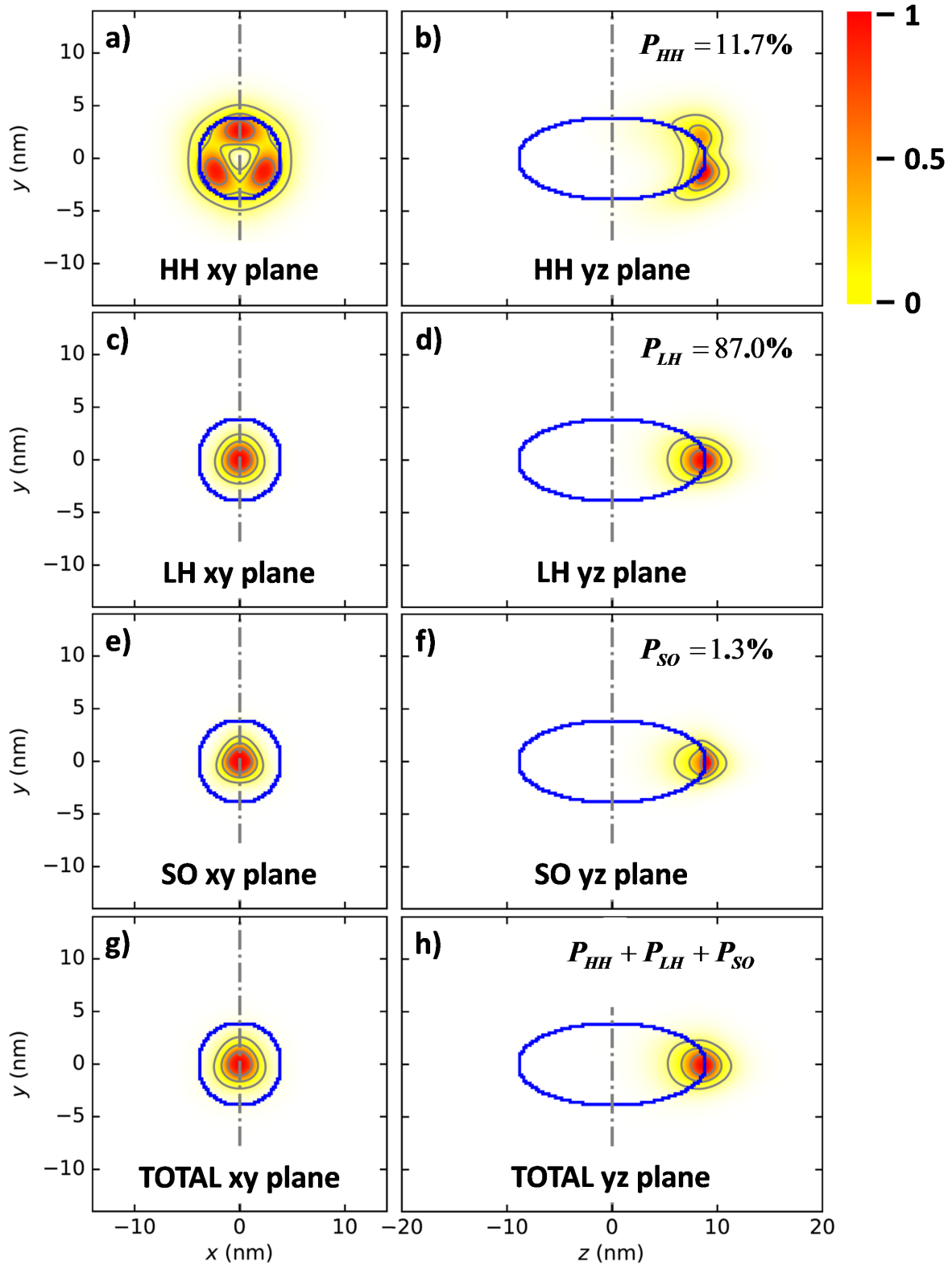
elongated quantum dots confinement is partially restored. As a result, the envelope ground state gets localized inside the dot with a leak towards the barriers.

This explains also why for the core shell nanowire, heavy hole - light hole switching threshold, shifts to larger values of L_{QD}/D_{QD}. The mismatch between ZnMgTe and ZnTe which is 0.8%, induces shear strain to the nanowire core which near the ZnTe-CdTe interface is 0.6 % compressive in plane. This extra strain is also responsible for weakening the confinement inside the dot as it further increases the ZnTe valence band edge. As the envelope function leaks outside the dot the potential generated by the compressive strain in the core, promotes heavy hole as the predominant component of the ground state. Moreover, as shown in Fig. 2.35 b), the first calculated level becomes quasi-degenerate with excited states which are predominantly of heavy hole type. As an example at $L_{QD}/D_{QD} = 1.75$, the first calculated level is 57% light hole, but it is also quasi-degenerate with the first two excited states which are respectively 62% and 61% of heavy hole type. Consequently if we average over these three degenerate states the ground state for this L_{QD}/D_{QD} is mostly heavy hole with $P_{HH} = 55.3\%$.

Due to enhancement of electron hole separation, oscillator strengths become weaker in comparison to type I case. In Fig. 2.41 we present the oscillator strength probability for a nanowire with and without a shell.
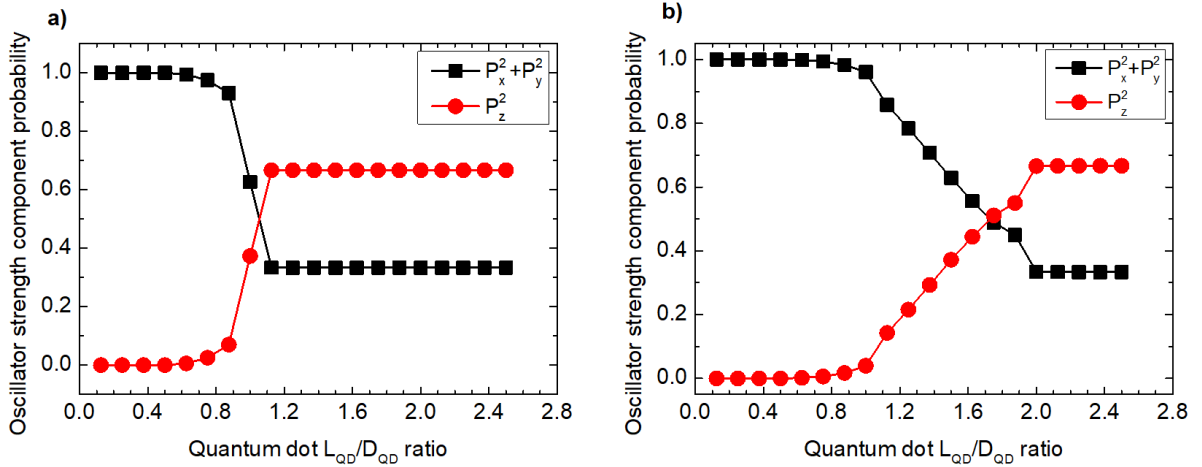
Figure 2.41 – The probability of in plane oscillator strength components $P_x^2 + P_y^2$ and along the nanowire axis P_z^2, associated with transitions polarized on xy plane and along z respectively, as a function of the quantum dot aspect ratio, for a CdTe quantum dot in a ZnTe nanowire a) and for a CdTe quantum dot in a ZnTe-ZnMgTe core-shell nanowire b)

More specifically, in absolute values they decrease by one order of magnitude. Nevertheless by calculating the probability of each component as discussed in the beginning of this chapter we confirm the switching from heavy to light hole at $L/D > 2$. In more details, for $L/D < 1$ only the in plane p_x and p_y momentum matrix elements contribute to optically bright transitions. This is an indication that mixing of heavy with light holes for small L_{QD}/D_{QD} as depicted in Fig.2.36 could be dark. In general we expect that as we reduce confinement, dark mixing between different hole states will become stronger. For values $1 < L_{QD}/D_{QD} < 2$, $|p_x|^2$ and $|p_y|^2$ start to decrease abruptly while there is a small increase of $|p_z|^2$. This is the range of aspect ratio where heavy and light holes are mixed and they contribute equivalently to optical transitions. When $L_{QD}/D_{QD} > 2$ we restore a pure light hole state where $|P_z|^2 = 2/3$ and $|P_x|^2 + |P_y|^2 = 1/3$.

Although confinement of the hole ground state is weak, this does not affect the symmetry of the ground state envelope as it still maintains its s-like shape. So far we explained the properties of valence band ground state for a flat and an elongated quantum dot.

After the study of a flat and an elongated quantum dot, we are interested to investigate an

intermediate case, where we know that mixing between heavy and light hole is stronger. In Fig. 2.42 we plot the colormaps for the envelope components presence probability projections for a dot of length $L_{QD} = 14$ nm and $L_{QD}/D_{QD} = 1.75$.

Figure 2.42 – The projections of presence probability components for a 20 meV weak type II elongated CdTe quantum dot in a ZnTe-ZnMgTe core-shell nanowire w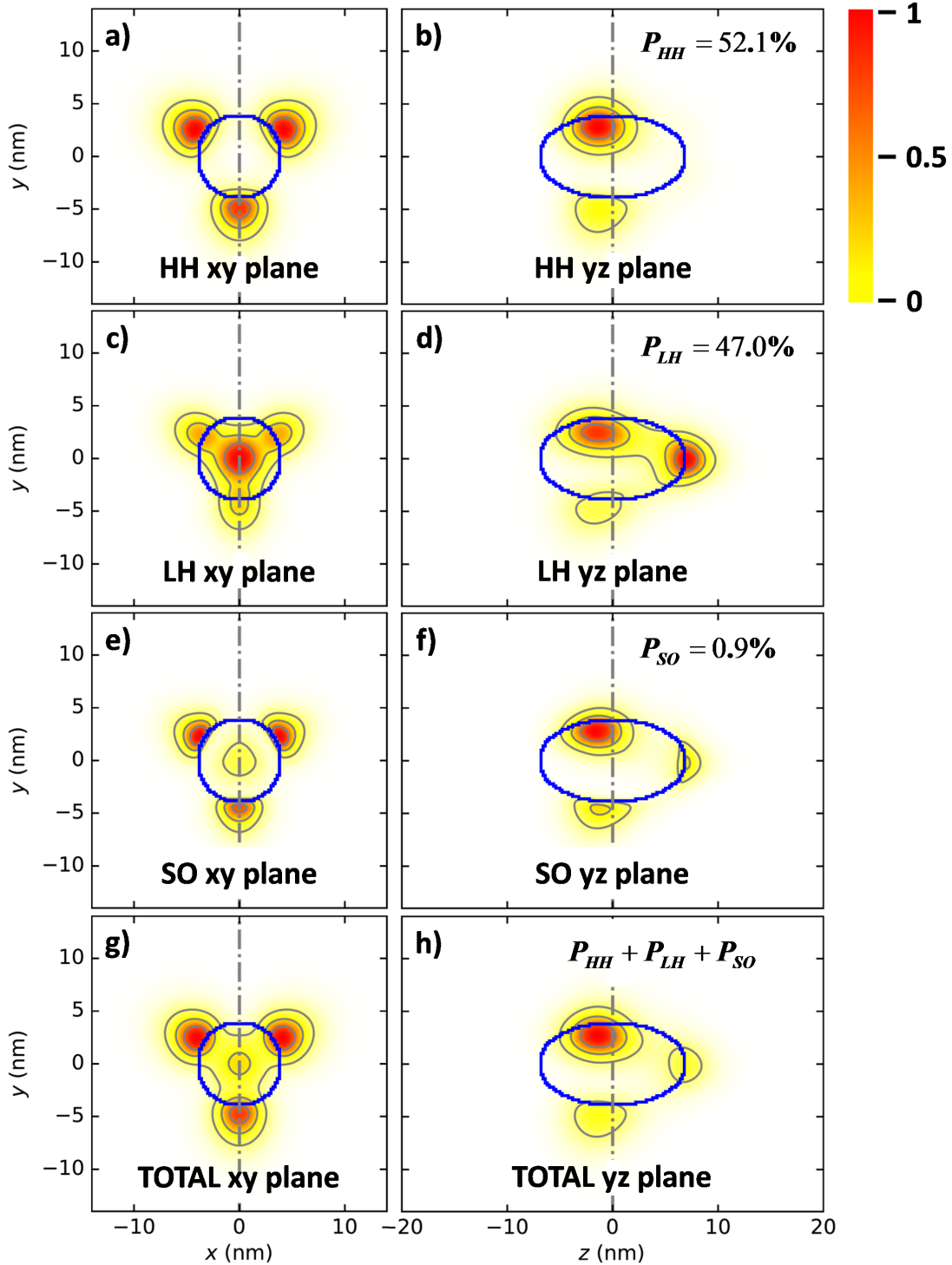ith $L_{QD}/D_{QD} = 1.75$. Heavy hole component on xy a) and yz b) plane. Light hole component on xy c) and yz d) plane. Split-off component on xy e) and yz f) plane. The sum of the three envelope components on xy g) and yz h) plane

The heavy hole component, which has the strongest contribution leaks outside the dot as for the strong type II case. Light hole is more interesting, as part of presence probability is still confined inside the dot, while the part which leaks outside exhibits the expected three fold symmetry. The part which is inside the dot is localized close to the pole, while the leaking part towards the equator. This explains the almost equivalent mixing in the amplitudes of transition probabilities, as heavy hole is the dominant component which strongly leaks outside the dot and only a small part is still inside while there is an important contribution of p_z transitions attributed to the light hole lobe which is still confined in the dot.

2.5 Conclusions

In this chapter we developed the techniques and discussed the results of numerical calculations on nanowire quantum dots based on the II-Te family of materials.
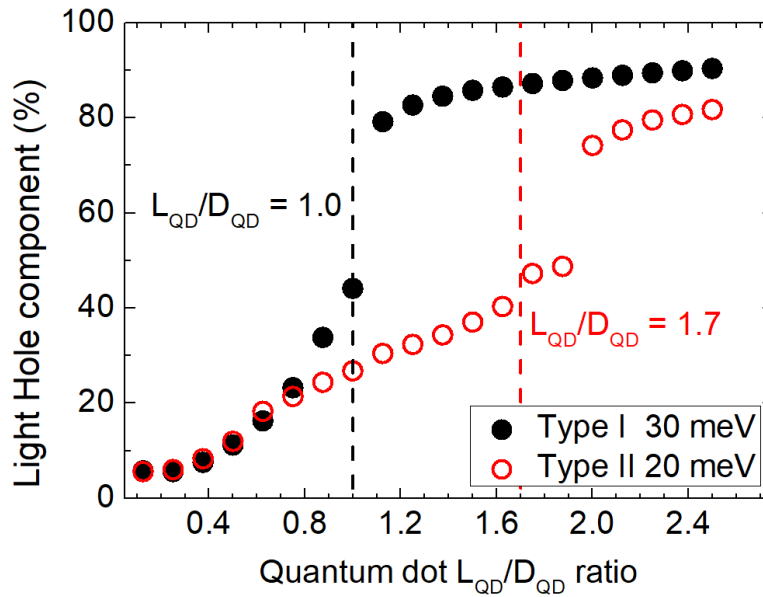
Figure 2.43 – Weight of the light-hole component for an ellipsoidal CdTe quantum in a ZnTe core passivated with a ZnMgTe shell as a function of L_{QD}/D_{QD} ratio. Black circles correspond to the confined valence band ground state, calculated for a weak type I band alignment with an offset of 30meV. Open red circles correspond to the calculations for a weak type II alignment with an offset of 20meV. For small values of the aspect ratio ground state is still confined, while for large values we obtain a multiplet leaking at the QD-core interface [59].

In the first part we presented briefly continuum elasticity, piezoelectric effects and the $\vec{k} \cdot \vec{p}$ theory upon which the numerical model is based.Then we presented the results for a range of quantum dot aspect ratios in $0.125 \leq L_{QD}/D_{QD} \leq 2.5$ switching from a confined state in a type I quantum dot to a leaking one in a type II. We investigated both the effect of strain and piezoelectric potential on the electronic and optical properties of the quantum dot. From these simulations we understood that by reducing confinement the ground state starts to leak outside the dot and becomes degenerate with excited states. As a consequence in the vicinity of $L_{QD}/D_{QD} \approx 1$ light holes start to mix with heavy holes but still for elongated quantum dots, ground state is predominantly of light hole type. This is not the case for a ZnTe-ZnMgTe core-shell nanowire, as the external shell induces a compressive strain in ZnTe which destabilizes the light hole. As a result, the switching from heavy to light hole takes place for values of $L_{QD}/D_{QD} > 1$. This was demonstrated in sections 2.4.3 and 2.4.4 by studying both the integrated presence probability o hole states and the oscillator strengths.

By analyzing the calculation results for a weakly confined type II dot, we confirmed that even for an elongated quantum dot where $L_{QD}/D_{QD} > 1.5$, the valence band ground state is predominantly heavy hole. This is shown in Fig. 2.43.

As a future perspective and for understanding better the parameters which determine the hole ground state in a real nanowire quantum dot, we have to carry out simulations for different dot geometries with a cylindrical or even an arbitrary shape. We also have to take into account second order piezoelectric effects due to hydrostatic strain.

Chapter 3

Numerical calculations of anisotropic quantum dots under exchange field

3.1 Motivation

The purpose of this chapter, is to study the spin properties of a quantum dot based on diluted magnetic semiconductors and how these are influenced by strain effects and confinement. As we saw in the previous chapter, strain properties are governed by the shape and size of the quantum dot, while confinement is affected by the valence band offset between the dot and the nanowire core. Another objective, is to interpret the experimental results obtained from magneto-optical measurements where there is a strong evidence that confinement is weak and the quantum dot ground state is not pure light hole, as reported in [27]. The role of confinement on spin properties is of major interest, that is why we studied both weak type I and type II band alignment. The drawback of numerical calculations is that they are computationally expensive, thus for carrying out a full study on a specific structure it requires a lot of time. As a consequence, another interesting aspect is to verify the validity and accuracy of models which can be developed analytically (eg. a quadruplet model) for interpreting both experimental results and those obtained from numerical calculations.

3.2 Calculation of giant Zeeman shift by an exchange field

In this section we discuss in detail the problem solved numerically through the TB_Sim package of codes, where for simulating the giant Zeeman effect we apply an exchange field inside the quantum dot which acts only on the spin. The structure which we simulate is a $Cd_{1-x}Mn_xTe$ quantum dot, in a ZnTe nanowire passivated with a ZnMgTe shell. As mentioned in the previous chapter, for conduction band calculations we solve a single band equation, therefore we do not take into account the electron spin. Consequently, as a first approach we can ignore any spin-orbit effects in conduction band and assume the the Zeeman shift for these states is similar to that of an electron with isotropic spin in space. Moreover, in this study we are not that interested in conduction band since we mostly want to investigate the Zeeman shift of valence band hole states and how this is influenced by the quantum dot L_{QD}/D_{QD} aspect ratio and valence band offset. In order to calculate numerically the Zeeman shift of the valence band states, we introduce a magnetic Hamiltonian to the 6 band $\vec{k} \cdot \vec{p}$ calculation which is given by

$$\mathcal{H} = \mu_B \vec{B} \cdot \vec{L} + g_e \mu_B \vec{B} \cdot \vec{S} \qquad (3.1)$$

where $g_e = 2.0023$ the electron Landé factor, $\mu_B = 5.788 \cdot 10^{-2}$ meV/T Bohr's magneton and $\vec{S}$ and $\vec{L}$ the spin and orbital angular momentum respectively. The main objective of this chapter

is to study the spin properties of the valence band ground state and their effect on the Zeeman shift. For this reason we will not consider the actual (spin and orbital) Zeeman effect (influenced also by orbital effects like the diamagnetic shift of an exciton, the modification of g factor or the Landau levels), but an exchange effect which is described only by a spin operator. Therefore in order to cancel the orbital terms, ignore the Hamiltonian term $\vec{B} \cdot \vec{L}$.

Since the concentration of Mn ions in an actual DMS alloy is around 10% we may consider that its effect on the elastic and electronic properties of the quantum dot is negligible [60]. It is therefore easier to ignore the presence of Mn and solve the problem directly for a CdTe quantum dot by introducing an exchange field which acts only on the hole spin. This in fact, is a field which produces the same energy splitting, as the giant Zeeman effect induced by the exchange interaction between the holes and Mn spins. The calculation of the Mn induced exchange field acting on the holes $B_{exc,h}^{Mn}$ is described in Chapter 1, section 1.4. Since in this chapter we discuss only the Zeeman shift of valence band states, we define for simplicity $B_{Mn} \equiv B_{exc,h}^{Mn}$. In order to calculate the exchange field in accordance to the conditions of the experimental measurements, we had to take into account the temperature of Mn ions in the cryostat environment, which in our case it is expected to be $T_{Mn} = 8$ K. The exchange field we used for the simulations of this chapter is calculated from the relation

$$B_{Mn} = \frac{B_{\frac{5}{2}}\left(\frac{5}{2}\frac{g_{Mn}\mu_B B}{k_B T_{Mn}}\right)\Delta E_{hh,z}^{sat}}{g_e \mu_B} \tag{3.2}$$

In the table below we present indicatively the actual values of magnetic field used in experiment and those of the exchange field used in numerical calculations, as well as the expected Zeeman splitting for each one of them. The exchange field is two orders of magnitude larger than the actual magnetic field and that is the reason why we can neglect any orbital effects in Eq. 3.1.

Table 3.1 – Selected values for magnetic field applied experimentally and the corresponding exchange field used in numerical calculations. The Zeeman splitting for a pure heavy hole ground state is shown to the right column.

Experimental magnetic field B(T)	Exchange field B_{Mn}(T)	Heavy hole giant Zeeman splitting ΔE_{hh} (meV)
0.2	29.8	3.5
0.5	74.2	8.6
1.0	146.5	17
3.0	389.2	45.2
6.0	588.8	68.4
11.0	701.5	81.5
⋮	⋮	⋮
∞	759.4	88

The value of exchange field at saturation is $B_{Mn} = \frac{\Delta E_{hh,z}^{sat}}{g_e \mu_B} = 759.4$ T. In the previous chapter we investigated eight different cases: A CdTe quantum dot in a ZnTe nanowire with and without an external ZnMgTe shell for a 200 meV strong type I, a 20 meV weak type I, a 200 meV strong type II and a 20 meV weak type II valence band offset between the quantum dot and the nanowire core. The structures on which we performed the numerical calculations under the exchange field, are identical to those described in Chapter 2. More specifically we wanted to investigate the Zeeman shift for both weakly and strongly confined holes, in flat and elongated CdTe quantum dots in ZnTe-ZnMgTe core-shell nanowires. In total we carried out simulations

for 20 values of the exchange field from 0 T to 701.5 T parallel and perpendicular to the quantum dot quantization axis, as depicted in Fig. 3.1
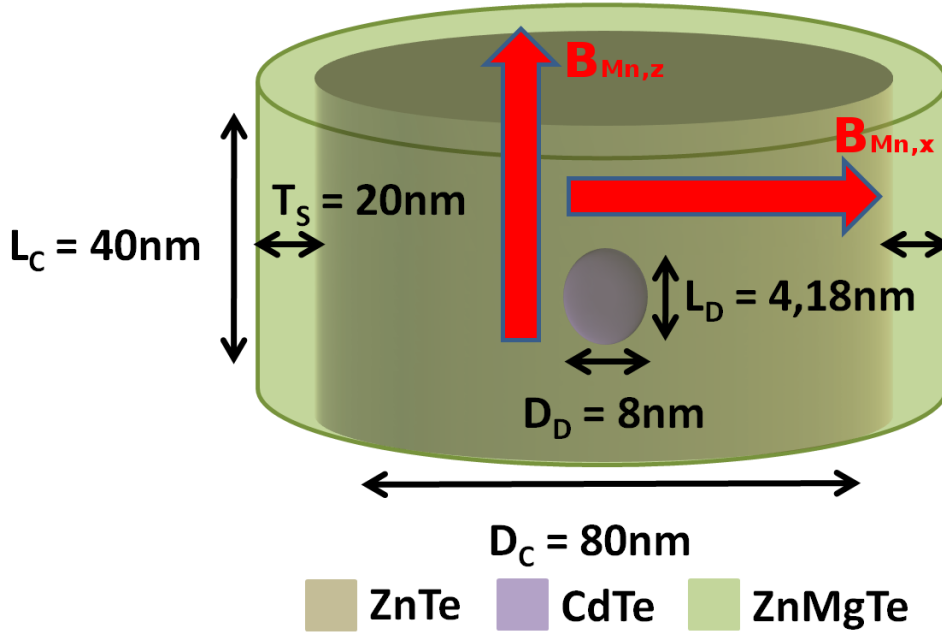

Figure 3.1 – Schematic representation of a CdTe quantum dot in a ZnTe-ZnMgTe core-shell nanowire. B_x is the exchange field oriented perpendicular to the quantization axis and B_z the one parallel.

The exchange field is only non vanishing and uniform inside the quantum dot. Everywhere outside the dot, $B_{Mn} = 0$.

3.3 Strongly confined type I dot

3.3.1 Flat dot

The most simple system with which we will begin the discussion, is a heavy hole ground state in a flat quantum dot. More specifically the structure on which we performed the numerical calculations was constituted of a CdTe quantum dot of length $L_{QD} = 4$ nm and diameter $D_{QD} = 8$ nm incorporated in a ZnTe-ZnMgTe core-shell nanowire. The chemical valence band offset between CdTe and ZnTe was a 200 meV type I. The structure is identical to the one studied in Chapter 2. As a reminder to the reader, the ground state wavefunction at 0 T is a Kramers doublet given by Eq. 2.66 and the contribution of each total angular momentum component by Eq. 2.70. For our study it is also very important to calculate the percentage of each envelope component which is confined inside the quantum dot. As we will see later, even a small leaking of the envelope affects the spin properties of the ground state, because there $B_{Mn} = 0$ outside the dot. In the table below we present the presence probability and its corresponding percentage inside the quantum dot of each total angular momentum component denoted as HH_{id}, LH_{id} and SO_{id}.

As regards the total envelope presence probability, 92.2 % of it, is confined inside the dot.

In the graph of Fig. 3.2 we present the Zeeman shift of the two components of the Kramers doublet as a function of the exchange field. More specifically in Fig. 3.2 a) the field is applied perpendicular and in in Fig. 3.2 b) parallel to the quantization axis of the dot. For convenience we identify the component which shifts towards lower energies as pseudo spin-up and the one which shifts towards lower energies as pseudo spin-down. As discussed in the previous section,

Table 3.2 – The presence probability of heavy hole, light hole and split-off, with their respective percentages inside the quantum dot, for a 200 meV strong type I flat CdTe quantum dot in a ZnTe-ZnMgTe core-shell nanowire.

P_{HH}	HH_{id}	P_{LH}	LH_{id}	P_{SO}	SO_{id}
0.956	94.6%	0.040	35%	0.004	27.8%

when the magnetic field is parallel to the x axis and for a pure and isolated heavy hole ground state, we would expect a vanishing Zeeman shift. This is not the case though, as there is a small contribution from light hole and from 0 T to 701.5 T both components of the first Kramers doublet shift towards lower energies. The fact the pseudo spin-down component moves also towards lower energies is attributed to the anticrossing with excited states. It is interesting to point out that Zeeman shift for both cases can be fitted very accurately using a third order polynomial. The only difference between the pseudo spin-up and spin-down components of the Kramers doublet is the sign of the cubic term which is respectively positive and negative. Another factor which may as well affect the ground state energy is the Zeeman shift of excited states. However we expect that this effect is weak due to the fact that the ground state is separated by 60 meV from the first excited state which is predominantly light hole. The figures with the Zeeman shift plot of all calculated energy levels, for a strong type I flat and elongated dot and for both directions of magnetic field, are shown in Appendix B.
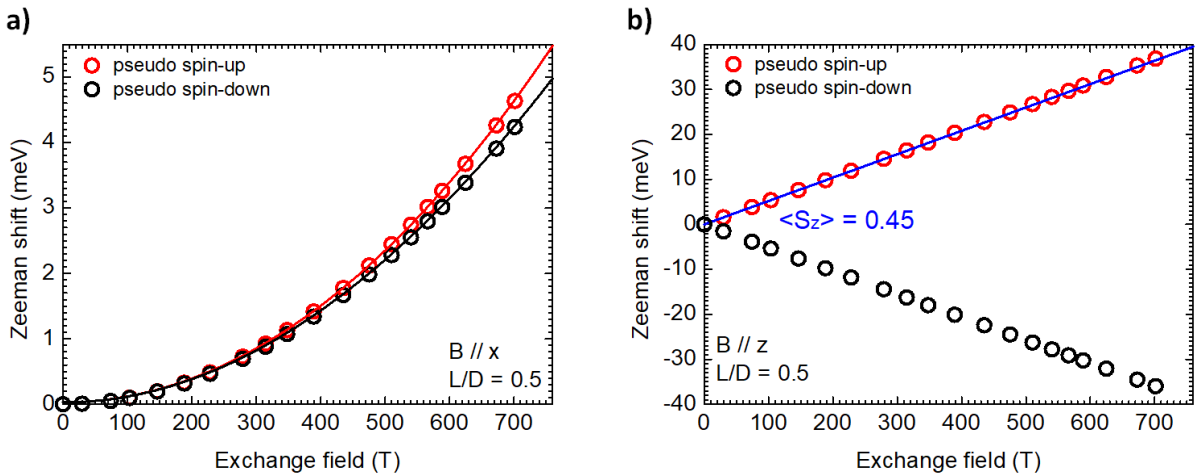
Figure 3.2 – Zeeman shift of the pseudo spin-up and pseudo spin-down component of the first Kramers doublet as a function of the exchange field used at calculations for a 200 meV type I flat quantum dot with $L_{QD}/D_{QD} = 0.5$ oriented perpendicular a) and parallel b) to the dot quantization axis.

For an exchange field applied parallel to the dot quantization axis, both Kramers doublet components shift with the pseudo spin-up moving towards lower energies and the spin-down towards higher. As expected both components shift linearly and at $B_{Mn} = 701.5$ T the Zeeman shift of pseudo spin up is 37 meV and the one of spin-down 36 meV. This difference is attributed to the fact that already for small values of field, the pseudo spin-down state and excited states repel each other. Nevertheless we can still trace its evolution and plot it to compare with the spin-up component shift.

From the slope of Zeeman shift plot for a field applied parallel to the nanowire axis, we can calculate the expectation value of spin $< S_z >$ using the equation

$$\frac{\Delta E}{\Delta B} = \mu_B g_e < S_z > \qquad (3.3)$$

where ΔE and ΔB, the energy and exchange field difference accordingly, of two consecutive points. From this calculation, we find that spin is smaller than the expectation value $< S_z >= 0.5$. This is attributed to the leaking of envelope and the small mixing of heavy hole with light hole and split-off. We can confirm that, by taking the sum of probabilities of each envelope component multiplied by its spin value and the corresponding percentage inside the quantum dot, $\frac{1}{2} \cdot P_{HH} \cdot HH_{id} + \frac{1}{6} \cdot P_{LH} \cdot LH_{id} + \frac{1}{6} \cdot P_{SO} \cdot SO_{id} = 0.45$. This of course affects the value of Zeeman splitting at saturation which is also smaller than 88 meV. We discuss this in detail in the next chapter where we will compare with the experimental results. To further expand our understanding about the spin properties of the ground state we want to visualize its values for each point of the nanowire quantum dot. By doing that we can directly observe the variation of spin in different areas of the heterostructure. In order to calculate the spin expectation value for each point of the nanostructure we define

$$< S_i > (\vec{r}) = \frac{\sum_{k,l}^{6} F_k(\vec{r}) S_{i(kl)} F_l^*(\vec{r})}{\sum_k^6 F_k(\vec{r}) F_k^*(\vec{r})} \qquad (3.4)$$

where $S_i, i = x, y, z$ the spin operator and $F_{k,l}(\vec{r})$ the envelope function components on the total angular momentum basis. In this case again and in order to reveal symmetry features as we did for the envelope function in the previous chapter, we plot the projection colormap of the spin operator.
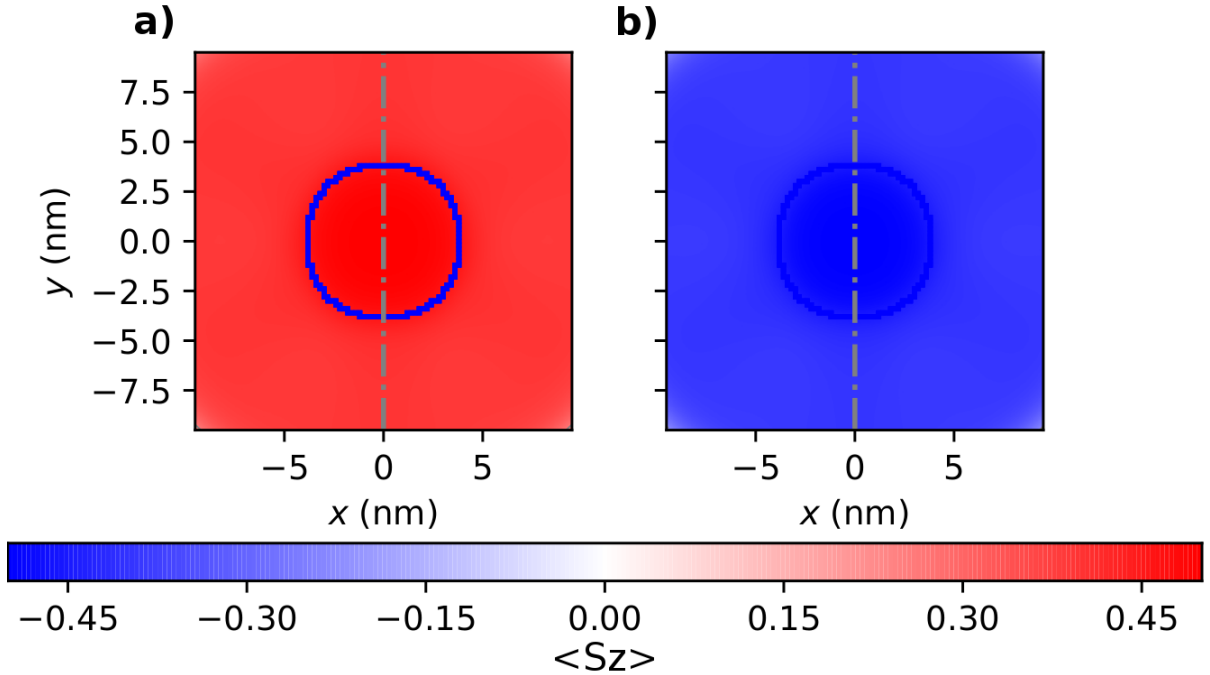
Figure 3.3 – Colormap of the spin expectation value $< S_z > (\vec{r})$ projection on xy plane for the pseudo spin-up component a) and pseudo spin-down b) of the first Kramers doublet of a 200 meV type I flat quantum dot at $B_{Mn} = 29.8$ T.

In Fig. 3.3 we present the plot of $< S_z > (\vec{r})$ projection colormaps on xy plane for the two Kramers doublets components at $B_{Mn} = 29.8$ T. The spin distribution inside the dot looks uniform with values $\frac{1}{2}$ and $-\frac{1}{2}$ for the pseudo spin-up and spin-down respectively. In order to reveal more information for the spin texture, we plot the profile of spin expectation value

$< S_z > (\vec{r})$ and we superimpose it with the profile of the total envelope function. This is shown in Fig. 3.4. From this plot we see clearly the spin variation inside the dot. We confirm that near the center of the quantum dot, where presence probability becomes maximum, it is $< S_z >= 0.5$. This is in agreement with the spin expectation value of a pure heavy hole which is what we expect at this point. From the envelope components of this structure, as shown in Fig. 2.19, both light hole and split-off presence probabilities are vanishing inside the dot. As we move away from the quantum dot center, heavy hole presence probability decreases, while the contribution from light hole and split-off increases. Nevertheless the presence probability of the total envelope decreases. This of course affects the value of spin which also decreases as we move away from the center of the quantum dot. At CdTe-ZnTe interface, $< S_z >= 0.44$ and by averaging for the 92 % of the envelope confined inside the dot, we calculate the expectation values for spin $< S_z > = 0.45$, which confirms the value obtained from Zeeman shift plot. Through this method we calculated the spin for all values of applied magnetic field from 0 T to 701.5 T and as expected, for the pseudo spin-up component they do not change by increasing magnetic field and remain constant. On the contrary, pseudo spin-down component gets mixed with excited states above 475.3 T, consequently any analysis of spin properties of this state becomes non-trivial.
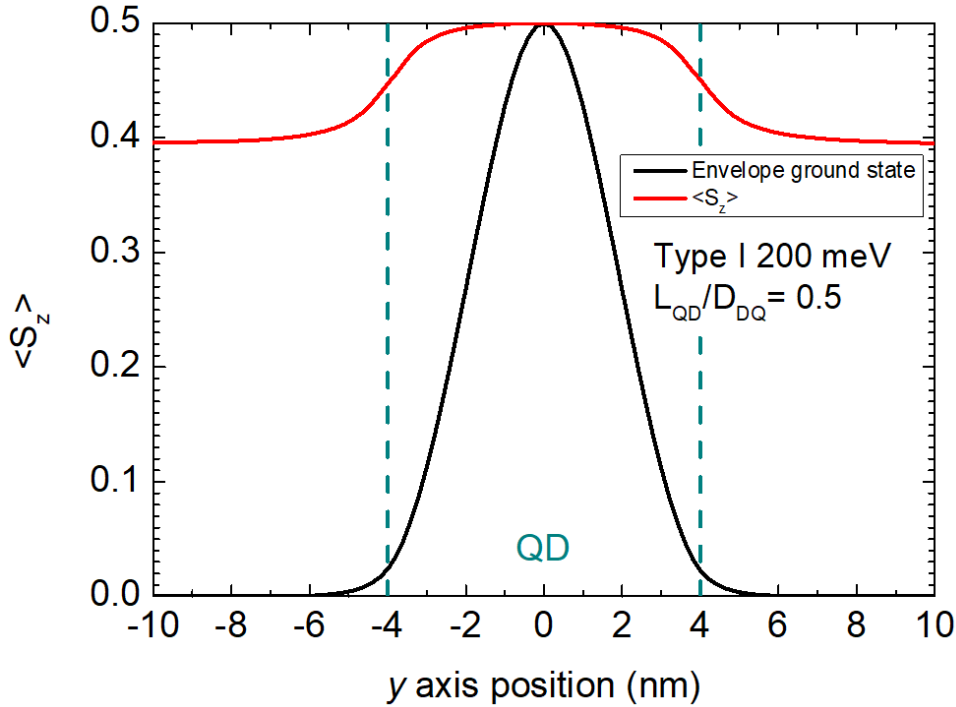
Figure 3.4 – Profile of the projections of spin expectation value $< S_z > (\vec{r})$ corresponding to the pseudo spin-up component and the total envelope function along y axis, for a 200 meV type I flat quantum dot with $L_{QD} = 4nm$, at $B_{Mn} = 29.8$ T.

Concerning spin along x, their expectation values for small field are vanishing, similarly to bulk and as the two components of the Kramers doublet are quasi-degenerate, plotting the projection of $< S_x > (\vec{r})$ does not provide any useful information.

3.3.2   Elongated quantum dot

The next structure we studied was a 200 meV type I elongated CdTe quantum dot with $L_{QD} = 18$ nm and $L_{QD}/D_{QD} = 2.25$ in a ZnTe-ZnMgTe core-shell nanowire. The structural properties of the nanowire quantum dot are identical to those of the heterostructures containing an elogated

dot, studied in the previous chapter. The integrated presence probability and percentage inside the dot of each total angular momentum component are given the following table.

Table 3.3 – The presence probability of heavy hole, light hole and split-off, with their respective percentages inside the quantum dot, for a 200 meV strong type I elongated CdTe quantum dot in a ZnTe-ZnMgTe core-shell nanowire.

P_{HH}	HH_{id}	P_{LH}	LH_{id}	P_{SO}	SO_{id}
0.031	36.1%	0.954	97.4%	0.015	90.5%

In total, 95.5 % of the envelope function is confined inside the dot, which is slightly stronger than the confinement of a flat dot. In that case, ground state is a light hole with a small mixing with heavy hole and split-off band. It is important to underline though, that the presence probability of split-off is stronger for the elongated quantum dot than for the flat one.

Similar to the flat dot case, we applied the exchange field along x and z axis. In Fig. 3.5a) we plot the Zeeman shif as a function of the exchange field applied perpendicular to the dot quantization axis ($B//x$) and in Fig. 3.5b) for an exchange field applied parallel ($B//z$).
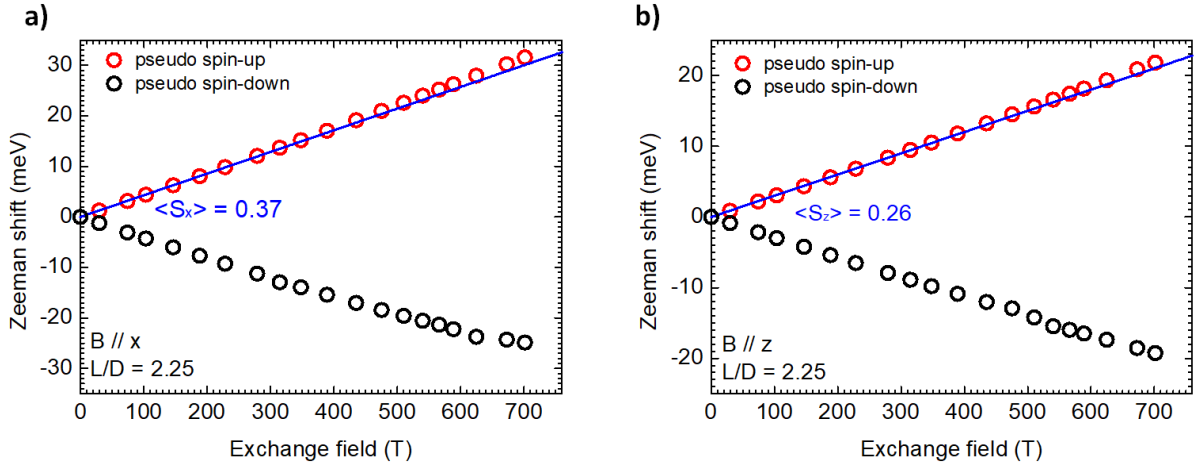
Figure 3.5 – Zeeman shift for a type I 200 meV elongated quantum dot with $L_{QD}/D_{QD} = 2.25$ as a function of the exchange field, oriented parallel to x axis a) and z axis b).

In that case we observe that the energy shift, weakly deviates from linear behaviour as we increase the exchange field. This is an indication that the spin expectation values for this structure, do not remain constant but they get affected by increasing the exchange field. Before further investigating spin at large fields we will first calculate its value at vanishing field from the slope of Zeeman shift of Fig. 3.5.

From the slopes for $B//x$ and $B//z$ we calculate accordingly the spin expectation values $< S_x >= 0.37$ and $< S_z >= 0.26$. Surprisingly, both values are larger from those expected for a light hole $< S_x >= \frac{1}{3}$ and $< S_z >= \frac{1}{6}$. Especially the spin expectation value $< S_z >$ is almost 40 % larger than the corresponding value for bulk. Here, contrary to the flat dot structure with a ground state predominantly of heavy hole type, there is no straightforward way to correlate spin values with the percentage of leaking and mixing between the total angular momentum components of the ground state envelope function.

Another way to investigate spin texture, is by calculating and plotting the projections of spin expectation values $< S_x > (\vec{r})$ and $< S_z > (\vec{r})$ as we did in the previous section. In Fig. 3.6 a) we present the projection of spin expectation value $< S_z > (\vec{r})$ for the pseudo spin-up envelope component and in Fig. 3.6 b) for the pseudo spin-down. First thing someone notices is that inside and outside the dot, spin sign is different. This is attributed to the R component
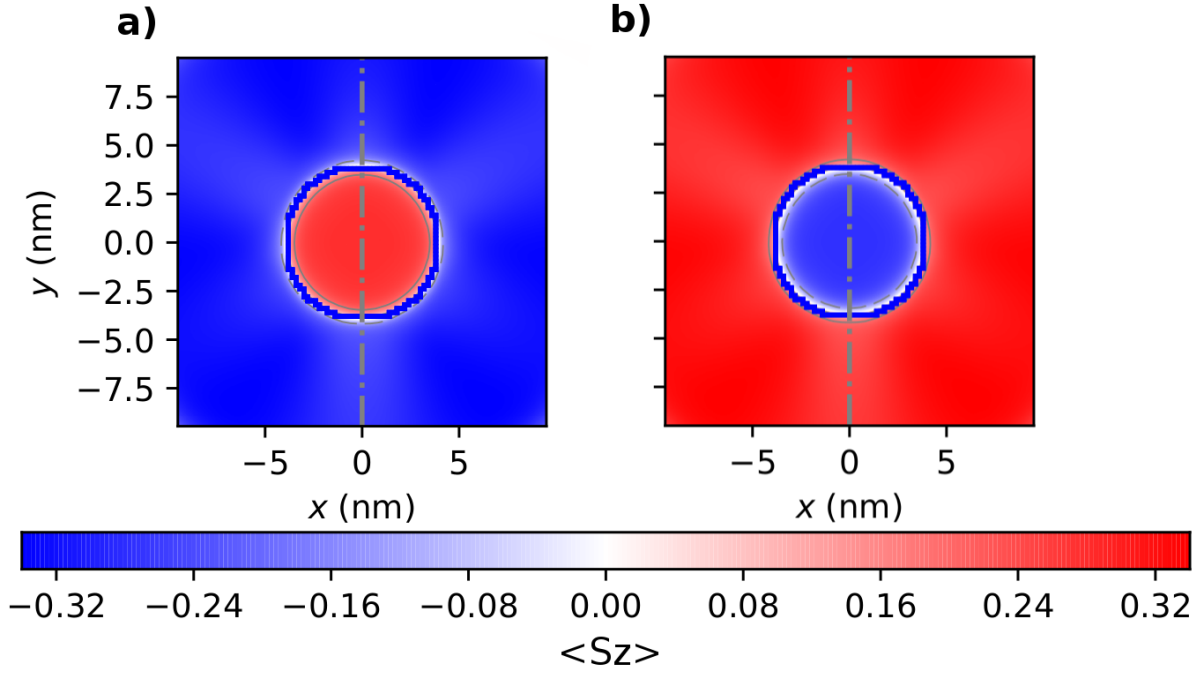
Figure 3.6 – Colormap of the spin expectation value $< S_z > (\vec{r})$ projection on xy plane for the pseudo spin-up component a) and pseudo spin-down b) of the first Kramers doublet of a 200 meV type I elongated quantum dot at $B_{Mn} = 29.8$ T.

of Bir-Pikus Hamiltonian shown in Fig. 2.37, which outside the dot is non-vanishing and is responsible for the mixing of heavy and light hole with opposite spin signs. Near the center of the quantum dot, spin expectation value for the pseudo spin-up component is $< S_z >= 0.28$ and for the pseudo spin-down $< S_z >= -0.28$. As we approach the CdTe-ZnTe interface spin vanishes.

In order to study more qualitatively spin variation inside the dot which is what we're interested in, we plot the profile of its expectation value superimposed with the total envelope as shown in Fig. 3.7. As with the flat quantum dot, spin values remain constant near the center, while as we approach the ZnTe core spin decreases abruptly. At the interface of CdTe and ZnTe spin becomes negative. This is due to the fact that R term is non zero also in this region where the presence probability on light hole decreases while that of heavy hole becomes maximum. The envelopes for this structure are shown in Fig. 2.20. For an accurate estimation of $< S_z >$, we calculate the average spin by integrating its values for all points along xy plane and inside the dot, ignoring the part that leaks outside. This results a spin value $< S_z >= 0.26$ at 29.8 T which is similar to that calculated from the slope. Concerning the pseudo spin-down component and for exchange field values smaller than those for which level anticrossing appears ($B_{Mn} < 389.2T$, see Appendix B), spin signs are opposite but their respective absolute values remain the same. For large fields though, pseudo spin-down component gets mixed with excited states, complicating significantly spin properties.

As a next step we studied the spin properties for a field applied perpendicular to the quantization axis.

In Fig. 3.8 a) we plot the colormap of the spin expectation value $< S_x > (\vec{r})$ projection for the pseudo spin-up component and in Fig. 3.8 b) for the spin-down. Near the quantum dot center, spin expectation value is $< S_x >= 0.38$ and $< S_x >= -0.38$ respectively. For both Kramers doublet components, spin distribution in absolute values is the same and only spin sign is different. For convenience, we will focus our discussion on $< S_x >$ values for pseudo spin-up. The interesting aspect here, is that as we move along y axis, spin increases and at
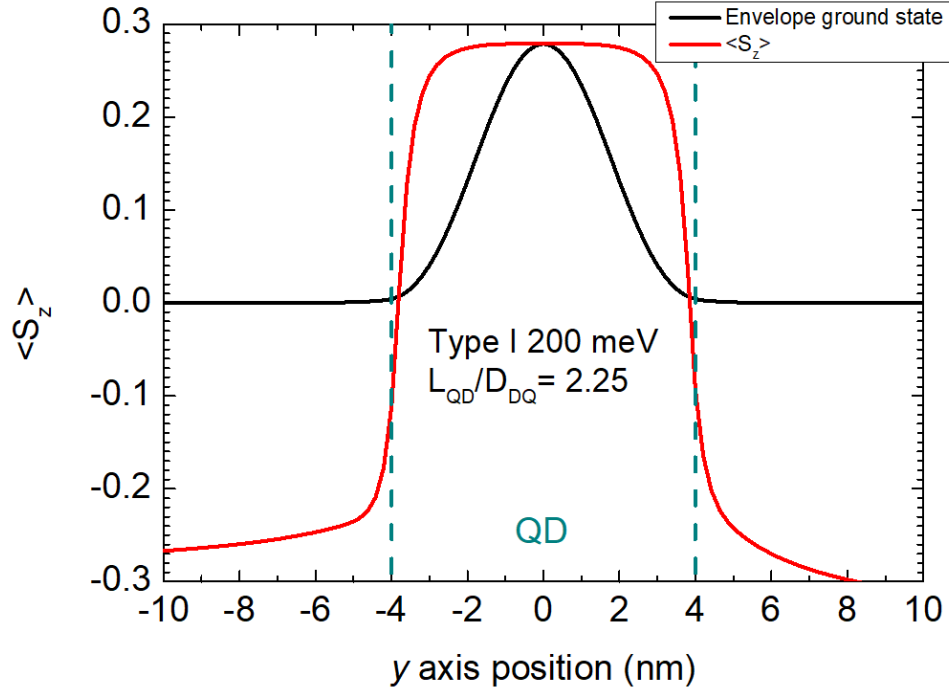
Figure 3.7 – Cross section of the projections of spin component $< S_z > (\vec{r})$ and the total envelope function for the pseudo spin-up component of the Kramers doublet along y axis for a 200 meV type I elongated quantum dot with $L_{QD} = 18nm$ at $B_{Mn} = 29.8$ T
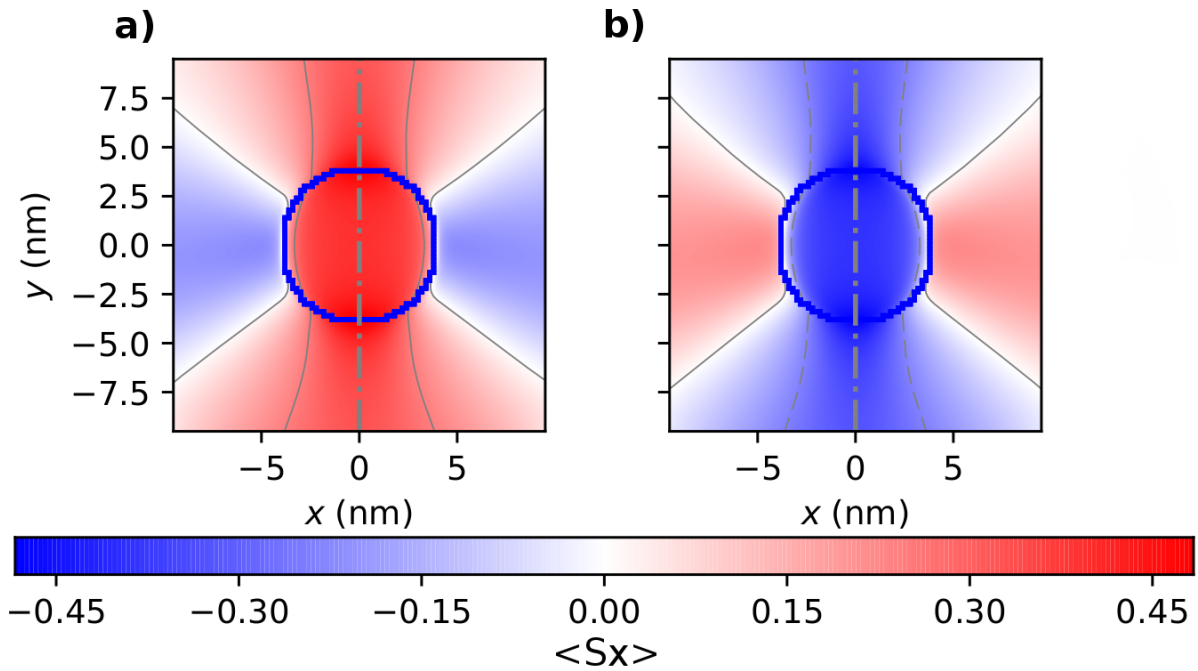
Figure 3.8 – Colormap of the spin expectation value $< S_x > (\vec{r})$ projection on xy plane for pseudo spin-up component of the Kramers doublet a) and pseudo spin-down b) at $B_{Mn} = 29.8$ T.

CdTe-ZnTe interface it becomes $< S_x > = 0.48$. On the contrary, as we move along x axis, spin decreases and at the interface is equal to $< S_x > = $ -0.15. This spin variation inside the dot is better understood by plotting the superposition of the spin expectation value and envelope

projection profile along both x and y axis as shown in Fig. 3.9 a) and b) respectively.

Figure 3.9 – Profiles of the projections of spin expectation value $< S_x > (\vec{r})$ and the total envelope function along y a) and x axis b) for a 200 meV type I elongated quantum dot with $L_{QD}/D_{QD} = 2.25$ at $B_{Mn} = 29.8$ T.

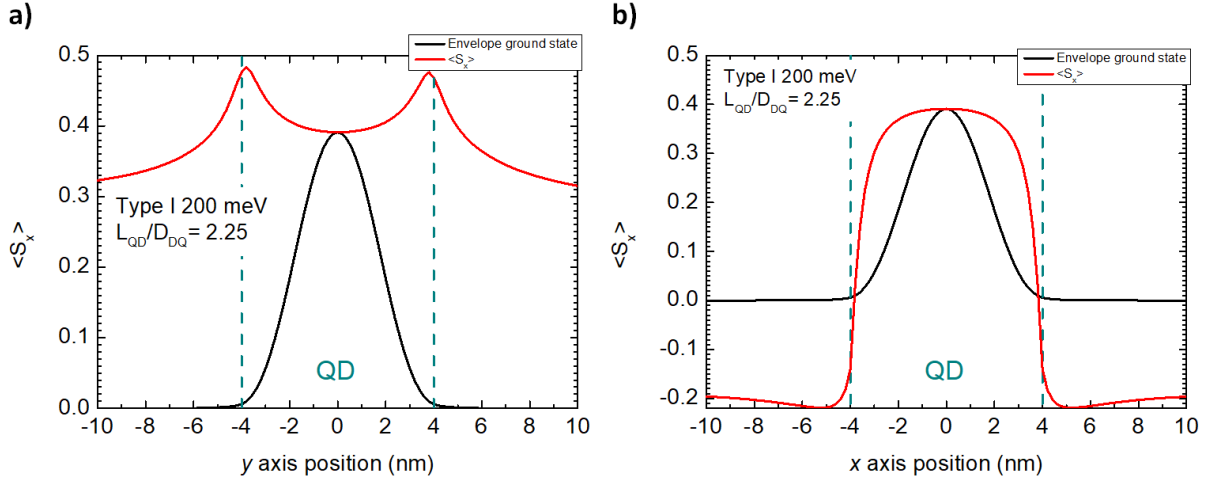By looking at spin values along x axis the spin profile is as expected, i.e. a plateau near the dot center and then a sharp decrease to negative values to the CdTe-ZnTe interface indicating a mixing with the $\left|\frac{3}{2}, -\frac{3}{2}\right\rangle$ envelope component due to R term. On the contrary, along y axis spin increases and close to the dot-nanowire interface it looks like we have a state of very strong heavy hole contribution. This is still not very well understood, but we will try to give a possible explanation. When the field is applied along x, the total angular momentum components corresponding to the different spin-up and spin-down valence band states are mixed equivalently. For instance, at $B_{Mn} = 29.8$ T, for both $\left|\frac{3}{2}, \frac{1}{2}\right\rangle$ and $\left|\frac{3}{2}, -\frac{1}{2}\right\rangle$, it is $P'_{LH} = 47.7$ %, giving a total light hole contribution of $P_{LH} = 95.4$ % as shown in the beginning of this section. For an elongated quantum dot, heavy hole is localized near the quantum dot-nanowire interface, while the presence probability of light hole at this region vanishes. As a consequence it is possible, due to mixing, to have a strong heavy hole contribution with its spin lying on xy plane. As mentioned earlier however, this mechanism is not well understood and needs further investigation.

By averaging the values of spin inside the quantum dot and taking into account the envelope leaking, in similar way as we did for $< S_z >$, we calculate $< S_x >= 0.37$ for $B_{Mn} = 29.8$ T. This result is in agreement with the value calculated from the slope.

Going back to Zeeman shift graphs, from the calculations results, we understand that there is a parameter which affects spin values of the elongated quantum dot ground state, as exchange field increases. By looking carefully at the envelope function decomposition in its individual total angular momentum components $|3/2, \pm 3/2\rangle$, $|3/2, \pm 1/2\rangle$ and $|1/2, \pm 1/2\rangle$ we realize that by increasing magnetic field we also increase the presence probability of split-off state.

This applies for both orientations of magnetic field along x and z axis. The evolution of split-off presence probability as a function of the exchange field is shown in Fig. 3.10. The first thing we notice is that the increase of split-off presence probability is stronger for a field applied along z axis. This can be an indication why the difference of spin expectation value $< S_z >$ is stronger than $< S_x >$. Also for the pseudo spin-down component of the Kramers doublet, we observe that locally the split-off presence probability increases abruptly for both orientations of magnetic field. This is attributed to the level crossing with excited states which also shift towards higher energies. The Zeeman shift for all calculated levels for an elongated quantum dot is shown in Appendix B, in Fig. B.2.

In Fig. 3.11 we plot the expectation values of spin $< S_z >$ and $< S_x >$ as a function of
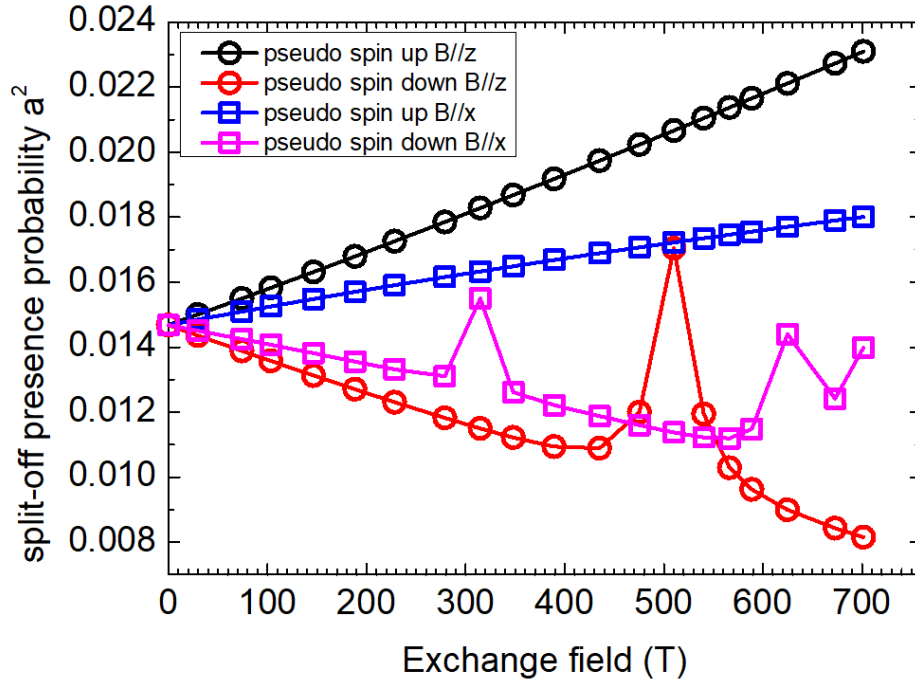
Figure 3.10 – The evolution of split-off presence probability as a function of the exchange field
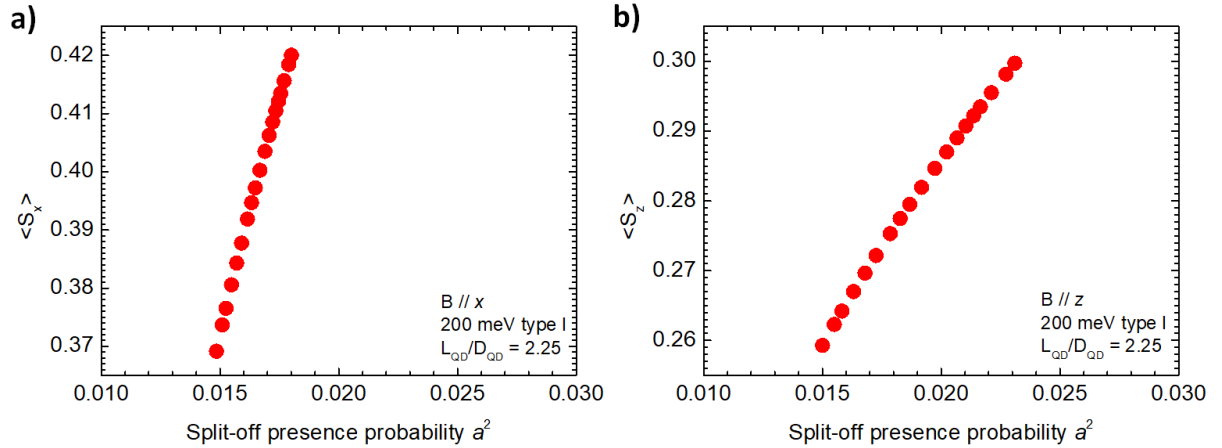
Figure 3.11 – Spin expectation values for magnetic field perpendicular a) and parallel b) to the nanowire quantization axis as a function of split-off presence probability for the pseudo spin-up component of the Kramers doublet.

the split-off component presence probability for the two orientations of magnetic field. The purpose of these graphs is to demonstrate a correlation between the values of spin and the mixing between light hole and split-off. More specifically, we observe that as split-off presence probability increases, spin values also increase for both directions of the exchange field. The proof aof this effect will be developed in detail in the next section. This observation is of great importance since a state is never pure and there is always a small mixing between different components further enhanced due to strain, even for a strongly confined system like the type I case we investigate in this section. What is really surprising though is that a small mixing in the order of 2 % can increase spin expectation value up to 40 % for $< S_z >$. In particular for light holes, their coupling is stronger with split-off than for heavy holes consequently the next step was to try and develop a more complete understanding of how spin is influenced by this

mixing. In the next section we present an analytical model through which the influence of light hole-split-off mixing on spin values is explained

3.4 Mixing between light hole and split-off band

In the previous section, we presented a correlation between the mixing of light hole with split-off and the spin expectation values. At 0 T this mixing is attributed to the induced axial shear strain, while we demonstrated that it increases as a function of exchange field. In Fig. 3.12 we plot the effective spin components calculated analytically for both z and x directions as a function of the split-off presence probability. From these plots we verify the assessment that even a small mixing between light hole and split-off modifies the values of spin. For $a > 0$, which in our convention corresponds to compressive quantum dots, small mixing between light hole and split-off increases the expectation values of spin. For $a < 0$, which is the case for tensile dots, small mixing between light hole and split-off results in the decrease of spin expectation values. In this section we will develop in detail an analytical model, originally proposed by Joël Cibert, which correlates axial shear strain to the mixing among split-off and light hole. From these results, we will extract the equations which give the spin expectation values as a function of split-off presence probability.
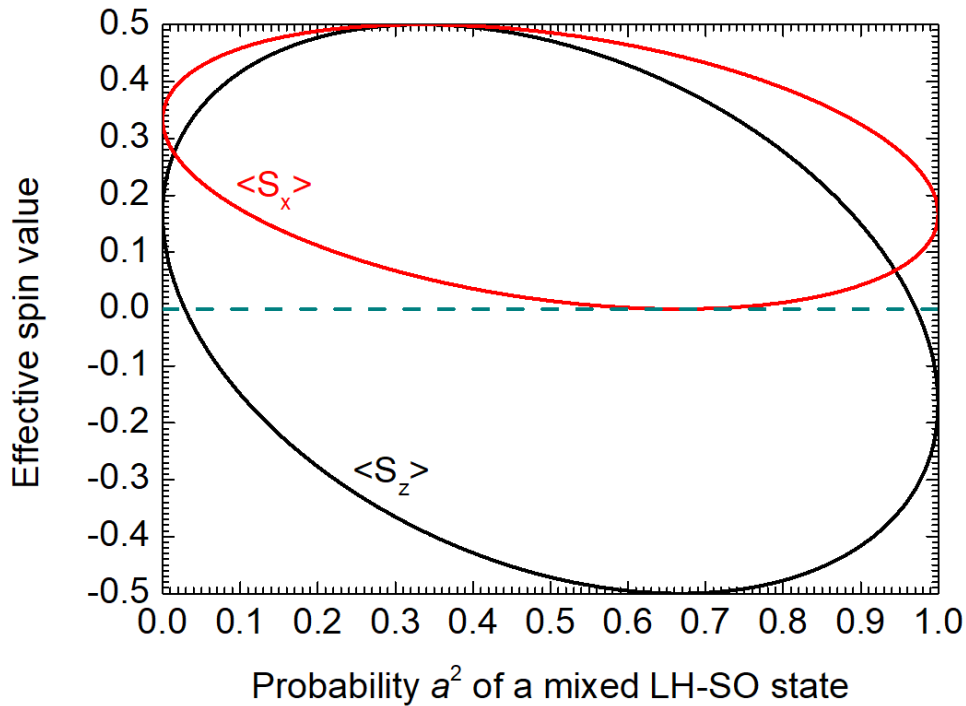
Figure 3.12 – The plot of effective spin components for the pseudo spin-up component of the first Kramers doublet as a function of the probability a^2 for a light hole state mixed with split-off. In the vicinity of $a^2 = 0$ which is the case for a pure light hole, the slope approaches infinity.

The first step for the model development is to introduce the spin matrices in the total angular momentum basis for the Γ_8 and Γ_7 manifolds. Valence band states are characterized by an orbital component $L = 1$ and a spin component $S = 1/2$. For the orbital part we identify three different states $|+1\rangle, |0\rangle, |-1\rangle$ and for the spin part two $|+\rangle, |-\rangle$. Following the convention of G. Fishman [50] we can write the heavy hole, light hole and split-off band states as follows

$$
\begin{aligned}
\left|\frac{3}{2}, \frac{3}{2}\right\rangle_{HH} &= |\mathcal{Y}_{11} \uparrow\rangle = |+1\rangle |+\rangle \\[2mm]
\left|\frac{3}{2}, \frac{1}{2}\right\rangle_{LH} &= \left|\sqrt{\frac{2}{3}}\mathcal{Y}_{10} \uparrow + \frac{1}{\sqrt{3}}\mathcal{Y}_{11} \downarrow\right\rangle = \sqrt{\frac{2}{3}}|0\rangle |+\rangle + \frac{1}{\sqrt{3}}|+1\rangle |-\rangle \\[2mm]
\left|\frac{3}{2}, -\frac{1}{2}\right\rangle_{LH} &= \left|\frac{1}{\sqrt{3}}\mathcal{Y}_{1-1} \uparrow + \sqrt{\frac{2}{3}}\mathcal{Y}_{10} \downarrow\right\rangle = \frac{1}{\sqrt{3}}|-1\rangle |+\rangle + \sqrt{\frac{2}{3}}|0\rangle |-\rangle \\[2mm]
\left|\frac{3}{2}, -\frac{3}{2}\right\rangle_{HH} &= |\mathcal{Y}_{1-1} \downarrow\rangle = |-1\rangle |-\rangle \\[2mm]
\left|\frac{1}{2}, \frac{1}{2}\right\rangle_{SO} &= \left|\frac{1}{\sqrt{3}}\mathcal{Y}_{10} \uparrow - \sqrt{\frac{2}{3}}\mathcal{Y}_{11} \downarrow\right\rangle = \frac{1}{\sqrt{3}}|0\rangle |+\rangle - \sqrt{\frac{2}{3}}|+1\rangle |-\rangle \\[2mm]
\left|\frac{1}{2}, -\frac{1}{2}\right\rangle_{SO} &= \left|\sqrt{\frac{2}{3}}\mathcal{Y}_{1-1} \uparrow - \frac{1}{\sqrt{3}}\mathcal{Y}_{10} \downarrow\right\rangle = \sqrt{\frac{2}{3}}|-1\rangle |+\rangle - \frac{1}{\sqrt{3}}|0\rangle |-\rangle
\end{aligned}
\tag{3.5}
$$

where $\mathcal{Y}_{lm}$ the spherical harmonics, written in the orbital basis X, Y, Z as

$$
\mathcal{Y}_{11} = i\frac{X + iY}{-\sqrt{2}}, \quad \mathcal{Y}_{10} = iZ, \quad \mathcal{Y}_{1-1} = i\frac{X - iY}{\sqrt{2}}
\tag{3.6}
$$

The Zeeman Hamiltonian is $\mathcal{H} = \vec{M} \cdot \hat{\mathcal{S}}$ where $\vec{M}$ is the normalized magnetization of the Mn ion multiplied by the Zeeman splitting of heavy hole at saturation. The spin operator $\hat{\mathcal{S}}_z$ along z is a 6×6 matrix with elements given by

$$
\langle u| \hat{S}_z |v\rangle, \quad \hat{S}_z |+\rangle = \frac{1}{2}|+\rangle, \quad \hat{S}_z |-\rangle = -\frac{1}{2}|-\rangle
\tag{3.7}
$$

where $|u\rangle, |v\rangle$ are the valence band states written in the total angular momentum basis as described above. Carrying out the operations we find the following non-zero diagonal matrix elements

$$
\begin{aligned}
\left\langle \frac{3}{2}, \frac{3}{2}\right| \hat{S}_z \left|\frac{3}{2}, \frac{3}{2}\right\rangle_{HH} &= \langle +| \langle +1| \hat{S}_z |+1\rangle |+\rangle = \langle +| \hat{S}_z |+\rangle \langle +1|+1\rangle = \frac{1}{2} \\[2mm]
\left\langle \frac{3}{2}, \frac{1}{2}\right| \hat{S}_z \left|\frac{3}{2}, \frac{1}{2}\right\rangle_{LH} &= \frac{2}{3}\langle +| \hat{S}_z |+\rangle \langle 0|0\rangle + \frac{1}{3}\langle -| \hat{S}_z |-\rangle \langle +1|+1\rangle = \frac{1}{6} \\[2mm]
\left\langle \frac{3}{2}, -\frac{1}{2}\right| \hat{S}_z \left|\frac{3}{2}, -\frac{1}{2}\right\rangle_{LH} &= \frac{2}{3}\langle -| \hat{S}_z |-\rangle \langle 0|0\rangle + \frac{1}{3}\langle +| \hat{S}_z |+\rangle \langle -1|-1\rangle = -\frac{1}{6} \\[2mm]
\left\langle \frac{3}{2}, -\frac{3}{2}\right| \hat{S}_z \left|\frac{3}{2}, -\frac{3}{2}\right\rangle_{HH} &= \langle -| \hat{S}_z |-\rangle \langle -1|-1\rangle = -\frac{1}{2} \\[2mm]
\left\langle \frac{1}{2}, \frac{1}{2}\right| \hat{S}_z \left|\frac{1}{2}, \frac{1}{2}\right\rangle_{SO} &= \frac{2}{3}\langle -| \hat{S}_z |-\rangle \langle +1|+1\rangle + \frac{1}{3}\langle +| \hat{S}_z |+\rangle \langle 0|0\rangle = -\frac{1}{6} \\[2mm]
\left\langle \frac{1}{2}, -\frac{1}{2}\right| \hat{S}_z \left|\frac{1}{2}, -\frac{1}{2}\right\rangle_{SO} &= \frac{2}{3}\langle +| \hat{S}_z |+\rangle \langle -1|-1\rangle + \frac{1}{3}\langle -| \hat{S}_z |-\rangle \langle 0|0\rangle = \frac{1}{6}
\end{aligned}
\tag{3.8}
$$

and the off-diagonal elements

$$\left\langle \frac{3}{2}, \frac{1}{2} \middle| \hat{S}_z \middle| \frac{1}{2}, \frac{1}{2} \right\rangle_{LH-SO} = \frac{\sqrt{2}}{3} \left\langle + \middle| \hat{S}_z \middle| + \right\rangle \left\langle 0 \middle| 0 \right\rangle - \frac{\sqrt{2}}{3} \left\langle - \middle| \hat{S}_z \middle| - \right\rangle \left\langle +1 \middle| +1 \right\rangle = \frac{\sqrt{2}}{3}$$

$$\left\langle \frac{3}{2}, -\frac{1}{2} \middle| \hat{S}_z \middle| \frac{1}{2}, -\frac{1}{2} \right\rangle_{LH-SO} = \frac{\sqrt{2}}{3} \left\langle + \middle| \hat{S}_z \middle| + \right\rangle \left\langle -1 \middle| -1 \right\rangle - \frac{\sqrt{2}}{3} \left\langle - \middle| \hat{S}_z \middle| - \right\rangle \left\langle 0 \middle| 0 \right\rangle = \frac{\sqrt{2}}{3}$$

(3.9)

As a consequence the spin operator $\hat{S}_z$ for the valence band is constructed by the diagonal elements of the heavy hole $\left(\pm\frac{1}{2} \right)$, light hole $\left(\pm\frac{1}{6} \right)$ and split-off $\left(\mp\frac{1}{6} \right)$ doublets and the off-diagonal elements originating from the coupling of light hole and split-off states with the same projection

$$\hat{S}_z = \begin{pmatrix} \frac{1}{2} & 0 & 0 & 0 & 0 & 0 \\ 0 & \frac{1}{6} & 0 & 0 & \frac{\sqrt{2}}{3} & 0 \\ 0 & 0 & -\frac{1}{6} & 0 & 0 & \frac{\sqrt{2}}{3} \\ 0 & 0 & 0 & -\frac{1}{2} & 0 & 0 \\ 0 & \frac{\sqrt{2}}{3} & 0 & 0 & -\frac{1}{6} & 0 \\ 0 & 0 & \frac{\sqrt{2}}{3} & 0 & 0 & \frac{1}{6} \end{pmatrix}$$

(3.10)

The array for $\hat{S}_z$ is a specific case of the general Hamiltonian expression given at [61]. The appearance of the off-diagonal elements is a confirmation that even a small mixing between light hole and split-off will affect the values of spin. In a similar way we construct the $\hat{S}_x$ spin operator along x by calculating the matrix elements

$$\left\langle u \middle| \hat{S}_x \middle| v \right\rangle, \quad \hat{S}_x \middle| + \right\rangle = \frac{1}{2} \middle| - \right\rangle \quad \hat{S}_x \middle| - \right\rangle = \frac{1}{2} \middle| + \right\rangle$$

(3.11)

In this case the non-zero elements are

$$\left\langle \frac{3}{2}, \frac{3}{2} \middle| S_x \middle| \frac{3}{2}, \frac{1}{2} \right\rangle_{HH-LH} = \frac{1}{\sqrt{3}} \left\langle +1 \middle| +1 \right\rangle \left\langle + \middle| S_x \middle| - \right\rangle = \frac{\sqrt{3}}{6}$$

$$\left\langle \frac{3}{2}, \frac{3}{2} \middle| S_x \middle| \frac{1}{2}, \frac{1}{2} \right\rangle_{HH-SO} = -\sqrt{\frac{2}{3}} \left\langle +1 \middle| +1 \right\rangle \left\langle + \middle| S_x \middle| - \right\rangle = -\frac{1}{\sqrt{6}}$$

$$\left\langle \frac{3}{2}, \frac{1}{2} \middle| S_x \middle| \frac{3}{2}, -\frac{1}{2} \right\rangle_{LH-LH} = \frac{2}{3} \left\langle 0 \middle| 0 \right\rangle \left\langle + \middle| S_x \middle| - \right\rangle = \frac{1}{3}$$

$$\left\langle \frac{3}{2}, \frac{1}{2} \middle| S_x \middle| \frac{1}{2}, -\frac{1}{2} \right\rangle_{LH-SO} = -\frac{\sqrt{2}}{3} \left\langle 0 \middle| 0 \right\rangle \left\langle + \middle| S_x \middle| - \right\rangle = -\frac{\sqrt{2}}{6}$$

$$\left\langle \frac{3}{2}, -\frac{1}{2} \middle| S_x \middle| \frac{3}{2}, -\frac{3}{2} \right\rangle_{LH-HH} = \frac{1}{\sqrt{3}} \left\langle -1 \middle| -1 \right\rangle \left\langle + \middle| S_x \middle| - \right\rangle = \frac{\sqrt{3}}{6}$$

(3.12)

$$\left\langle \frac{3}{2}, -\frac{1}{2} \middle| S_x \middle| \frac{1}{2}, \frac{1}{2} \right\rangle_{LH-SO} = \frac{\sqrt{2}}{3} \left\langle 0 \middle| 0 \right\rangle \left\langle - \middle| S_x \middle| + \right\rangle = \frac{\sqrt{2}}{6}$$

$$\left\langle \frac{3}{2}, -\frac{3}{2} \middle| S_x \middle| \frac{3}{2}, -\frac{1}{2} \right\rangle_{HH-LH} = \frac{1}{\sqrt{3}} \left\langle -1 \middle| -1 \right\rangle \left\langle - \middle| S_x \middle| + \right\rangle = \frac{\sqrt{3}}{6}$$

$$\left\langle \frac{3}{2}, -\frac{3}{2} \middle| S_x \middle| \frac{1}{2}, -\frac{1}{2} \right\rangle_{HH-SO} = \sqrt{\frac{2}{3}} \left\langle -1 \middle| -1 \right\rangle \left\langle - \middle| S_x \middle| + \right\rangle = \frac{1}{\sqrt{6}}$$

$$\left\langle \frac{1}{2}, \frac{1}{2} \middle| S_x \middle| \frac{1}{2}, -\frac{1}{2} \right\rangle_{SO-SO} = -\frac{1}{3} \left\langle 0 \middle| 0 \right\rangle \left\langle + \middle| S_x \middle| - \right\rangle = -\frac{1}{6}$$

Operator $\hat{\mathcal{S}}_x$ has no diagonal elements and in matrix form is written

$$\hat{\mathcal{S}}_x = \begin{pmatrix} 0 & \frac{\sqrt{3}}{6} & 0 & 0 & -\frac{1}{\sqrt{6}} & 0 \\ \frac{\sqrt{3}}{6} & 0 & \frac{1}{3} & 0 & 0 & -\frac{\sqrt{2}}{6} \\ 0 & \frac{1}{3} & 0 & \frac{\sqrt{3}}{6} & \frac{\sqrt{2}}{6} & 0 \\ 0 & 0 & \frac{\sqrt{3}}{6} & 0 & 0 & \frac{1}{\sqrt{6}} \\ -\frac{1}{\sqrt{6}} & 0 & \frac{\sqrt{2}}{6} & 0 & 0 & -\frac{1}{6} \\ 0 & -\frac{\sqrt{2}}{6} & 0 & \frac{1}{\sqrt{6}} & -\frac{1}{6} & 0 \end{pmatrix} \tag{3.13}$$

The quantity which mixes states with different angular momentum is the shear strain induced due to lattice mismatch. In terms of orbital angular momentum, we can describe strain through the Hamiltonian

$$\begin{aligned} \mathcal{H}_{strain} &= \mathcal{H}_s^{hydrostatic} + \mathcal{H}_s^{shear} \\ &= -a_v(e_{xx} + e_{yy} + e_{zz}) - \frac{d}{2\sqrt{3}}\left[\left(L_z^2 - \frac{1}{3}L^2\right)e_{zz} + c.p.\right] \end{aligned} \tag{3.14}$$

where a_v, d the valence band deformation potentials and $c.p.$, cyclic permutations [62]. At this point we underline that this Hamiltonian is an expression of P and Q terms written as operators. The off-diagonal terms are ignored for two reasons: The first one is that they do not couple light hole with split-off (see Hamiltonian matrix in Eq. 2.43) and the second one because in the case of bulk (but also inside a quantum dot), they are vanishing. From the expression above, we can write the shear strain Hamiltonian which splits $|0\rangle$ orbital from $|\pm 1\rangle$ orbitals as

$$\mathcal{H}_{shear} = c'\left[L_z^2 - \frac{l(l+1)}{3}\right] \tag{3.15}$$

where c' a constant with a unit of energy. This operator is invariant to any rotation around the axis, consequently we expect to find non-zero elements between states with the same projection of total angular momentum J_z. From Eq. 3.5, we calculate the non vanishing matrix elements

$$\begin{aligned} \left\langle \frac{3}{2}, \frac{3}{2}\right| \mathcal{H}_{shear} \left|\frac{3}{2}, \frac{3}{2}\right\rangle_{HH-HH} &= \left[\langle + | \langle 1 | L_z^2 - \frac{l(l+1)}{3} |1\rangle |+\rangle\right]c' \\ &= \left[\langle 1| L_z^2 |1\rangle - \langle 1| \frac{l(l+1)}{3} |1\rangle\right]c' = \frac{1}{3}c' \\ \left\langle \frac{3}{2}, \frac{1}{2}\right| \mathcal{H}_{shear} \left|\frac{3}{2}, \frac{1}{2}\right\rangle_{LH-LH} &= \left[\frac{2}{3}\langle 0| L_z^2 |0\rangle - \frac{2}{3}\langle 0| \frac{l(l+1)}{3} |0\rangle + \frac{1}{3}\langle 1| L_z^2 |1\rangle \right. \\ &\left. -\frac{1}{3}\langle 1| \frac{l(l+1)}{3} |1\rangle\right]c' = -\frac{1}{3}c' \\ \left\langle \frac{3}{2}, \frac{1}{2}\right| \mathcal{H}_{shear} \left|\frac{1}{2}, \frac{1}{2}\right\rangle_{LH-SO} &= \left[\frac{\sqrt{2}}{3}\langle 0| L_z^2 |0\rangle - \frac{\sqrt{2}}{3}\langle 0| \frac{l(l+1)}{3} |0\rangle \right. \\ &\left. -\frac{\sqrt{2}}{3}\langle 1| L_z^2 |1\rangle + \frac{\sqrt{2}}{3}\langle 1| \frac{l(l+1)}{3} |1\rangle\right]c' \\ &= -\frac{\sqrt{2}}{3}c' \end{aligned} \tag{3.16}$$

$$\left\langle \frac{3}{2}, -\frac{1}{2} \right| \mathcal{H}_{shear} \left| \frac{3}{2}, -\frac{1}{2} \right\rangle_{LH-LH} = \left[\frac{2}{3} \langle 0| L_z^2 |0\rangle - \frac{2}{3} \langle 0| \frac{l(l+1)}{3} |0\rangle \right.$$

$$\left. + \frac{1}{3} \langle -1| L_z^2 |-1\rangle - \frac{1}{3} \langle -1| \frac{l(l+1)}{3} |-1\rangle \right] c'$$

$$= -\frac{1}{3} c'$$

$$\left\langle \frac{3}{2}, -\frac{1}{2} \right| \mathcal{H}_{shear} \left| \frac{1}{2}, -\frac{1}{2} \right\rangle_{LH-SO} = \left[-\frac{\sqrt{2}}{3} \langle 0| L_z^2 |0\rangle + \frac{\sqrt{2}}{3} \langle 0| \frac{l(l+1)}{3} |0\rangle \right.$$

$$\left. + \frac{\sqrt{2}}{3} \langle -1| L_z^2 |-1\rangle - \frac{\sqrt{2}}{3} \langle -1| \frac{l(l+1)}{3} |-1\rangle \right] c'$$

$$= \frac{\sqrt{2}}{3} c'$$

$$\left\langle \frac{3}{2}, -\frac{3}{2} \right| \mathcal{H}_{shear} \left| \frac{3}{2}, -\frac{3}{2} \right\rangle_{HH-HH} = \left[\langle -1| L_z^2 |-1\rangle - \langle -1| \frac{l(l+1)}{3} |-1\rangle \right] c' = \frac{1}{3} c'$$

We observe that the diagonal elements for the two split-off band states are equal to zero. This is expected since shear strain does not influence the states of Γ_6 and Γ_7 manifolds. By shifting the zero of energy to the light hole level and including the spin-orbit term we calculate the shear strain Hamiltonian

$$\mathcal{H}'_{shear} = \mathcal{H}_{shear} - \left(\left\langle \frac{3}{2}, \pm\frac{1}{2} \right| \mathcal{H}_{shear} \left| \frac{3}{2}, \pm\frac{1}{2} \right\rangle_{LH-LH} \cdot I_6 \right) + \mathcal{H}_{SO} \tag{3.17}$$

where I_6, the 6×6 identity matrix and $\mathcal{H}_{SO}$ the spin orbit Hamiltonian. The energy difference between heavy and light hole is $E_{LH} = \frac{2}{3} c'$. In matrix form, $\mathcal{H}'_{shear}$ is written

$$\mathcal{H}'_{shear} = \begin{pmatrix} E_{LH} & 0 & 0 & 0 & 0 & 0 \\ 0 & 0 & 0 & 0 & -\frac{E_{LH}}{\sqrt{2}} & 0 \\ 0 & 0 & 0 & 0 & 0 & \frac{E_{LH}}{\sqrt{2}} \\ 0 & 0 & 0 & E_{LH} & 0 & 0 \\ 0 & -\frac{E_{LH}}{\sqrt{2}} & 0 & 0 & \frac{E_{LH}}{2} + \Delta_{SO} & 0 \\ 0 & 0 & \frac{E_{LH}}{\sqrt{2}} & 0 & 0 & \frac{E_{LH}}{2} + \Delta_{SO} \end{pmatrix} \tag{3.18}$$

Since we want to study the effect of mixing between light hole and split-off band, we can simplify the problem by ignoring states at Γ_7 and consider only those at Γ_8. In order to do that we have to calculate a perturbed light hole state $\left| \widetilde{\frac{3}{2}, \pm\frac{1}{2}} \right\rangle$ which will include the mixing with split-off. From perturbation theory, the wavefunction with first order correction is written

$$|\psi_n\rangle = |\phi_n\rangle + \sum_{n \neq m} \frac{\langle \phi_m| \widehat{\mathcal{H}} |\phi_n\rangle}{E_n^0 - E_m^0} \Rightarrow \left| \widetilde{\frac{3}{2}, \pm\frac{1}{2}} \right\rangle = \left| \frac{3}{2}, \pm\frac{1}{2} \right\rangle + \frac{\langle \frac{1}{2}, \pm\frac{1}{2}| \mathcal{H}'_{shear} |\frac{3}{2}, \pm\frac{1}{2}\rangle}{\Delta_{SO}} \tag{3.19}$$

Only the matrix elements with same m_j are non-zero, as shown in the calculations above. In other words the first order corrections are the off-diagonal elements of $\mathcal{H}'_{shear}$. The denominator corresponds to the energy difference between light hole and split-off band and is equal to Δ_{SO}. The perturbed states for light hole including the split-off contribution in Γ_8 are

$$\left|\widetilde{\frac{3}{2},\frac{1}{2}}\right\rangle = \left|\frac{3}{2},\frac{1}{2}\right\rangle - \frac{E_{LH}}{\sqrt{2}\Delta_{SO}}\left|\frac{1}{2},\frac{1}{2}\right\rangle$$

$$\left|\widetilde{\frac{3}{2},-\frac{1}{2}}\right\rangle = \left|\frac{3}{2},-\frac{1}{2}\right\rangle + \frac{E_{LH}}{\sqrt{2}\Delta_{SO}}\left|\frac{1}{2},-\frac{1}{2}\right\rangle \qquad (3.20)$$

The next step is to construct the Zeeman Hamiltonian $\mathcal{H}_z = \sum_{i=x,y,z} M_i \cdot \mathcal{S}_i$ on the basis $|3/2, 3/2\rangle, |\widetilde{3/2, 1/2}\rangle, |\widetilde{3/2, -1/2}\rangle, |3/2, -3/2\rangle$ where M_i is the normalized magnetization vector which contains the Lande g factor, Bohr's magneton and the giant Zeeman term. At this point we underline that since we apply perturbation theory up to first order we ignore split-off - split-off interaction which is proportional to $\frac{1}{\Delta_{SO}^2}$ for the calculation of matrix elements. The non zero diagonal elements are

$$\left\langle\frac{3}{2},\frac{3}{2}\right|M_z\mathcal{S}_z\left|\frac{3}{2},\frac{3}{2}\right\rangle = \frac{M_z}{2}$$

$$\left\langle\widetilde{\frac{3}{2},\frac{1}{2}}\right|M_z\mathcal{S}_z\left|\widetilde{\frac{3}{2},\frac{1}{2}}\right\rangle = \left\langle\frac{3}{2},\frac{1}{2}\right|M_z\mathcal{S}_z\left|\frac{3}{2},\frac{1}{2}\right\rangle - 2\frac{1}{\sqrt{2}}\frac{E_{LH}}{\Delta_{SO}}\left\langle\frac{3}{2},\frac{1}{2}\right|M_z\mathcal{S}_z\left|\frac{1}{2},\frac{1}{2}\right\rangle$$

$$= \frac{M_z}{6}\left(1 - \frac{4E_{LH}}{\Delta_{SO}}\right)$$

$$\left\langle\widetilde{\frac{3}{2},-\frac{1}{2}}\right|M_z\mathcal{S}_z\left|\widetilde{\frac{3}{2},-\frac{1}{2}}\right\rangle = \left\langle\frac{3}{2},-\frac{1}{2}\right|M_z\mathcal{S}_z\left|\frac{3}{2},-\frac{1}{2}\right\rangle \qquad (3.21)$$

$$+ 2\frac{1}{\sqrt{2}}\frac{E_{LH}}{\Delta_{SO}}\left\langle\frac{3}{2},-\frac{1}{2}\right|M_z\mathcal{S}_z\left|\frac{1}{2},-\frac{1}{2}\right\rangle = -\frac{M_z}{6}\left(1 - \frac{4E_{LH}}{\Delta_{SO}}\right)$$

$$\left\langle\frac{3}{2},-\frac{3}{2}\right|M_z\mathcal{S}_z\left|\frac{3}{2},-\frac{3}{2}\right\rangle = -\frac{M_z}{2}$$

and the off-diagonal

$$\left\langle\frac{3}{2},\frac{3}{2}\right|M_x\mathcal{S}_x\left|\widetilde{\frac{3}{2},\frac{1}{2}}\right\rangle = \left\langle\frac{3}{2},\frac{3}{2}\right|M_x\mathcal{S}_x\left|\frac{3}{2},\frac{1}{2}\right\rangle$$

$$- \frac{E_{LH}}{\sqrt{2}\Delta_{SO}}\left\langle\frac{3}{2},\frac{3}{2}\right|M_x\mathcal{S}_x\left|\frac{1}{2},\frac{1}{2}\right\rangle = \frac{\sqrt{3}}{6}M_x\left(1 + \frac{E_{LH}}{\Delta_{SO}}\right)$$

$$\left\langle\widetilde{\frac{3}{2},\frac{1}{2}}\right|M_x\mathcal{S}_x\left|\widetilde{\frac{3}{2},-\frac{1}{2}}\right\rangle = \left\langle\frac{3}{2},\frac{1}{2}\right|M_x\mathcal{S}_x\left|\frac{3}{2},-\frac{1}{2}\right\rangle + \frac{E_{LH}}{\sqrt{2}\Delta_{SO}}\left\langle\frac{3}{2},\frac{1}{2}\right|M_x\mathcal{S}_x\left|\frac{1}{2},-\frac{1}{2}\right\rangle$$

$$- \frac{E_{LH}}{\sqrt{2}\Delta_{SO}}\left\langle\frac{1}{2},\frac{1}{2}\right|M_x\mathcal{S}_x\left|\frac{3}{2},-\frac{1}{2}\right\rangle = \frac{1}{3}M_x\left(1 - \frac{E_{LH}}{\Delta_{SO}}\right) \qquad (3.22)$$

$$\left\langle\frac{3}{2},-\frac{3}{2}\right|M_x\mathcal{S}_x\left|\widetilde{\frac{3}{2},-\frac{1}{2}}\right\rangle = \left\langle\frac{3}{2},-\frac{3}{2}\right|M_x\mathcal{S}_x\left|\frac{3}{2},-\frac{1}{2}\right\rangle$$

$$+ \frac{E_{LH}}{\sqrt{2}\Delta_{SO}}\left\langle\frac{3}{2},-\frac{3}{2}\right|M_x\mathcal{S}_x\left|\frac{1}{2},-\frac{1}{2}\right\rangle = \frac{\sqrt{3}}{6}M_x\left(1 + \frac{E_{LH}}{\Delta_{SO}}\right)$$

By adding the spin matrix elements including magnetization to the 4×4 strain Hamiltonian $\mathcal{H}'_{shear}$ we construct the Hamiltonian matrix

87

$$\mathcal{H}_{4\times4} =$$

$$\begin{pmatrix} E_{LH} + \frac{M_z}{2} & \frac{\sqrt{3}}{6}M_x\left(1 + \frac{E_{LH}}{\Delta_{SO}}\right) & 0 & 0 \\ \frac{\sqrt{3}}{6}M_x\left(1 + \frac{E_{LH}}{\Delta_{SO}}\right) & \frac{M_z}{6}\left(1 - \frac{4E_{LH}}{\Delta_{SO}}\right) & \frac{1}{3}M_x\left(1 - \frac{E_{LH}}{\Delta_{SO}}\right) & 0 \\ 0 & \frac{1}{3}M_x\left(1 - \frac{E_{LH}}{\Delta_{SO}}\right) & -\frac{M_z}{6}\left(1 - \frac{4E_{LH}}{\Delta_{SO}}\right) & \frac{\sqrt{3}}{6}M_x\left(1 + \frac{E_{LH}}{\Delta_{SO}}\right) \\ 0 & 0 & \frac{\sqrt{3}}{6}M_x\left(1 + \frac{E_{LH}}{\Delta_{SO}}\right) & E_{LH} - \frac{M_z}{2} \end{pmatrix} \quad (3.23)$$

With this matrix and as a first order approximation including both strain and magnetization, we can describe a state consisting of a heavy hole - light hole superposition including as a perturbation the small mixing with split-off. The energy separation between the two hole states is $E_{LH} \approx 2Q$, where Q is the Bir-Pikus component resulting from the axial shear strain, as discussed in the previous chapter. At this point we will attempt to fit the Zeeman shift for a flat quantum dot with a heavy hole ground state for $B_{Mn} \parallel x$. We can do that by either diagonalizing directly the matrix of Eq. 3.23, imposing $M_z = 0$, or more simply by diagonalizing the 2×2 matrix which describes the heavy hole - light hole and light - hole interaction

$$H'_{2\times2} = \begin{pmatrix} E_{LH} & \frac{\sqrt{3}}{6}M_x\left(1 + \frac{E_{LH}}{\Delta_{SO}}\right) \\ \frac{\sqrt{3}}{6}M_x\left(1 + \frac{E_{LH}}{\Delta_{SO}}\right) & \frac{M_x}{3}\left(1 - \frac{E_{LH}}{\Delta_{SO}}\right) \end{pmatrix} \quad (3.24)$$

In Fig. 3.13 we fit the Zeeman shift as calculated in the previous section for a field applied along x, for a flat quantum dot with a ground state being predominantly of heavy hole type. For fitting the calculated values we considered a heavy hole - light hole splitting $E_{LH} = 200$ meV, a giant Zeeman term equal to 85 meV and the spin orbit splitting $\Delta_{SO} = 900$ meV. For this structure, $Q = 108$ meV inside the dot, consequently the energy difference between heavy and light hole, is in good agreement with this value.

For the pseudo-spin up component, the analytical model fits accurately the values obtained from the $k \cdot p$ calculation, while for the pseudo spin-down there is a small deviation for large fields, which at 701.5 T is equal to 0.4 meV. A reason for this deviation could be that this fit does not take into account excited states or second order effects which could affect the Zeeman shift.

As regards the elongated dot, before discussing the influence of split-off to spin expectation values, we will investigate the effect of applied field on its presence probability. In order to do that we have to ignore any contribution from heavy hole by reducing the total Hamiltonian to a matrix containing only the light hole and split-off. The 6×6 Hamiltonian including strain and magnetization along x and z axis is

$$\mathcal{H}_{6\times6} = \mathcal{H}'_{shear} + M_x\hat{S}_x + M_z\hat{S}_z \quad (3.25)$$
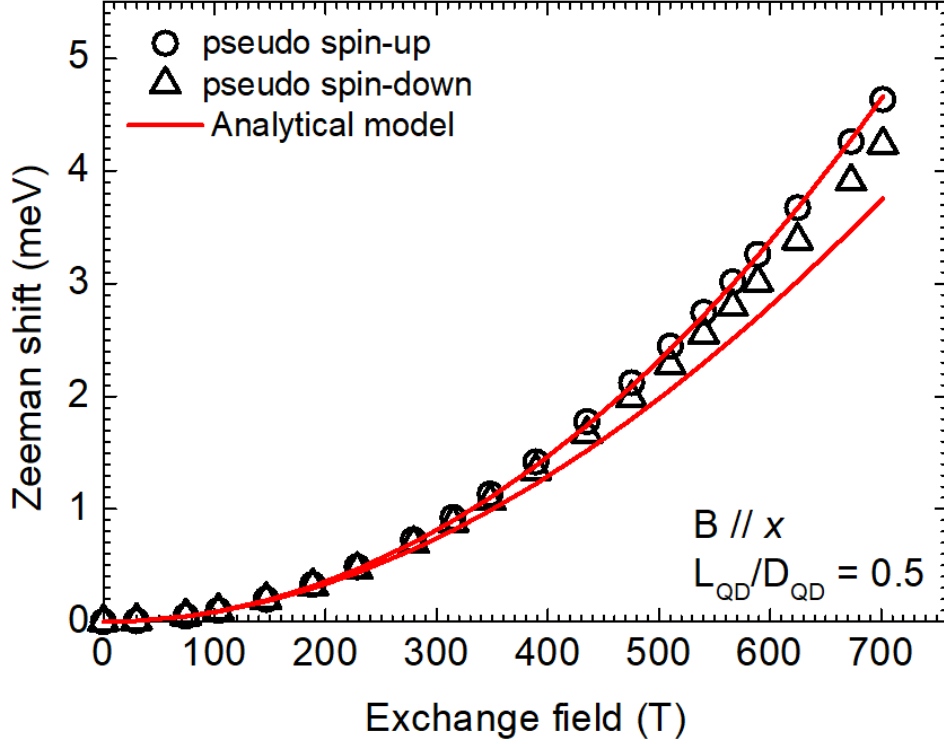
and in matrix form

Figure 3.13 – Fitting of the Zeeman shift as a function of the exchange field $B_{Mn} \; // \; x$, for the pseudo spin-up and pseudo spin-down component of the first Kramers doublet of a 200 meV type I flat quantum dot with $L_{QD}/D_{QD} = 0.5$.

$$\mathcal{H}_{6 \times 6} =$$

$$\begin{pmatrix} E_{LH} + \frac{1}{2}M_z & \frac{\sqrt{3}}{6}M_x & 0 & 0 & -\frac{1}{\sqrt{6}}M_x & 0 \\ \frac{\sqrt{3}}{6}M_x & \frac{1}{6}M_z & \frac{1}{3}M_x & 0 & -\frac{E_{LH}}{\sqrt{2}} + \frac{\sqrt{2}}{3}M_z & -\frac{\sqrt{2}}{6}M_x \\ 0 & \frac{1}{3}M_x & -\frac{1}{6}M_z & \frac{\sqrt{3}}{6}M_x & \frac{\sqrt{2}}{6}M_x & \frac{E_{LH}}{\sqrt{2}} + \frac{\sqrt{2}}{3}M_z \\ 0 & 0 & \frac{\sqrt{3}}{6}M_x & E_{LH} - \frac{1}{2}M_z & 0 & \frac{1}{\sqrt{6}}M_x \\ -\frac{1}{\sqrt{6}}M_x & -\frac{E_{LH}}{\sqrt{2}} + \frac{\sqrt{2}}{3}M_z & \frac{\sqrt{2}}{6}M_x & 0 & \frac{E_{LH}}{2} + \Delta_{SO} - \frac{1}{6}M_z & -\frac{1}{6}M_x \\ 0 & -\frac{\sqrt{2}}{6}M_x & \frac{E_{LH}}{\sqrt{2}} + \frac{\sqrt{2}}{3}M_z & \frac{1}{\sqrt{6}}M_x & -\frac{1}{6}M_x & \frac{E_{LH}}{2} + \Delta_{SO} + \frac{1}{6}M_z \end{pmatrix}$$
$$(3.26)$$

From the expression above, we can extract the 2×2 matrices describing only light hole and split-off states. The two matrices for the spin up $\left| \widetilde{\frac{3}{2}, \frac{1}{2}} \right\rangle$ and down $\left| \widetilde{\frac{3}{2}, -\frac{1}{2}} \right\rangle$ states are

$$H_{2 \times 2}^{\uparrow} = \begin{pmatrix} \frac{1}{6}M_z & -\frac{E_{LH}}{\sqrt{2}} + \frac{\sqrt{2}}{3}M_z \\ -\frac{E_{LH}}{\sqrt{2}} + \frac{\sqrt{2}}{3}M_z & \frac{E_{LH}}{2} + \Delta_{SO} - \frac{1}{6}M_z \end{pmatrix}$$

$$H_{2 \times 2}^{\downarrow} = \begin{pmatrix} -\frac{1}{6}M_z & \frac{E_{LH}}{\sqrt{2}} + \frac{\sqrt{2}}{3}M_z \\ \frac{E_{LH}}{\sqrt{2}} + \frac{\sqrt{2}}{3}M_z & \frac{E_{LH}}{2} + \Delta_{SO} + \frac{1}{6}M_z \end{pmatrix}$$
$$(3.27)$$

By calculating the eigenvectors of the matrices above, we will fit the calculated values of split-off

presence probability as a function of the applied field along z for the pseudo spin-up and pseudo spin-down component of the first Kramers doublet as shown in Fig. 3.10. For our purpose it is more convenient to use the normalized magnetization derived from the division of different effective magnetic field values and the value of field at saturation which is 759.4 T. We will also take into account that light hole contributes 97% to the total envelope, of which 3% leaks outside the dot. For $E_{LH} = 183$ meV, $\Delta_{SO} = 900$ meV and a giant Zeeman shift at saturation $\Delta E_{sat} = 85.5$ meV we fit the split-off presence probability as shown in Fig. 3.14. The analytical model fits good the split-off presence probability and the deviation for small values of magnetization is attributed to the crossing of the pseudo spin-down component with excited states as discussed in the previous section. In the analytical model we do not take into account any excited states and their influence on the ground state. The value for the energy splitting between heavy and light hole which fits the data is larger than expected. For this specific structure, the average value of Q component inside the quantum dot is 77 meV so normally we should expect $E_{LH} \approx 155$ meV. Also we do not know the energy position of heavy hole for this structure since we have calculated only the first six valence band Kramers doublets which are all predominantly light hole type. By being able to calculate the energy levels up to heavy hole would be very useful to compare with $2Q$. Unfortunately, from the perspective of computational demand this would be extremely demanding -if possible at all- since we should calculate levels in the order of 100 meV below the ground state.
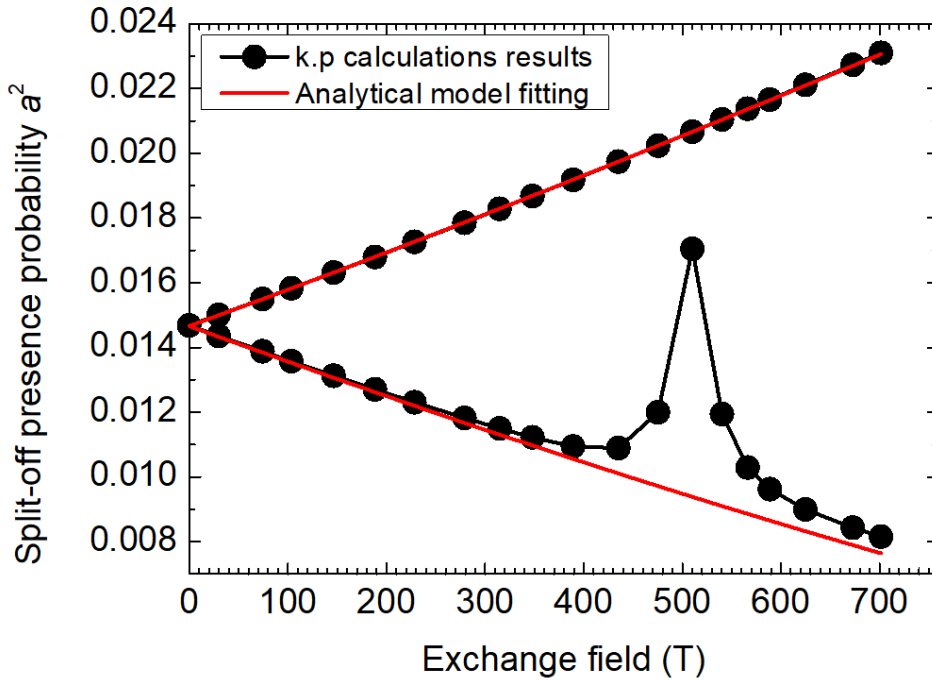
Figure 3.14 – Fitting of the split-off presence probability as a function of the exchange field applied along z axis, for the pseudo spin-up and pseudo spin-down component of the first Kramers doublet.

In general, the analytical model, fits well the split-off presence probability. Again sone has to take into account that it is developed up to first order perturbation for bulk semiconductors. However, it can also be applied for the case of a strongly confined type I quantum dot, as the off-diagonal terms are vanishing, $R = S = 0$.

At this point, we will investigate the effect of general mixing between the hole states and the split-off band on the expectation values of the effective spin operators. For this purpose we will consider a perturbed state comprising of light hole, arbitrarily mixed with split-off band. These states are written

$$\left|\widetilde{\frac{3}{2},\frac{1}{2}}\right\rangle = \sqrt{1-a^2}\left|\frac{3}{2},\frac{1}{2}\right\rangle - a\left|\frac{1}{2},\frac{1}{2}\right\rangle$$

$$\left|\widetilde{\frac{3}{2},-\frac{1}{2}}\right\rangle = \sqrt{1-a^2}\left|\frac{3}{2},-\frac{1}{2}\right\rangle + a\left|\frac{1}{2},-\frac{1}{2}\right\rangle$$

(3.28)

where the unstrained case corresponds to $a = 0$. The expectation values for the effective spin operators for magnetization parallel to z axis are defined through the matrix elements

$$\left\langle\widetilde{\frac{3}{2},\frac{1}{2}}\right|\mathcal{S}_z\left|\widetilde{\frac{3}{2},\frac{1}{2}}\right\rangle = (1-a^2)\left\langle\frac{3}{2},\frac{1}{2}\right|\mathcal{S}_z\left|\frac{3}{2},\frac{1}{2}\right\rangle - 2a\sqrt{1-a^2}\left\langle\frac{3}{2},\frac{1}{2}\right|\mathcal{S}_z\left|\frac{1}{2},\frac{1}{2}\right\rangle$$

$$+ a^2\left\langle\frac{1}{2},\frac{1}{2}\right|\mathcal{S}_z\left|\frac{1}{2},\frac{1}{2}\right\rangle = \frac{1}{6}(-2a^2 - 4\sqrt{2}a\sqrt{1-a^2} + 1)$$

$$\left\langle\widetilde{\frac{3}{2},-\frac{1}{2}}\right|\mathcal{S}_z\left|\widetilde{\frac{3}{2},-\frac{1}{2}}\right\rangle = (1-a^2)\left\langle\frac{3}{2},-\frac{1}{2}\right|\mathcal{S}_z\left|\frac{3}{2},-\frac{1}{2}\right\rangle$$

(3.29)

$$+ 2a\sqrt{1-a^2}\left\langle\frac{3}{2},-\frac{1}{2}\right|\mathcal{S}_z\left|\frac{1}{2},-\frac{1}{2}\right\rangle + a^2\left\langle\frac{1}{2},-\frac{1}{2}\right|\mathcal{S}_z\left|-\frac{1}{2},\frac{1}{2}\right\rangle$$

$$= -\frac{1}{6}(-2a^2 - 4\sqrt{2}a\sqrt{1-a^2} + 1)$$

For magnetization parallel to x axis, the picture becomes more complicated. The components which are coupled by $\hat{\mathcal{S}}_x$ are $\left|\frac{3}{2},\pm\frac{3}{2}\right\rangle$ with $\left|\widetilde{\frac{3}{2},\pm\frac{1}{2}}\right\rangle$ and $\left|\widetilde{\frac{3}{2},\frac{1}{2}}\right\rangle$ with $\left|\widetilde{\frac{3}{2},-\frac{1}{2}}\right\rangle$. The coupling between heavy holes and the mixed light hole - split-off states is

$$\left\langle\frac{3}{2},\frac{3}{2}\right|\mathcal{S}_x\left|\widetilde{\frac{3}{2},\frac{1}{2}}\right\rangle = \sqrt{1-a^2}\left\langle\frac{3}{2},\frac{3}{2}\right|\mathcal{S}_x\left|\frac{3}{2},\frac{1}{2}\right\rangle - a\left\langle\frac{3}{2},\frac{3}{2}\right|\mathcal{S}_x\left|\frac{1}{2},\frac{1}{2}\right\rangle$$

$$= \frac{\sqrt{3}}{6}(\sqrt{1-a^2} + \sqrt{2}a)$$

(3.30)

$$\left\langle\frac{3}{2},-\frac{3}{2}\right|\mathcal{S}_x\left|\widetilde{\frac{3}{2},-\frac{1}{2}}\right\rangle = \left\langle\frac{3}{2},\frac{3}{2}\right|\mathcal{S}_x\left|\widetilde{\frac{3}{2},\frac{1}{2}}\right\rangle = \frac{\sqrt{3}}{6}(\sqrt{1-a^2} + \sqrt{2}a)$$

In our model, we consider that the ground state is a doublet described by Eq. 3.28, where the heavy hole state is energetically remote. As a result its contribution vanishes, consequently we ignore the matrix elements for heavy holes as calculated in 3.30. The spin matrix $\hat{\mathcal{S}}_x$ does not have diagonal elements. In order to describe the effect of light hole split-off mixing on $< S_x >$, we have to either introduce a small magnetic field along x axis and treat the Zeeman shift as a perturbation, or try to find states which diagonalize $\hat{\mathcal{S}}_x$. From the $\vec{k} \cdot \vec{p}$ calculations, we observe that when we apply the exchange field along x, we mix $\left|\frac{3}{2},\pm\frac{1}{2}\right\rangle$ with $\left|\frac{1}{2},\pm\frac{1}{2}\right\rangle$, where the integrated presence probability of $\left|\frac{3}{2},\frac{1}{2}\right\rangle$ is equal to that of $\left|\frac{3}{2},-\frac{1}{2}\right\rangle$ and the one of $\left|\frac{1}{2},\frac{1}{2}\right\rangle$ equal to that of $\left|\frac{1}{2},-\frac{1}{2}\right\rangle$. Ignoring any heavy hole contribution, we define the states

$$\left|\widetilde{\frac{3}{2},\frac{1}{2}}\right\rangle_+ = \frac{1}{\sqrt{2}}\left[\left|\widetilde{\frac{3}{2},\frac{1}{2}}\right\rangle + \left|\widetilde{\frac{3}{2},-\frac{1}{2}}\right\rangle\right]$$

$$\left|\widetilde{\frac{3}{2},-\frac{1}{2}}\right\rangle_- = \frac{1}{\sqrt{2}}\left[\left|\widetilde{\frac{3}{2},\frac{1}{2}}\right\rangle - \left|\widetilde{\frac{3}{2},-\frac{1}{2}}\right\rangle\right]$$

(3.31)

By carrying out the operations, we confirm that these states diagonalize the matrix $\hat{\mathcal{S}}_x$.

$$
\begin{aligned}
{}_+\widetilde{\left\langle \frac{3}{2},\frac{1}{2}\right|}\hat{\mathcal{S}}_x\widetilde{\left|\frac{3}{2},\frac{1}{2}\right\rangle}_+ &= \frac{1}{2}(1-a^2)\left\langle \frac{3}{2},\frac{1}{2}\right|\hat{\mathcal{S}}_x\left|\frac{3}{2},-\frac{1}{2}\right\rangle + \frac{1}{2}a\sqrt{1-a^2}\left\langle \frac{3}{2},\frac{1}{2}\right|\hat{\mathcal{S}}_x\left|\frac{1}{2},-\frac{1}{2}\right\rangle \\
&\quad + \frac{1}{2}(1-a^2)\left\langle \frac{3}{2},-\frac{1}{2}\right|\hat{\mathcal{S}}_x\left|\frac{3}{2},\frac{1}{2}\right\rangle - \frac{1}{2}a\sqrt{1-a^2}\left\langle \frac{3}{2},-\frac{1}{2}\right|\hat{\mathcal{S}}_x\left|\frac{1}{2},\frac{1}{2}\right\rangle \\
&\quad - \frac{1}{2}a\sqrt{1-a^2}\left\langle \frac{1}{2},\frac{1}{2}\right|\hat{\mathcal{S}}_x\left|\frac{3}{2},-\frac{1}{2}\right\rangle - \frac{1}{2}a^2\left\langle \frac{1}{2},\frac{1}{2}\right|\hat{\mathcal{S}}_x\left|\frac{1}{2},-\frac{1}{2}\right\rangle \\
&\quad + \frac{1}{2}a\sqrt{1-a^2}\left\langle \frac{1}{2},-\frac{1}{2}\right|\hat{\mathcal{S}}_x\left|\frac{3}{2},\frac{1}{2}\right\rangle - \frac{1}{2}a^2\left\langle \frac{1}{2},-\frac{1}{2}\right|\hat{\mathcal{S}}_x\left|\frac{1}{2},\frac{1}{2}\right\rangle \\
&= \frac{1}{6}(2-a^2-2\sqrt{2}a\sqrt{1-a^2}) \\[6pt]
{}_+\widetilde{\left\langle \frac{3}{2},\frac{1}{2}\right|}\hat{\mathcal{S}}_x\widetilde{\left|\frac{3}{2},-\frac{1}{2}\right\rangle}_- &= {}_-\widetilde{\left\langle \frac{3}{2},-\frac{1}{2}\right|}\hat{\mathcal{S}}_x\widetilde{\left|\frac{3}{2},\frac{1}{2}\right\rangle}_+ = 0 \\[6pt]
{}_-\widetilde{\left\langle \frac{3}{2},-\frac{1}{2}\right|}\hat{\mathcal{S}}_x\widetilde{\left|\frac{3}{2},-\frac{1}{2}\right\rangle}_- &= -\frac{1}{2}(1-a^2)\left\langle \frac{3}{2},\frac{1}{2}\right|\hat{\mathcal{S}}_x\left|\frac{3}{2},-\frac{1}{2}\right\rangle - \frac{1}{2}a\sqrt{1-a^2}\left\langle \frac{3}{2},\frac{1}{2}\right|\hat{\mathcal{S}}_x\left|\frac{1}{2},-\frac{1}{2}\right\rangle \\
&\quad - \frac{1}{2}(1-a^2)\left\langle \frac{3}{2},-\frac{1}{2}\right|\hat{\mathcal{S}}_x\left|\frac{3}{2},\frac{1}{2}\right\rangle + \frac{1}{2}a\sqrt{1-a^2}\left\langle \frac{3}{2},-\frac{1}{2}\right|\hat{\mathcal{S}}_x\left|\frac{1}{2},\frac{1}{2}\right\rangle \\
&\quad + \frac{1}{2}a\sqrt{1-a^2}\left\langle \frac{1}{2},\frac{1}{2}\right|\hat{\mathcal{S}}_x\left|\frac{3}{2},-\frac{1}{2}\right\rangle + \frac{1}{2}a^2\left\langle \frac{1}{2},\frac{1}{2}\right|\hat{\mathcal{S}}_x\left|\frac{1}{2},-\frac{1}{2}\right\rangle \\
&\quad - \frac{1}{2}a\sqrt{1-a^2}\left\langle \frac{1}{2},-\frac{1}{2}\right|\hat{\mathcal{S}}_x\left|\frac{3}{2},\frac{1}{2}\right\rangle + \frac{1}{2}a^2\left\langle \frac{1}{2},-\frac{1}{2}\right|\hat{\mathcal{S}}_x\left|\frac{1}{2},\frac{1}{2}\right\rangle \\
&= \frac{1}{6}(-2+a^2+2\sqrt{2}a\sqrt{1-a^2})
\end{aligned}
$$

$$(3.32)$$

Using the relations calculated in Eq. 3.29 and Eq. 3.32, for $-1 \le a \le 1$, we plot the dependence of spin on split-off presence probability as shown in Fig. 3.12, in the beginning of this section. The first thing someone notices is that even for a small mixing between light hole and split-off the effective spin value is heavily affected. This is in agreement with the results obtained from numerical calculations. For a split-off presence probability $a^2 = 0$ we restore the expected spin values $<S_z> = 1/6$ and $<S_x> = 1/3$.

Of course it is unrealistic to discuss cases with values of a^2 above a few percent and spin dependence for $a^2 = 0$ to 1 is shown for demonstration purposes.

In Fig. 3.15 b) we present the calculated spin expectation values $<S_z>$ at 0 T and 701.5 T and we compare it with the analytical model. The red circles correspond to the value of spin near the center of the quantum dot and with the blue squares we depict the values of spin affected by the small leaking of the envelope. At 0 T spin value is determined only by strain induced mixing between light hole and split-off. We confirm that for vanishing field, the analytical model is in perfect agreement with the calculated values. Although for the development of the analytical model we didn't take into account second order effects including field induced mixing, we see that even at high field it is in good agreement with the numerical results. In the same graph we also present the values of spin influenced by the envelope leaking in order to compare with the spin if the envelope was 100% confined in the dot. Of course it is of no use to compare with the analytical model as it is also developed for a fully confined state.
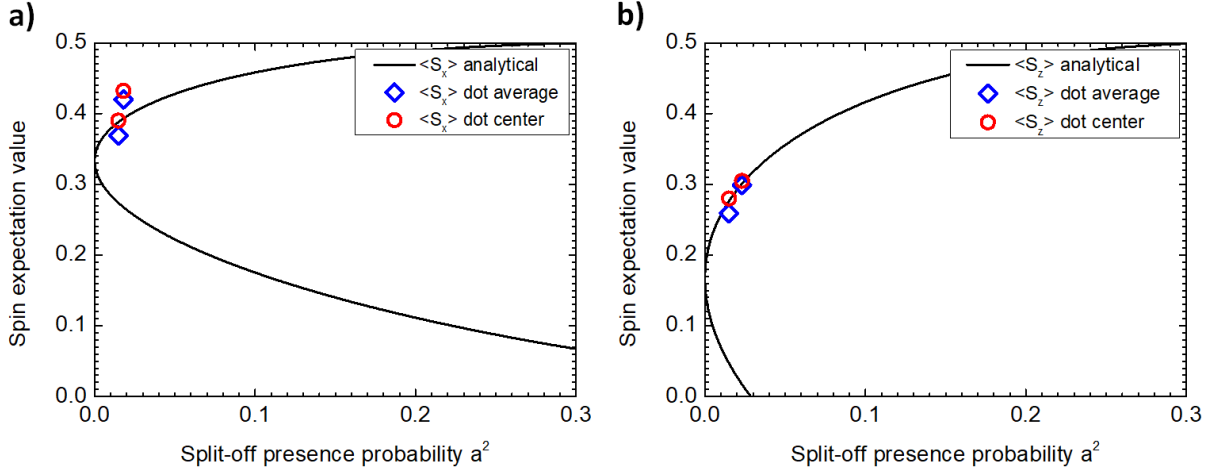
Figure 3.15 – Calculated expectation values of spin $< S_z >$ for a magnetic field applied parallel a) and S_x for a magnetic field applied perpendicular b) to the nanowire axis as a function of split-off band presence probability and comparison with the analytical model at 0 T and 701.5 T. For comparison between them we present both the spin values considering 100% confinement in the dot and those calculated by taking into account the envelope leaking. For both orientations, small values of spin correspond to 0 T and large values of spin at 701.5 T.

For the strong type I case we discuss here, the influence of leaking is not that prominent, but we will see in the following sections that be decreasing confinement spin values get heavily affected

In Fig. 3.15 a), we present the spin expectation value $< S_x >$ at 0 T and 701.5 T and we compare with the graph obtained from the analytical model, as we did for $< S_z >$. In this case again and for vanishing field the value obtained from the $k \cdot p$ calculation is in good agreement with the one given by the analytical function. At large fields however, spin expectation value as a function of split-off presence probability is much larger for the numerical calculation in comparison to the analytical model. A possible explanation is that for the construction of the analytical relation for $< S_x >$ as a function of split-off presence probability a^2, we do not take into account any heavy hole contribution. This model is developed for a state which is a mixture of light hole with split-off band, while adding also the contribution for heavy hole is non trivial. It is obvious that spin expectation values $< S_x >$ for a field applied perpendicular to the quantum dot quantization axis are influenced by field induced mixing between heavy and light hole. The reason why this mixing affects so strongly $< S_x >$ is not clear yet, however the difference between calculated values and those obtained by the analytical function ranges from 4 % at $B_{Mn} = 29.8$ T to 6 % at $B_{Mn} = 701.5$ T, which overall is not that large.

3.5 Weakly confined type I dot

After understanding the effect of envelope leaking and the mixing between light hole and split-off, we continued the series of numerical calculations by studying a CdTe quantum dot in a ZnTe-ZnMgTe core-shell nanowire with a reduced type I chemical valence band offset of 20 meV. For the nanowire quantum dots studied experimentally which will be discussed in the following chapter we expect to have a similar offset.

3.5.1 Flat dot

As with the strong type I quantum dot, we will begin by discussing the flat dot case, characterized by $L_{QD}/D_{QD} = 0.5$. The contribution of each hole state and the corresponding percentage localized inside the dot, are given in the table below.

Table 3.4 – The presence probability of heavy hole, light hole and split-off, with their respective percentages inside the quantum dot, for a 20 meV weak type I flat CdTe quantum dot in a ZnTe-ZnMgTe core-shell nanowire.

P_{HH}	HH_{id}	P_{LH}	LH_{id}	P_{SO}	SO_{id}
0.904	82.4%	0.091	44%	0.005	37.5%

As regards the total envelope function, 79.2% is confined inside the dot. Comparing to the strong type I quantum dot, we observe that leaking in this case is stronger.

In Fig. 3.16 we plot the Zeeman shift of the pseudo spin-up component of the Kramers doublet for an exchange field applied perpendicular a) and parallel b) to the dot quantization axis.
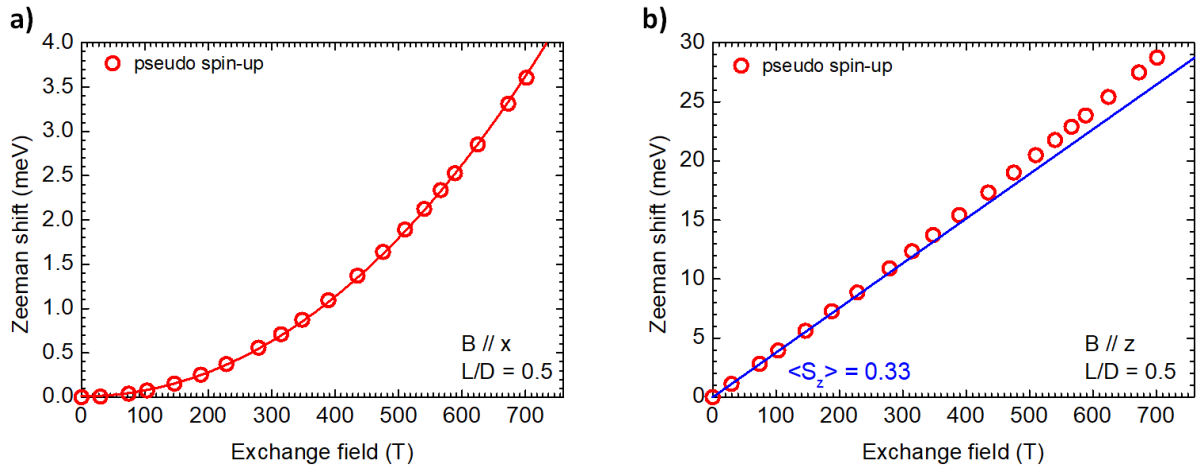

Figure 3.16 – Zeeman shift of the pseudo spin-up component of the first Kramers doublet as a function of the exchange field used at calculations for a 20 meV type I flat quantum dot with $L_{QD}/D_{QD} = 0.5$ applied perpendicular a) and parallel b) to the dot quantization axis.

The reason we present only the pseudo spin-up is due to the fact that by reducing confinement, the energy difference between the calculated states decreases. As a result, Zeeman shift of the pseudo spin-down component crosses fast with that of excited states, consequently it becomes more difficult to trace it by increasing field. The reader can find the figures with the Zeeman shift of all levels for both orientations of magnetic field in Appendix C. For the field applied along x, the evolution of energy as a function of the exchange field is similar to that of the strong type I case, with a weak shift for large values of field. When we apply the exchange field along z axis though, the picture changes in comparison to type I. The first thing we notice is that the shift is weaker at large fields, while the deviation from linear behaviour is stronger. Also, the value of spin expectation value decreases significantly. This again is explained by considering the increased leaking of the different envelope components towards the ZnTe core. For this case we do not show the spin expectation value projection colormap, since it is identical to that of the strong type I and it does not provide any new information. It is more useful to discuss directly the superposition of the total envelope and spin expectation value projections profiles as shown in Fig. 3.17.

As already mentioned, spin expectation values inside the dot do not change between strong and weak type I. There is a plateau near the center of the dot where spin is constant and equal to $\frac{1}{2}$ while as we move away from it spin decreases and at CdTe - ZnTe interface it is equal to 0.44. The envelope function profile though is different. First of all the leaking due to weakening of confinement becomes evident and the fact that it is not symmetric in the two sides, is an
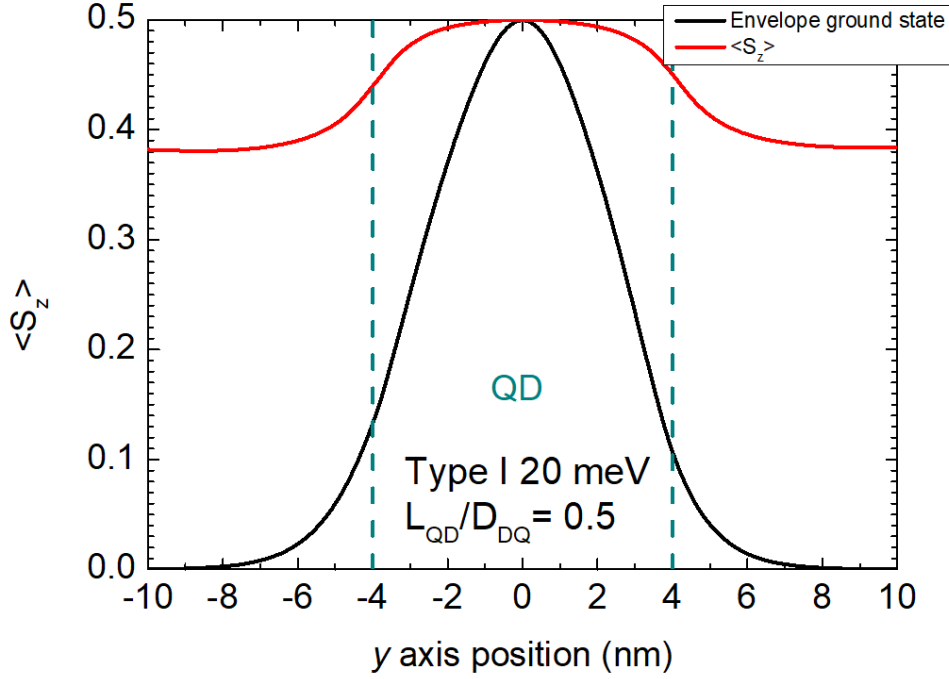
Figure 3.17 – Cross section of the projections of spin component $< S_z > (\vec{r})$ and the total envelope function along y axis for a 20 meV type I flat quantum dot with $L_{QD} = 4nm$

indication that the envelope begins to get affected by the cubic field. This effect can also be seen in Fig. 2.24 where the colormaps of envelope projections for the different hole states are shown. As a final remark concerning spin, by averaging the values inside the dot for the 79.3 % of the total envelope which is confined in it we retrieve the value obtained from the slope.

3.5.2 Elongated dot

In this section we will continue the discussion by investigating the spin properties of an elongated CdTe quantum dot with $L_{QD}/D_{QD} = 2.25$ in a ZnTe-ZnMgTe core-shell nanowire, with a weak type I valence band offset between the dot and the core. In the table below we summarize the integrated presence probability for each hole state and the percentage of confinement inside the quantum dot.

Table 3.5 – The presence probability of heavy hole, light hole and split-off, with their respective percentages inside the quantum dot, for a 20 meV weak type I elongated CdTe quantum dot in a ZnTe-ZnMgTe core-shell nanowire.

P_{HH}	HH_{id}	P_{LH}	LH_{id}	P_{SO}	SO_{id}
0.144	8.2%	0.844	68.3%	0.012	52.5%

For the total envelope function, 59.8% is confined inside the dot. In this case, confinement is even weaker and this can be also confirmed from the envelope presence probabilities colormaps as shown in Fig. 2.26.

Similarly to all studied cases, we applied an exchange field along two directions and in Fig. 3.18 a) we present the Zeeman shift for a field applied perpendicular to the dot quantization axis and in Fig. 3.18 b) the shift for a field applied parallel.

Comparing with the strong type I, for both cases the Zeeman shift is weaker and the deviation from linear behaviour even stronger. As we have shown already, spin expectation values decrease
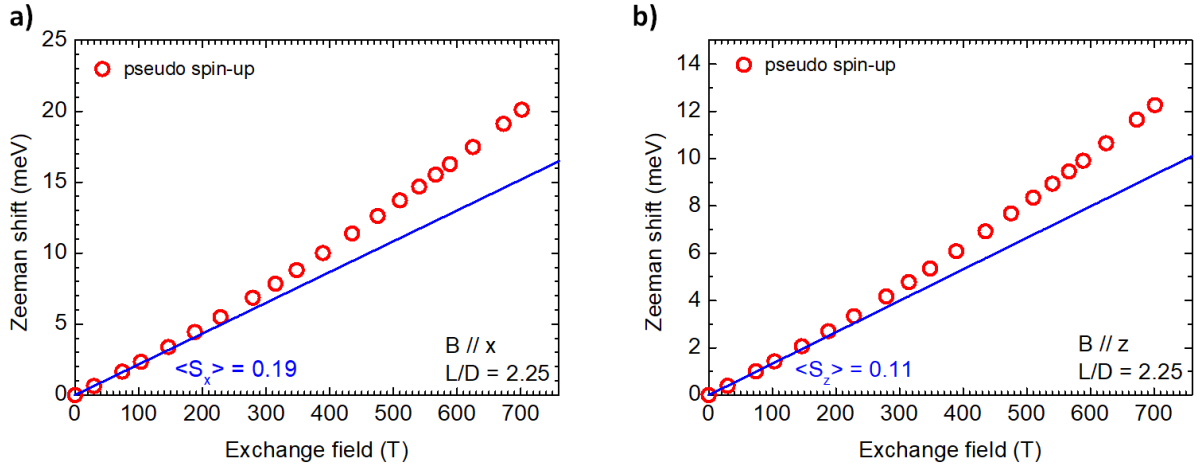
Figure 3.18 – Zeeman shift of the pseudo spin-up component of the first Kramers doublet as a function of the exchange field used at calculations for a 20 meV weak type I elongated quantum dot with $L_{QD}/D_{QD} = 2.25$ applied perpendicular a) and parallel b) to the dot quantization axis.

due to leaking and for the flat dot case they are in agreement with the presence probability of each envelope component inside the quantum dot. With the elongated dot though we cannot have a quantitative estimation of spin expectation values by looking only at envelope leaking. This is due to the fact that the relation between spin expectation values and split-off presence probability is non-linear.

Obviously envelope leaking towards the barrier in combination with mixing will affect the spin distribution inside the dot. In Fig. 3.19 a) we present the colormap of the spin expectation value projection for the pseudo spin-up component and in Fig. 3.19 b) for the pseudo spin-down for $B_{Mn} = 29.8$ T parallel to z axis.

Near the center of the quantum dot, where presence probability is maximum, spin expectation values are $< S_z >= 0.27$ and $< S_z >= $ -0.27 for the pseudo spin-up and spin-down respectively which are similar to the strong type I case and in agreement to the integrated presence probability of split-off band. By looking carefully at the figures, it seems that spin values decrease faster in comparison to strong type I case, something which is confirmed by plotting its profile along y axis as shown in Fig. 3.20.

The in plane confinement of the envelope is strong in this case and the leaking is predominantly from the poles of the quantum dot. This is better visualized in Fig. 2.26 where we also see that the heavy hole component tends to expand on xy plane and leak also from the side of the quantum dot. As a result, there is a region near the CdTe-ZnTe interface where the presence probability of heavy hole dominates over that of light hole. As mentioned before, in that region R is non vanishing like in the center of the quantum dot, consequently light hole gets mixed with the heavy hole component of opposite spin sign. This results the switching of spin sign from positive to negative values and vice versa for the pseudo spin-up and spin-down Kramers doublet components. The part of heavy hole which leaks along xy plane starts to adopt the 3-fold symmetry of the strain and piezoelectric potential outside the dot. This explains why spin values in that region start to have the same symmetry.

As regards spin expectation values along x axis $< S_x > (\vec{r})$, the picture becomes more complicated. In Fig. 3.21 a) we present the colormap of spin expectation value $< S_x > (\vec{r})$ projection for the pseudo spin-up component and in Fig. 3.21 b) for the pseudo spin-down. As regards spin values near the quantum dot center they are $< S_x >= 0.38$ and $< S_x >= -0.38$ for the pseudo spin-up and spin-down respectively. These values are similar to those obtained for the strong type I case. Regarding spin distribution inside the dot, also the behaviour is
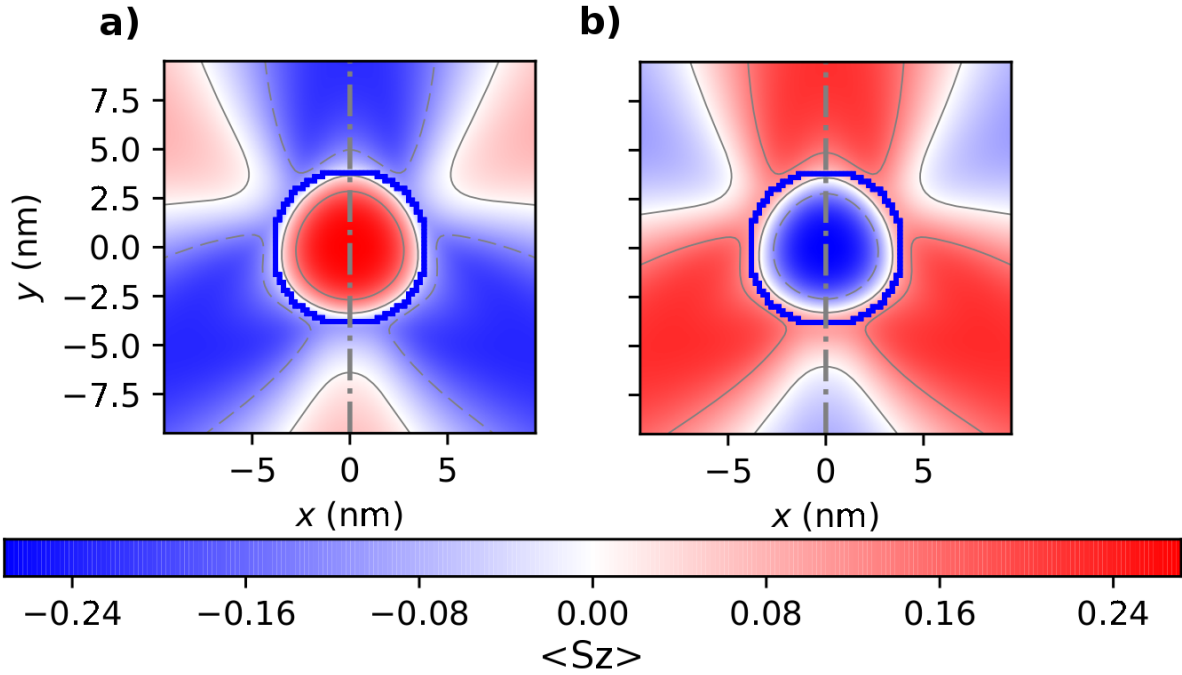
Figure 3.19 – Colormap of the spin expectation value $< S_z > (\vec{r})$ projection on xy plane for the pseudo spin-up component of the Kramers doublet a) and pseudo spin-down b) at $B_{Mn} = 29.8$ T for a weak type I elongated quantum dot
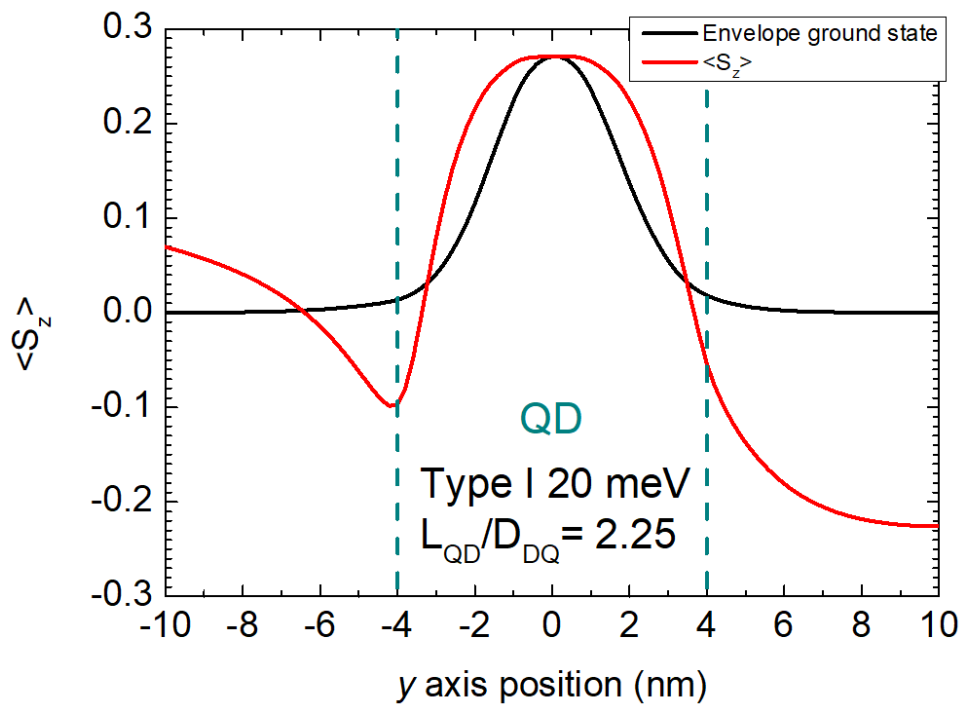
Figure 3.20 – Profile of the projections of spin component $< S_z > (\vec{r})$ and the total envelope function along y axis for a 20 meV weak type I elongated quantum dot with $L_{QD} = 18nm$, at $B_{Mn} = 29.8$ T.

similar, as along x axis spin decreases and along y it increases, taking maximum values near the interface between CdTe and ZnTe. The big difference here in comparison to strong type I

case, is the braking of symmetry along y axis.
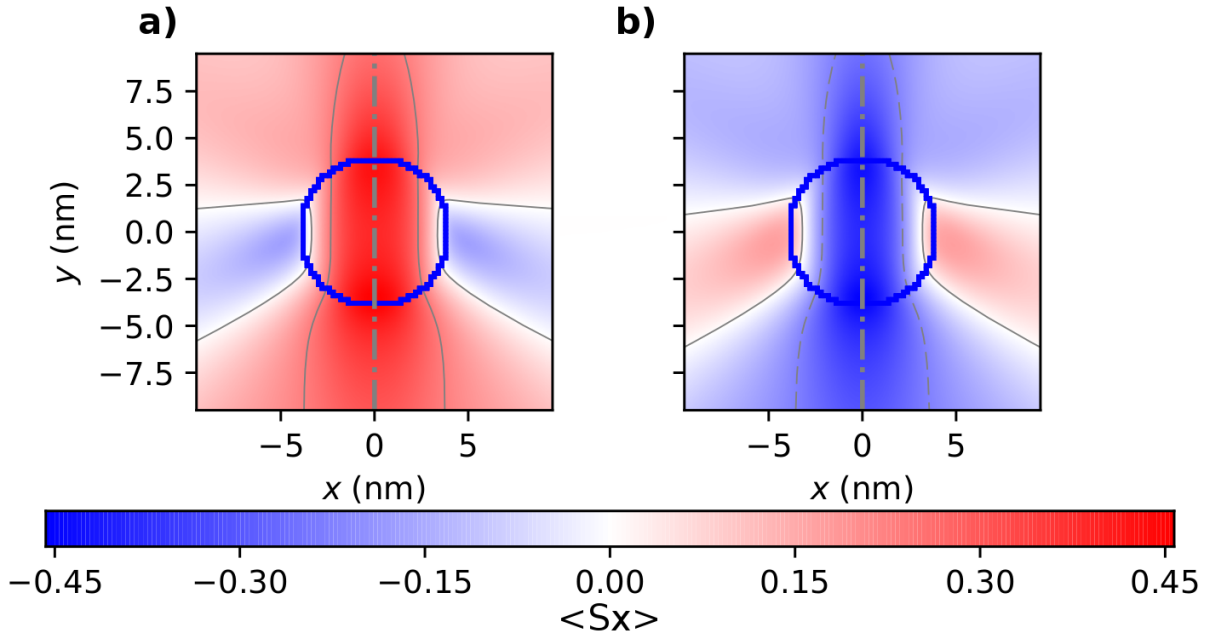
Figure 3.21 – Colormap of the spin expectation value $< S_x > (\vec{r})$ projection on xy plane for the pseudo spin-up component of the Kramers doublet a) and pseudo spin-down b) at $B_{Mn} = 29.8$ T for a weak type I elongated quantum dot

This is shown in Fig. 3.21, where the spin values in the two local maxima are $< S_x >= 0.45$ and $< S_x >= 0.42$.

Figure 3.22 – Cross section of the projections of spin component $< S_x > (\vec{r})$ and the total envelope function along y axis for a 20 meV type I elongated quantum dot with $L_{QD} = 4nm$

The breaking of symmetry is attributed to the leaking of the envelope along xy plane, which

tends to adopt the three fold symmetry as mentioned earlier. Also we recall to the reader, that all total angular momentum components are mixed and the increase of spin towards values close to $\frac{1}{2}$ is an indication of a heavy hole component with the spin 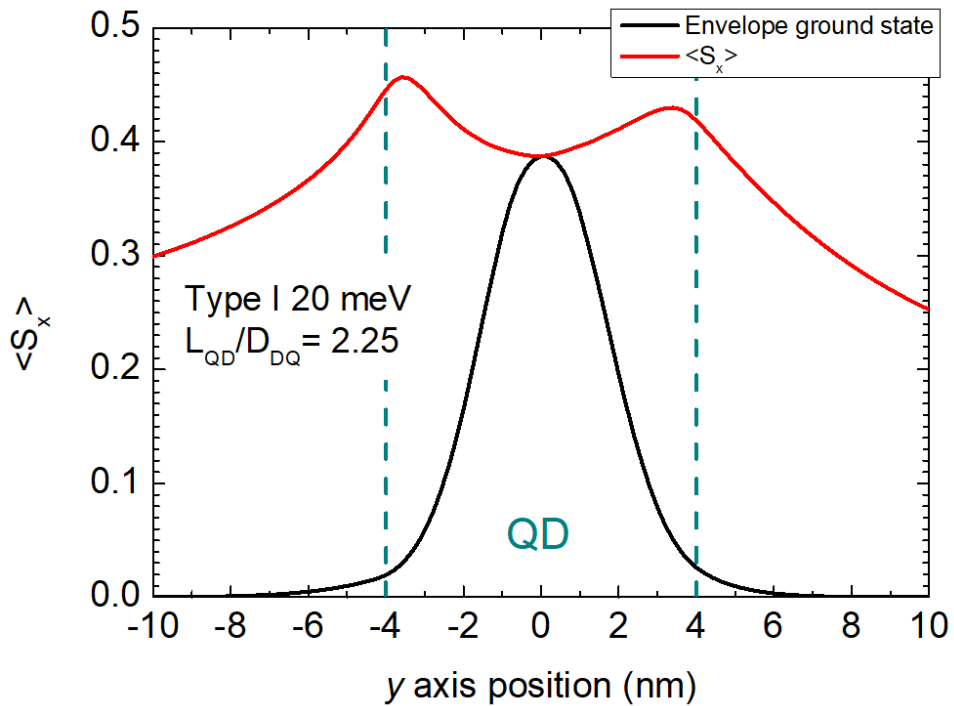lying on xy plane. As we take the cross-section along y axis, in one side the presence probability of light hole (and by extent of total envelope function) is stronger than in the other, as a result spin values are smaller. Outside the quantum dot, there are two pockets with opposite spin signs, similar to the strong type I case. In the context of this discussion however we will focus on spin properties inside the quantum dot and we will ignore any effects outside.

In Fig. 3.23 a) we plot the average expectation value of spin $< S_x >$ for $B_{Mn}//x$ as a function of split-off integrated presence probability and in Fig. 3.23 b) the expectation value of spin $< S_z >$ for $B_{Mn}//z$. As predicted already, spin values increase, with that of $< S_z >$ being stronger than $< S_x >$. From these observations we understand that envelope confinement also changes inside the dot by increasing field. It is expected that the exchange field "digs" deeper the confinement potential, thus increasing the valence band offset between CdTe and ZnTe. This was not very obvious in the 200 meV type I case, as confinement was already strong.
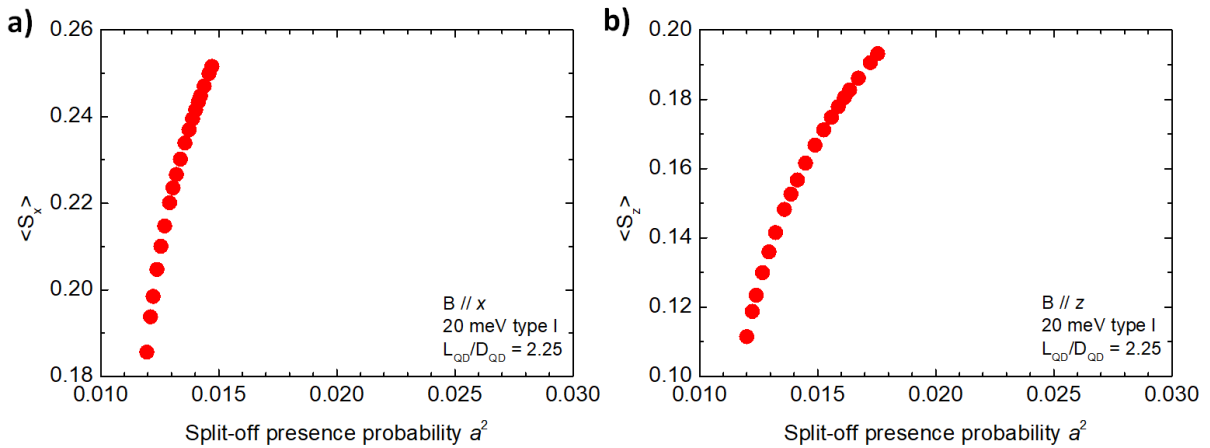

Figure 3.23 – Spin expectation values for magnetic field perpendicular a) and parallel b) to the nanowire quantization axis as a function of split-off presence probability for the pseudo spin-up component of the Kramers doublet for a 20 meV weak type I quantum dot.

We confirm that the exchange field restores confinement of the pseudo spin-up state, by plotting the percentage of the total envelope inside the quantum dot as a function of it, shown if Fig. 3.24.

Going from 0 T, where leaking is close to 40%, to 701.5 T, we restore confinement by 12% for field applied along z and 15% for the field along x. This is also consistent to the fact that $< S_x >$ increases more than $< S_z >$. This observation is of major importance as it can help us interpret experimental data, for which until recently we did not consider any difference in confinement by increasing the applied magnetic field. At this point it is interesting to mention that confinement increases for all envelope components apart from that corresponding to split-off $|1/2, -1/2\rangle$. For this state, the percentage inside the quantum dot actually decreases with field for both pseudo spin-up and pseudo spin-down components of the Kramers doublet. The reason why this happens is not clear and requires further investigation.

In order to conclude the discussion we present in one figure spin as a function of split-off as predicted by the analytical model, the values obtained from numerical calculations and the same values modified due to leaking of the envelope. Concerning the values at 0 T near the center of the dot (red circles), they are in perfect agreement with the analytical model for both $< S_x >$ and $< S_z >$ as shown in Fig. 3.25 a) and Fig. 3.25 b) respectively. At 701.5 T, where also the split-off presence probability is maximum $< S_z >$ is still in good agreement with the analytical model, while $< S_x >$ not. This is expected since as we already mentioned, this specific model
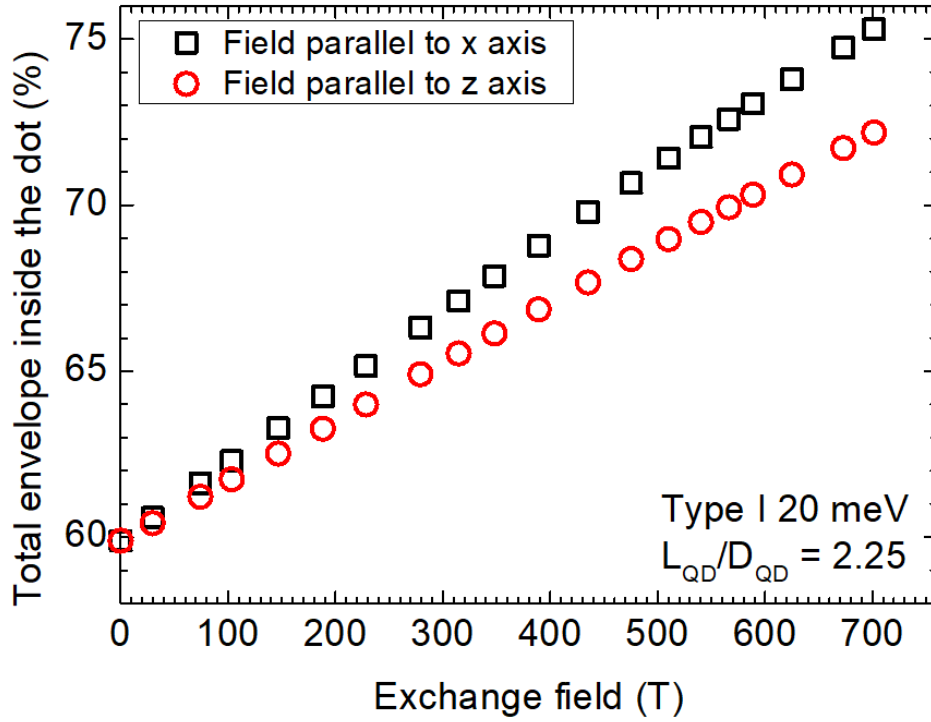
Figure 3.24 – Variation of confinement for the pseudo spin-up component of the Kramers doublet of a weak type I elongated quantum dot, with the magnetic field applied both along x and z axis.
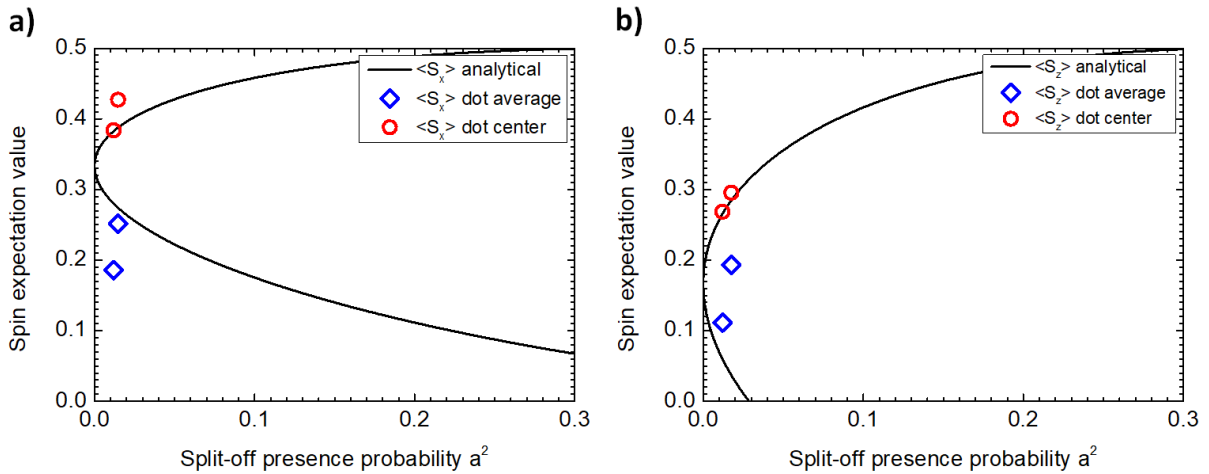
Figure 3.25 – Calculated expectation value of spin $< S_x >$ and $< S_z >$ for a vanishing field and at 701.5 T applied respectively perpendicular a) and parallel b) to the nanowire axis as a function of split-off band presence probability and comparison with the analytical model. For both orientations, small values of spin correspond to 0 T and large values of spin at 701.5 T.

does not take into account second order effects ot the coupling with heavy holes. The blue squares correspond to the average value of spin inside the dot including also the leaking of the envelope, which are also equal to those obtained from the slope of Zeeman shift for two consecutive points. The reason we present them is to compare with the values near the center of the dot considering full confinement and show the influence of leaking. Of course there is no point comparing to the analytical model as it is developed for a fully confined state.

3.6 Weak type II dot

After discussing the effect of magnetic field on a strong type I nanowire quantum dot and demonstrating both numerically and analytically the effect of mixing between light hole and split-off on spin values, we want to extend our study to the influence of an applied magnetic field on a weak type II quantum dot.

3.6.1 Flat dot

In this section we will investigate the effect of reduced valence band offset on Zeeman shift and spin in a flat quantum dot with $L_{QD}/D_{QD} = 0.5$. The dimensions and geometry of this heterostructure are identical to the structure studied in the first section with the difference that the chemical valence band offset is 20 meV type II. In the following table we present the integrated presence probability and the percentage of each hole state confined in the dot at 0 T.

Table 3.6 – The presence probability of heavy hole, light hole and split-off, with their respective percentages inside the quantum dot, for a 20 meV weak type II flat CdTe quantum dot in a ZnTe-ZnMgTe core-shell nanowire.

P_{HH}	HH_{id}	P_{LH}	LH_{id}	P_{SO}	SO_{id}
0.876	61%	0.119	8%	0.005	10%

Totally, 55 % of the envelope function is inside the dot, while 45 % leaks to the ZnTe nanowire core. As expected, leaking in this case is much stronger and as a consequence we expect to further affect both Zeeman shift and spin values. As we have shown in the previous chapter, in a type II structure, the energy difference between calculated levels becomes smaller and in some cases states become quasi-degenerate. As a result, Zeeman shift of excited states will have a stronger influence to that of ground state in comparison to type I structure. This is shown in the figures of Appendix D. Again we will mostly focus the discussion on the pseudo spin-up component of the Kramers doublet.
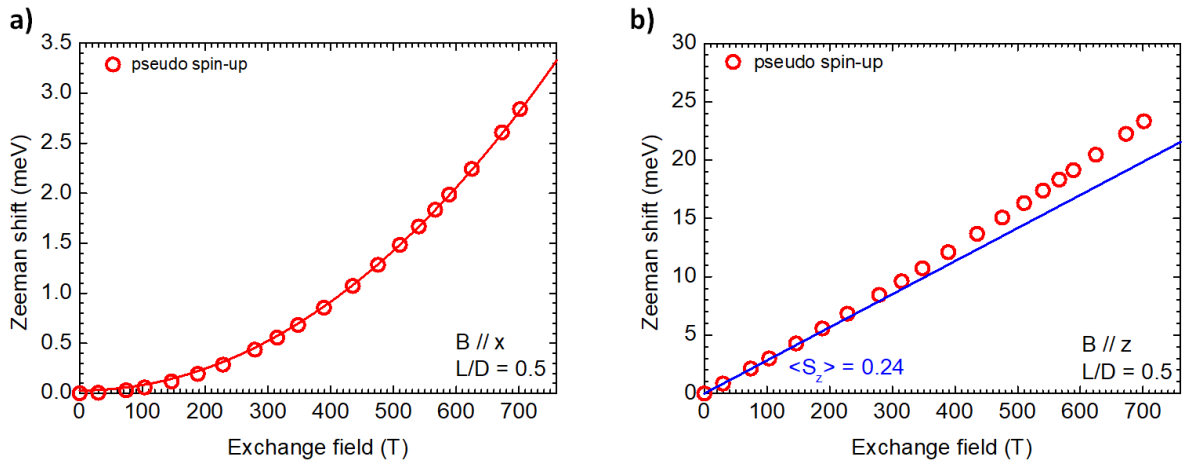
Figure 3.26 – Zeeman shift of the spin-up component of first Kramers doublet as a function of the exchange field used as calculation input applied perpendicular a) and parallel b) to the quantization axis of a 20 meV type II flat quantum dot with $L_{QD} = 4$ nm

In Fig. 3.26 a) we present the plot of Zeeman shift as a function of the exchange field applied perpendicular to the nanowire axis. Here, the behaviour is similar to the one observed

in both strong and weak type I quantum dots and the data can be perfectly fitted with a third order polynomial. In Fig. 3.26 b) we present the Zeeman shift for an exchange field applied parallel to the nanowire axis. Zeeman shift is weaker and the deviation from linear behaviour even stronger. In a similar way as for the type I quantum dots, from the slope of this graph we calculated the expectation value of spin $< S_z > = 0.24$ at vanishing field. This value is again in very good agreement with the percentage of envelope which is confined in the dot and the mixing between different hole states. As discussed earlier, we can also calculate spin expectation values by plotting their distribution colormaps using Eq. 3.4 and then averaging inside the dot. For a flat dot studied here we do not expect any major differences in comparison to the colormaps of a strong type I and we present them only for demonstration purposes.
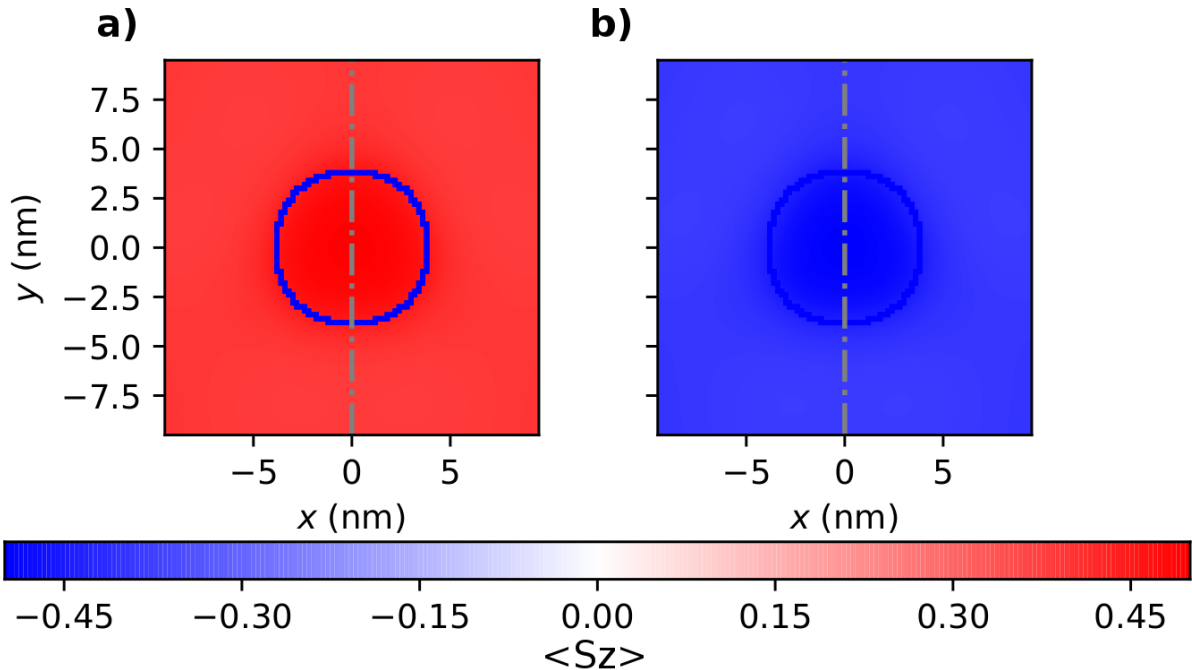

Figure 3.27 – Projection of $< S_z > (\vec{r})$ expectation value for a flat CdTe quantum dot in a ZnTe-ZnMgTe core-shell nanowire at $B_{Mn} = 29.8$ T for the pseudo spin-up component a) and pseudo spin-down b) of the first calculated Kramers doublet.

In Fig. 3.27 a) we present the projection of spin expectation value $< S_z > (\vec{r})$ for the pseudo spin-up component and in Fig. 3.27 b) for the pseudo spin-down of the Kramers doublet, at $B_{Mn} = 29.8$ T. For such a small value of magnetic field both levels remain unaffected by the Zeeman shift of excited states. Inside the dot and in the vicinity of its center, spin vales are $S_z = 0.5$ and $S_z = -0.5$ for pseudo spin-up and spin-down respectively. As we move away from the center of the dot, spin values decrease and on average inside the dot is $< S_z > = 0.48$. This of course without taking into account the envelope leaking.

The variation of spin becomes more clear by plotting the profile of its projection along y axis, as shown in Fig. 3.28. At the same figure we superimpose also the projection of the envelope where we observe that the expected profile of an s-like orbital gets even more distorted due to leaking. As a reminder, in Fig. 2.39 we can see the effect of envelope leaking and breaking of symmetry due to the strain. By taking into account only the part of the envelope which is confined inside the dot, we retrieve the spin expectation value $< S_z > = 0.25$, which is similar to what we calculated previously. From the Zeeman shift presented in Fig. 3.26 b), we observe for the first time a strong effect of field on confinement, for a structure containing a flat quantum dot, as the energy shift deviates strongly from linear behaviour.

For the strong type I flat dot for $B_{Mn}//z$ and from 0T to 701.5 T, the difference in confinement
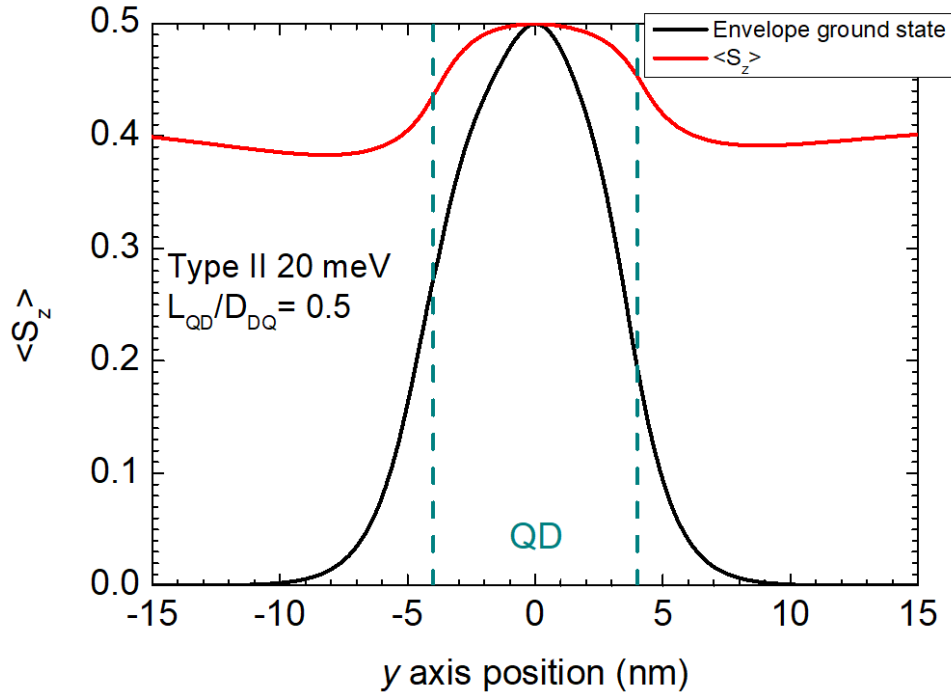
Figure 3.28 – Profile of the projections of spin component $< S_z > (\vec{r})$ and the total envelope function along y axis for a 20 meV type II flat quantum dot with $L_{QD} = 4nm$
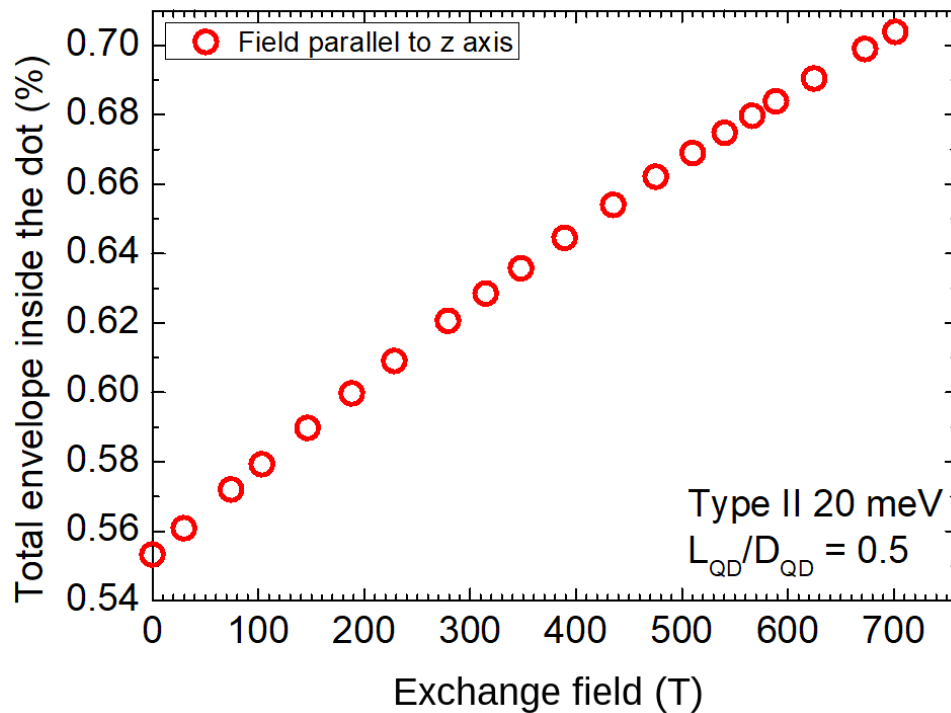
Figure 3.29 – Variation of confinement for the pseudo spin-up component of the Kramers doublet of a weak type II flat quantum dot, with the magnetic field applied parallel to z axis.

was only 1%. For the weak type I it became larger, at 10% and for the type II, the difference is 15%, as we see in Fig. 3.29.

3.6.2 Elongated quantum dot

In this section we discuss the effect of magnetic field in a 20 meV type II elongated CdTe quantum dot in a ZnTe-ZnMgTe core-shell nanowire with $L_{QD}/D_{QD} = 2.25$. In the table below, we show the integrated presence probability and the percentage of each hole state, confined inside the quantum dot.

Table 3.7 – The presence probability of heavy hole, light hole and split-off, with their respective percentages inside the quantum dot, for a 20 meV weak type II elongated CdTe quantum dot in a ZnTe-ZnMgTe core-shell nanowire.

P_{HH}	HH_{id}	P_{LH}	LH_{id}	P_{SO}	SO_{id}
0.202	5%	0.787	50%	0.011	36%

In total, 41 % of the envelope function is inside the dot. As a reminder to the reader, the envelope components for this structure at 0 T are shown in Fig. 2.40. From these numbers we confirm that envelope leaking is larger in comparison to the flat quantum dot and mixing with split-off is stronger.

In Fig. 3.30 a) we present the Zeeman shift for the pseudo spin-up component of the Kramers doublet for the exchange field applied perpendicular to the dot quantization axis and in Fig. 3.30 b) for the exchange field applied parallel.
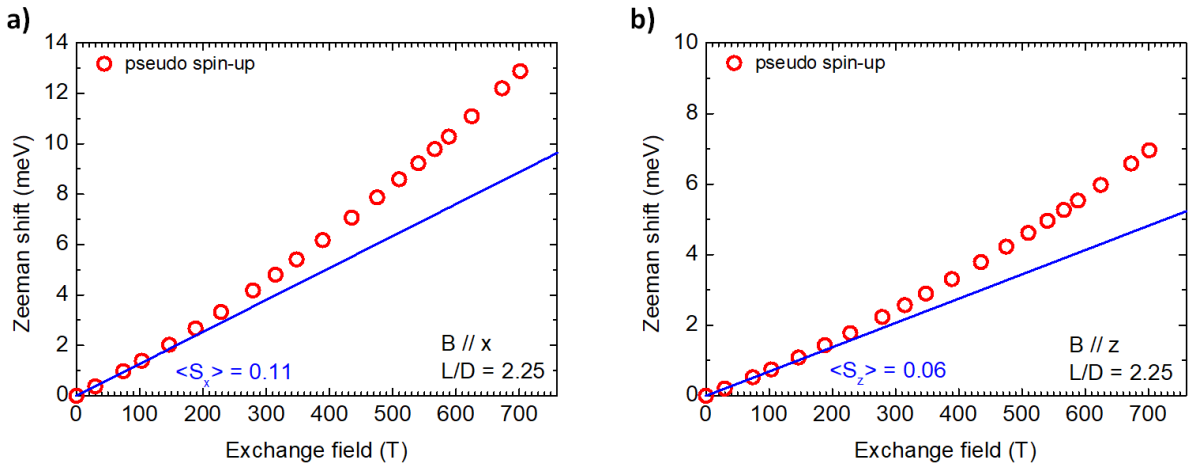
Figure 3.30 – Zeeman shift for a 20 meV type II elongated quantum dot with $L_{QD}/D_{QD} = 2.25$ as a function of the exchange field, oriented parallel to x axis a) and z axis b).

It is not of surprise that in both cases, Zeeman shift is even weaker and that the deviation from a linear behaviour is even stronger. From the Zeeman shift slopes and at vanishing field, we calculate the spin expectation values for both directions x and z, which are respectively $< S_x >= 0.11$ and $< S_z >= 0.06$.

In Fig. 3.31 we present the colormap of the projection of spin expectation value for the pseudo spin-up a) and pseudo spin-down b) component of the first Kramers doublet. Near the center of the quantum dot, where the projection of envelope presence probability is maximum, spin expectation value for the pseudo spin-up component is $< S_z > = 0.26$, while as we move towards ZnTe barrier, spin values decrease abruptly. This is depicted in Fig. 3.32, where the profile of spin projection is superimposed with the envelope cross section along y axis. Regarding the pseudo spin-down component, near the quantum dot center it is $< S_z >=-0.26$ and the spin texture in absolute values is the same with that of pseudo spin-up. For simplicity reasons again, we will focus the discussion on the pseudo spin-up component. At ZnTe-CdTe

Figure 3.31 – Projection of $< S_z > (\vec{r})$ expectation value for an elongated CdTe quantum dot in a ZnTe-ZnMgTe core-shell nanowire for the pseudo spin-up component a) and pseudo spin-down b) of the first calculated Kramers doublet at $B_{Mn} = 29.8$ T.
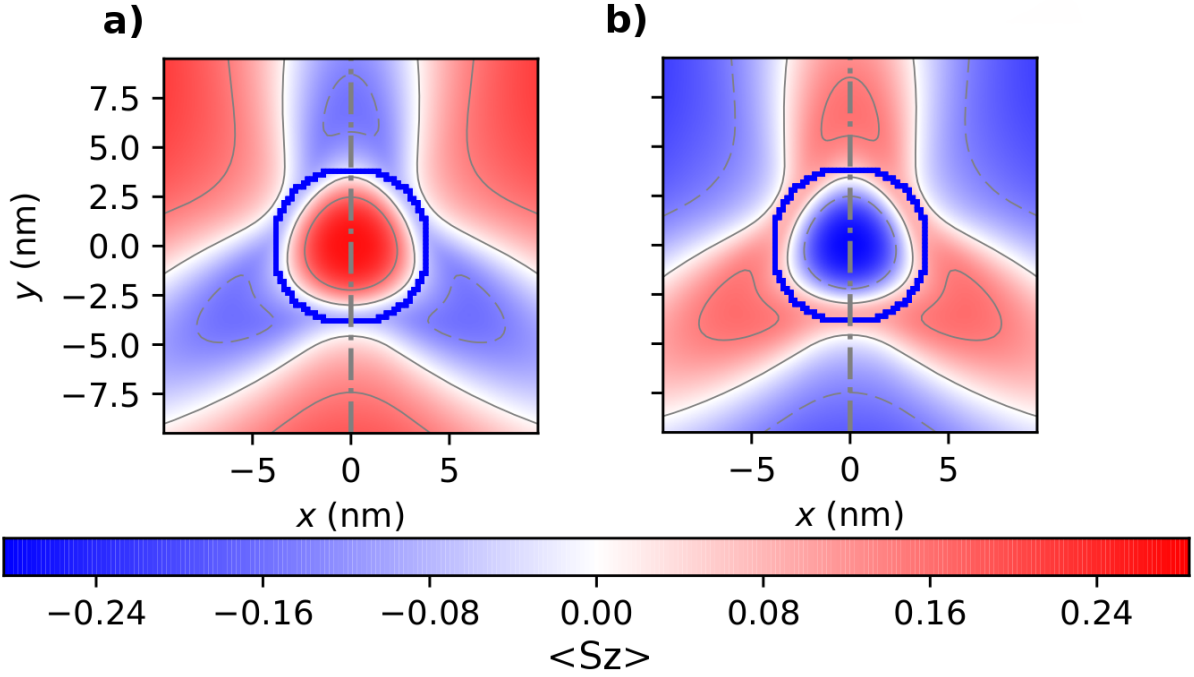
interface spin becomes negative and outside the dot, there are pockets adopting a three fold symmetry with opposite spin signs. This is again attributed to envelope leaking and the mixing between heavy hole and light hole with opposite spin signs, due to the non-vanishing R term outside the quantum dot. If we look back at Fig. 2.40, we see that the heavy hole component of the envelope function has the same symmetry with the negative spin component projection of Fig. 3.31 a). The average spin value in that region is $< S_z >= -0.08$ which is in a good agreement with the percentage of heavy hole leaking outside the dot and its contribution to the total envelope. Also the positive sign component adopts a three fold symmetry similar to that of a light hole leaking around the equator of an elongated quantum dot in a weakly confined system.

As regards spin expectation values for a magnetic field applied along x axis, $< S_x > (\vec{r})$ distribution is less uniform inside the dot and near the interface of CdTe and ZnTe there are pockets where spin sign gets reversed for both spin-up 3.33 a) and spin-down 3.33 b) components of the Kramers doublet. Outside the dot and similar to what we observed for the weak type I case, for both components of the Kramers doublet, there are only two pockets where spin sign gets reversed. In principle it is more difficult to correlate the spin expectation values projections with the envelope presence probability for this case, but if we take the average spin value in the vicinity of the center of the quantum dot, considering also the envelope presence probability we find $< S_x >= 0.37$. This value is in good agreement to what is expected according to split-off presence probability.

Similar to the type I case, split-off presence probability increases as a function of the applied magnetic field for both orientations. As a result spin expectation values also increase and this is shown at Fig. 3.35 a) for B applied perpendicular and 3.35 b) for B applied parallel to the wire axis.

For the weak type II case, both expectation values, $< S_x >$ and $< S_z >$ increase faster in comparison to type I case. Comparing though the calculated values to those obtained from the analytical model as a function of split-off presence probability the difference never exceeds 4%.

Figure 3.32 – Profile of the projections of spin component $< S_z > (\vec{r})$ and the total envelope function along y axis for a 20 meV type II CdTe elongated quantum dot with $L_{QD} = 18$ nm in a ZnTe-ZnMgTe core-shell nanowire.
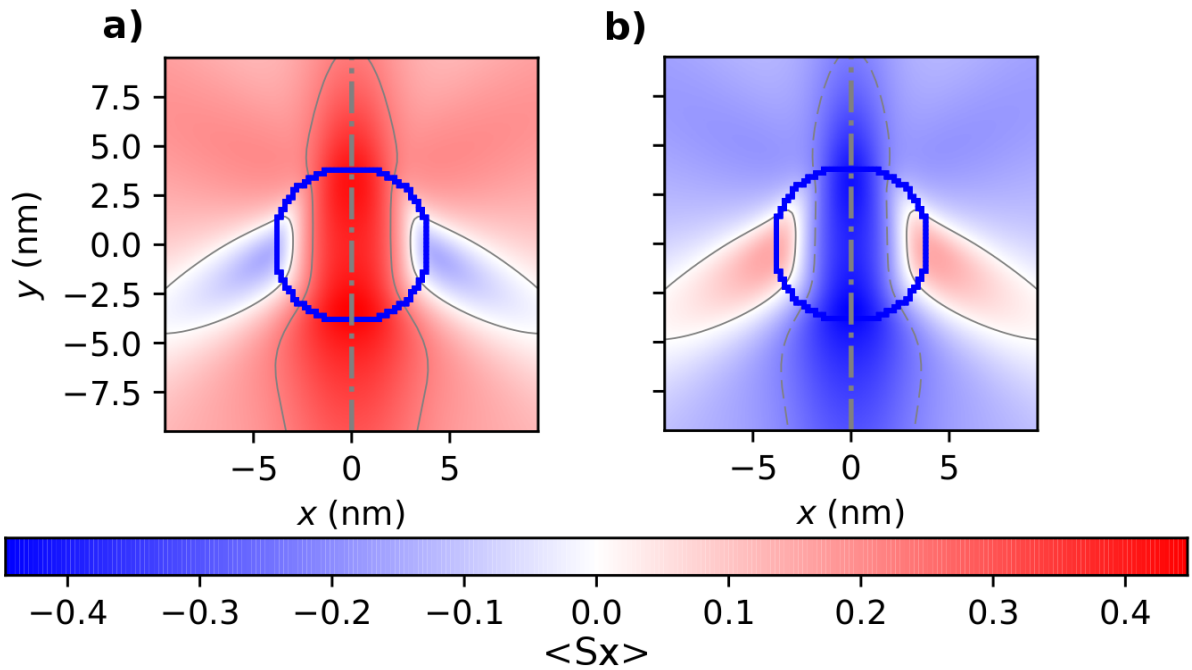
Figure 3.33 – Projection of $< S_x > (\vec{r})$ expectation value for an elongated CdTe quantum dot in a ZnTe-ZnMgTe core-shell nanowire for the pseudo spin-up a) and pseudo spin-down b) component of the first calculated Kramers doublet at $B = 0.2$ T.

In Fig. 3.37 a) we present the spin expectation value $< S_x >$ at 0 T and 701.5 T in the center of the dot (red circles) and by taking into account he leaking of presence probability (blue squares). As regards the spin expectation values inside the dot, there is no difference in comparison to the
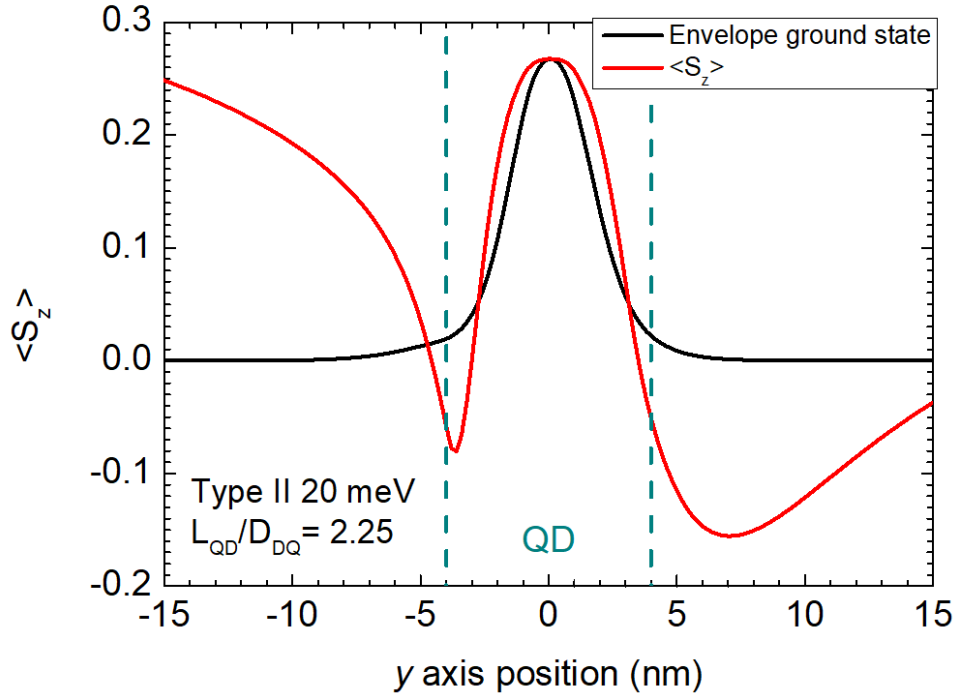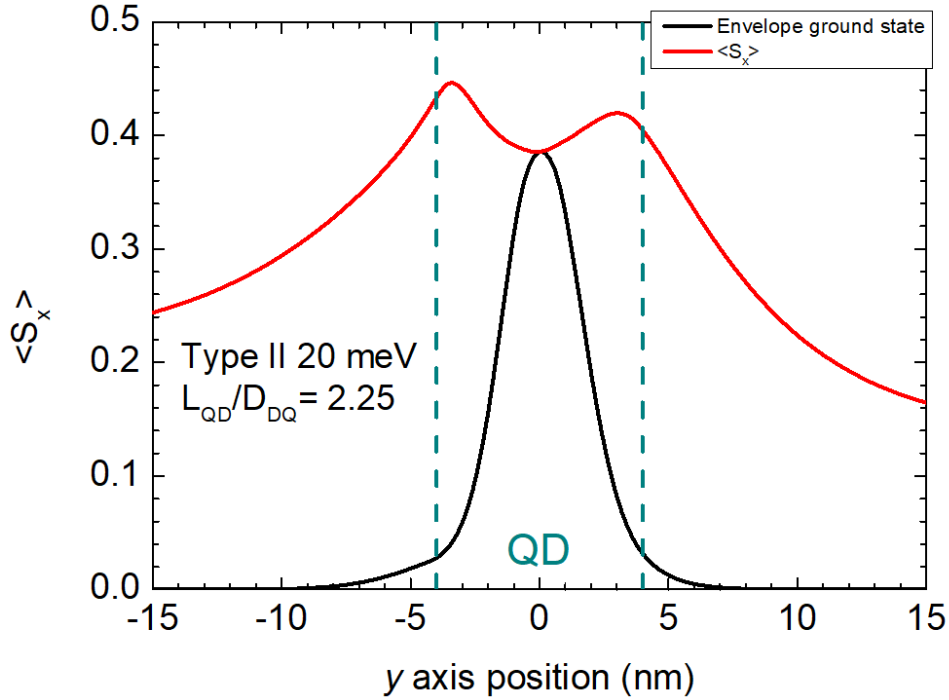
Figure 3.34 – Cross section of the projections of spin component $< S_z > (\vec{r})$ and the total envelope function along x axis for a 20 meV type II CdTe flat quantum dot with $L_{QD} = 18$ nm in a ZnTe-ZnMgTe core-shell nanowire.
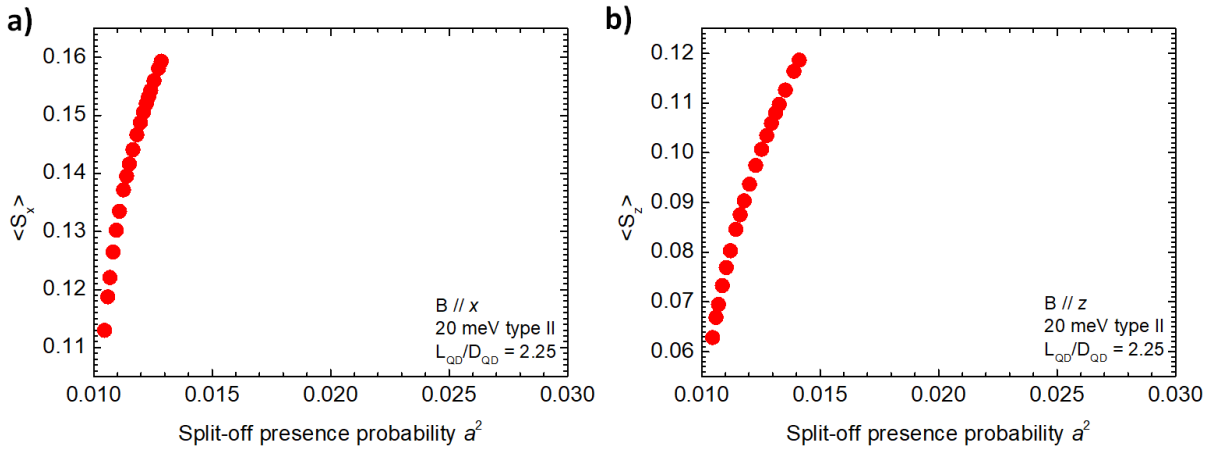
Figure 3.35 – Spin expectation values inside the quantum dot as a function of split-of presence probability for a magnetic field applied perpendicular a) and parallel b) to the dot quantization axis.

type I cases. At 0 T, the analytical model is in perfect agreement with numerical calculations, while at large field the value deviates. By considering the envelope leaking however we confirm that spin values are further reduced in comparison to type I. In a similar way, in Fig. 3.37 b) we present the average value of $< S_z >$ near the center of the quantum at 0 T and 701.5 T(red circles) and by taking into account envelope leaking (blue squares). Again the picture is no different for the values inside the dot in comparison to the type I cases. Increased envelope leaking however comparing with weak type I further reduces the values of spin. In both cases though we confirm both the effect of reconfinement and increasing mixing of light hole with split-off, as the value of spin at high field is always larger than that in vanishing field.
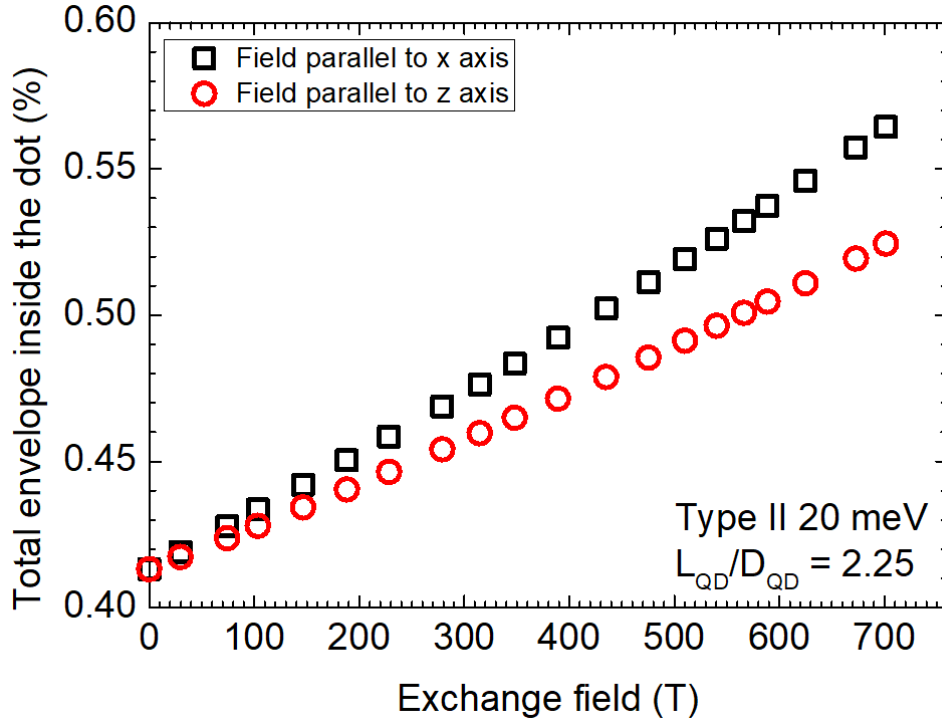
Figure 3.36 – Variation of confinement for the pseudo spin-up component of the Kramers doublet of a weak type I elongated quantum dot, with the magnetic field applied both along x and z axis.
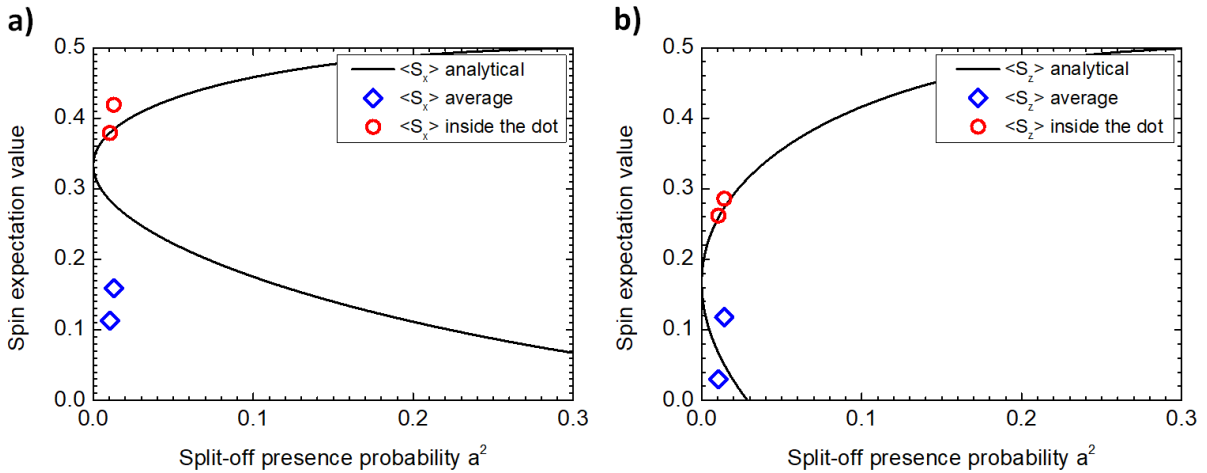
Figure 3.37 – Calculated expectation value of spin $< S_x >$ and $< S_z >$ for a vanishing field and at 701.5 T applied respectively perpendicular a) and parallel b) to the nanowire axis as a function of split-off band presence probability and comparison with the analytical model. For both orientations, small values of spin correspond to 0 T and large values of spin at 701.5 T.

3.7 Link between numerical calculations and experiments

Before concluding this chapter, we explain how a phenomenological model can be built from the results of numerical calculations under exchange field, in order to analyze the experimental data. One effect which was discussed thoroughly and will be taken into account, is the strain induced mixing between light hole and split-off and the subsequent renormalization of spin expectation values $< S_x >= \delta_{SO}/3$ and $< S_z >= \beta_{SO}/6$. Two other important concepts which

have a strong effect on Zeeman shift, is the field induced reconfinement which becomes stronger as valence band offset decreases and the anticrossing of the ground state with excited states.

For fitting the Zeeman shift measured experimentally, the most common method employed is through a quadruplet model assuming a heavy and a light hole state which are energetically separated [12], [27], [33]. For a strong type I case, where the energy difference between heavy and light holes is large and their mixing small, this model is still valid and there is a weak effect due to anticrossing especially when field becomes large as shown in Fig. 3.2. In Fig. B.1 b) we present the Zeeman shift for a heavy hole in a flat dot for $B//z$. The pseudo spin-up component evolves linearly with field, while the pseudo spin-down crosses with the excited hole state. This crossing is characteristic of states which are orthogonal to each other, like $|\phi_s(\vec{r})\rangle |3/2, 3/2\rangle$ and $|\phi_{p_z}(\vec{r})\rangle |3/2, \pm 3/2\rangle$ for instance, which correspond to a pure heavy hole for both ground and excited state. The picture is similar for light holes as shown in Fig. B.2, where the pseudo spin-down component crosses with excited states, with a very weak anticrossing effect for large field parallel to x axis and a weak non linear component added to the linear shift (not shown).

By reducing the valence band offset however, mixing between heavy holes and light holes becomes stronger and for an elongated quantum dot for example, ground state $|\phi_s(\vec{r})\rangle |3/2, 1/2\rangle + |\phi_{p_z}(\vec{r})\rangle |3/2, \pm 3/2\rangle$ and excited states $|\phi_s(\vec{r})\rangle |3/2, 1/2\rangle + \left|\phi_{p_{(x,y)}}(\vec{r})\right\rangle |3/2, \pm 3/2\rangle$ have a significant contribution of heavy hole component. In this case, ground state is still orthogonal with excited states, but this automatically imposes that for their individual components expressed in total angular momentum basis, orthogonality vanishes. This is the reason of anticrossing and its effect on Zeeman shift. This is clearly shown in Fig. C.2 and Fig. D.3.

Figure 3.38 – Zeeman shift as a function of magnetic moment for the pseud spin-up and pseudo spin-down component of the first Kramers doublet for a weak 20 meV type I elongated quantum dot. The exchange field is applied perpendicular to the nanowire axis

In Fig. 3.38 we present the Zeeman shift of the two components of the first Kramers doublet, as a function of magnetic moment and it allows us to discuss the different contributions to the linear and non-linear terms in Eq. 3.33. The dotted line includes the split-off contribution and the probability of light hole in the dot and it is in good agreement with the numerical calculation results for small field values. The dashed line adds also the field induced reconfinement, while

with the green line we take into account also the effect of anticrossing. Through this plot we confirm that for the ground state, which corresponds to the pseudo spin-up component, we can still use a quadratic function in order to fit the Zeeman shift. On the contrary, looking at the pseudo-spin down we observe a strong effect due to anticrossing with light hole. Since we are interested only to the ground state however we ignore the pseud-spin down component and we attempt to fit the Zeeman shift of the ground state using a quadratic function.
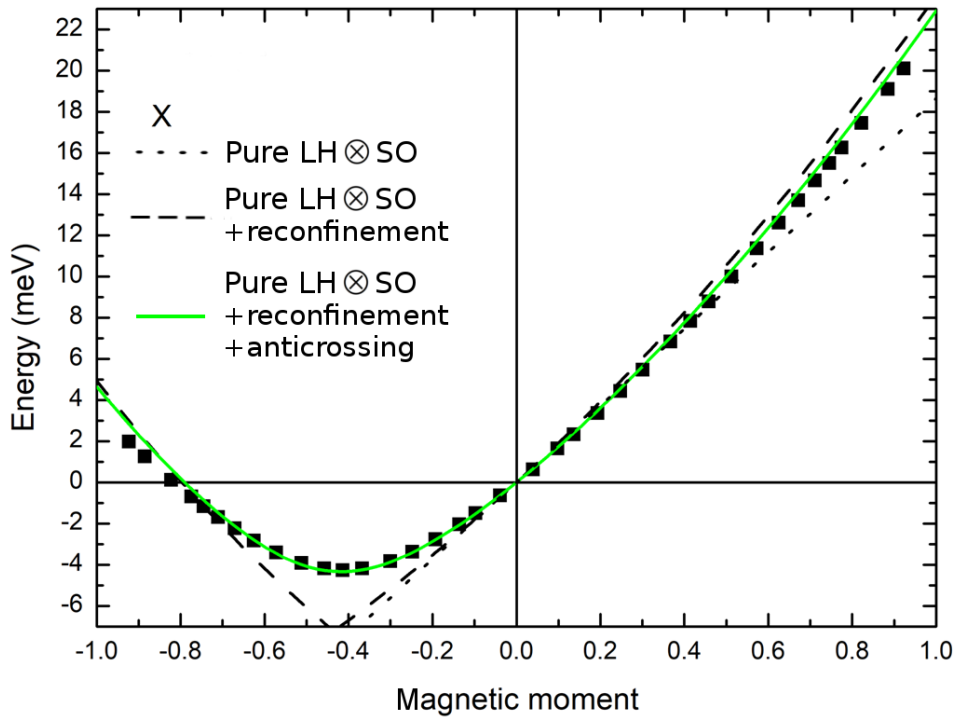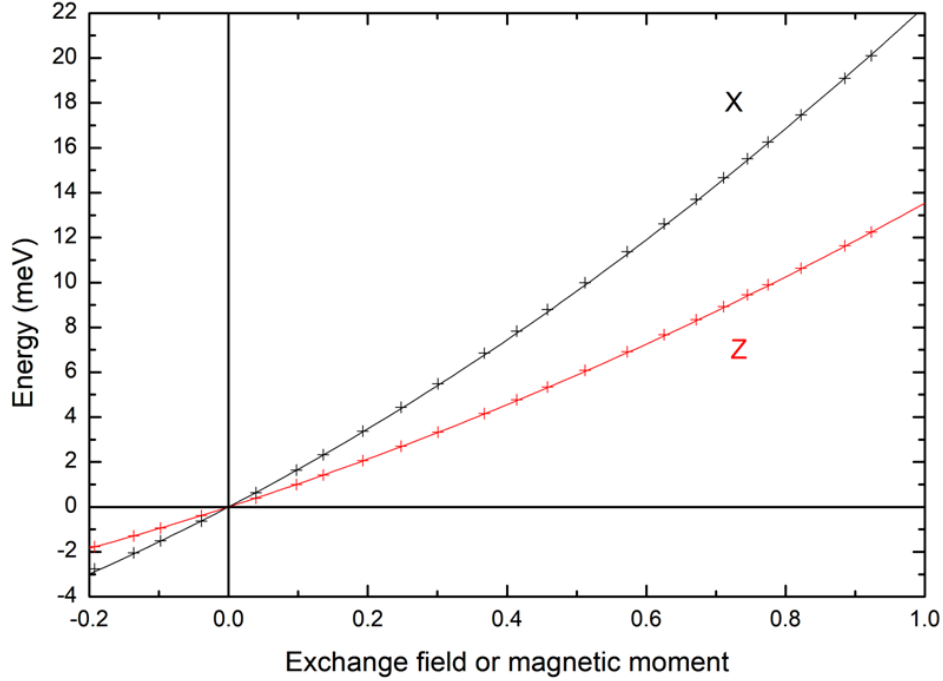

Figure 3.39 – Zeeman shift as a function of magnetic moment for the pseud spin-up component of the first Kramers doublet for a weak 20 meV type I elongated quantum dot. The Exchange field is applied both parallel to z and x axis.

In Fig. 3.39 we present the Zeeman shift only of the pseudo spin-up component of the first calculated Kramers doublet for both orientations of exchange field. We fit the data by using the following expressions

$$\text{Along x,} \quad \Delta E_x = 16.2 M_x (1 + 0.38 M_x)$$
$$\text{Along z,} \quad \Delta E_z = 9.9 M_z (1 + 0.36 M_z) \tag{3.33}$$

further confirming that indeed we can ignore any effects due to anticrossing.

Another important parameter which has to be taken into account, is the effect due to field induced reconfinement of the hole envelope, for an increasing exchange field. We prompt the reader to look back at Fig. 3.24 and 3.36, where we plot the percentage of an envelope in the dot as a function of the exchange field for a weak type I and type II quantum dot respectively. Depending on the field orientation, for both cases of a weak valence band offset, confinement gets restored, by almost 15 %. This effect which takes into account all contributions, is included the model for fitting the experimental data, through a factor c, which is introduced in the general expression of the Zeeman Hamiltonian for light holes

$$\mathcal{H}_{zh} = cM \Delta E_{hh}^{sat} \sigma_{zh} \cos \theta + cM \Delta E_{hh}^{sat} \sigma_{xh} \sin \theta \tag{3.34}$$

where ΔE_{hh}^{sat} is the Zeeman splitting at saturation for heavy holes, as discussed in detail in

Chapter 1 and M the magnitude of magnetic moment. This factor is given in terms of the free parameters c_0 and c_1, which must satisfy the energy shifts

$$\text{Along x,} \quad \Delta E_x = \Delta E_{hh}^{sat} \frac{\delta_{SO}}{3} \frac{M_x}{M_{sat}} \left(c_0 + c_1 \frac{\delta_{SO}}{3} \frac{M_x}{M_{sat}} \right)$$

$$\text{Along z,} \quad \Delta E_z = \Delta E_{hh}^{sat} \frac{\beta_{SO}}{6} \frac{M_z}{M_{sat}} \left(c_0 + c_1 \frac{\beta_{SO}}{6} \frac{M_z}{M_{sat}} \right) \tag{3.35}$$

From c_0 and c_1, we calculate c as follows

$$c = c_0 + c_1 M \frac{\sqrt{\cos^2(\theta)\frac{\beta^2}{36} + \sin^2(\theta)\frac{\delta^2}{9}}}{(3/\delta)^2} \tag{3.36}$$

The purpose of this discussion, is to explain how we will use the results obtained from numerical calculations, in order to analyze the behaviour of a real quantum dot under magnetic field. The model we use for fitting the experimental data is fully developed in the next chapter, section 4.4.4.3

3.8 Conclusions

In this chapter we investigated the effect of an applied exchange field on the hole ground state of a flat and an elongated CdTe quantum dot, in ZnTe-ZnMgTe core-shell nanowires. The structures on which we performed the calculations are identical to those of Chapter 2. From the numerical calculations, we investigated the spin properties of the hole ground state for a strong type I, a weak type I and a weak type II valence band offset. We confirmed that Zeeman shift is influenced by the effect of field induced reconfinement, the anticrossing with excited states and the renormalization of spin expectation values $< S_x >$ and $< S_z >$ due to the mixing of light hole with split-off. Spin renormalization is confirmed by both $k \cdot p$ calculations and an analytical model using perturbation theory for a mixed light hole-split-off state without taking into account heavy hole. We also observed that field induced mixing of heavy with light hole also has an effect on spin values but incorporating mixing of the two states in an analytical model is not trivial.

In a strong type I Cd(Mn)Te quantum dot, we validate the phenomenological model based on a Γ_8 quadruplet, given that built-in strain is so large the light hole / heavy hole splitting (150 meV) makes anticrossing very weak. Also due to this strong strain, the light hole/split-off mixing produces a significant effect. This is due to the fact that the relevant states are linked by both the strain and giant Zeeman Hamiltonian, so that the effect is linear in field and not quadratic as the light hole - heavy hole anticrossing. This effect is represented by a modification of the spin operator.

In the shallow type I quantum dot (and even more in the slightly type II structure) two additional mechanisms take place:

• The confinement is weak and it is re-enforced by the giant Zeeman effect for the ground spin state.

• Anticrossing appears with excited light - hole states, that affects only weakly the pseudo spin-up component of the ground state, but it is clearly visible on the pseudo spin-down.

As a consequence, in the phenomenological model used for analyzing experimental data, the effect of reconfinement and anticrossing with excited light hole states has to be taken into account. For the ground state however, fitting the shift with a quadratic function makes a good representation.

As a future perspective it is interesting to investigate the spin properties of strong type II structures, where the hole envelope will be in the shell. In that case mixing of the different spin states due to off-diagonal strain terms could probe some interesting spin properties

Chapter 4

Experimental results

4.1 Introduction

In this chapter we describe the experimental strategies we employed for stabilizing a light hole ground state and probing a spin texture in a nanowire quantum dot and we discuss the results obtained from optical measurements on individual nanowires.

The main technique we used was micro-photoluminescence spectroscopy, through which we studied the polarization properties of emitted light, the dependence of emission on excitation power, the photogenerated carriers lifetime and the second order correlation function. This ensemble of optical measurements constitutes the essential toolbox for studying the excitonic properties of a quantum dot. The nanowire heterostructures were additionally characterized by cathodoluminescence and energy dispersive X-ray (EDX) spectroscopy.

In total we investigated three different types heterostructures. Their characteristics and properties are illustrated in Fig. 4.1.

First we discuss the properties of a ZnTe quantum dot in a ZnMgTe nanowire, where the sign of lattice mismatch becomes negative and for a flat dot shear strain becomes compressive along z axis. This is opposite to the CdTe - ZnTe structure which we have already discussed in the previous chapter. In this case we expect to stabilize a light hole ground state for a flat quantum dot with $L_{QD}/D_{QD} < 1$.

Following that, we describe the attempted study of a strong type II system, where the idea was to probe different spin textures, leading potentially to a skyrmion like magnetic order. More precisely the idea was to incorporate ZnSe inclusions in a ZnTe nanowire, where we know that the valence band offset between the two materials would be a strong type II. Additionally, the large lattice mismatch will induce a strong radial confinement associated with complex spin properties. Unfortunately as we will see later in this chapter the realization of this structure was not that trivial.

In the final part of this chapter we present the results obtained by measuring compressive CdTe quantum dots in ZnTe nanowires passivated with a ZnMgTe shell. In this type of heterostructures we introduced also Mn ions in the quantum dots in order to measure the micro-photoluminescence under magnetic field, in CdMnTe quantum dots inserted in ZnMgTe. The results from magneto-optical measurements, in combination with the theoretical models developed in the previous chapter, will provide us with a quantitatively description of the valence band ground state properties in order to identify a light hole state.

In this work we characterized 16 different samples in total, belonging to the categories described above, out of which we made a selection with the most interesting results which we present in this report. All samples were grown under the supervision of Edith Bellet-Amalric at INAC-CEA. For reasons of convenience and to make the descriptions more accessible, in the table below we present the name of the samples, their properties and the names of nanowires we measured.
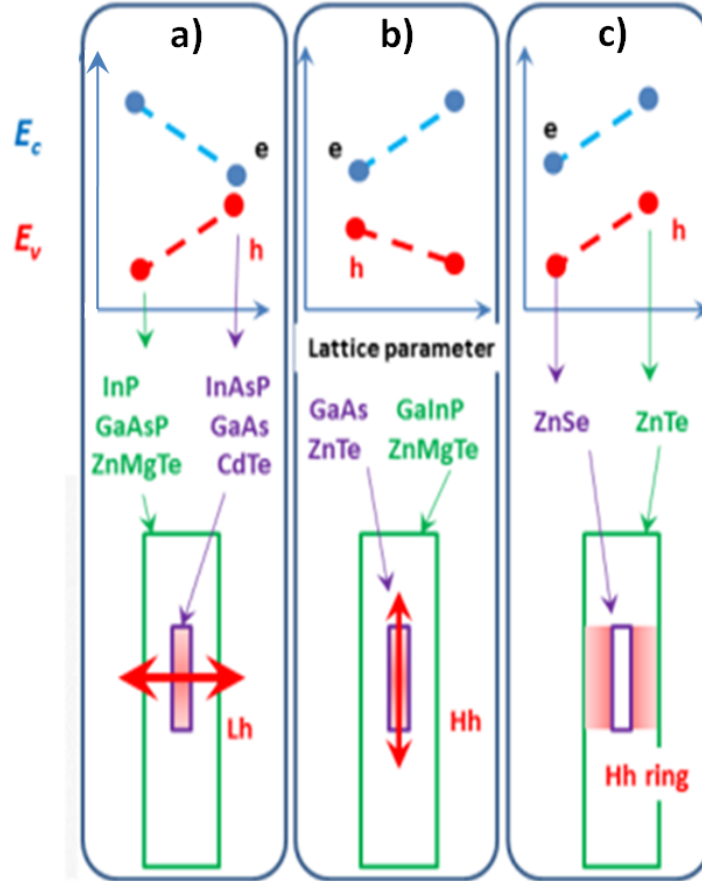
Figure 4.1 – Schematic representation of the three different types of heterostructures we studied. A compressive Cd(Mn)Te quantum dot in a ZnTe nanowire, where induced strain reduces the difference between valence and conduction band a). A tensile ZnTe quantum dot in a ZnMgTe nanowire, where strain has the opposite effect and the energy difference between valence and conduction band increases b). A ZnSe inclusion in a ZnTe nanowire with a strong type II valence band offset resulting a strong leaking of the hole state c).

As mentioned before, the main method we used for the characterization and identification of the optical properties of the nanowire heterostructures is micro-photoluminescence spectroscopy. In Fig. 4.2 we present the micro-photoluminescence setup we used to characterize the nanowire quantum dots in this work.

For the basic characterization and depending on the emission energy of the sample we wanted to study we used the lines of two different diode lasers at 405 nm and at 488 nm. For the characterization of Cd(Mn)Te dots we used exclusively the 488 nm laser, while the 405 nm was used in some special cases which will be discussed later. For measuring carrier lifetimes we used the frequency doubled line of a tunable pulsed Ti:Sapph oscillator at 440 nm. The laser pulse frequency is 76 MHz and the material of the frequency doubling crystal is β-BaB$_2$O$_4$ (BBO). The laser beam passes through a spatial filtering assembly in order to become cleaner. Initially an objective lens focuses the beam on a pinhole. Then through a second objective we collect the pinhole image and we redirect it through a 50/50 non-polarizing cubic beamsplitter towards a long working distance microscope objective with NA=0.55 and 100x magnification. For tuning the excitation power we used a rotating neutral density gradient filter before the beamsplitter. The laser excitation power was measured just before the objective lens. The samples were mounted on a He flow cryostat cooling down to 4 K. In order to study the photoluminescence intensity with respect to polarization angle we used a rotating $\lambda/2$ retarder placed in front of

Table 4.1 – Description of studied nanowire heterostructures.

Name	Sample description	Nanowire indexing and measurements
m3429	Tensile ZnTe quantum dot in a ZnMgTe nanowire	W-1 : micro-photoluminescence W-2 : cathodoluminescence
m3361	Type II ZnSe inclusion in a ZnTe nanowire	W-3 : micro-photoluminescence W-4 : cathodoluminescence W-5 : cathodoluminescence W-5(a-b) : EDX
m3393	An elongated CdTe quantum dot in a ZnTe-ZnMgTe core-shell nanowire	W-6 : micro-photoluminescence W-7 : micro-photoluminescence W-8 : cathodoluminescence
m3390	ZnTe-ZnMgTe core-shell nanowire	W-9 : micro-photoluminescence
m3408	An elongated Cd(Mn)Te quantum dot surrounded by ZnMgTe in a ZnTe-ZnMgTe core-shell nanowire	W-10 : magneto-optical dispersed W-11 : magneto-optical as-grown W-12 : magneto-optical as-grown

a linear polarizer. The axis of the polarizer is parallel to the axis of the spectrometer slits. For linearly polarized light the $\lambda/2$ waveplate rotates the angle of the electric field of the emitted light with respect to the polarizer axis. The intensity of emitted light as a function of angle follows Malus's law. The quantum dot emission is analyzed by a 0.46 m spectrometer equipped with a 600 gr/mm grating which is blazed in the visible range. The spectra are recorded by a Peltier cooled charged coupled device (CCD) of resolution 1024×256 pixels. In order to record the carrier lifetimes we used a time-correlated single photon counting module (TCSPC) [63], where one channel was connected to a photodiode which was detecting the laser pulses, triggering the counting process and the second one to an avalanche photodiode (APD), detecting the emitted light at a specific wavelength. For the autocorrelation measurements and in order to measure the second order correlation function we used a Handbury Brown - Twiss (HBT) setup as described in [64] consisting of two APDs connected to the TCSPC module.

A special technique we used to reveal more information as regards the radiative transitions, was by recording the pattern of emitted light through k-space imaging. In order to record the far field emission, we used a 63x / NA = 0.75 small working distance objective lens and through a Fourier lens, we focused the various angles of the emitted photoluminescence cone, on different pixels of the CCD.

Another important characterization technique was cathodoluminescence, through which we can identify the emission position and localization of specific wavelengths along the nanostructure. Cathodoluminescence measurements were carried out in collaboration with Fabrice Donatini.

In Fig. 4.3, we present a schematic representation of a cathodoluminescence setup. where the sample is excited by the electron beam of a SEM and the emitted light is collected by a parabolic mirror and further analyzed by a spectrometer in a similar way to the micro-photoluminescence setup. The only drawback of cathodoluminescence is that the emission efficiency is 3 orders of magnitude lower compared to photoluminescence, while the electron beam has detrimental effects on the nanostructures, consequently it is considered a destructive technique.

In order to optically characterize individual objects, the nanowires were mechanically dispersed on patterned Si substrates. Prior to the optical measurements, we recorded SEM images from the surface of the sample in order to locate isolated nanowires.

In Fig. 4.4 we present a typical SEM image showing the dispersed nanowires on the Si substrate. In order to put the selected nanowire under the laser spot in the micro-photoluminescence setup,
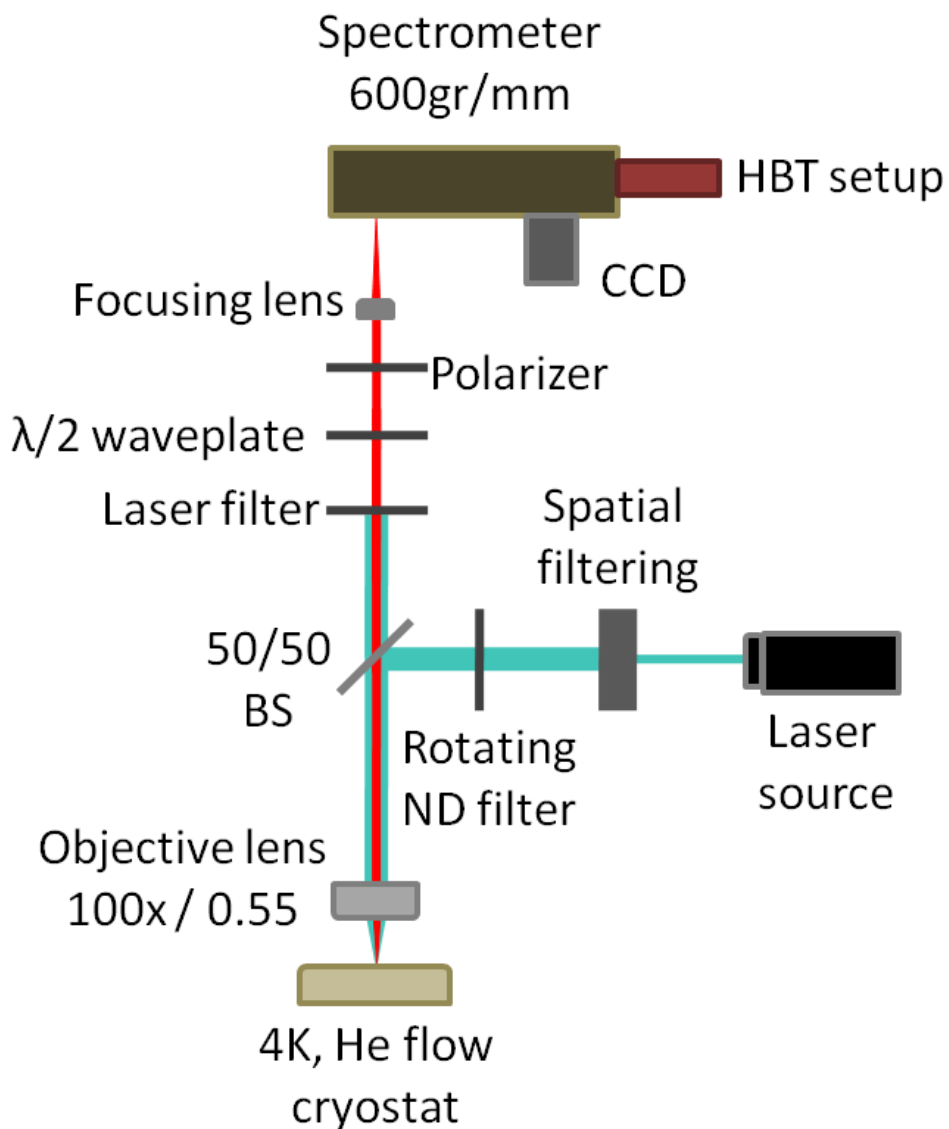
Figure 4.2 – Schematic representation of the micro-photoluminescence setup we used for the basic optical characterization of the nanowire quantum dots.
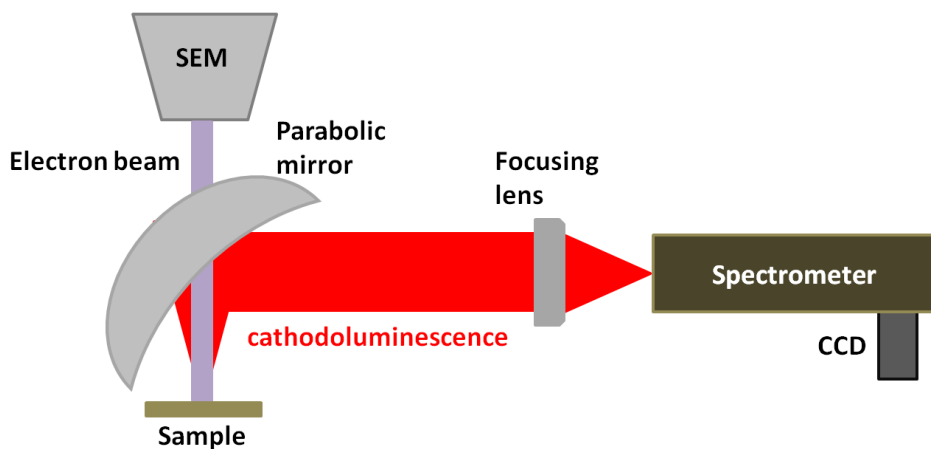

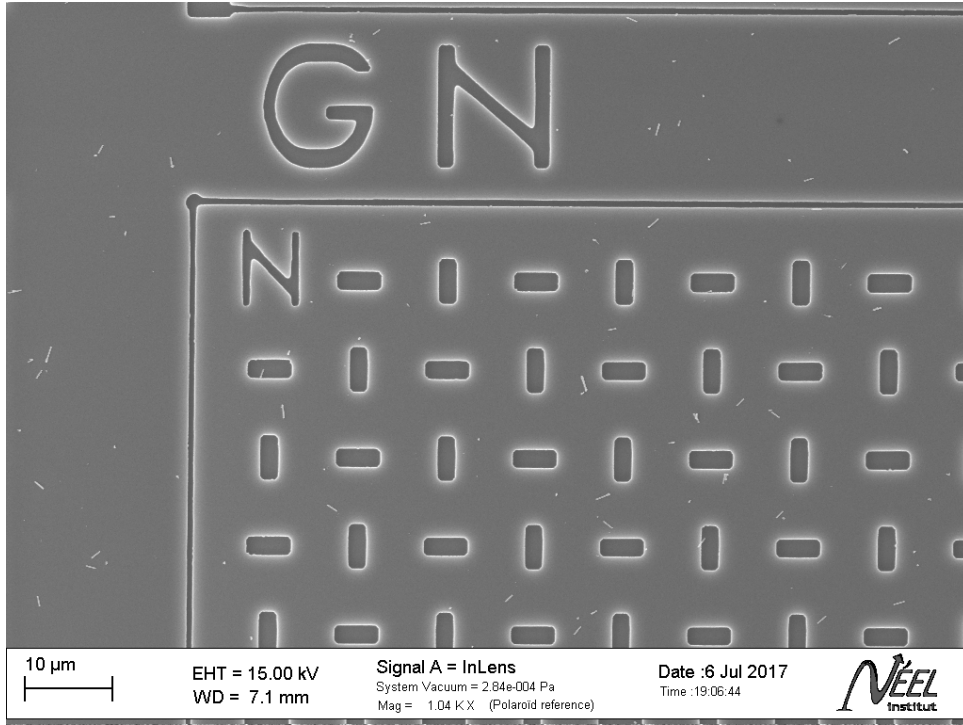Figure 4.3 – Schematic representation of the cathodoluminescence setup.

Figure 4.4 – A typical SEM image showing the patterned Si substrate with the dispersed nanowires, which we use in order to navigate and select the nanowires on which we perform the optical measurements.

we used a white light beam aligned on the same path as the laser.

4.2 Determination of the hole ground state in tensile ZnTe - ZnMgTe nanowire - quantum dots

A possible approach to stabilize a light hole ground state is through a flat ZnTe quantum dot in a ZnMgTe nanowire. This concept was explored in [23] using a complex III-V structure. A sketch of the nanowire heterostructure studied can be seen in Fig. 4.5 a).

The nanowires were grown on (111) GaAs substrates by MBE through the Vapor-Solid-Solid mechanism (VSS), where a gold droplet acts as the catalyst. Initially the ZnTe nanowire core is grown for 15 minutes. Then sequentially, a layer of ZnMgTe is grown for 20 seconds, followed by a 5 second growth of ZnTe and finishing with 20 more seconds of ZnMgTe growth. Through this way a ZnTe inclusion in the form of a flat quantum dot is expected to be grown, confined in three dimensions by ZnMgTe. The procedure ends by the additional growth of ZnTe for the completion of the nanowire core and finally the structure is passivated by a ZnMgTe in order to protect it from oxidation and enhance its optical quality.

In Fig. 4.5 b) we present a SEM image of a nanowire dispersed on a Si substrate. This nanowire is similar to those we studied by micro- photoluminescence measurements. By analyzing different SEM images, we observe that the nanowires have a needle like shape. Close to the bottom, the diameter is on average 150 nm and their height 2 μm. According to the growth conditions and using previously grown samples as a reference, we expect that the quantum dot diameter will be $D_{QD} \approx 10$ nm and the length $L_{QD} = 5 - 7$ nm. The ZnTe length versus growth time can be deduced from EDX study, as shown in Fig. 4.19. The conditions were optimized in order to achieve a Mg content of 12%. At this concentration the lattice constant of $Zn_{0.88}Mg_{0.12}Te$ is $a = 6.142$ Å. As a reminder to the reader, the lattice parameter for ZnTe
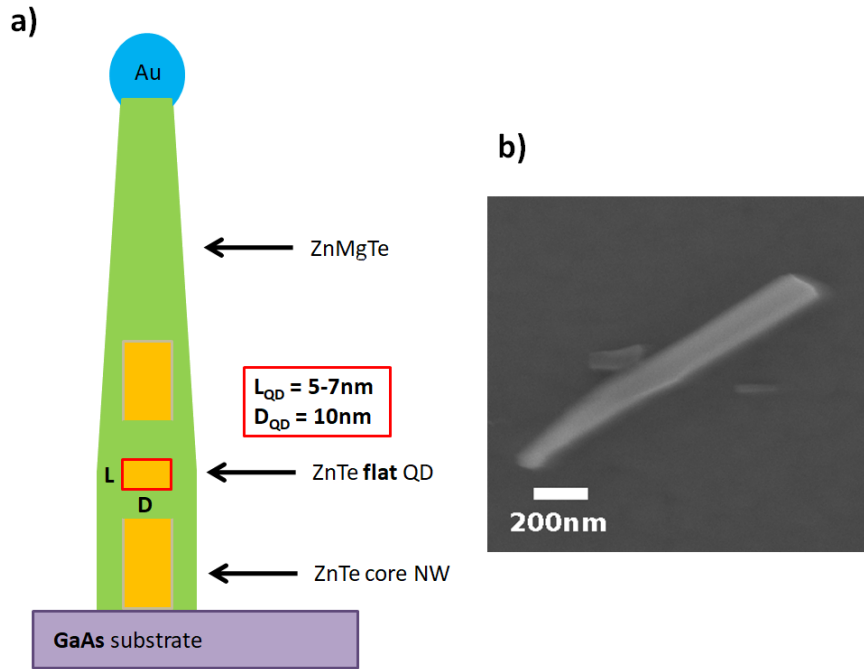
117

Figure 4.5 – Schematic representation of an as-grown ZnMgTe nanowire with a ZnTe core and a ZnTe flat quantum dot a). An SEM image of the actual nanowire dispersed on a Si substrate in order to carry out the micro-photoluminescence measurements b).

and CdTe are respectively $a_{ZnTe} = 6.104$ Åand $a_{CdTe} = 6.481$ Å. For a ZnTe quantum dot in a ZnMgTe nanowire, when $L_{QD}/D_{QD} < 1$ axial shear strain is compressive along z axis while for $L_{QD}/D_{QD} \geq 1$ it becomes compressive on xy plane.

4.2.0.1 Optical measurements

In order to carry out micro-photoluminescence measurements on individual nanowires, we mechanically dispersed them from the as-grown sample on patterned Si substrates, as explained earlier in the introduction. For the excitation we used a 405 nm diode laser and all measurements were performed in 4 K. In total we measured 9 nanowires. By analyzing the recorded spectra we observed that the emission pattern was similar among different nanowires. In Fig. 4.6 we present the emission spectra for nanowire W-1 at different excitation powers as a function of energy. The different values of excitation power correspond to those as measured before the entrance of laser beam in the objective lens.

From the recorded photoluminescence spectra we identify three energy ranges in emission. At low energies and from 2260 meV - 2300 meV we record the photoluminescence emission from the ZnTe nanowire core. The center of the emission is at 2285 meV, being redshifted by 96 meV from the emission of bulk ZnTe. This energy shift is attributed to the compressive strain induced to the core from the ZnMgTe shell [65], [66]. This observation will be further confirmed by cathodoluminescence measurements discussed later.

At high energies and between 2440 meV and 2520 meV, we recorded a very weak photoluminescence signal constituted by multiple lines. This emission originates from ZnMgTe and the fact that it is weak is attributed predominantly to the strong confinement of carriers in ZnTe. Another reason explaining both the weakness of signal and the large energy range is the optical quality of ZnMgTe influenced by lattice discontinuities, localization of carriers in non-radiative centers, non-uniform distribution of Mg and surface oxidation.

Between the lines of ZnTe and ZnMgTe, discussed above and from 2365 meV to 2380 meV,
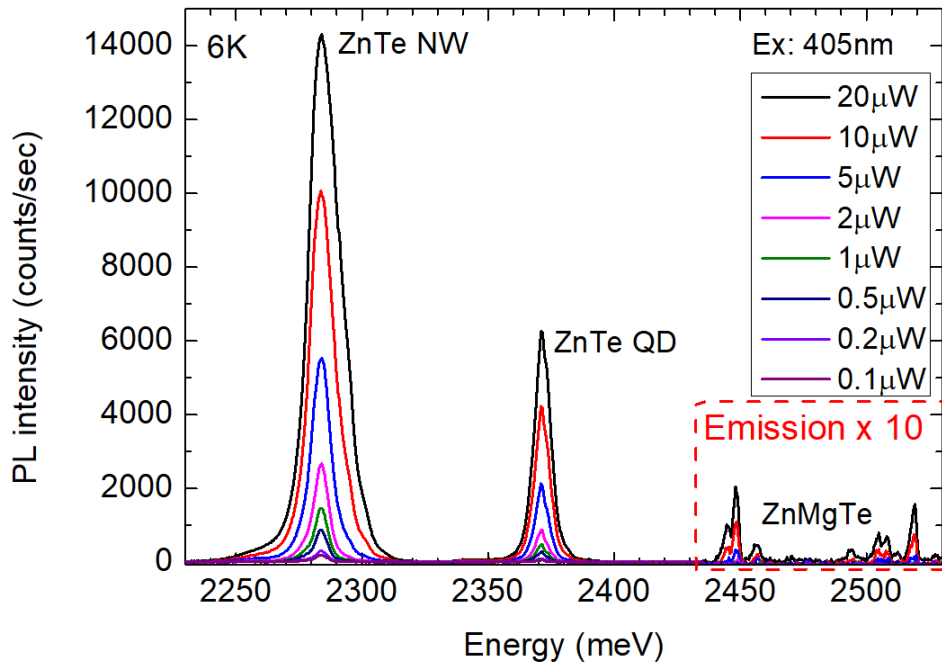
Figure 4.6 – Micro-photoluminescence intensity of nanowire W-1 as a function of emission energy for different excitation powers. From the spectra we identified three regions of emission corresponding to a ZnTe nanowire core, a ZnTe inclusion of smaller dimensions and ZnMgTe

we record photoluminescence blueshifted by 85 meV from the signal originating from ZnTe core. This emission is consistent with a ZnTe quantum dot (also bulk ZnTe) which emits in higher energies due to the effect of quantum confinement. Unfortunately up to the point this chapter had been written, there were no EDX measurements to confirm the chemical composition and by extent the structural properties of this heterostructure. Consequently we had to rely only on the results of optical measurements.

A way to determine Mg content is through the graph presented in Appendix E and using the fit of the data reported at [67]. According to this fit, the emission at 2520 meV corresponds to a Mg content near 19% - 20% . Lower energy transitions are associated to carriers confined in localized potentials formed by segments of much lower Mg content, which is not indicative of the average Mg distribution along the nanowire axis.

A more accurate method to calculate Mg content in the barrier, is through the strain induced redshift of ZnTe. According to the study reported in [53], [65] and with the parameters of ZnTe for a strained core - shell nanowire, the exciton emission energies associated to heavy and light hole are respectively

$$
\begin{aligned}
E_X^{hh} &= E_X - 8.8 \left(1 - \frac{1}{\eta}\right) f \\
E_X^{lh} &= E_X - 4.4 \left(1 - \frac{1}{\eta}\right) f
\end{aligned}
\tag{4.1}
$$

where E_X is the exciton emission energy of bulk, f the lattice mismatch and η the ratio of the total nanowire area over the core nanowire area. In our case, the emission originating from ZnTe core is expected to be associated to a heavy hole transition. As a first estimation and since we do not have any images of the ZnTe core (EDX or SEM) we can assume that its diameter will be close to that of the Au droplet used as catalyst for the nanowire growth. From previous studies, it is shown systematically that the Au diameter is near 10 nm. In that case and from

SEM analysis, the ZnMgTe shell thickness has to be around 70 nm, resulting $\eta = 225$. For $E_X =2381$ meV (bulk ZnTe) and $E_X^{hh} =2285$ meV, this results in a lattice mismatch between ZnTe and ZnMgTe of $f =0.010$. For $a_{MgTe} = 6.42\text{\AA}$ and by applying Vegard's law, we calculate a Mg content of 21%, which is in good agreement to our previous calculation.

As regards the calculation of Mg content from the redshift of ZnTe emission due to strain, the only ambiguous quantity is the radius of the nanowire core. As a first approach we may consider that core thickness might be very close to the radius of Au droplet. However, by analyzing SEM images of ZnTe nanowires without an external shell we have measured core diameters from 10 nm up to 30 nm in some cases. For this reason and since we do not have any measurements (EDX, TEM) to reveal the nanowire core thickness, we had to investigate thoroughly its influence on the emission energy.
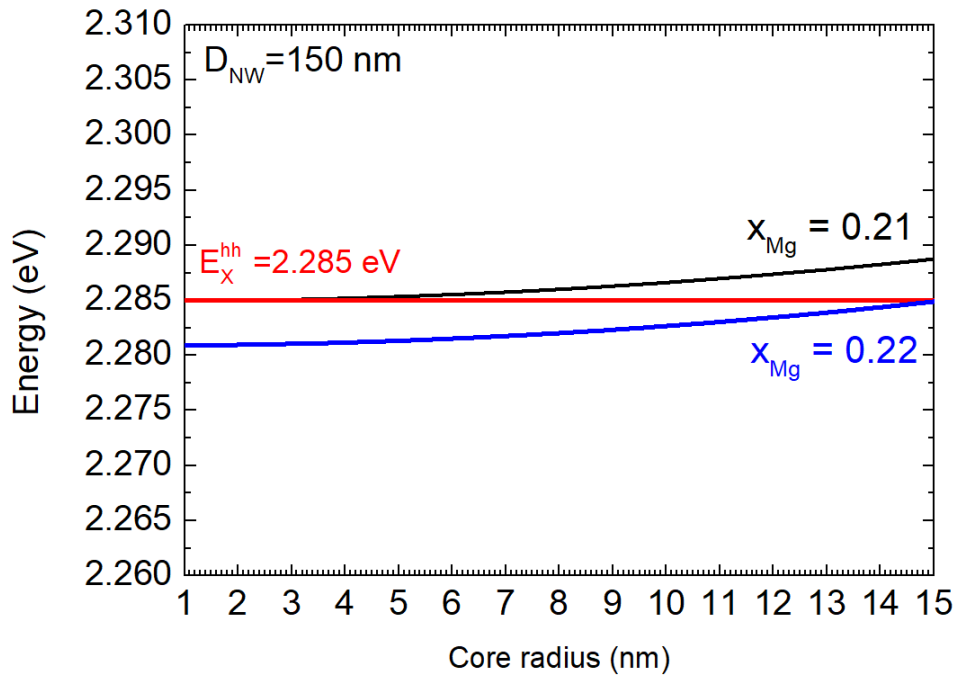
Figure 4.7 – ZnTe emission energy as a function of the core radius, for a Mg content of 0.21 (black curve) and 0.22 (blue curve). The nanowire diameter is 150 nm

In Fig. 4.7 we present the emission from ZnTe core as a function of its radius. By considering the extreme case with a ZnTe core of diameter equal to 30 nm, emission energy from ZnTe is blueshifted by 3 meV from what we would expect. This means that if the nanowire core was 30 nm thick, corresponding to the extreme case, then in order to observe emission at 2285 meV, Mg content should be 22%. This difference of 1% is small and we confirm that even if we do not know explicitly the dimensions of the core, we can estimate quite accurately the content of Mg.

At this point we have to underline, that from the calculated values, there is a significant deviation from the target of 12% Mg content, as is expected from the growth conditions.

After identifying the origin of photoluminescence lines and the ZnMgTe shell properties, we focused our study on what we believe is the signal of ZnTe inclusion in the form of a quantum dot. In Fig. 4.8 we present the photoluminescence spectrum emitted by the ZnTe inclusion of W-1 using an excitation power of 5 μW before the objective lens.

From the spectrum of Fig. 4.8 we observe that in the emission of the ZnTe quantum dot there is contribution from at least two overlapping peaks, where from power dependent measurements we observe that the intensity of the line at low energy is always stronger that that at high energy. The linewidth of the emission is $\Delta E = 5.9$ meV and this broadening is compatible with

Figure 4.8 – Micro-photoluminescence intensity of the ZnTe inclusion confined in three dimensions by a ZnMgTe barrier in a ZnTe-ZnMgTe core-shell nanowire.

spectral diffusion discussed later in the chapter.

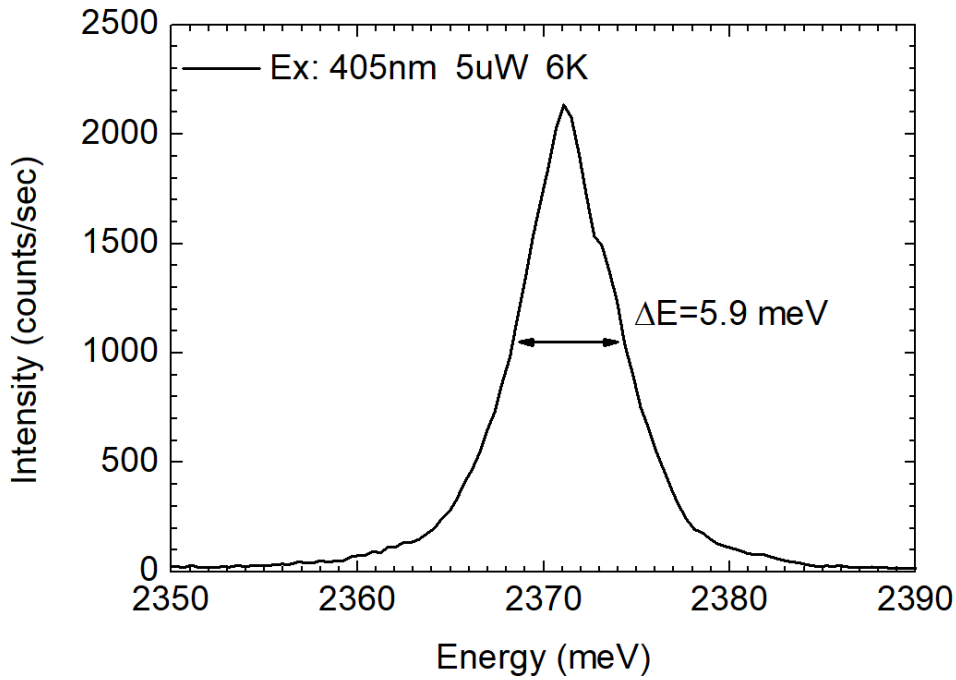Following the standard optical characterization procedures, we performed photoluminescence measurements on the same nanowire by resolving the emission in polarization. In Fig. 4.9 we present the normalized intensity of photoluminescnce as a function of the polarization angle, as emitted from both the ZnTe nanowire core and the inclusion for W-1. The spectra were recorded for an excitation power of 2 μW, measured before the objective lens.

The angle of the nanowire in respect to the spectrometer slits can be determined using an SEM image and an optical microscope image. As regards the ZnTe core, photoluminescence intensity becomes maximum when the polarization angle is perpendicular to the nanowire axis. This is what we expect for a heavy hole type excitonic transition, characterized by a rotating electric dipole, perpendicular to the dot quantization axis. A similar result is obtained also for the case of a core-shell ZnTe-ZnMgTe nanowire which will be discussed later. The degree of polarization for the nanowire core is 60 %. Concerning the ZnTe inclusion, photoluminescence intensity becomes maximum when the polarization angle is parallel to the nanowire axis and by extent to the dot quantization axis. This is a strong indication of a light hole type ground state where the strongest contribution to photoluminescence emission is from an electric dipole oriented parallel to the nanowire axis (see the optical selection rules are presented in Fig. 1.3). The polarization degree of photoluminescence emitted from the ZnTe inclusion is 90%.

Although for this particular case we have a strong indication that the photoluminescence emitted from the ZnTe inclusion has a strong π type contribution, associated to a light hole transition, it is difficult to quantify the fraction of light hole component in the ground state. The fact that photoluminescence intensity becomes stronger for a polarization angle parallel to the nanowire axis could be due to the effect of dielectric screening which suppresses the rotating dipole oriented perpendicular to the nanowire axis. This effect will be discussed in more detail in section 4.4.3. Another issue is that from nanowire to nanowire there is some dispersion and the measurements are not always the same. In total we measured the degree of polarization of 5 nanowires, where in two of them we observed that emission from the ZnTe quantum dot is oriented parallel to the nanowire axis. In the other three, the ZnTe quantum dot emission
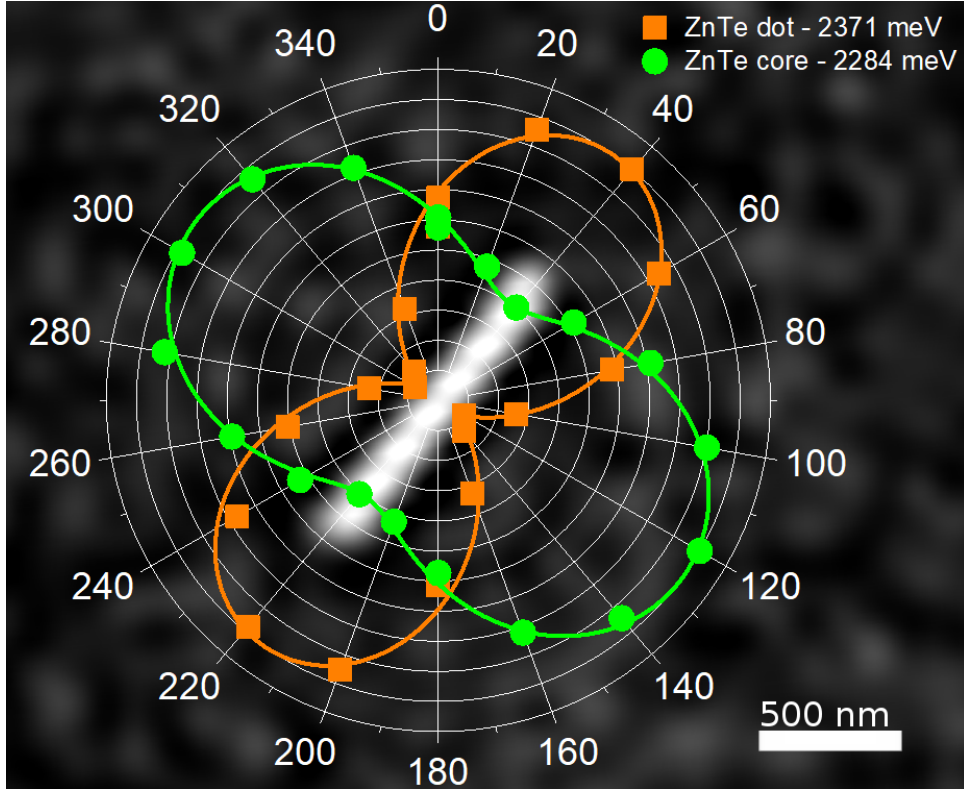
Figure 4.9 – Normalized photoluminescence intensity of a single nanowire as a function of the polarization angle in emission. The green circles correspond to the signal recorded from the nanowire core and the orange squares from the ZnTe inclusion. Both emissions are fitted using Malus's law.

was rotated with respect to the wire axis, however the degree of polarization was near 90%. A possible explanation for this, is that the quantization axis of the dot is also rotated in respect to the nanowire axis.

From these observations it becomes evident that more measurements need to be carried out like polarization resolved Fourier spectroscopy.

In order to confirm that the emission at 2365 meV corresponds to the one of a ZnTe quantum dot, we had to carry out autocorrelation measurements in order to measure the second order correlation function $g^2(\tau)$. In order to perform this measurement, we had to reduce the excitation power up to the point where any overlapping emission to the main peak would be suppressed. At the same time however, we would still need to record a sufficient number of counts on the APDs so as to integrate for a reasonable amount of time. This was not easy since even at power as low as 0.2 μW we could still record two lines with significant overlap in emission. Finally, for the measurement the power was lowered to 1 μW, providing us with a marginal number of counts in the order of 10^3, which is already very low. The total integration time to record the second order correlation function was 17 hours and the autocorrelation measurements result for W-1 is shown in Fig. 4.10.

Of course the result is not what we would expect from an autocorrelation measurement, but we cannot rule out however that the presence of a characteristic deep (in our case $g^2(0) \approx 0.6$) could be an indication of single photon emission. On the other hand the curve is very noisy and the abrupt increase in both sides raises questions about the validity of the measurement. It has been reported for Si based APDs, that the charge carriers avalanche is accompanied by the emission of photons [68], [69]. If the number of counts from the single photon source on the APDs is not large enough this effect does alter the measurement, as in our case.
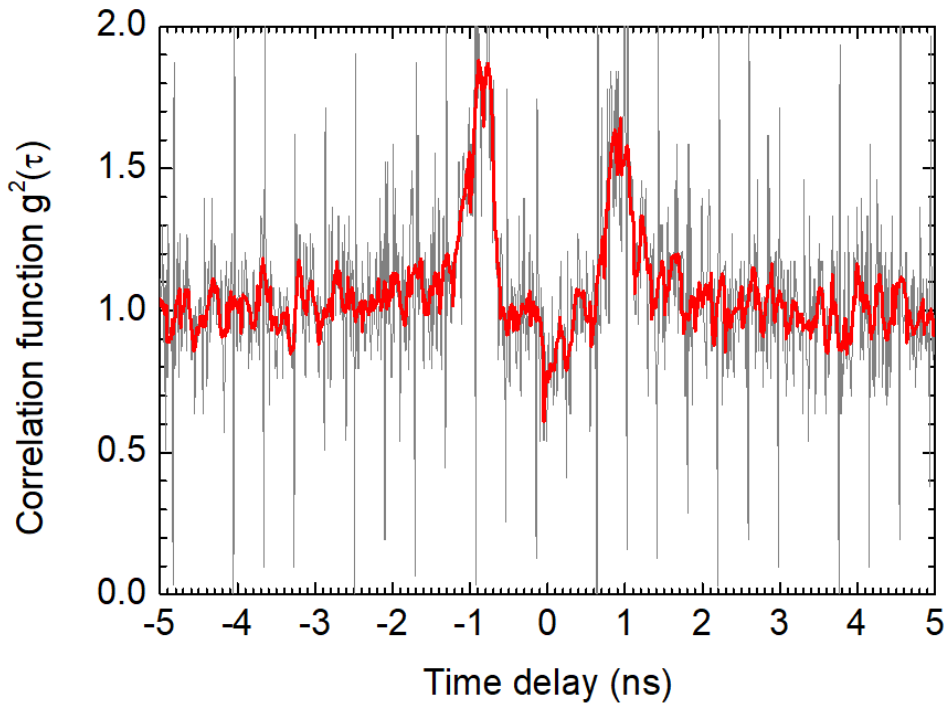
Figure 4.10 – Autocorrelation curve using 1 μW excitation power. The spectrometer grating was centered at 2371 meV, corresponding to the lowest energy peak of the ZnTe inclusion

The final measurement we did on this sample was cathodoluminescence. On purpose we didn't do the measurement on the nanowires we studied extensively with micro-photoluminescence in order not to destroy them. This was in case we planed to perform any future measurements to them. Instead we measured another nanowire designated as W-2, with similar behaviour in emission to others and we carried out the measurement on it.

The cathodoluminescence measurements results for W-2, are shown in Fig. 4.11.
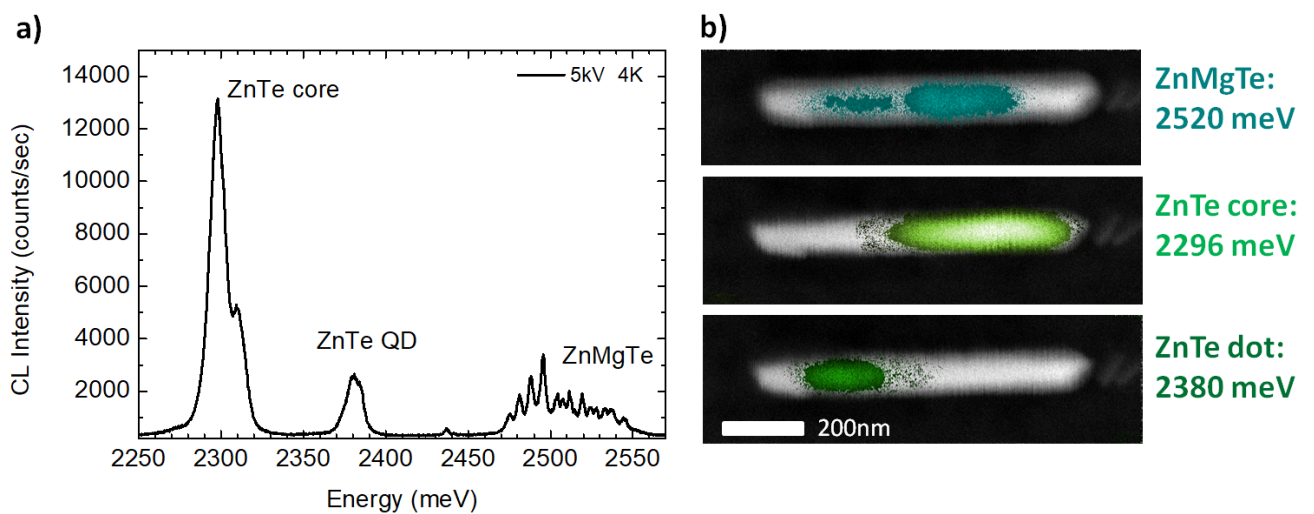
Figure 4.11 – Cathodoluminescence spectrum of a single nanowire a) amnd superposition of cathodoluminescence as recorded for different energies, superimposed with the nanowire SEM image.

Similar to micro-photoluminescence measurements, from the cathodoluminescence spec-

trum, we identified three regions of emission. Also the intensity of light emitted at higher energies, which is attributed to ZnMgTe, is stronger. At 2296 meV we record a bright emission starting from the bottom of the nanowire which extends along its axis. This emission originates from the ZnTe core. At 2380 meV we recorded the light emitted from a region localized above the nanowire core, which we attribute it to the ZnTe inclusion of smaller dimensions. At 2520 meV which is the center of the broad emission at high energies we record signal all along the nanowire axis. This is light emitted from ZnMgTe. The fact that intensity varies along the nanowire axis, is a confirmation of the non-uniformity of ZnMgTe. If we scan along the broad ZnMgTe emission, we observe that at different energy peaks, light intensity becomes stronger close to the top and weaker to the nanowire bottom.

The cathodoluminescence distribution from the three different regions along the nanowire axis, is in good agreement as regards to what we expect for the structure of this sample. Also from the emission of ZnMgTe we expect a Mg content of near 20%. As a result, we would expect to record the emission from ZnTe core close to the energy position of W-1 which we studied by micro-photoluminescence. The emission energy however of ZnTe for W-2, is blueshifted by 11 meV which according to the fit for strain induced redshift, corresponds to a Mg content of 19%.

From the study carried out so far, it seems indeed that there is an inclusion of ZnTe confined in three dimensions by a ZnMgTe barrier where the Mg content is near 20% corresponding and $2Q = 50$ meV. However, a clear confirmation of quantum dot like confinement from autocorrelation measurements remains to be done.

4.2.0.2 Numerical calculations

In order to understand better the valence band ground state properties of this structure, we also had to run numerical calculations, in a similar way we did for the CdTe quantum dot. In Fig. 4.12 we present the evolution of the valence band energy levels, as a function of the quantum dot aspect ratio, L_{QD}/D_{QD}. The calculations were carried out before analyzing the data obtained from optical spectroscopy, as a result we used the Mg content expected from growth conditions which is near 12%. For this series of calculations we used a chemical valence band offset between ZnTe and ZnMgTe of 73 meV.
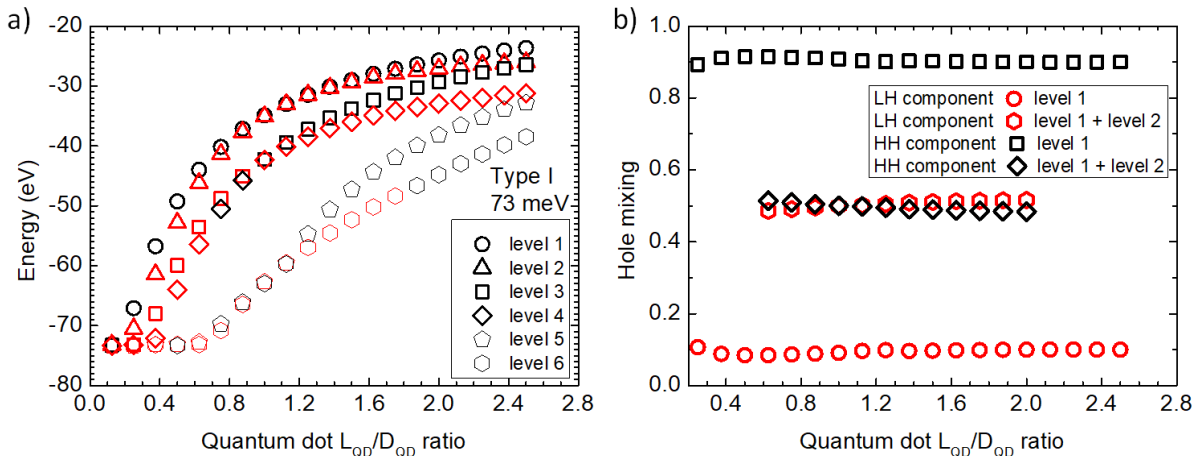
Figure 4.12 – Valence band energy levels of the first six Kramers doublets as a function of the quantum dot L_{QD}/D_{QD} ratio, for a ZnTe quantum dot in a $Zn_{0.88}Mg_{0.12}Te$ nanowire where the dominant hole component of each state is designated accordingly a). Mixing between heavy and light holes as a function of the L_{QD}/D_{QD} ratio b).

As shown in Fig. 4.12 a), for $L_{QD}/D_{QD} < 0.6$ the ground state is predominantly heavy hole. For $0.7 < L_{QD}/D_{QD} < 1.9$ the first two calculated energy levels come close and the energy

separation between heavy and light holes becomes very small. For $L_{QD}/D_{QD} > 2$ the energy difference between heavy and light holes start to increase and the ground state is predominantly a heavy hole. In Fig. 4.12 b) we present the contribution of each hole component considering both one and two Kramers doublets. If we look only at the first Kramers doublet, the ground state for all L_{QD}/D_{QD} is 90% heavy hole. On the other hand, for $0.9 < L_{QD}/D_{QD} < 1.9$, if one considers degeneracy between the first two Kramers doublets, then heavy holes become strongly mixed to light holes with a contribution near 50%. These results, could be an explanation why we do not confirm single photon emission from autocorrelation measurements. For our samples we expect an aspect ratio $L_{QD}/D_{QD} = 0.5 - 0.7$, which means that we possibly record signal associated to two transitions. Moreover, from the micro-photoluminescence spectrum and after a Gaussian fitting, we indeed resolve two overlapping lines separated by 1.5 meV. A possible explanation is by attributing that to two transitions associated to heavy and light hole.

To summarize:

• In these calculations, for a Mg content of 12% and $2Q = 30$ meV we do not observe switching from heavy to light hole.

• For $L_{QD}/D_{QD} > 2$ the valence band ground state is a heavy hole, as expected from strain.

• For $L_{QD}/D_{QD} < 0.6$, heavy hole ground state is in agreement with confinement

• For $0.7 \leq L_{QD}/D_{QD} \leq 1.9$ the splitting between heavy and light holes is small and experimental observations depend on the resolution.

Discussion

In this part we analyze the results by taking into account the confinement energy and strain from Eshelby's model, as discussed in Chapter 1, section 1.3. This treatment was originally proposed by Joël Cibert. At first we need to carry out an estimation for the confinement energies of heavy and light holes, which they are along (111) direction for an infinitely deep parallelepipedic dot

$$
\begin{aligned}
E_{HH} &= \frac{\hbar^2}{2m_0}(\gamma_1 - 2\gamma_3)\left(\frac{\pi}{L}\right)^2 + \frac{\hbar^2}{2m_0}(\gamma_1 + \gamma_3)\left(\frac{\pi}{D}\right)^2 \\
E_{LH} &= \frac{\hbar^2}{2m_0}(\gamma_1 + 2\gamma_3)\left(\frac{\pi}{L}\right)^2 + \frac{\hbar^2}{2m_0}(\gamma_1 - \gamma_3)\left(\frac{\pi}{D}\right)^2
\end{aligned}
\tag{4.2}
$$

where γ_1 and γ_3 the Luttinger parameters. These expressions are obtained by neglecting the off-diagonal terms of Luttinger Hamiltonian. For a quantum dot with $L_{QD} = 6$ nm and $D_{QD} = 10$ nm it is $E_{HH} = 31$ meV and $E_{LH} = 85$ meV. For the real structure where the valence band offset is 77 meV, we expect strongly reduced confinement energy. By considering a weaker confinement for heavy and light holes respectively we can assume a phenomenological dependence in the form

$$
E_{HH}\left(\frac{D}{L}\right)^a \quad and \quad E_{LH}\left(\frac{D}{L}\right)^a
\tag{4.3}
$$

where E_{HH}, E_{LH} and $a < 2$ are adjustable parameters. As already mentioned in Chapter 2, the splitting between heavy and light hole is $2Q$ and it is proportional to the analytical expressions of Eshelby's model (discussed in the introduction) describing the shear strain of an ellipsoidal inclusion in an infinite matrix. For (111) direction, Q is given by

$$
Q = \frac{d_v}{2\sqrt{3}}\left(\varepsilon_{zz} - \frac{\varepsilon_{xx} + \varepsilon_{yy}}{2}\right)
\tag{4.4}
$$

where d_v the deformation potential. We can then plot the evolution of energy as a function of the L_{QD}/D_{QD} ratio through the expressions

$$E_{hh} = E_0 + E_{HH} \cdot \left[\left(\frac{D}{L} \right)^a - 1 \right] + Q(L/D)$$

$$E_{lh} = E_0 + E_{LH} \cdot \left[\left(\frac{D}{L} \right)^a - 1 \right] - Q(L/D)$$

(4.5)

where E_0 is the energy term taking into account other effects like lateral confinement.
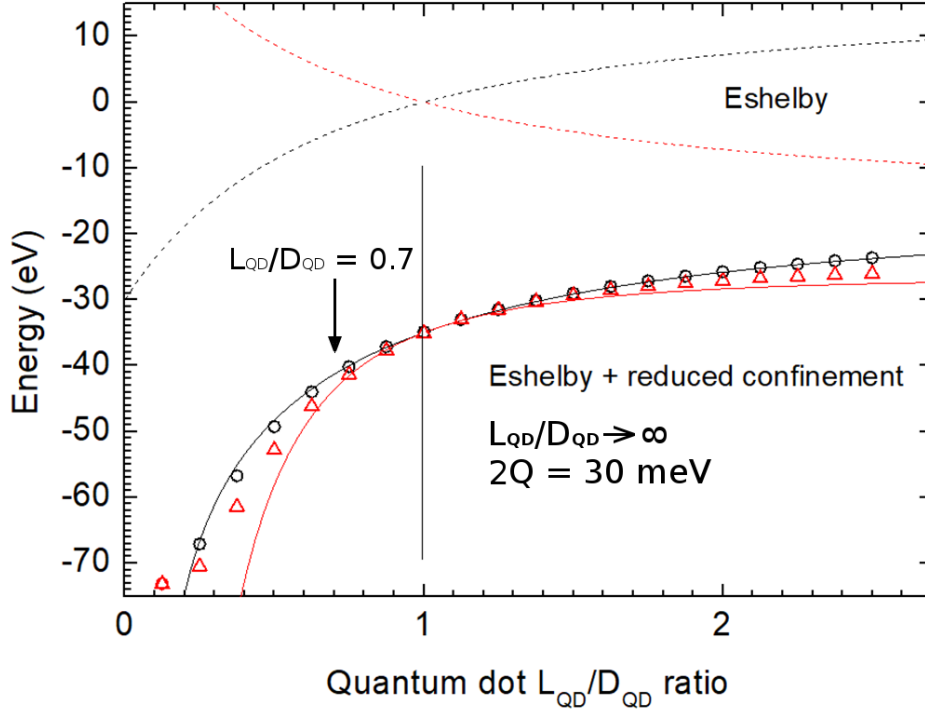
Figure 4.13 – The first two calculated energy levels as a function of L_{QD}/D_{QD} ratio, superimposed for comparison with the analytical equations of Eshelby's model for a ZnTe quantum dot in a $Zn_{0.88}Mg_{0.12}Te$ nanowire.

In Fig. 4.13 we present the first two calculated energy levels as a function of L_{QD}/D_{QD} using both the results of numerical calculations and those of Eshelby's model. The diameter D_{QD} is constant and we modify only the nanowire length L_{QD}. For a core-shell configuration ($L_{QD}/D_{QD} \to \infty$) the splitting between heavy and light hole due to strain is $2Q = 30$ meV. The energy values of the adjustable parameters for producing the curves, are respectively $E_{HH} = 3.5$ meV, $E_{LH} = 24.5$ meV and $a = 1.2$. As expected the values are smaller to those describing the energy levels of a heavy and a light hole in an infinitely deep quantum dot.

From the calculations it becomes clear that in order to promote a light hole for $L_{QD}/D_{QD} < 1$, we have to increase the induced shear strain and by extent the content of Mg. The drawback is that for a Mg content above 40% the semiconductor compound starts to become unstable in standard conditions making any experimental measurement (if not in-situ) particularly difficult.

As a conclusion, for a Mg content of 12 %, the kinetic energy destabilizes the light hole in a flat tensile quantum dot and this is shown qualitatively by using Eshelby's model, and by estimating the hole confinement energy. In a flat quantum dot with tensile mismatch, confinement and strain have opposite effects. As an example, in [23] the induced strain was increased up to the point that the light hole was favored by more than the linewidth of 100 μeV. A ZnTe quantum dot in a $Zn_{0.8}Mg_{0.2}Te$ is an example where the contribution of strain and confinement are particularly well balanced.

From the calculations we confirm no switching from heavy to light hole. On the other hand, for $L_{QD}/D_{QD} \approx 0.7$ the splitting between heavy and light holes is probably smaller than the resolution of our experimental setup. This is not in contradiction with experiments. Looking at the polarization dependent measurements in Fig. 4.9, emission from the ZnTe quantum dot is strongly polarized along z axis which is indicative of a π transition. This could be attributed to a light hole state mixed with heavy holes where $\sigma^{\pm}$ transitions are suppressed due to dielectric screening.

4.3 Probing a spin texture in a type II ZnSe ZnTe nanowire quantum dot

In this section we want to investigate, the formation of a skyrmion like a spin texture in a type II ZnSe-ZnTe nanowire quantum dot. Skyrmions in magnetic structures are currently studied [70], [71], but similar spin textures can be designed in a type II DMS nanowire. In this type of heterostructure, the valence band offset between ZnSe and ZnTe is a strong type II, as a result the hole envelope will leak towards the interface and outside the inclusion as we have shown in the calculations presented in Chapter 2. The lattice parameter of ZnTe is $a_{ZnTe} = 6.104$ Åand the parameter of ZnSe $a_{ZnSe} = 5.667$ Å, consequently strain becomes tensile in xy plane for a flat inclusion and tensile along z for an elongated one.
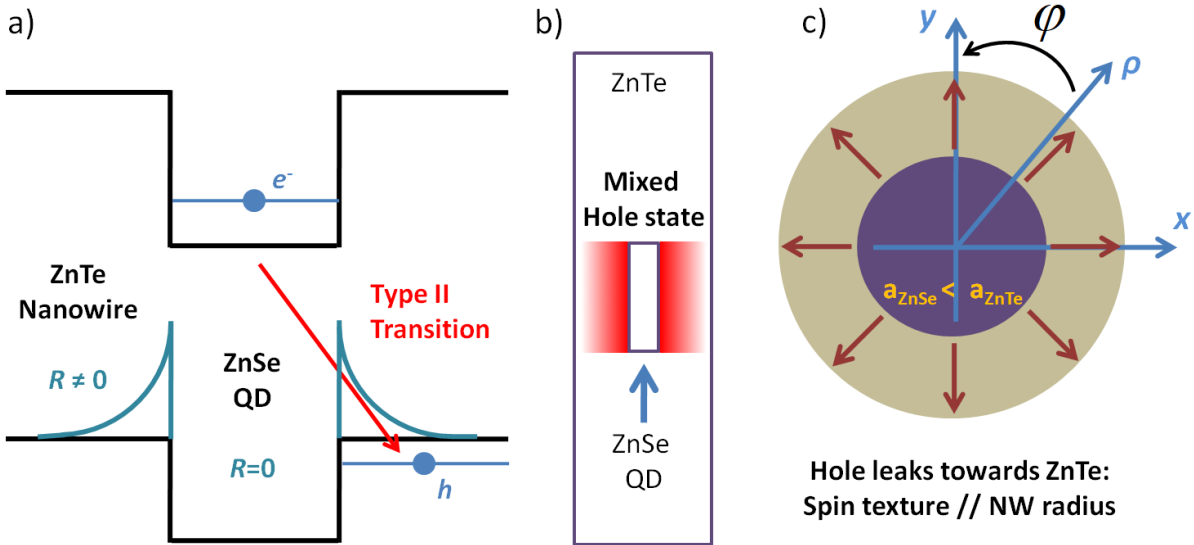
Figure 4.14 – The profile of a type II band alignment similar to that we expect for a ZnSe inclusion in a ZnTe nanowire a). Schematic representation of hole ground state leaking towards ZnTe b). The spin texture oriented parallel to the nanowire radius imposed by the strain c).

The band alignment of a ZnSe - ZnTe nanowire - quantum dot is strong type II, near 1 eV [72], [73]. In another work, a valence band offset of 880 meV is reported [74]. A type II band alignment is shown schematically in Fig. 4.14 a). Due to the strong type II band alignment, confinement vanishes and the hole wavefunction will be localized in the shell. A qualitative sketch of the leaking hole wavefunction is shown in Fig. 4.14 b). As we have shown in Chapter 2, the R component of Bir-Pikus Hamiltonian is zero in the dot, but outside dot $|R| \propto \frac{1}{\rho}e^{-2i\phi}$ [53], therefore the valence band ground state is confined near the ZnSe/ZnTe interface and light holes get strongly mixed with heavy holes. $|R|$ depends on the angle ϕ, consequently the mixing of light holes with heavy holes will also be angle dependent. This mixing is responsible for the formation of a complex spin texture. Since $a_{ZnSe} < a_{ZnTe}$, mismatch is tensile and

we expect that the strain field will promote a non uniform radial spin orientation within the envelope function, as shown in Fig. 4.14 c). For an opposite mismatch we expect a tangential spin texture.

The growth protocol for this nanowire heterostructure was similar to that used for the growth of CdTe quantum dots in ZnTe nanowires. The difference here is that CdTe gets replaced by ZnSe growth. By analyzing SEM images the nanowire diameter was 30 nm - 60 nm and their length varied from 800 nm - 1 μm. Following the usual procedure for the micro-photoluminescence measurements, the nanowires were dispersed on patterned Si substrates. For the measurements we used a 405 nm diode laser as we anticipated, alongside ZnTe photoluminescence, to record also some very weak emission from ZnSe in the range 2450 meV - 2550 meV. This is a typical value for an optically bright transition in a ZnSe quantum dot. The micro-photoluminescence results from individual nanowires however were very surprising.
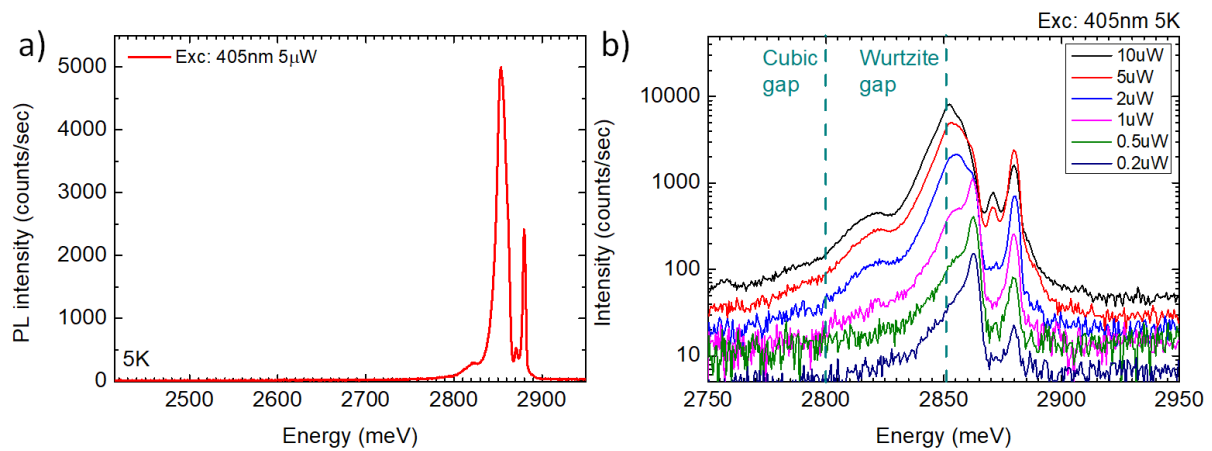

Figure 4.15 – Micro-photoluminescence spectra of a single ZnTe nanowire with a ZnSe inclusion (as predicted according to growth conditions) a). Micro-photoluminescence from the same nanowire for different excitation powers b).

In Fig. 4.15 a) we present the micro-photoluminescence spectra from a single nanowire -named as W-3- dispersed on Si substrate. The emission range was from 2820 meV - 2890 meV, originating only from ZnSe, since ZnTe emits in lower energies (2240 meV to 2340 meV) as we saw in previous sections. More specifically, the main emission near 2850 meV is attributed to the wurtzite gap of ZnSe [75], while the lines at higher energy may result from residual Te inclusions [76]. From the emission spectrum we understand that the properties of this heterostructure are not those expected, in accordance at least with the growth protocol, as we recorded photoluminescence originating only from ZnSe. From power dependence measurements, as shown in Fig. 4.15 b), we observe a broad emission consisting of many lines which vary linearly or quasi-linearly with excitation power, confirming a typical nanowire emission.

Nanowires from the same sample were further studied by EDX spectroscopy, in collaboration with Eric Robin.
In Fig. 4.16 we present the EDX measurements carried out on nanowires W-5a and W-5b. From these measurements, we confirm our assessments deduced by the analysis of micro-photoluminescence spectra. All along its axis the nanowire is constituted of ZnSe, where in some cases, a weak Te distribution near the bottom is observed. Near the tip of the nanowire is localized a small ZnTe segment which, from micro-photoluminescence measurements at least, is optically inert.
To finalize the optical characterization of this sample, we carried out cathodoluminescence measurements in order to identify the origin and distribution of light emission along the nanowire axis. In Fig. 4.17 we present the cathodoluminescence emission from at 2883 meV, obtained
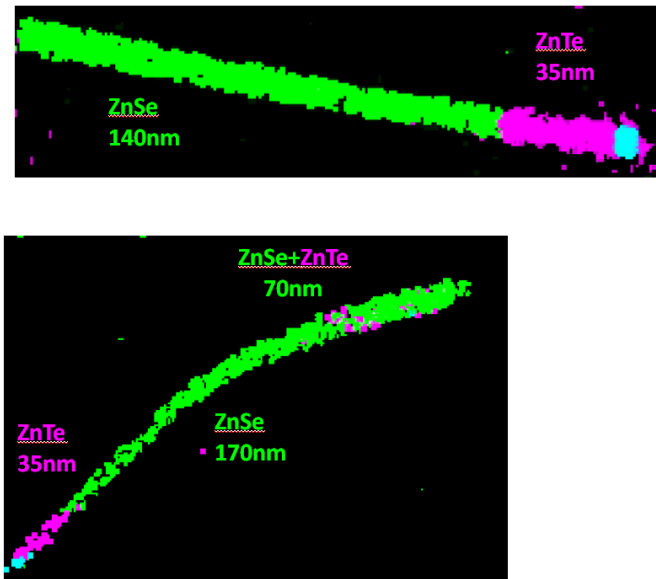
Figure 4.16 – EDX measurements of single nanowires, where along their axis they are composed almost exclusively of ZnSe with some Te inclusions near to the bottom. The nanowire tip is constituted of ZnTe, while at the top we see the catalyst Au droplet.
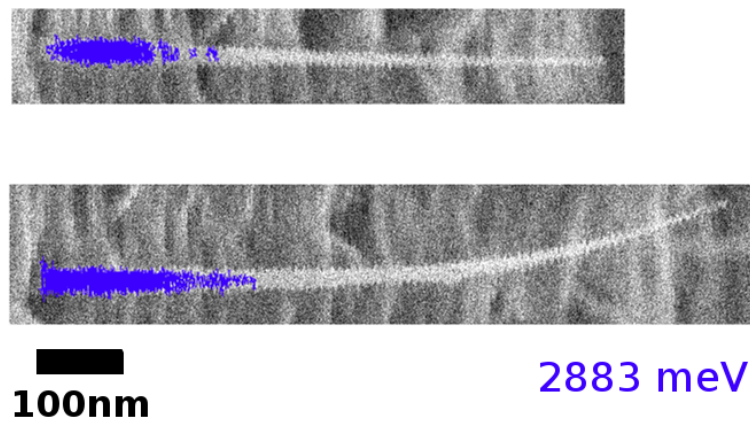
Figure 4.17 – Cathodoluminescence emission from two nanowires recorded directly from the as-grown sample. The emission is at 2883 meV and the temperature 5 K.

directly from the as-grown sample for two different nanowires. We named these nanowires as W-4 and W-5. We attempted to perform the measurement on a dispersed nanowire, but the signal was bleaching very quickly, without being able to retrieve it again afterwards. This is an indication that the electron beam damages the nanowire and it is something we have observed all the times when we attempted to measure II-Se based heterostructures. The recorded cathodoluminescence always originates from the bottom of the nanowire, as we approach the tip, the objects become dark. From studies carried out on ZnTe nanowires [65] it was demonstrated that cathodoluminescence efficiency does not change along the nanowire axis. As regards cathodoluminescence intensity however, it is determined by the excitation density which is proportional to the square of nanowire diameter, D^2 [65]. This explains why as we approach the tip, where the diameter becomes smaller, cathodoluminescence emission vanishes.

From all optical measurements we carried out so far, it seems that the structures we are studying are pure ZnSe nanowires. This initially was confusing but by looking at literature we found reports of atom substitution during epitaxial growth or processing. Some examples are the heat induced substitution of GaAs by Au [77], [78] , the formation of NiInAs in InAs nanowire by solid source reaction [79] and the thermal diffusion of Fe [80] or Ni [81],[82] to Si nanowires with the subsequent formation of Fe_3Si and NiSi alloys respectively. As regards the II-VI materials, there was also one report describing the transformation of ZnTe to CdTe nanowires through vapor transport [83].

From the information reported in literature and from our results, we confirm that Se attacked Te during growth and that the ZnTe core is transformed into ZnSe. Some Te inclusions are expected but additional measurements are required in order to verify the crystalline quality and Se distribution in the nanowire.

Although through this method we didn't achieve the anticipated heterostructure, the results are far from discouraging. Since the growers managed to grow a ZnSe core nanowire the second step is to attempt and deposit a ZnTe shell around it. If growth is successful then we will have a core-shell ZnSe-ZnTe nanowire which is very similar to the structure we want to study, where we expect to reveal a spin texture. In parallel, for understanding the spin properties of this structure we need to carry out numerical calculations similar to those presented in Chapter 3. To conclude, this is a very interesting system to investigate and challenging to implement.

4.4 Compressive Cd(Mn)Te quantum dots in ZnTe nanowires

4.4.1 Description of samples

As regards heterostructures incorporating Cd(Mn)Te quantum dots we studied 14 samples grown under different conditions, the structural and by extent the optical properties of which, varied significantly. In this text we focus only to those from which we obtained the most interesting and conclusive results.

The nanowires were grown by molecular beam epitaxy on a ZnTe buffer layer deposited on (111) GaAs substrates, through the vapor-solid-solid (VSS) mechanism [84] where a gold droplet acts as a catalyst. In general we can separate the samples in two main categories, those passivated with a ZnMgTe shell and those without. II-VI materials are sensitive to oxidation, as a result without passivation a bad quality oxide forms around the nanowire core, which degrades the overall optical quality of the nanowire. On the contrary and as we will see in the following section, the nanowires with the external ZnMgTe shell were very bright and we could easily identify the emission from the nanowire core and the quantum dot and further proceed with the optical characterization. The growth of nanowires without the shell however, was useful in order to extract the dimensions (length, diameter) of the ZnTe core, by analyzing the corresponding SEM images. The length of the nanowire core varied from 600 nm to 900 nm and the diameter from 25 nm to 50 nm.

Since our objective was to stabilize a light hole ground state, the conditions were optimized in order to achieve the growth of an elongated quantum dot. Finding the proper growth conditions was a demanding task, for that reason the growers had to prepare several series of trial samples. In Fig. 4.18 a) we present a sketch of the cross-section of the nanowire heterostructure. In Fig. 4.18 b) we present a SEM image of a dispersed nanowire on Si substrate, similar to those on which we performed the optical measurements. The diameter of the nanowires varied from 120 nm - 150 nm and their length from 1 μm - 1.2 μm. From this significant increase in both length and diameter we understand that the ZnMgTe shell was grown successfully.

From SEM images we can extract information as regards the nanowire dimensions as a whole, but for a detailed study of the chemical composition and dimensions of the quantum dot, EDX measurements were required.

Figure 4.18 – Schematic representation of the cross section of an as-grown ZnTe-ZnMgTe core-shell nanowire, incorporating an elongated CdTe quantum dot a). SEM image of a dispersed nanowire on a Si substrate similar to those we carried out the micro-photoluminescence measurements b).
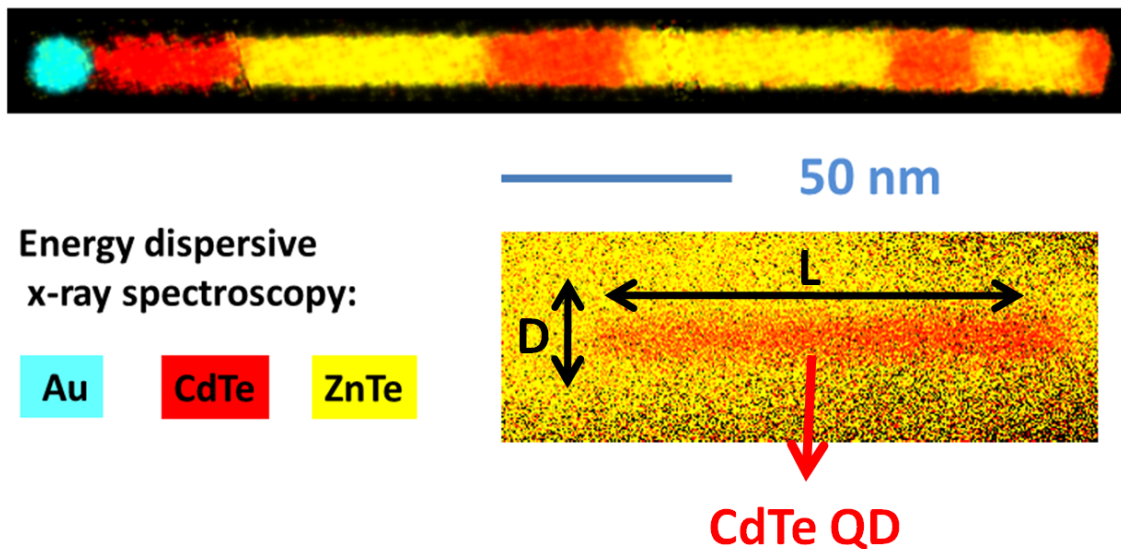
Figure 4.19 – Multiple CdTe inclusions of varying length in a ZnTe nanowire (top). An elongated CdTe quantum dot in a ZnTe nanowire (bottom). This nanowire is from sample m3393 which we also studied with micro-photoluminescence spectroscopy. Image taken from [85]

In Fig. 4.19 (top) we present the EDX results for a ZnTe a nanowire, where multiple inclusions of CdTe were grown. By growing samples like this, the growers developed a model predicting the growth rates of ZnTe and CdTe [85]. Through this model the optimal conditions required, in order to grow an elongated quantum dot were assessed. Here, we also underline the importance, alongside with dimensions, to be able to control Cd content and distribution. Indeed we confirm

that long dots with sharp ZnTe-CdTe interfaces can be grown. In the bottom of Fig. 4.19 we present an EDX profile of a nanowire taken from the same sample we used for the optical measurements. The length of the quantum dot was $L_{QD} \approx 90$nm and diameter $D_{QD} \approx 10$nm, resulting an aspect ratio close to 9.

As we discussed in the introduction, the valence band offset between CdTe and ZnTe is not known exactly, but it is small and it may vary from type I to type II. Introduction of Mn in CdTe, which is required for the magneto-optical measurements, further reduces the valence band offset between the dot and the barrier, switching to type II. This is attributed to the fact that Mn doping increases the gap of CdTe. This results in a stronger leaking of the hole wavefunction, thus increasing the value of the quantum dot aspect ratio L_{QD}/D_{QD}, required for the switching from heavy to light hole. This effect is explained in detail in Chapter 2, at sections 2.4.2 and 2.4.3. In order to tackle this issue and restore confinement, a ZnMgTe barrier was grown around the Cd(Mn)Te quantum dots [59]. A sketch of the nanowire we studied is shown in Fig. 4.20 a).

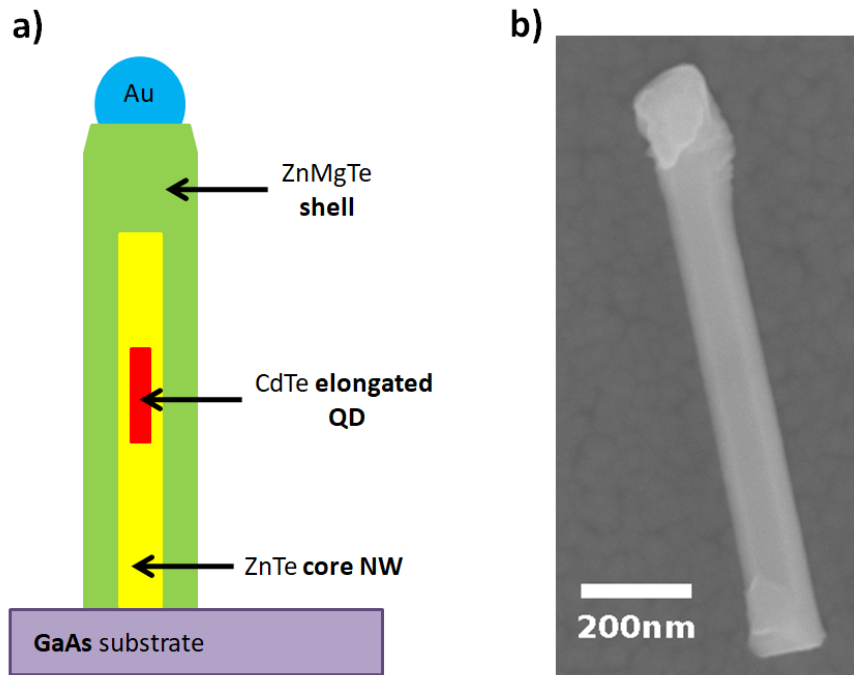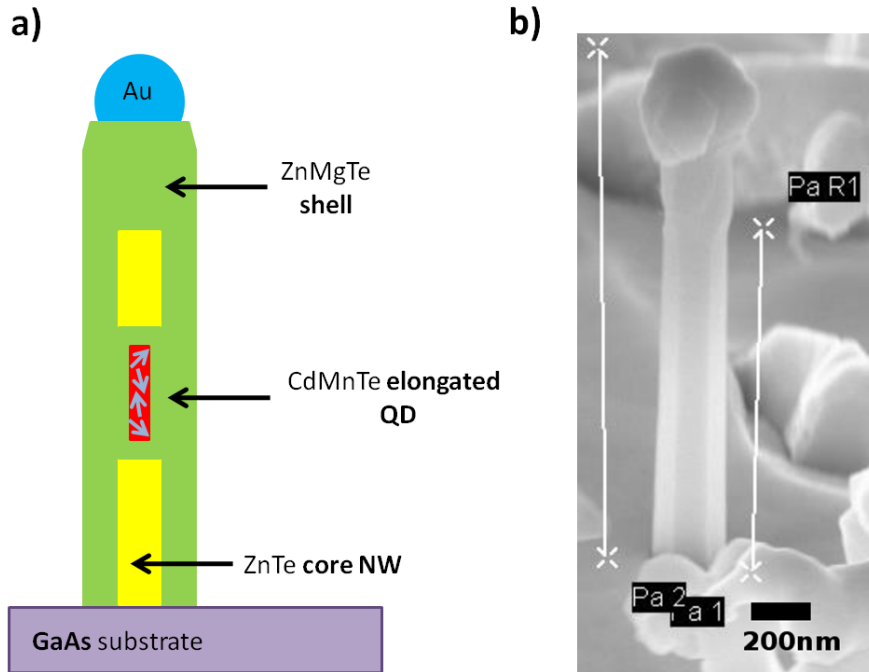Figure 4.20 – Sketch of the cross section of an as-grown ZnTe-ZnMgTe core-shell nanowire, with an elongated CdMnTe quantum dot, surrounded by ZnMgTe a). SEM image of the as-grown sample showing a nanowire similar to that we performed the micro-photoluminescence measurements.

The growth conditions for the Mn doped nanowire quantum dots were similar to those employed for a sample with $L_{QD}/D_{QD} \approx 2$, as described in [59]. The difference in our case, is that before and after the growth of the quantum dot, a layer of ZnMgTe was grown. The parameters during the growth of the CdMnTe quantum dot, were adjusted in order to achieve a nominal Mn concentration of 10%. In Fig. 4.20 b) we present a nanowire image directly from the as-grown sample. The length of nanowires varied from 1.2 μm to 1.5 μm and the diameter from 150 nm to 200 nm.

For these nanowire quantum dots, up to the point this report is written there were no EDX measurements. As we will see though in the following sections, their photoluminescence spectra are similar to those of the nanowires without the magnetic ions, with the exception of anticipated line broadening from the quantum emission due to Mn spin fluctuations .

4.4.2 Light hole ground state in a non magnetic CdTe quantum dot

In this section we discuss the valence band ground state properties by analyzing the micro-photoluminescence measurements results obtained from two nanowires.

Figure 4.21 – Full micro-photoluminescence spectrum from which we identified the emission from ZnTe core and CdTe dot a). Micro-photoluminescence emission from the CdTe quantum dot where we resolved the emission from exciton X and biexciton XX.

In Fig. 4.21 a) we present the full micro-photoluminescence emission from nanowire W-6. From this spectrum we observe a weak emission at 2250 meV, possibly attributed to ZnTe. This energy however is smaller in comparison to that of other nanowires. the emission from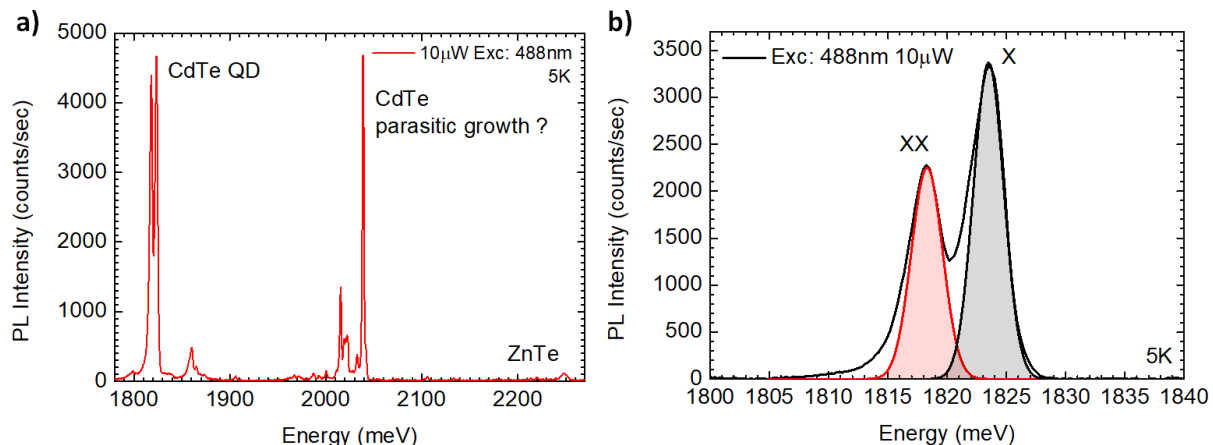 CdTe inclusion redshifted in the range of 1800 meV to 1830 meV and finally some lines between the emission from the core and the dot, from 1960 meV to 2050 meV which we attributed to parasitic or side wall CdTe growth, similar to that reported in [86]. From the numerical calculations and for a weak type I elongated quantum dot with $L_{QD}/D_{QD} = 2.25$ the electron - hole transition energy is 1844 meV. The 25 meV redshift from the experimental measurements could be attributed to the larger piezoelectric potential as the inclusion is much longer in comparison to that studied numerically. We do not take into account also the exciton binding energy which further reduces the emission energy, as it becomes negligible due to large piezoelectric potential.

In order to record the spectra, we used a filter at 500 nm to block the laser, as a result we do not have any information concerning the emission from ZnMgTe. From the quantum dot spectrum, as shown in Fig. 4.21 b) we resolved two lines centered at 1818.3 meV and 1823.5 meV. From a Gaussian fitting we deduced that the line-width of both peaks is 3 meV. The emission is much broader with respect to what is typically expected for a quantum dot (100μeV) and this is attributed to spectral diffusion [87], which is essentially the exciton Stark shift induced by charge accumulation on the nanowire surface (time dependent fluctuations). This effect is commonly encountered in II-VI materials.

In Fig. 4.22 a) we present the photoluminescence spectra of the CdTe quantum dot of nanowire W-6 for different excitation powers, which is a common way to identify the excitonic transitions. At large powers, the peak at high energy which corresponds to the exciton is saturated. As power decreases, the intensity of emitted light from the peak at low energy, decreases abruptly and below 20 μW emission from the line at high energy becomes stronger. This is a typical behaviour of excitons and biexcitons confined in a quantum dot and is better presented in Fig. 4.22 b). In the same figure, by fitting the slopes of the intensity versus power in a log-log plot at low power and below switching, we retrieve the values m=1 for the line at high energy and m=2 for the line at low energy. This is the signature of an exciton and a biexciton respectively with a linear and a quadratic dependence with the excitation power.

A very important measurement in order to verify that indeed the CdTe inclusion is a quan-
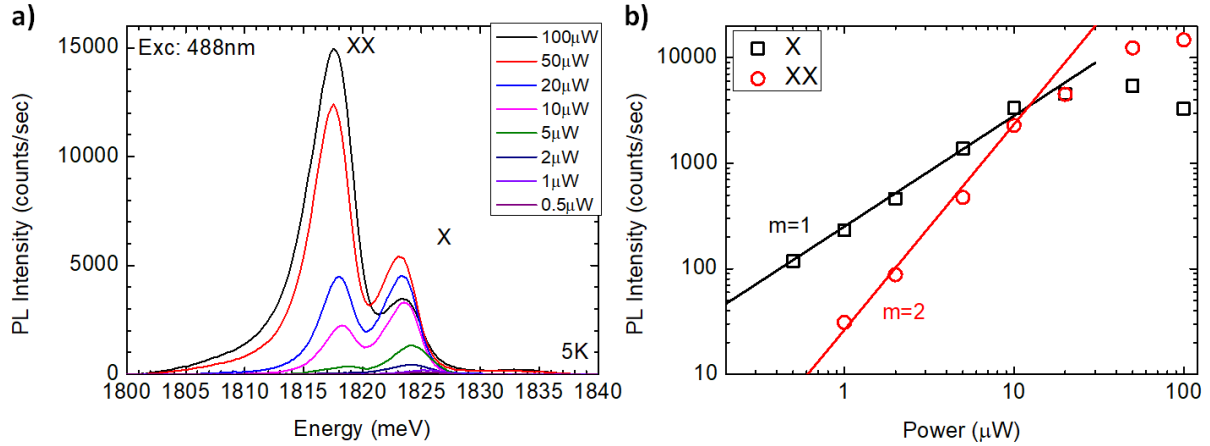
Figure 4.22 – Quantum dot emission spectra for different excitation powers a) Peak intensity of photoluminescence emission from exciton and biexciton as a function of excitation power at logarithmic scale with the corresponding linear fit.

tum dot, is autocorrelation. In Fig. 4.23 we present autocorrelation measurement result for the quantum dot exciton line at 1823.5 meV for nanowire W-6.
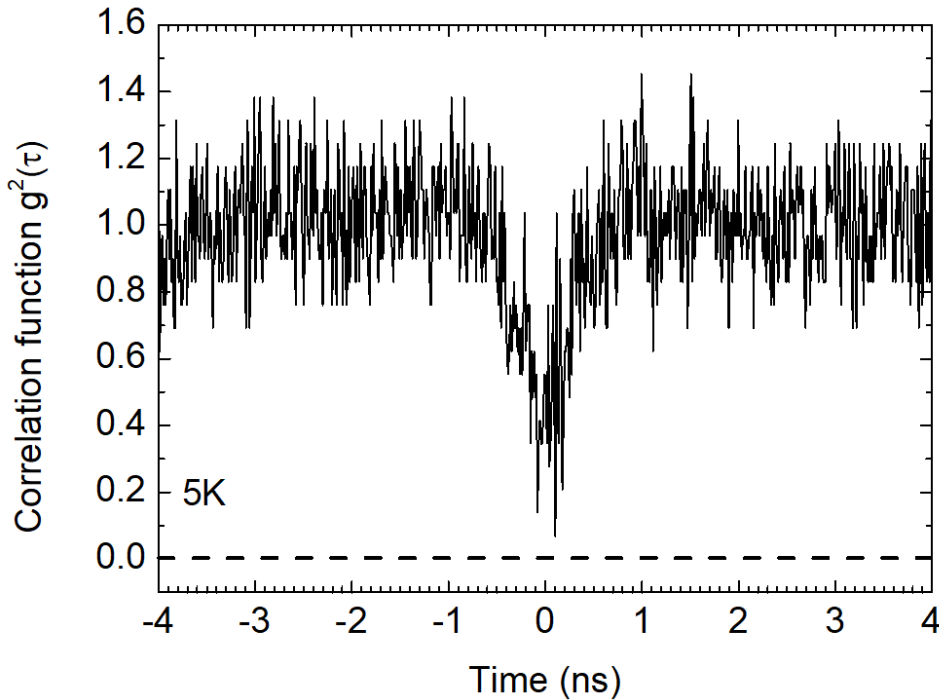
Figure 4.23 – The second order correlation function $g^2(\tau)$ measured for the exciton line at 1823.5 meV. The excitation power we used for the measurement was 1 μW.

From the second order correlation function we observe the characteristic anti-bunching where $g^2(0) = 0.35$. This is indicative of a single photon source and a confirmation that the CdTe inclusion is a quantum dot. In another nanowire discussed later we will develop an accurate way to analyze the second order correlation function measurements and extract the characteristic time.

Although the results obtained from the quantum dot of wire W-6 were very promising, as our study progressed we traced a major drawback which made imperative the search for another nanowire. The problem was that this nanowire was both kinked and broken. This

was not obvious from the first SEM observation as for the substrate mapping we used low magnification. When we did cathodoluminescence measurements though we saw clearly that the object we measured was part of a kinked nanowire which was broken and attached to another nanowire. This is shown in Fig. 4.24.
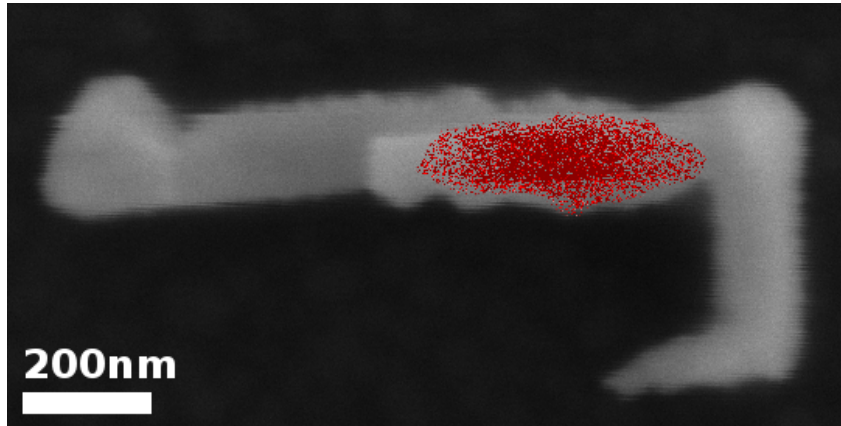
Figure 4.24 – Cathodoluminescence measurement from a broken and kinked nanowire attached on another nanowire. Emission energy shown in red is at 1823 meV (680 nm).

From the SEM image we confirm that someone could be easily confused and consider this object as a single nanowire which was just kinked at the top, especially with a low magnification image similar to that used for the navigation on the patterned substrate. This could also possibly explain the very weak emission from ZnTe, as both objects are broken.

This was one of the first nanowires we attempted to measure from this sample. When we tried to look for new candidates we made sure that indeed we measured an elongated and uniform object. In Fig. 4.25 a) we present the full photoluminescence spectrum obtained from another nanowire, designated as W-7.
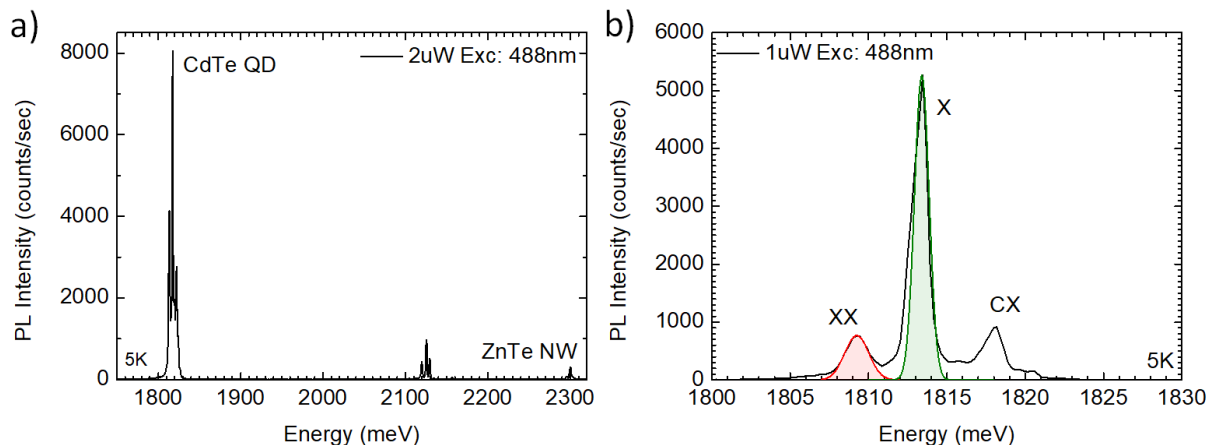
Figure 4.25 – Full micro-photoluminescence spectrum of a CdTe quantum dot in a ZnTe-ZnMgTe core-shell nanowire a). Micro-photoluminescence emission from the CdTe quantum dot where we identified three emission lines from exciton, biexciton and an excited state .

Again from this spectrum we can identify three different emission regions. At high energy and centered at 2300 meV we record the emission from the ZnTe core. The emission from 1805 meV to 1820 meV is attributed to the CdTe inclusion and from 2115 meV - 2135 meV we observe again some weak lines originating mos probably from parasitic growth of CdTe.

The difference with the first nanowire we discussed, is that for this case, from CdTe emission

we analyze three lines instead of two, as shown in Fig. 4.25 b). This is something we observed systematically in almost all nanowires we measured from the same sample. By fitting the peaks at 1809 meV and 1813 meV we find a linewidth of 1.8 meV and 1.1 meV respectively. Comparing to the other nanowire, the linewidths are narrower, but still quite large for a quantum dot.
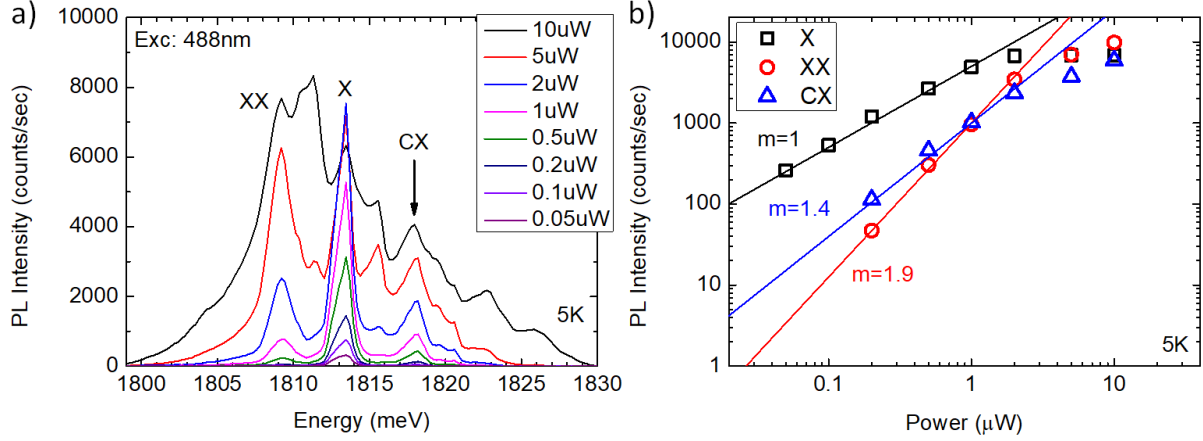
Figure 4.26 – Quantum dot emission for different excitation powers a) Peak intensity of photo-luminescence emission from exciton, biexciton and the excited state as a function of excitation power at logarithmic scale with the corresponding linear fit.

In order to characterize the excitonic transitions, Fig. 4.26 a) we studied the photoluminescence emission spectra of the quantum dot embedded in wire W-7 for different excitation powers, as shown in Fig. 4.26 a). At 10 μW we retrieve a broad emission since different states are populated and in order to start resolving individual lines we have to go down to 2 μW. This behaviour in power is typical for quantum dots. In Fig. 4.26 b) we plot the peak intensity of the three lines we resolve at 1 μW (Fig. 4.25 b)) as a function of the excitation power. For the two peaks at 1809 meV and 1813 meV we fit the photoluminescence intensity with a slope m=1.9 and m=1 and this is what we expect for biexciton and exciton emission respectively. The next step was to try and identify the nature of the transition at high energy. From the linear fit we calculate the slope m=1.4. This value, is compatible with what we expect for a charge exciton CX. For flat quantum dots it is usually expected that the emission energy of a charge exciton lies between that of exciton and biexciton. It has been reported however, that for elongated inclusions, strong piezoelectric effects shift the charge exciton emission at higher energies and this can also be the case for the emission we record at high energy [88].

The next step was to carry out autocorrelation measurements on the quantum dot of W-7. In Fig. 4.27 we present the second order correlation function measurement for the exciton line at 1813 meV. The excitation power was 1 μW.

In this case we did a more detailed analysis of the $g^2(\tau)$ measurements. For this we took into account the noise level of the APDs which correspond to near 10% of the recorded signal and the temporal resolution of each diode which is near 50 ps. The collection efficiency ρ of the quantum dot is defined as

$$\rho = \frac{I_{QD}}{I_{QD} + I_{background}} \tag{4.6}$$

where I_{QD} the intensity of light emitted from the quantum dot and $I_{background}$ the intensity of background noise. From the APDs background we calculate $\rho = 0.9$ and for temporal resolution limitation we convoluted the signal with a Gaussian line of width $\sigma = 0.1$ ns. For fitting the second order correlation function, we use the relation
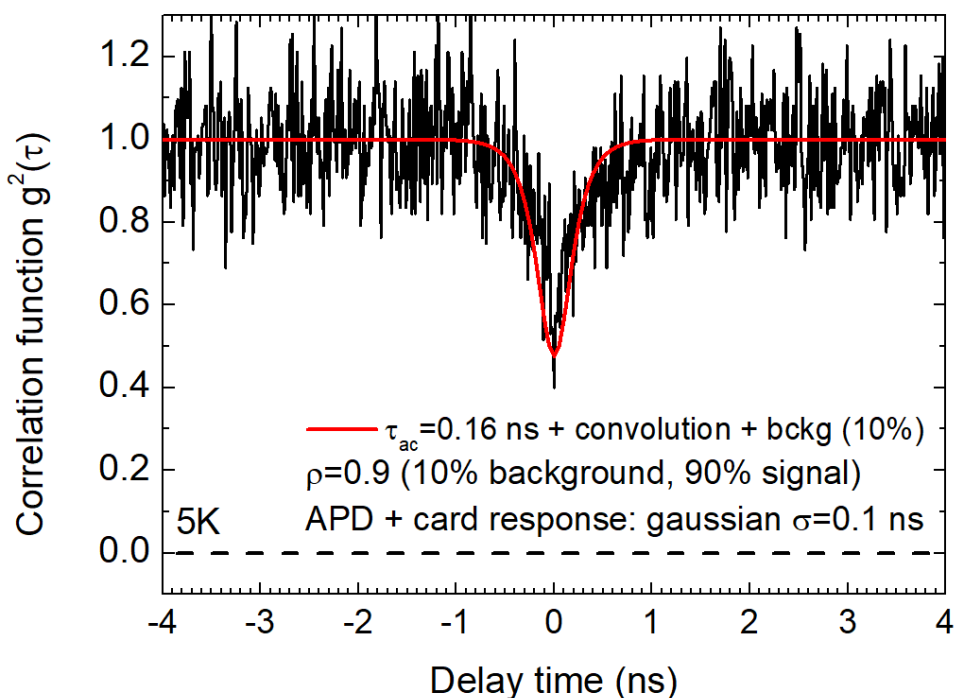
Figure 4.27 – The second order correlation function $g^2(\tau)$, measured for the exciton line at 1813 meV.

$$g^2(t) = 1 - e^{\frac{|t|}{\tau_{ac}}} \tag{4.7}$$

where we find $\tau_{ac} = 0.16$ ns and a $g^2(0) = 0.45$. The fact that $g^2(0)$ is not equal to 0 is attributed to the temporal resolution of the APDs. For comparison, without applying the aforementioned corrections and only from the exponential fit, the characteristic time of the $g^2(\tau)$ measurements is 0.25 ns. These results are in good agreement with the values reported for CdTe-ZnTe nanowire quantum dots, $\tau = 0.2$ ns and $g^2(0) = 0.35$ in [12]. In another work the values $\tau_{ac} = 0.5$ ns and $g^2(0) = 0.2$ are reported [89]. It is important to note however, that in the decay time we measured, we have no information about possible contributions from non-radiative processes. For self assembled quantum dots grown through the Stranski-Krastanov method the values $\tau_{ac} = 0.4$ ns and $g^2(0) = 0.3$ are reported [90].

After the confirmation of single photon emission from the CdTe quantum dot, we were interested to study the radiative lifetime of W-7 which could provide us with further information about the carrier dynamics.

In Fig. 4.28 we present the decay curve for the exciton line of the quantum dot. The measurement was carried out for an excitation power of 50 nW, due to the fact that we wanted to study only the exciton line and suppress emission from any excited states. The curve can be fitted with a single exponential from which we calculate the characteristic exciton lifetime $\tau_{rad} = 1$ ns. In the same graph, the deviation from linear behaviour above 4 ns is attributed to the APD diffusion tail as reported in [91]. This diffusion tail depends on the energy of detected photon and it appears due to carrier generation below the avalanche region of the APD. For the II-VI family of materials and in particular for CdSe and CdTe self assembled quantum dots grown along (001) direction, the exciton decay times vary between 200 ps - 300 ps [92], [93], [94]. The lifetime we measure is significantly larger, implying a stronger electron - hole separation. This can be attributed to both strong piezoelectric potential and due to the fact that confinement is weak as the valence band offset between CdTe and ZnTe is small. From continuous wave ex-
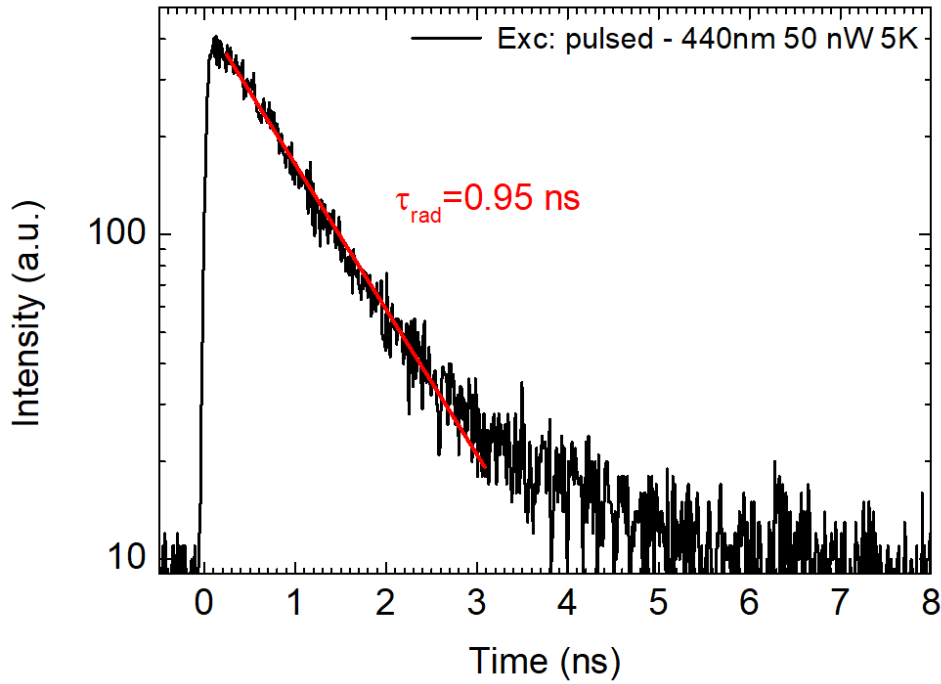
Figure 4.28 – Carrier lifetime of the exciton line at 1813 meV using an excitation power of 50 nW.

periments, the radiatative lifetime τ_{rad} and the autocorrelation characteristic time τ_{ac} for which the quantum dot reaches a stationary exciton population are related through the equation

$$\frac{1}{\tau_{ac}} = g + \frac{1}{\tau_{rad}} \tag{4.8}$$

where g is the generation rate, denoting the number of electron - hole pairs generated at a certain time. For its calculation one has to solve the rate equations in the quantum dot [95]. For this the depopulation rates of all excitonic complexes $\gamma_{Xn} = 1/\tau_{rad}^{Xn}$ have to be determined. In our case we confirm that $\tau_{ac} < \tau_{rad}$ as expected. Nevertheless, we didn't measure the decay time of biexciton or the charged exciton, consequently we can not deduce the generation rate of the autocorrelation measurements.

A confirmation of weak carrier confinement is by looking at the energy difference between exciton and biexciton lines. For this nanowire, the difference is $\Delta E = 4$ meV which is much smaller than the reported biexciton binding energy of Stranski-Krastanov CdTe quantum dots which is between 13 meV - 14 meV [96].

In order to understand the localization of emitted light along the nanowire axis, we carried out cathodoluminescence measurements. We recorded the cathodoluminescence from another wire, named as W-8, of comparable dimensions and similar emission spectra.
In Fig. 4.29 a) we present the cathodoluminescence spectrum of nanowire W-8. Centered at 1823 meV is the emission from CdTe quantum dot. From 2210 meV to 2310 meV we recorded the emission from ZnTe core and from 2490 meV to 2550 meV we obtained a very weak signal from ZnMgTe shell. As regards the ZnTe core, we measured the cathodoluminescence at the wavelength where emission intensity is maximum. The emission from ZnTe core is strong all along the nanowire axis, with exception a region close to the tip. From this area of the nanowire we obtain strong signal at 1823 meV corresponding to the CdTe quantum dot. This is expected as according to growth conditions the quantum dot should be located between the middle and the tip of the nanowire. The fact that cathodoluminescence from ZnTe is vanishing at this region

Figure 4.29 – Cathodoluminescence spectrum of a single nanowire where we observed emission from the CdTe quantum dot, the ZnTe core and the ZnMgTe shell.
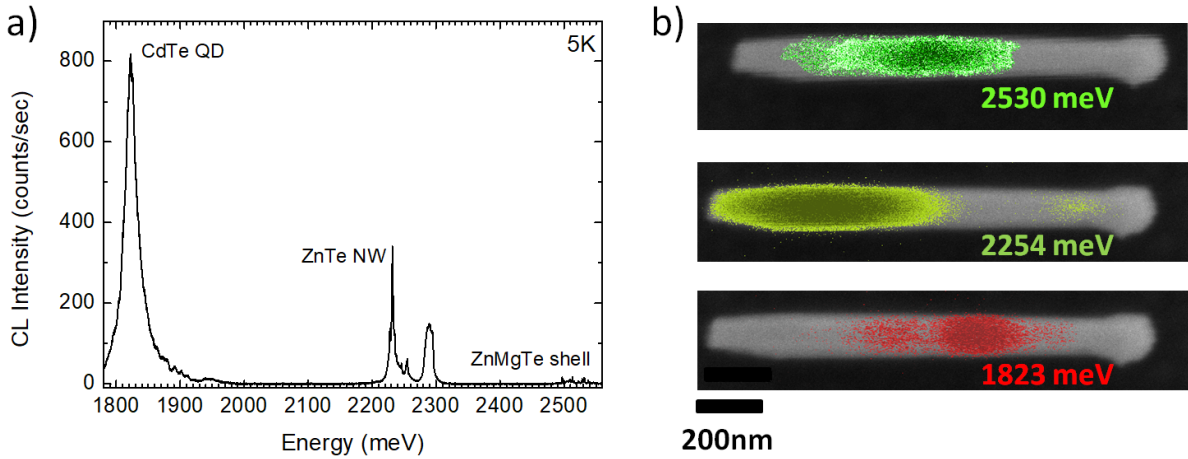
is also reasonable, as we expect that the excitons are trapped inside the quantum dot. From cathodoluminescence measurements we were able for the first time to obtain emission from the ZnMgTe shell and map it along the nanowire axis although it was weak. Again we centered the grating of the spectrometer at 2530 meV which is the energy where ZnMgTe signal intensity is the strongest. The emission of the shell at this energy was localized near the center of the nanowire axis, extending weakly towards the tip and the bottom. The emission of ZnMgTe is consistent with a Mg content near 20%, as discussed in section 4.2.0.1. This content is also confirmed from ZnTe emission barycenter which is near 2280 meV. This specific nanowire did not emit light between the peaks of ZnTe core and CdTe dot, but from other nanowires we measured (not shown here), this emission was localized below the quantum dot position, strengthening the assumption that it originates from sidewall growth of CdTe.

4.4.3 Study of the hole ground state from the emission polarization

The next step, after the basic optical characterization of the nanowire quantum dots, was to identify the properties of the valence band ground state.

The optical transitions between valence and conduction band are depicted in Fig. 1.3, in Chapter 1, section 1.1. An essential experiment which can provide us with information as regards the hole ground state is by measuring the intensity of photoluminescence as a function of its polarization angle. The emission of an elongated quantum dot, with a light hole ground state, is characterized predominantly by a dipole with an electric field oscillating parallel to the nanowire axis, where there is also a smaller contribution from a rotating dipole oriented perpendicular to the nanowire axis. On the contrary, transitions associated to heavy holes, are characterized only by a rotating dipole oriented perpendicular to the nanowire axis. The corresponding transitions for a dipole oriented parallel or perpendicular to the wire axis are π and $\sigma^{\pm}$.

Initially we will discuss the polarization in emission measurement for a core - shell ZnTe - ZnMgTe nanowire. The measurement of a core-shell nanowire was necessary for the characterization of the ZnTe core, as in the samples containing the CdTe dot the emission associated to the core was extremely weak. The growth conditions for the core and the shell were the same as those employed for the growth of the nanowire quantum dot samples.

In Fig. 4.30 a) we present the micro-photoluminescence spectrum of a ZnTe - ZnMgTe core-shell nanowire, designated as W-9. From the emission we identify two regions. The low energy line, centered at 2304 meV originates from the ZnTe core and it is redshifted by 77 meV from the
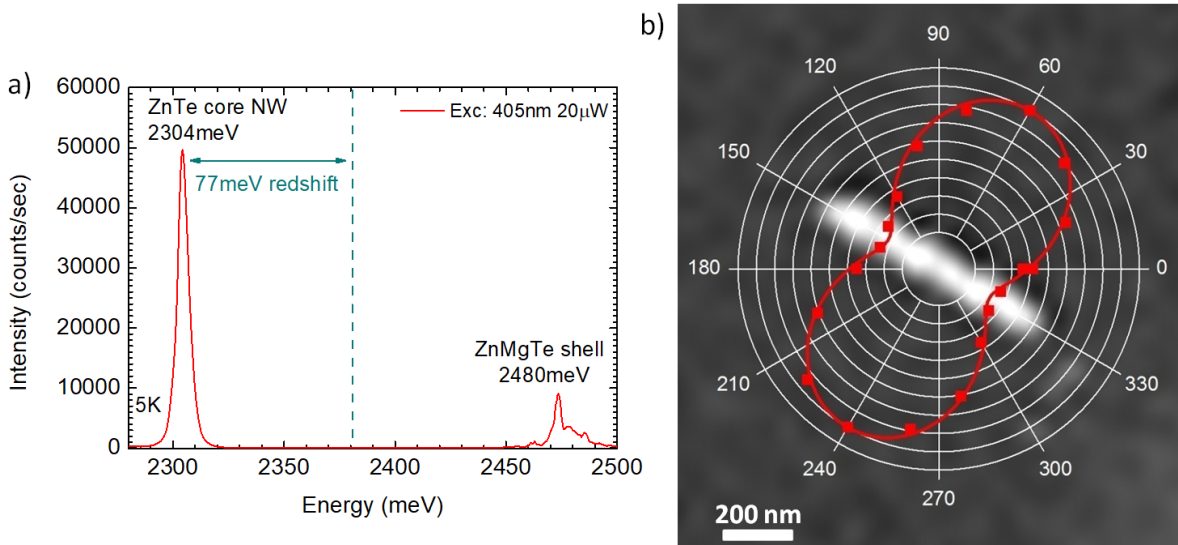
Figure 4.30 – Micro-photoluminescence spectrum of an individual core-shell ZnTe-ZnMgTe nanowire a). Normalized photoluminescence intensity from ZnTe core as a function of polarization angle of the same nanowire b).

corresponding bulk value due to the compressive strain induced by the shell. From 2450 meV - 2500 meV we record a broad emission from ZnMgTe. The redshift of ZnTe and the emission from the shell are in agreement with a Mg content of 18%.

The polarization study of this heterostructure was very important since strain promotes a predominantly heavy hole ground state in the ZnTe core. In Fig. 4.30 b) we present the polar graph of photoluminescence intensity from the ZnTe core as a function of polarization angle for W-9, superimposed with a digitally magnified SEM image of the nanowire. We observe that photoluminescence intensity becomes stronger for a polarization angle perpendicular to the nanowire axis and this is what we expect for a heavy hole ground state. The degree of linear polarization for this nanowire is 50% and it is lower than expected. By studying other nanowires from the same sample however, we measured a polarization degree of around 70%, while still the intensity was stronger for a polarization angle perpendicular to the nanowire axis.

At this point we go back to nanowire W-7 in order discuss the results obtained from an elongated CdTe quantum dot in a ZnTe-ZnMgTe core-shell nanowire.

In the polar plot of Fig. 4.31 we present the polarization dependent photoluminescence intensity from the quantum dot exciton line at 1813 meV of nanowire W-7. Similar to the core shell case we discussed previously, the polar plot is superimposed with the digitally magnified SEM image of the studied nanowire. The emission spectrum from the quantum dot is shown in Fig. 4.26 a). In this case, photoluminescence emission becomes stronger for a polarization angle parallel to the nanowire axis and the degree of polarization is near 90%. This result is very promising since this is what we expect for a ground state with a strong light hole contribution, where the emitted light is predominantly associated with a π transition which is linearly polarized along the nanowire axis.

In Fig. 4.32 we present a sketch of the two dipole orientations in respect to the nanowire axis. In Fig. 4.32 a) we illustrate a $\sigma^{\pm}$ transition associated to a rotating dipole oriented perpendicular to the nanowire axis and in Fig. 4.32 b) a π transition for a dipole oriented parallel to the wire axis. We prompt the reader to look back at Fig. 1.3 in Chapter 1, showing the optical selection rules for the different transitions. Using bulk optical selection rules, the amplitudes of the optical dipoles are
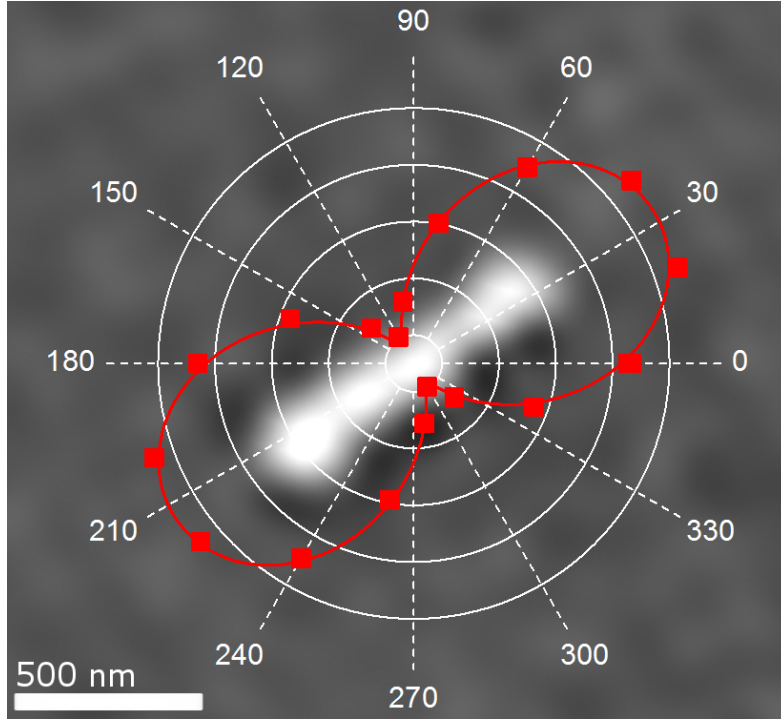
Figure 4.31 – Normalized photoluminescence intensity of the exciton line at 1813 meV from the nanowire quantum dot discussed in the previous chapter, as a function of polarization angle.
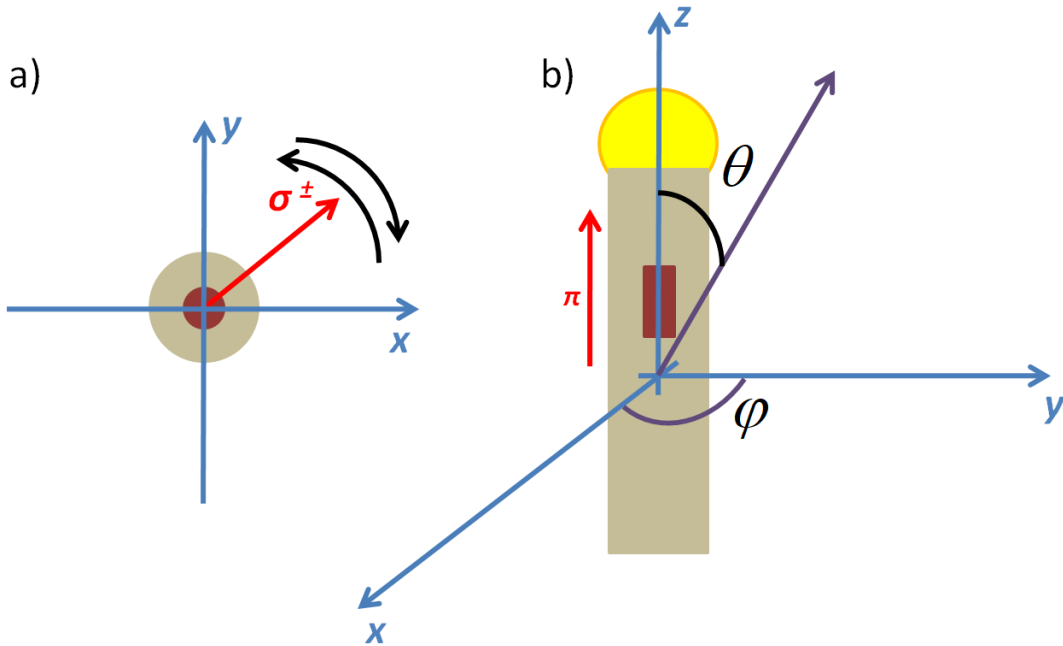
Figure 4.32 – A cross section of the nanowire on xy plane, showing the orientation of the dipole associated to a $\sigma^{\pm}$ transition a). The nanowire along z axis with a π transition where the light is polarized parallel to the nanowire axis b).

$$
\begin{aligned}
\pi \quad &\text{dipole:} \quad \vec{p} = \pi\vec{e}_z \quad \text{with} \quad |\pi|^2 = 2/3 \\
\sigma^{\pm} \quad &\text{dipole:} \quad \vec{p} = \sigma\left(\frac{\vec{e}_x \pm i\vec{e}_y}{\sqrt{2}}\right) \quad \text{with} \quad |\sigma|^2 = 1/3
\end{aligned}
\tag{4.9}
$$

The emission in vacuum for the two dipoles is given by the relations

$$I_\pi(\theta, \phi) = \frac{3}{8\pi} sin^2(\theta)|\pi|^2$$
$$I_{\sigma^\pm}(\theta, \phi) = \frac{3}{8\pi} \left(\frac{1 + cos^2\theta}{2}\right)|\sigma|^2$$

(4.10)

For a light hole exciton in a nanowire of very large diameter deposited on a substrate and for an angle $\theta = \pi/2$ the intensity for the two transitions becomes

$$I_\pi \approx \frac{3}{8\pi}|\pi|^2 \quad \text{with} \quad |\pi|^2 = 2/3$$
$$I_\sigma \approx \frac{3}{8\pi}\frac{|\sigma|^2}{2} \quad \text{with} \quad |\sigma|^2 = 1/3$$

(4.11)

and the resulting degree of polarization of emitted light is

$$\mathcal{P} \approx \frac{I_\pi - I_\sigma}{I_\pi + I_\sigma} = \frac{2/3 - 1/6}{2/3 + 1/6} = 0.6$$

(4.12)

This means that by measuring the degree of polarization, we expect that emitted light will be polarized by 60% along z axis. What we observe however is different and this is attributed to the effect of dielectric screening which strongly influences the measured degree of polarization. This is also the major drawback of polarization dependent measurements and as a consequence, we can not rely solely to the results obtained through them for characterizing the valence band ground state. It has been shown, that the difference between the refractive index of the semiconductor material and vacuum may affect a dipole oriented along the radius of a nanowire and reduce the intensity of emitted light associated to it [97]. As a result the emission originating from any dipole oriented parallel to the nanowire axis will be stronger and this will be manifested in polarization dependent measurements. The effect of dielectric screening and the ratio between the electric field inside and outside a cylinder of dimensions smaller than the wavelength, is explained in detail in [98], [99]. If the emitted light is polarized perpendicular to the nanowire axis, the electric field outside the wire in respect to that inside it, is given by

$$E_{in} = \frac{2\varepsilon_0}{\varepsilon_{ZnMgTe} + \varepsilon_0} E_{out}$$

(4.13)

where ε_{ZnMgTe} the dielectric constant of ZnMgTe near 680 nm which is the emission wavelength of the quantum dot. According to [100] the refractive index of ZnMgTe near the wavelength of interest with a Mg content of 12% is 2.9. The intensity of emitted light is given by the square of the electric field, consequently, for the dipole oriented perpendicular to the nanowire axis, the intensity will be attenuated by a screening factor inversely proportional to the refractive index as follows

$$I_{\sigma^\pm}\left(\frac{2}{1 + n^2}\right)^2 \approx \frac{I_{\sigma^\pm}}{22}$$

(4.14)

This means that the recorded intensity of light with a polarization oriented perpendicular to the nanowire axis is attenuated by 22 times in respect to the intensity of light with a polarization parallel to the wire axis and the expected degree of linear polarization becomes

$$\mathcal{P} = \frac{2/3 - 1/6 \times 1/22}{2/3 + 1/6 \times 1/22} \approx 0.97 \qquad (4.15)$$

This result is in agreement with a light hole π transition, where any contribution of $\sigma^{\pm}$ transitions in suppressed due to dielectric screening. Of course this is a qualitative approach, as for an accurate estimation of the polarization degree we need to take into account the effects of the substrate and nanowire eventual guided modes and implement a complicated finite element or finite difference time domain (FDTD) calculation.

From the above analysis, we understand that it becomes very difficult to extract any information about the purity of the ground state by studying only polarization. To further extend our study, with the nanowire W-7 we recorded also the far field emission for different polarization angles. Far field emission measurements were performed in collaboration with Gilles Nogues. In this experiment, we use a Fourier lens after the objective, in order to image its back focal plane on the CCD. Through this method we can map the plane waves emitted at different angles on different pixels of the detector. The purpose of this measurement was to reveal more information for the hole ground state by analyzing the emission diagram. As mentioned in the introduction, for this measurement we used a small working distance objective with a large numerical aperture (NA =0.75) in order to collect a wide range of angles from the emitted photoluminescence cone. In order to record the emission originating only from the quantum dot and block the emission from the ZnTe core, we used a longpass filter at 650 nm.
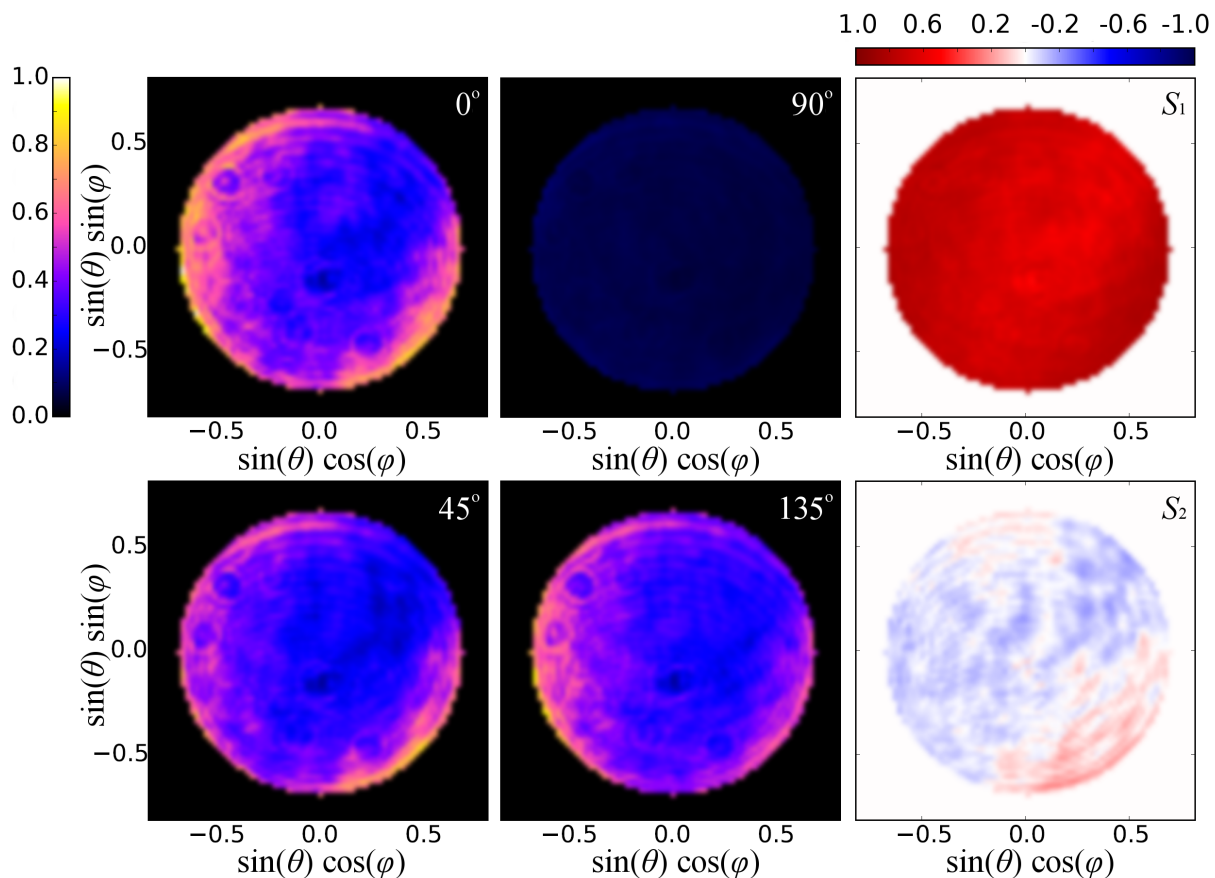

Figure 4.33 – Far field emission of the CdTe dot for different angles of a rotated polarizer. From 0° (parallel to the nanowire axis) and 90°, a) and b) accordingly we calculated S_1 stokes parameter c) and from 45° and 135°, d) and e), we calculated S_2 f).

In Fig. 4.33 a), b), d), e) we present the emission diagram of nanowire W-7 as collected for

different angles of a rotating polarizer. Light emission is integrated over the azimuthal angle φ, while θ corresponds to the polar angle of the emitted photoluminescence cone. The maximum angle θ' for which we can collect the photoluminescence signal and map it on different pixels of the CCD is that for $\sin\theta' = \mathrm{NA} = 0.75$. Directly from the emission diagrams we can not draw any conclusions as regards the dipole properties, apart from the fact that when the polarization angle is perpendicular to the wire axis (4.33 b)), the radiation pattern intensity vanishes. A way to quantify the information of light polarization from the far field measurements while discarding the influence of intensity is through the Stoke's parameters S_1 and S_2, given by

$$S_1 = \frac{I_0 - I_{90}}{I_0 + I_{90}} \qquad S_2 = \frac{I_{45} - I_{135}}{I_{45} + I_{135}} \tag{4.16}$$

In Fig. 4.33 c) we present the S_1 stokes parameter calculated from the emission diagrams recorded for a polarization angle parallel (0°) and perpendicular (90°) to the nanowire axis. We confirm that for this configuration, the S_1 parameter is uniform and close to the maximum value 1 for all angles, being in agreement with what we expect for a dipole associated to a π transition from a nanowire deposited on a substrate. From this plot however we cannot extract any information about the purity of the state and any contribution from $\sigma^{\pm}$ transitions. On the contrary for a 45° and 135° orientation in respect to the wire axis, the parameter S_2 reveals a weak texture but it is almost vanishing. By integrating the recorded emission diagrams for a full rotation of the polarizer we calculate the degree of polarization
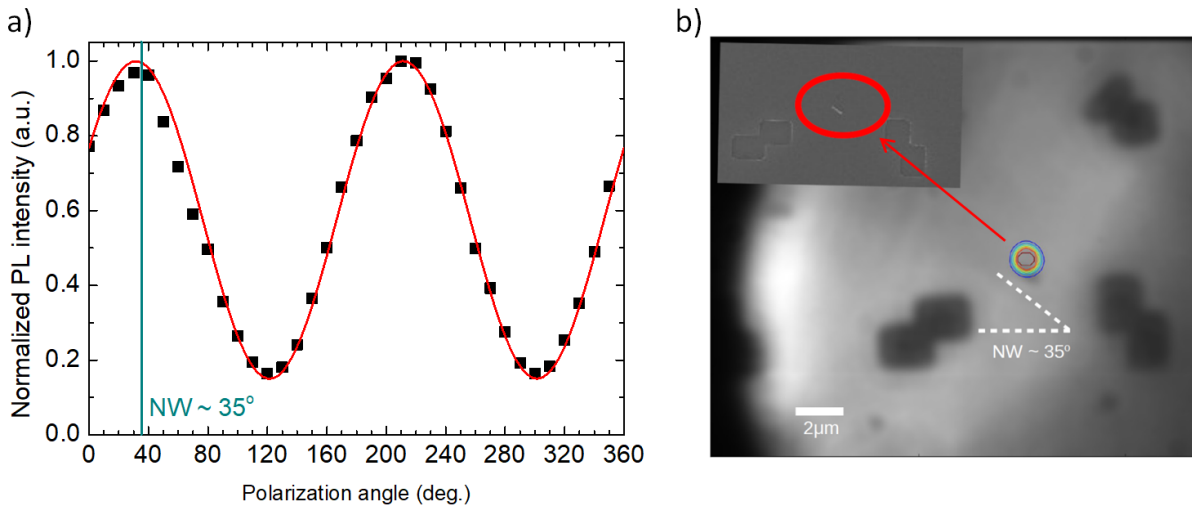
Figure 4.34 – The integrated intensity of recorded emission diagrams as a function of the polarizer angle a). Optical microscope image of nanowire W-7 with the emitted photoluminescence profile superimposed b). On the left corner of this figure the SEM image of W-7 is pasted, from which we calculated the nanowire orientation.

In Fig. 4.34 a) we present the degree of polarization from the quantum dot emission of nanowire W-7. The points are fitted using Malus's law and as expected the intensity becomes stronger when the polarizer is oriented parallel to the wire axis. In Fig. 4.34 b) we present the surface of the substrate on which W-7 is deposited. From the photoluminescence profile image superimposed to it, we confirm that we indeed collect light only from this object while no other parasitic emission in observed. The two images are slightly shifted in respect to each other due to focus adjustments.

To conclude this section, the photoluminescence intensity for the elongated CdTe quantum dot, becomes larger for a polarization angle parallel to the nanowire axis. This is consistent to a π like transition which is associated to a light hole component. In these measurements however,

we do not take into account dielectric screening and guided mode effects as reported in [27], as a result we are not able to quantify the purity of the hole state and the degree of mixing between heavy and light hole. At the same time, the analysis of far field emission for nanowires dispersed on Si is non-trivial, as for understanding the results a thorough investigation of how the dielectric environment affects the radiation pattern is required which goes beyond the scope of this work. Instead of that we will try to understand better the valence band ground state by studying Mn doped quantum dots through magneto-optical measurements.

4.4.4 Light hole ground state in CdMnTe quantum dots

For the magneto-optical measurements we used a setup similar to the one depicted in Fig. 4.2. The only major difference was the cryostat device, where instead of a He flow one, we used two different bath cryostats, which incorporated Nb-Ti superconductive coils for the application of magnetic field. The first cryostat had a single coil so we could apply a magnetic field of up to 11 T (absolute value) only along one axis. This imposed limitations as we could not study the same object under different orientations of magnetic field. For this reason and in order to carry out a complete study of a single nanowire, we used also a vectorial magnet with three coils, where we could apply the magnetic field along all x, y and z directions. The absolute maximum values for each direction are 3 T , 1 T and 7 T respectively.
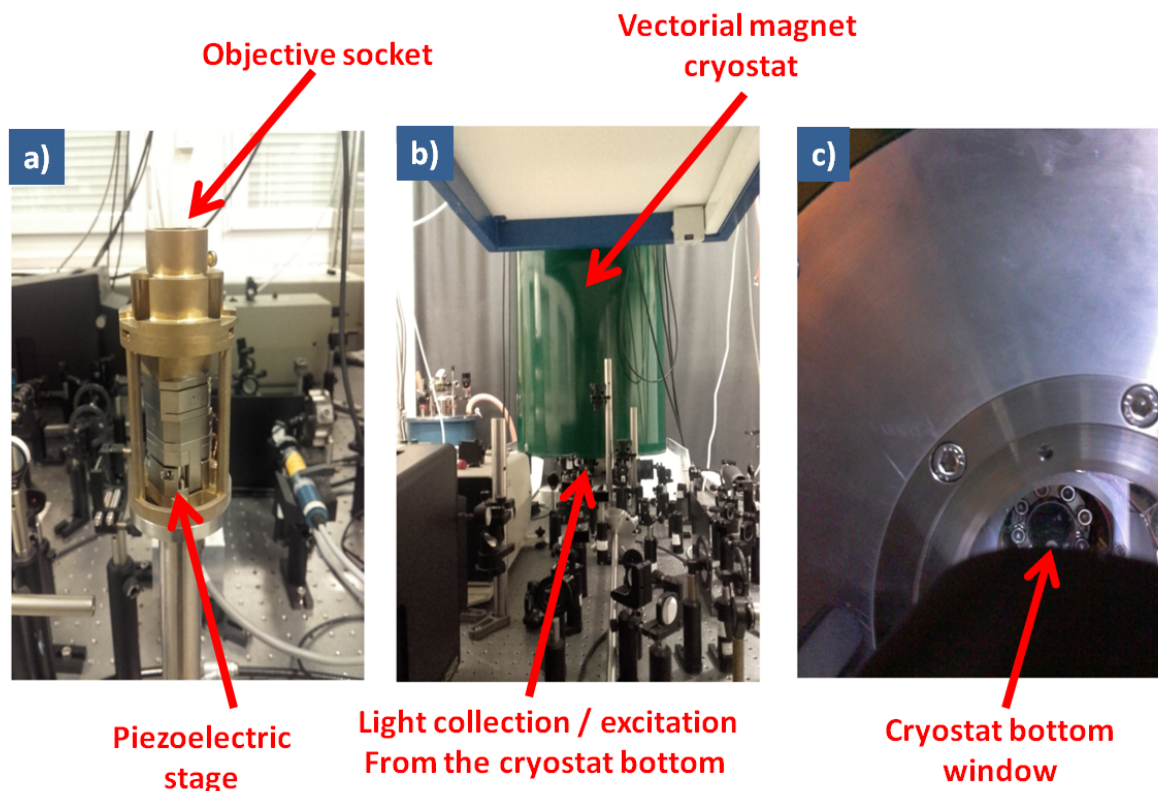
Figure 4.35 – The cryostat transfer rod with the objective and piezoelectric stage assembled a). Picture of the vectorial magnet cryostat b). The window located at the bottom of the cryostat c).

The finger on which the samples were attached is mounted on a stage of three piezoelectric elements, through which we can control the sample movement along z axis and xy plane. On top of the sample, there is a socket, where the objective lens used for excitation and light collection is mounted. The lens is of small working distance with a 40x magnification and a NA=0.4. The piezoelectric stage assembly with the objective mount is shown in Fig. 4.35

a). After the sample and the objective are mounted, the whole system is inserted in the bath cryostat pictured in Fig. 4.35 b). The magnet coils which surround the sample are submerged in liquid He. The sample can be cooled down to 4 K by using the He vapors from the magnet chamber. Usually we work in higher temperature because liquid He tends to condensate on the bottom of the cryostat, where the formed bubbles make more difficult the collection of emitted light. In Fig. 4.35 b) we present an image of the cryostat window located at the bottom. Not shown in this picture but the cryostat is fixed on the top of a base designed and constructed at institute Neél - CNRS, which includes an extension stage to the optics table, where all the required optical elements are placed. Through this assembly we can excite the sample and record the photoluminescence from the bottom of the cryostat.

4.4.4.1   Measurements with a uniaxial magnet at large field

In this section we discuss the results obtained by measuring two different nanowires with the single coil cryostat. The major advantage of this magnet is that we can carry out measurements in large fields up to 11 T and study the Zeeman shift near saturation. In this case however, in order to investigate the effect of magnetic field along two different directions, we had to measure one nanowire dispersed on Si substrate and one from the as-grown sample. By using the uniaxial magnet we remain with the so called Faraday configuration where the magnetic field is parallel to the excitation and collection of light. Opposite to that is the Voigt configuration, where the applied field is perpendicular to the direction of emitted light. Since we had to measure two different objects, we did multiple measurements on both the sample with the dispersed nanowires and the as-grown one and we chose to discuss those which shared a similar emission spectra at zero field. This is an indication that the two nanowires also share similar structural properties.

• Magnetic field applied perpendicular to the nanowire axis

We begin the discussion with the results obtained from a nanowire dispersed on Si.
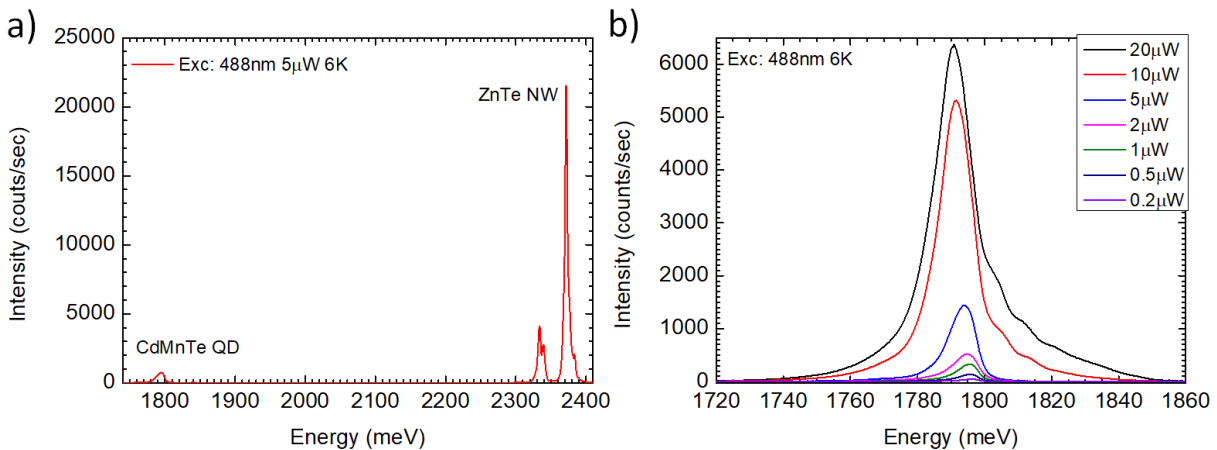
Figure 4.36 – Micro-photoluminescence spectrum of a single nanowire, where we identified the emission from ZnTe core and the CdMnTe quantum dot a). Micro-photoluminescence emission from the CdMnTe quantum dot under different excitation power b).

In Fig. 4.36 we present the micro-photoluminescence spectrum of a single dispersed nanowire designated as W-10. From 2300 meV to 2400 meV we identified the emission from ZnTe core and from 1780 meV to 1805 meV a broad emission attributed to the CdMnTe inclusion. Opposite to the CdTe quantum dots we did not observe any emission between those of the core and the dot, indicating that for this sample there was no sidewall CdMnTe deposition. From power

dependent measurements as shown in Fig. 4.36 b), we always resolved one broad line centered at 1794 meV. The linewidth at 0.2 μW is 7 meV and it is broader than the one of CdTe dots. This broadening is attributed to the spin fluctuation of the magnetic dopant, as reported in [101]. As shown in Chapter 1, section 1.4, for a heavy hole exciton under a magnetic field perpendicular to the nanowire axis we expect a Zeeman shift given by

$$\Delta E_{X-hh,x} = \frac{\Delta E_e^{sat}}{2}\frac{m_x(B)}{m_{sat}} \tag{4.17}$$

indicating, that at low $|\vec{m}|$ at least, we observe only the Zeeman shift of the electron. For a light hole exciton the Zeeman shift is

$$\Delta E_{X-lh,x} = \frac{\left(\Delta E_e^{sat} + \frac{2}{3}\Delta E_{hh}^{sat}\right)}{2}\frac{m_x(B)}{m_{sat}} \tag{4.18}$$

as both electron and light hole energies shift with increasing magnetic field.

In Fig. 4.37 we present the micro-photoluminescence spectra of the CdMnTe quantum dot emission under different magnetic fields from 0 T - 11 T, for nanowire W-10. The excitation power before the objective was 0.8 μW and the temperature was set at 6 K. From the emission we observe a large Zeeman shift towards lower energies, equal to ΔE =36 meV at 11 T. As we discussed in the previous chapter, for a pure and isolated heavy hole, a small Zeeman shift (about $\approx 11 meV = \frac{\Delta E_e^{sat}}{2}$) is expected for a magnetic field applied perpendicular to the nanowire axis and obviously this is not the case here.

In Fig. 4.38 we present the energy shift of the quantum dot emission as a function of magnetic field for wire W-10. The points for plotting the shift correspond to the energy position at the barycenter of the main emission line of the quantum dot. In order to compare with a light hole exciton, close to saturation and for $\Delta E_e^{sat} = 22$ meV and $\Delta E_{hh}^{sat} = 88$ meV, the expected Zeeman shift is

$$\frac{\left(\Delta E_e^{sat} + \frac{2}{3}\Delta E_{hh}^{sat}\right)}{2} = 11 + \frac{2}{3}44 \approx 40\,\text{meV} \tag{4.19}$$

This makes clear that we are in a very good agreement with a light hole ground state.

Before investigating the Zeeman shift for a magnetic field applied parallel to the nanowire axis, we will discuss the energy shift of the same dispersed nanowire at higher excitation power. The reason for that is to describe the effect of laser power on the thermalization of Mn spins and its influence on Zeeman shift.

In Fig. 4.39 we present the same spectra as in Fig. 4.37 for an excitation power 5 times higher. Since we increase the excitation power, we start to probe excited states: the main emission line splits in a doublet. The excited state is indicated with arrows in Fig. 4.39. For plotting the energy shift this time, we took the barycenter of the line at high energy and we ignored the one at low energy.

In Fig. 4.40 we present the energy shift as a function of a magnetic field applied perpendicular to the axis of nanowire W-10. In this case up to 6 T the evolution of energy is linear and at 11 T the Zeeman shift is 31 meV, being 5 meV smaller than that we measured at 0.8 μW. This reveals the effect of Mn heating by the laser. By increasing the excitation power, we expect to also increase the temperature of Mn ions. Such a dependence on excitation power can be used as an evidence for a temperature dependence of the giant Zeeman effect. As Mn temperature increases, the magnetic moment of Mn ions gets reduced under the presence of an applied field and as a result, the amplitude of the Zeeman shift decreases.

Figure 4.37 – Micro-photoluminescence spectra of the CdMnTe quantum dot in wire W-10 under a magnetic field applied perpendicular to the nanowire axis. The field was from 0 T - 11 T and the emission was recorded every 0.5 T.

To conclude with the field applied perpendicular to the nanowire axis, we have a clean evidence of a giant Zeeman effect with a significant light hole contribution. Before attempting a quantitative fit, we present results obtained with the field along the axis on another nanowire.

● **Magnetic field applied parallel to the nanowire axis**

In order to investigate the effect of magnetic field applied parallel to the wire axis, we introduced the as-grown sample in the cryostat. Our priority, was to find a nanowire, with similar photoluminescence profile in comparison to the dispersed one. We label this nanowire as W-11. In Fig. 4.41 a) we present the micro-photoluminescence emission of nanowire W-11 from the as-grown sample. From 2200 meV and above we observe the emission from ZnTe and from
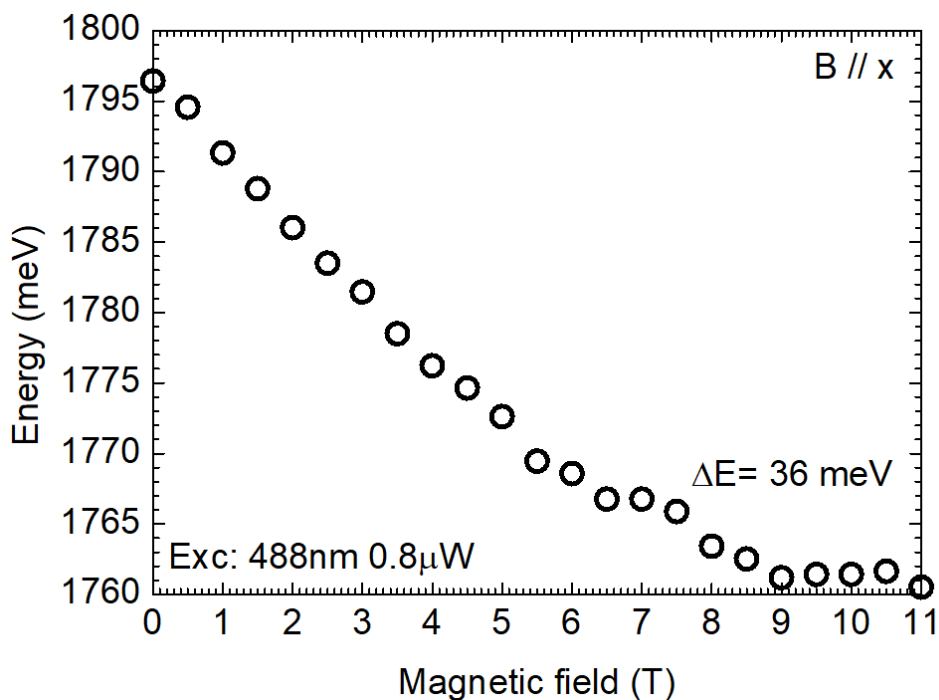
Figure 4.38 – The energy shift as a function of the applied magnetic field along x axis for nanowire W-10.

1820 meV to 1878 meV the emission from CdMnTe dot, where the intensity gets maximized at 1864 meV. The emission of ZnTe is shifted at lower energies, while the emission of CdMnTe at higher. An explanation for that, is that the ZnMgTe shell is thicker. Comparing to the dispersed nanowire, the quantum dot emission is around 70 meV blueshifted. From all the bright objects studied from the as-grown sample and within a window of 100 meV, this was the best candidate in order to compare with the dispersed nanowire. Despite the energy difference of 70 meV, the two quantum dots show the same spin physics, because as we will confirm later, the hole ground state is a light hole, strongly decoupled from heavy holes. In Fig. 4.41 b) we present the photoluminescence emission from the quantum dot for different excitation powers. The dominant peak is centered near 1864 meV and at high excitation power we observe a second line.

In Fig. 4.42 we present the micro-photoluminescence spectra of the Cd(Mn)Te quantum dot embedded in nanowire W-11 under magnetic field, using an excitation power of 6 μW. The drawback with this nanowire was that the emission intensity was weak so we had to use a relatively high excitation power. In Fig. 4.43 we plot the energy position of the quantum dot emission of nanowire W-11 as a function of magnetic field. In this case, we observe that the energy begins to shift for magnetic field values above 2 T. By looking at the peak position, it becomes obvious that the shift is weaker in comparison to the wire where we applied the field perpendicular to its axis and this is what we expect for a light hole ground state. Another thing we notice, is that for a magnetic field up to 2 T, Zeeman shift is almost vanishing. This will be better visible with the measurements done at low fields with the vectorial magnet, discussed in section 4.4.4.2. In order to understand better this behavior, we plot the energy shift as a function of the applied magnetic field.

Up to this point, the energy position is almost constant with some small fluctuations. By looking at Zeeman shift, up to 2 T the slope is vanishing, something which is not expected. Normally we would expect a linear decrease of Zeeman shift by increasing the magnetic field. Also near saturation, the Zeeman shift is reduced and quantitatively is smaller than the expected value.
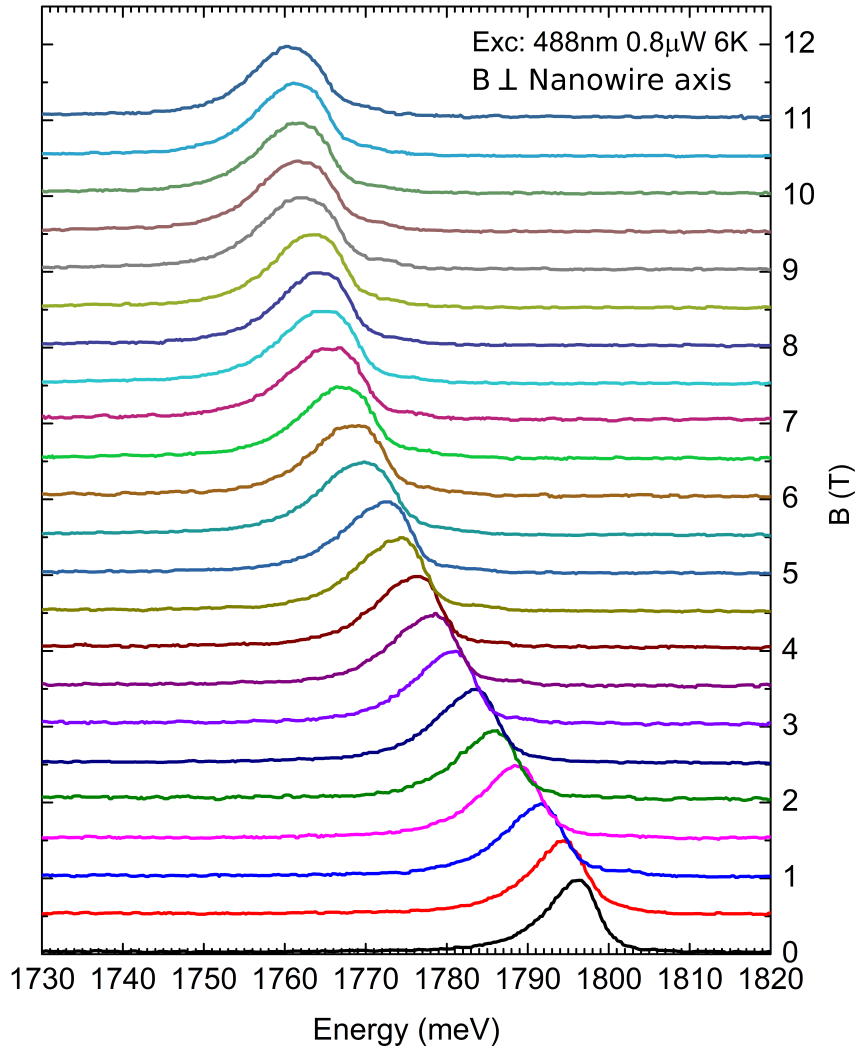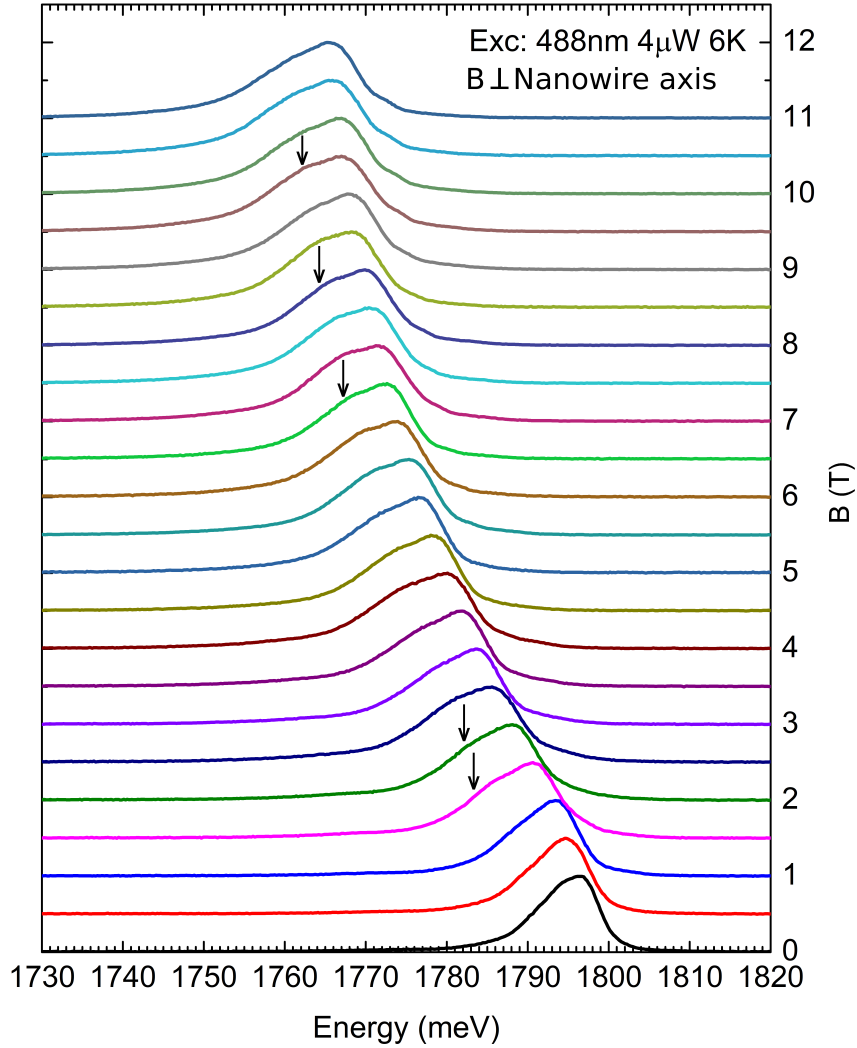
Figure 4.39 – Micro-photoluminescence spectra of the CdMnTe quantum dot embedded in nanowire W-10 under magnetic field applied perpendicular to the wire axis. The excitation power in this case is 4 μW. The field was from 0 T - 11 T and the emission was recorded every 0.5 T. Arrows indicate a new line appearing at high excitation power.

More specifically, near saturation it is $\Delta E_{sat} \approx \Delta E(11\text{T}) = 15$ meV. The expected value in that case, should be near

$$\frac{\left(\Delta E_e^{sat} + \frac{1}{3}\Delta E_{hh}^{sat}\right)}{2} = 11 + \frac{1}{3}44 \approx 25 \, \text{meV} \tag{4.20}$$

We attributed this to the formation of magnetic polaron, which is described in section 1.5 and will be discussed in more detail later in this chapter.

Another important indication of the magnetic polaron formation effect, is from temperature dependent measurements. This effect is explained later, when we will take into account the
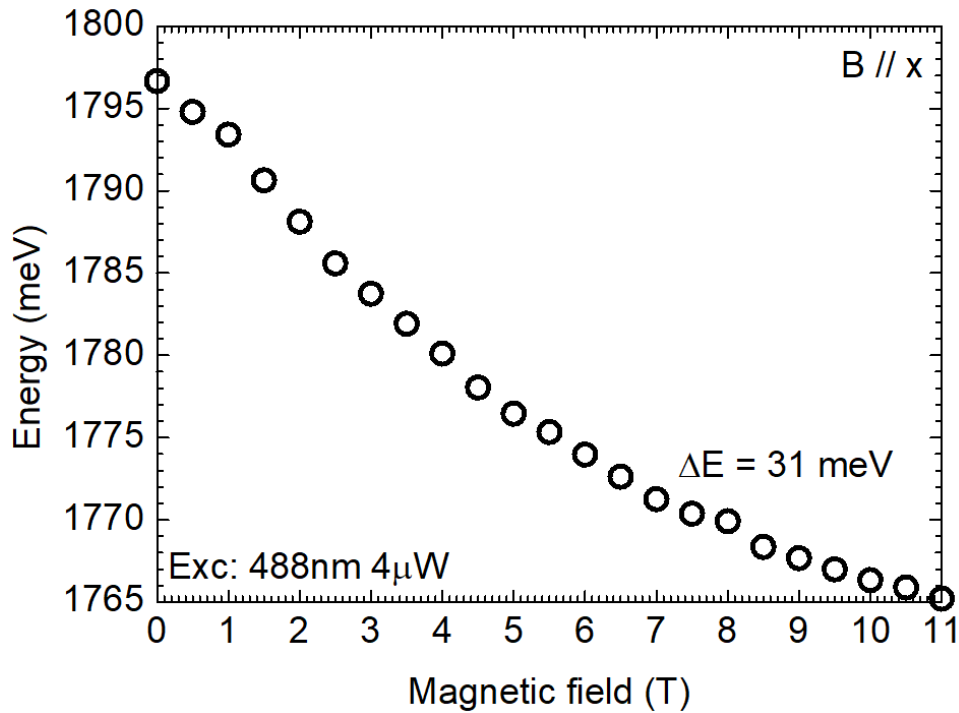
Figure 4.40 – The energy shift as a function of the applied magnetic field for nanowire W-10 at an excitation power of 4 μW.
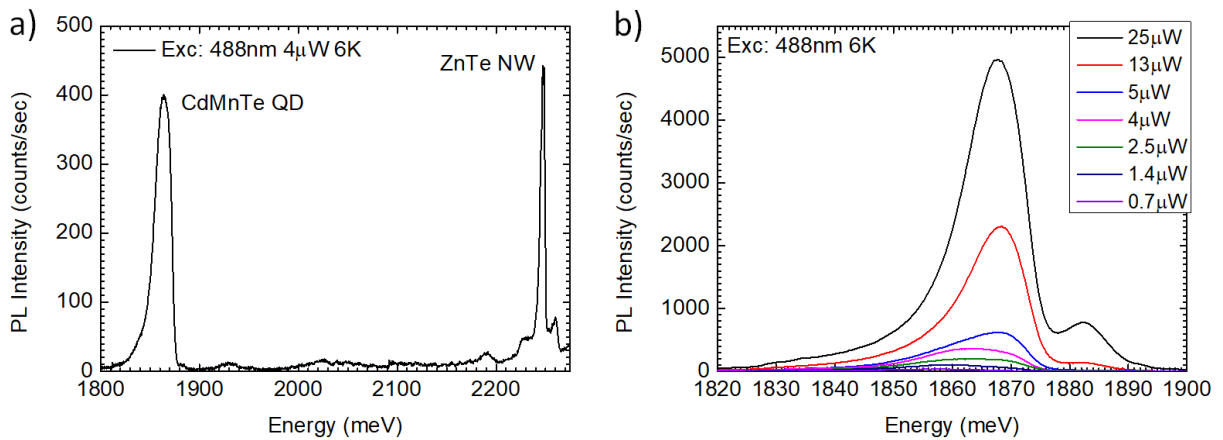
Figure 4.41 – Micro-photoluminescence spectrum of nanowire W-11, obtained from the as-grown sample. Similarly to the dispersed one, we identified the emission from ZnTe core and the CdMnTe quantum dot a). Micro-photoluminescence emission from the CdMnTe quantum dot under different excitation power b).

carrier exchange field.

In Fig. 4.44 we present the photoluminescence emission of the CdMnTe quantum dot embedded in nanowire W-11, for different values of temperature. The excitation power was further lowered in order to avoid thermalization effects on Mn and this also explains the emission redshift at 8 K. In Appendix F we present the micro-photoluminescence spectra of nanowire W-11 in logarithmic scale where at low excitation power we confirm the shift at lower energies. Already by looking at the spectra we observe that by increasing the temperature, emission shifts initially to higher energies. This is better depicted in Fig. 4.44 b) where from 8 K up to 31 K emission blueshifts and above this temperature it begins to follow Passler's law which describes the band
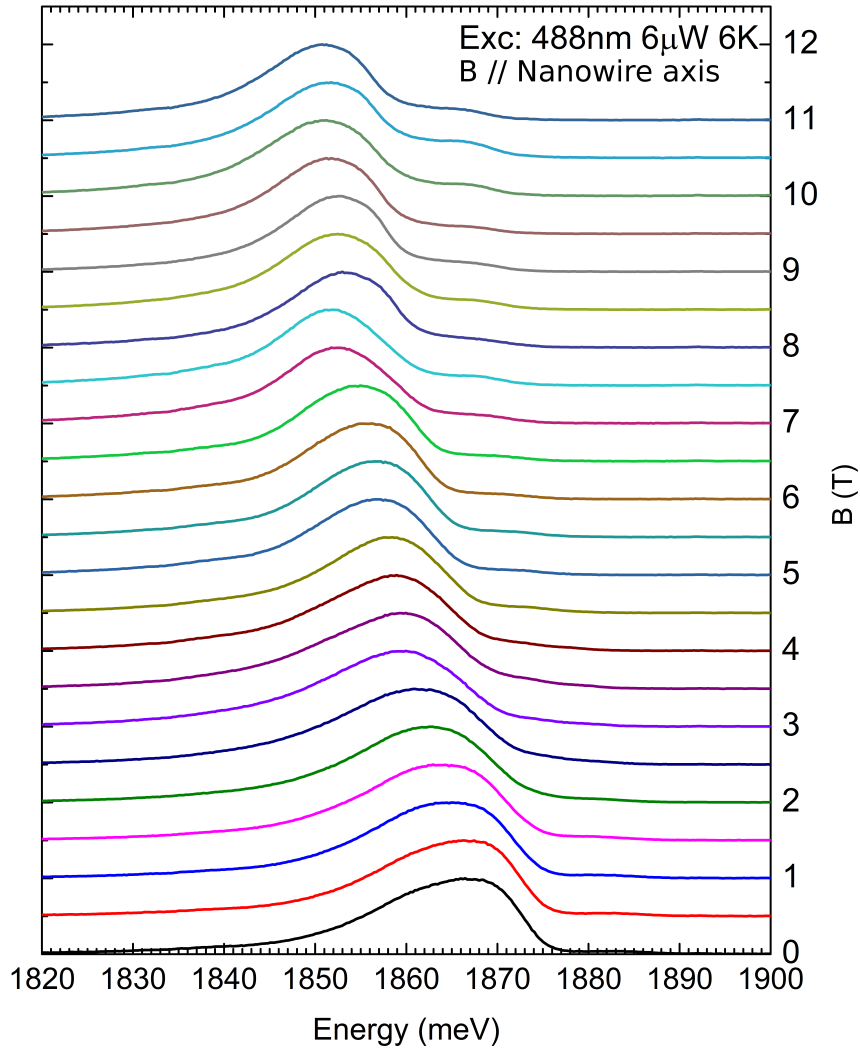
Figure 4.42 – Micro-photoluminescence spectra of the CdMnTe quantum dot of nanowire W-11 from the as-grown sample under magnetic field. In this case the field is applied parallel to the nanowire axis. The excitation power is 6 μW. The field was from 0 T - 11 T and the emission was recorded every 0.5 T.

gap variation with temperature [102]. The fit in this Figure is only to demonstrate the non-monotonous behaviour of energy shift. The polaron effect exists even at the energy maximum and the correct scheme is shown in Fig. 4.57 discussed later. This behaviour in temperature, suggests that a magnetic polaron is formed during the lifetime of the exciton. As we decrease the temperature in a semiconductor, the energy gap increases and photoluminescence emission shifts to higher energies. In a diluted magnetic semiconductor, spins introduced by magnetic ions, become polarized by the photo-generated carriers exchange field. More specifically for a light hole ground state, Mn spins align anti-parallel to the hole spins and parallel to the electron spin. Due to Mn spin alignment, a magnetization appears, which shifts the photoluminescence emission towards low energies. By increasing the temperature, Mn magnetization decreases and
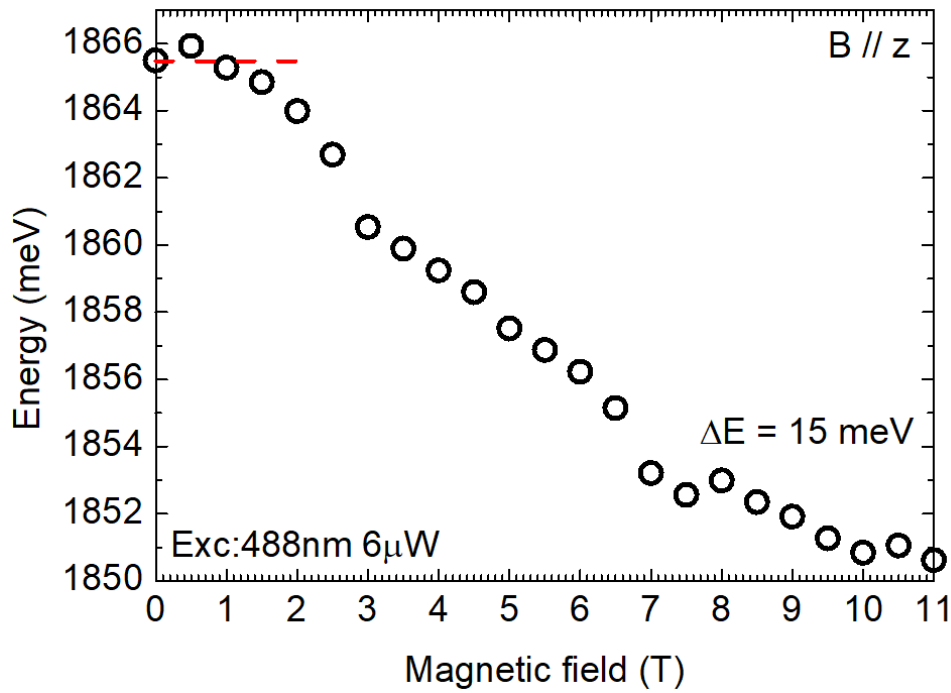
Figure 4.43 – The energy shift as a function of the applied magnetic field along z axis for nanowire W-11 from the as-grown sample.
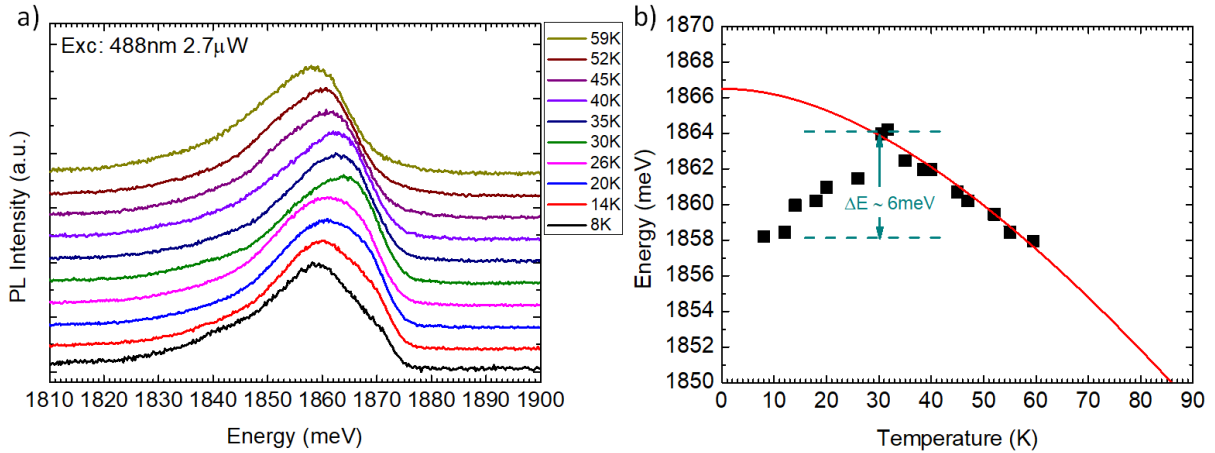
Figure 4.44 – Photoluminescence emission of the CdMnTe quantum dot of nanowire W-11 under different temperatures a). The energy position as a function of temperature superimposed with Passler's empirical law b).

above a certain temperature, a Passler like evolution of energy gets restored. In the following paragraph, we discuss more quantitatively the effect of magnetic polaron formation on the Zeeman shift of a light hole and we explain the nature of the characteristic plateau observed experimentally at small values of field applied parallel to the nanowire axis.

● **Expected Zeeman shift if a magnetic polaron is formed with a pure light hole**

The magnetic polaron effect emerges due to the polarization of Mn spins induced by the exchange field of the photo-generated carriers. In this analysis, originally proposed by David Ferrand, we will focus on the effect of a pure light hole ground state on the polarization of Mn spins, in a

mean field approach (no fluctuations). The effect of the electron is not taken into account.
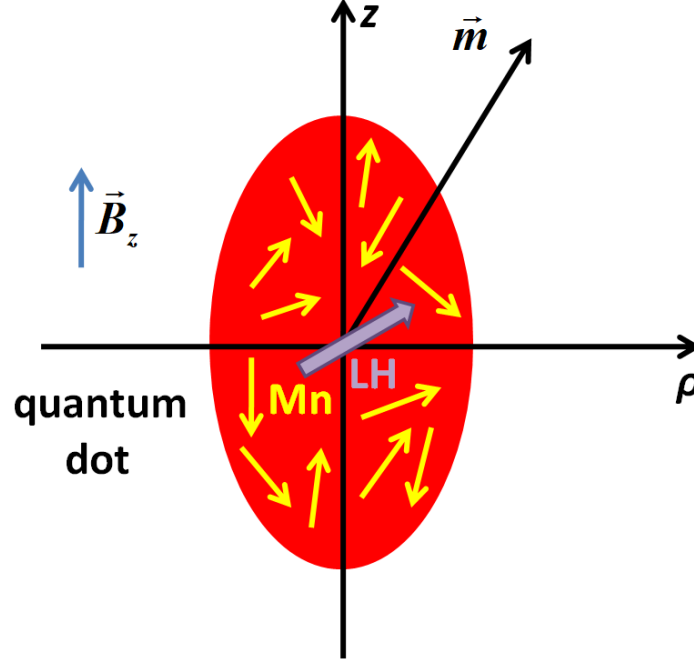
Figure 4.45 – Sketch of a quantum dot doped with Mn ions where the magnetic moment vector rotates by increasing the magnetic field along z.

In Fig. 4.45 we present a sketch of an elongated quantum dot with a light hole ground state, where the magnetic field is applied along z axis. Inside the quantum dot, we have N_{eff} polarized spins. Typical values of the number $N_{eff} = 50$ to 100 (4% in a quantum dot volume $V_{QD} \approx 100$ nm^3) and each Mn atom is characterized by 6 spin states. As a consequence, the number of quantum states is beyond the limit of an exact calculation. Another way to calculate the Mn spin properties is by using the Helmholtz free energy from thermodynamics. The vector of magnetic moment attributed to the ferromagnetic alignment of Mn spins which is induced by the light hole exchange field, rotates as the magnetic field increases. In order to describe the effect of magnetic polaron we have to take into account the magnetization induced by the light hole exciton exchange field through the Hamiltonian we introduced in Chapter 1, section 1.4, Eq. 1.24.

$$\mathcal{H}_{exc} = \Delta E_{hh}^{sat} \frac{\vec{m}}{M_{sat}} \cdot \vec{\sigma}_{lh} = \frac{\Delta E_{hh}^{sat}}{M_{sat}} \begin{pmatrix} \frac{m_z}{6} & \frac{m_x - im_y}{3} \\ \frac{m_x + im_y}{3} & -\frac{m_z}{6} \end{pmatrix} \tag{4.21}$$

where $M_{sat} = g_{Mn}\mu_B S_{Mn} N_{eff}$. We remind to the reader, that the spin matrices for a light hole, are given in Eq. 1.26. The eigenvalues of the exchange Hamiltonian are calculated as follows

$$\lambda = \pm \left[\frac{m_z^2}{6^2} + \frac{m_x^2}{3^2} + \frac{m_y^2}{3^2} \right]^{1/2} \tag{4.22}$$

For a light hole inside the dot the shift is

$$E_{lh} = -\frac{\Delta E_{hh}^{sat}}{M_{sat}} \sqrt{\frac{m_z^2}{6} + \frac{(m_x^2 + m_y^2)}{3^2}} \tag{4.23}$$

and by setting $B_{lh,z} = \frac{1}{6}\frac{\Delta E_{hh}^{sat}}{M_{sat}}$, we write the shift as

$$\pm E_{lh} = \pm B_{lh,z}\sqrt{m_z^2 + 4m_\rho^2} \quad \text{with} \quad m_\rho^2 = m_x^2 + m_y^2 \tag{4.24}$$

From the equation above, we define the quantity $\tilde{m} = m_z^2 + 4m_\rho^2$.

Mn spin properties under magnetic field

At thermal equilibrium without carriers in the dot and at low field (linear regime), we can write the free energy of Mn spins as [38]

$$F_{Mn}(\vec{m}, T, \vec{B}) = \frac{\vec{m}^2}{2\chi_{Mn}} - m_z B_z - m_x B_x$$
$$\text{where} \quad \chi_{Mn} = \frac{(g_{Mn}\mu_B)^2 S(S+1)N_{eff}}{3k_B(T+T_0)} \tag{4.25}$$

the magnetic susceptibility of Mn ions. The conditions at equilibrium satisfy

$$\frac{\partial F_{Mn}}{\partial m_z} = 0 \Rightarrow \frac{m_z}{\chi_{Mn}} - B_z = 0 \Rightarrow m_z = \chi_{Mn}B_z$$
$$\frac{\partial F_{Mn}}{\partial m_x} = 0 \Rightarrow \frac{m_x}{\chi_{Mn}} - B_x = 0 \Rightarrow m_x = \chi_{Mn}B_x \tag{4.26}$$

From the above conditions, we understand that without carriers the Mn magnetic moment is isotropic, $\vec{m} = \chi_{Mn}\vec{B}$.

Mn and light hole properties under magnetic field

In presence of a light hole in the dot, we write the free energy as

$$F_{Mn-lh}(\vec{m}, T, \vec{B}) = F_{Mn}(\vec{m}, T, \vec{B}) + F_{lh} \tag{4.27}$$

where

$$F_{lh} = -k_B T \ln(Z) = -k_B T \ln\left[e^{\frac{-E_{lh}}{k_B T}} + e^{\frac{E_{lh}}{k_B T}}\right] \tag{4.28}$$

At low temperatures it becomes

$$F_{lh} \approx -E_{lh} = -B_{lh,z}\sqrt{m_z^2 + 4m_\rho^2} \tag{4.29}$$

as a result, the free energy of Mn and light hole, becomes

$$F_{Mn-lh} = \frac{\vec{m}^2}{2\chi_{Mn}} - m_z B_z - m_x B_x - B_{lh,z}\sqrt{m_z^2 + 4m_\rho^2} \tag{4.30}$$

• **Field parallel to x axis**

For a magnetic field applied along x axis, we set $B_z = 0$ and $B_x = B$, then

$$F_{Mn-lh} = \frac{\vec{m}^2}{2\chi_{Mn}} - m_x B - B_{lh,z}\sqrt{m_z^2 + 4m_\rho^2} \tag{4.31}$$

By applying again the equilibrium conditions, we find

$$\frac{\partial F}{\partial m_z} = 0 \Rightarrow \frac{m_z}{\chi_{Mn}} - \frac{B_{lh,z}m_z}{\tilde{m}} = 0 \tag{4.32}$$

with $\tilde{m} = \sqrt{m_z^2 + 4m_\rho^2}$ and we get $m_z = 0$ and $\tilde{m} = 2m_\rho$.
Along x and y, the conditions at equilibrium are respectively

$$\frac{\partial F}{\partial m_y} = 0 \Rightarrow \frac{m_y}{\chi_{Mn}} - \frac{B_{lh,z}m_y}{\tilde{m}} = 0$$
$$\Rightarrow m_y = 0 \Rightarrow \tilde{m} = 2m_x \tag{4.33}$$

$$\frac{\partial F}{\partial m_x} = 0 \Rightarrow \frac{m_x}{\chi_{Mn}} - B_x - \frac{4B_{lh,z}m_x}{\tilde{m}} = 0$$
$$\Rightarrow m_x = \chi_{Mn}[B_x + 2B_{lh,z}] \tag{4.34}$$

This corresponds to a Brillouin function shifted by $B_{lh,x} = 2B_{lh,z}$. The expected light hole Zeeman shift is $E_{lh}(B) = -4B_{lh,z}m_x = -4B_{lh,z}\chi_{Mn}[B + 2B_{lh,z}]$.

• **Field parallel to z axis**

At this point we will examine the case where field is applied along z axis and $B_x = 0$, $B_z = B$. The free energy for light hole and Mn is

$$F_{Mn-lh} = \frac{\vec{m}}{2\chi_{Mn}} - m_z B - B_{lh,z}\sqrt{4(m_x^2 + m_y^2) + m_z^2} \tag{4.35}$$

The equilibrium conditions are

$$\frac{\partial F}{\partial m_x} = \frac{m_x}{\chi_{Mn}} - \frac{4B_{lh,z}m_x}{\tilde{m}} = 0 \tag{4.36}$$

$$\frac{\partial F}{\partial m_y} = \frac{m_y}{\chi_{Mn}} - \frac{4B_{lh,z}m_y}{\tilde{m}} = 0 \tag{4.37}$$

If $m_\rho \neq 0$ ($m_x \neq 0$ or $m_y \neq 0$) then

$$\frac{1}{\chi_{Mn}} - \frac{4B_{lh,z}}{\tilde{m}} = 0 \Rightarrow \tilde{m} = 4\chi_{Mn}B_{lh,z} \tag{4.38}$$

As a result the energy shift will be

$$E_{lh}(B) = -B_{lh,z}\tilde{m} \Rightarrow$$
$$E_{lh}(B) = -4\chi_{Mn}B_{lh,z}^2 \tag{4.39}$$
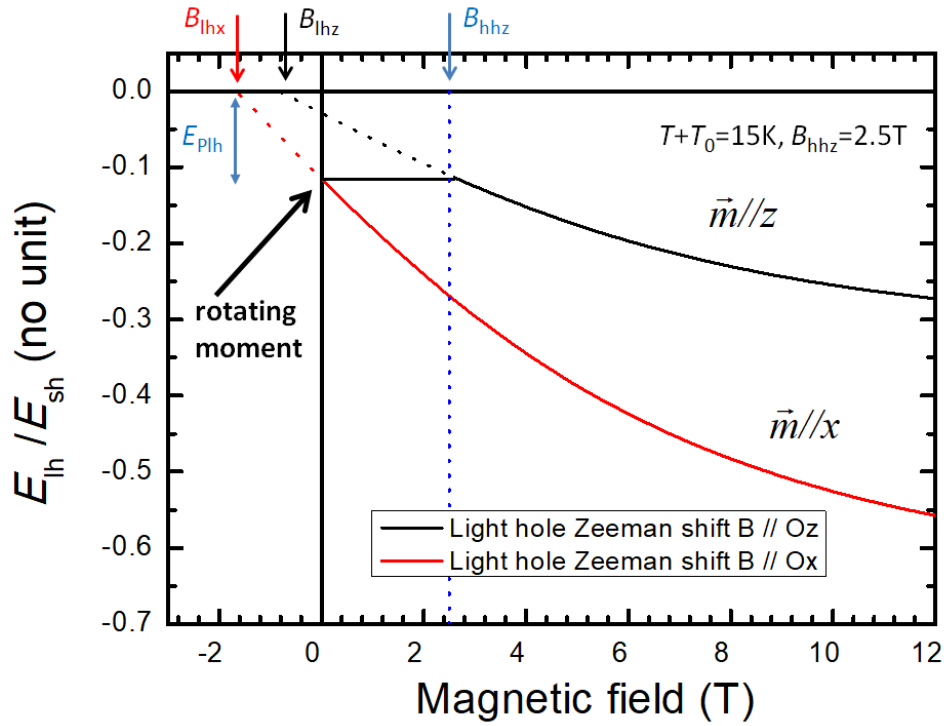
Figure 4.46 – Zeeman shift for a field applied along x and z axis, represented with two Brillouin functions shifted with respect to each other due to the magnetic polaron effect.

which is constant and equal to the polaron energy at B = 0 T. This also is the reason we observe the characteristic plateau in the Zeeman shift at low field.

In Fig. 4.46 we present the evolution of energy as a function of magnetic field by two Brillouin functions shifted with respect to each other. For a field applied along z axis which is parallel to the nanowire axis, the Brillouin function is shifted by an energy equal to that of magnetic polaron.

By applying the equilibrium conditions along z we find

$$\frac{\partial F}{\partial m_z} = 0 \Rightarrow \frac{m_z}{\chi_{Mn}} - B - \frac{B_{lh,z} m_z}{\tilde{m}} = 0$$

$$\Rightarrow \frac{3}{4} \frac{m_z}{\chi_{Mn}} = B \Rightarrow m_z = \frac{4}{3} \chi_{Mn} B$$

(4.40)

The expression above is valid only on the plateau region.

● **Orientation of the magnetic moment**

In this final part of the analysis we calculate the orientation of magnetic moment $\vec{m}$. We begin from the expression of $\tilde{m}$

$$\tilde{m}^2 = 4m_\rho^2 + m_z^2 \Rightarrow 4m_\rho^2 = \tilde{m}^2 - m_z^2 = (4\chi_{Mn}B_{lh,z})^2 - \left(\frac{4}{3}\chi_{Mn}B\right)^2$$

$$\Rightarrow m_\rho^2 = \frac{1}{4}\left[(4\chi_{Mn}B_{lh,z})^2 - \left(\frac{4}{3}\chi_{Mn}B\right)^2\right] \tag{4.41}$$

$$\Rightarrow m_\rho = 2\chi_{Mn}\left[B_{lh,z}^2 - \frac{B}{3}\right]^{1/2}$$

The polar angle of magnetic moment, is calculated as follows

$$\tan(\theta) = \frac{m_\rho}{m_z} = \frac{2\chi_{Mn}\left[B_{lh,z}^2 - \left(\frac{B}{3}\right)^2\right]}{\frac{4}{3}\chi_{Mn}B}$$

$$= \frac{1}{2}\sqrt{\left(\frac{3B_{lh,z}}{B}\right)^2 - 1} \tag{4.42}$$

By setting $B_c = 3B_{lh,z} = B_{hh,z}$, we have for $B = B_c$, $\theta = 0$ ($\vec{m}$ aligned parallel to z axis). If $B > B_c = 3B_{lh,z}$, along z we have $m_x = m_y = 0$, thus $\tilde{m} = m_z$. By applying the equilibrium condition, we find

$$\frac{\partial F}{\partial m_z} = 0 \Rightarrow \frac{m_z}{\chi_{Mn}} - B - B_{lh,z} = 0 \Rightarrow m_z = \chi_{Mn}(B + B_{lh,z}) \tag{4.43}$$

which corresponds to a Brillouin function shifted by $B_{lh,z}$. Then the light hole energy shift is

$$E_{lh}(B) = -B_{lh,z}m_z = -\chi_{Mn}B_{lh,z}(B + B_{lh,z}) \tag{4.44}$$

The results of the above calculation are plotted in Fig. 4.46. In this section we developed the theory which explains the plateau corresponding to a shifted Brillouin function for a field applied parallel to the nanowire axis, by taking into account only the exchange field induced by the light hole. A complete qualitative treatment of the experimental data, taking into account electrons, the coupling between light hole and split-off and the magnetic fluctuations, is done in section 4.4.4.3.

Measurement of circular polarization degree

A very interesting experiment which can provide us with information about the valence band ground state is the measurement of the degree of circular polarization. In order to perform this measurement we used a quarter waveplate $\lambda/4$ placed in front of a linear polarizer at an angle of $\pi/2$ and we collected the emitted photoluminescence from -11 T to 11 T with a step of 0.5 T. Then we calculated the S_3 stokes parameter which gives us the degree of circular polarization from the relation

$$S_3 = \frac{I_+ - I_-}{I_+ + I_-} \tag{4.45}$$

where I_+ the photoluminescence intensity for a positive field and I_- for the negative with the same magnitude.
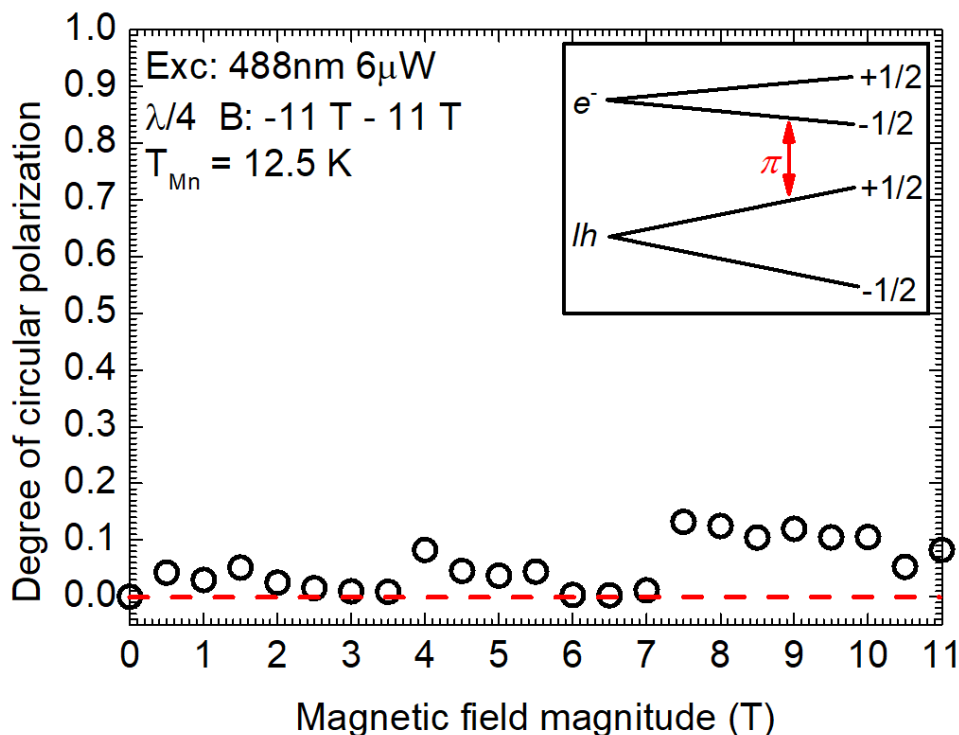
Figure 4.47 – The degree of circular polarization as a function of magnetic field magnitude for the CdMnTe quantum dot of nanowire W-11, measured in Faraday configuration.

In Fig. 4.47 we plot the circular polarization degree of the CdMnTe quantum dot in nanowire W-11 as a function of the magnitude of magnetic field. The measurement was carried out in Faraday configuration, where both the magnetic field and light collection are parallel to the nanowire axis and the effective Mn temperature is $T_{Mn} = 12.5$ K. The polarization degree is almost constant and very small for all values of magnetization. This is what we expect for a π type transition originating from dipole parallel to the nanowire axis, which by extent is associated to a ground state of a very pure light hole type.

The results obtained by studying the samples in the uniaxial magnet are very promising and although we carried out the measurements for a field parallel and perpendicular to the wire axis on two different nanowires and under different excitation conditions, we managed to confirm a light hole ground state in both cases. For a more consistent and quantitatively robust investigation though, we had to study the same nanowire under different field orientations. This could be achieved only by performing magneto-optical measurements in a vectorial magnet.

4.4.4.2 Anisotropy on the same nanowire using a vectorial magnet

As regards the study of CdMnTe - ZnTe nanowire - quantum dots, using the vectorial magnet, we carried out the experiments only on the as-grown sample. This was due to the fact that the piezoelectric stage begun to malfunction, consequently we didn't manage to measure any dispersed nanowire. Again, similar to what we did before we tried to identify a bright object where we could resolve both the emission from ZnTe core and CdMnTe quantum dot. The nanowire we measured is labeled W-12.

In Fig. 4.48 we present the photoluminescence obtained from the CdMnTe quantum dot in nanowire W-12 for a magnetic field applied perpendicular (Fig. 4.48 a)) and parallel (Fig. 4.48 b)) to the nanowire axis. The main line emission of the CdMnTe quantum dot is in the range of 1830 meV to 1850 meV and it is very close to that of both nanowires we studied in the uniaxial magnet. The range of magnetic field values for which we recorded the spectra was 0
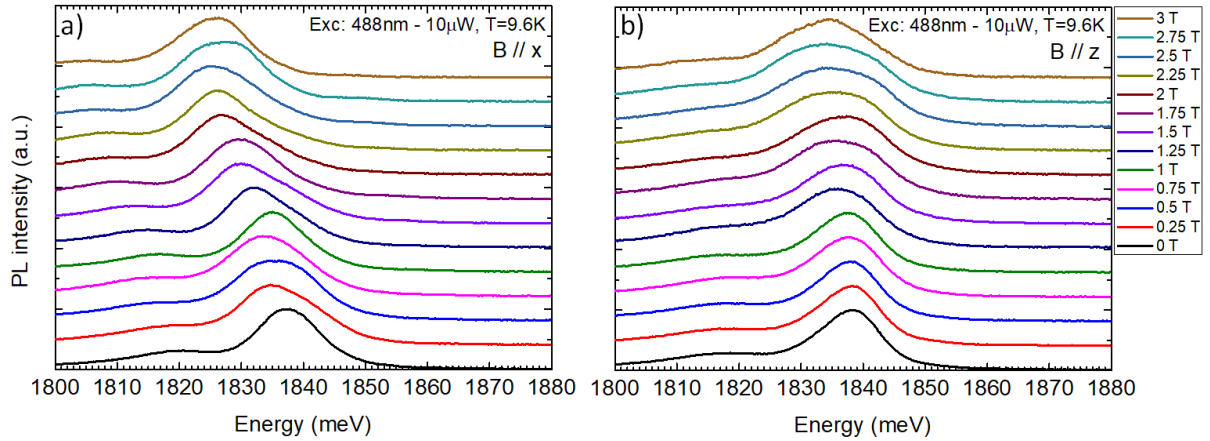
Figure 4.48 – Micro-photoluminescence emission from CdMnTe quantum dot obtained from nanowire W-12 on the as-grown sample for a magnetic field applied perpendicular a) and parallel b) to the nanowire axis.

T - 3 T (which is the maximum field we could reach along x axis) with a step of 0.25 T. The temperature as measured by the controller was 9.6 K and the excitation power was 10 μW. When the field is applied along x axis we can clearly see a shift towards lower energies, even at small field values, while for the field applied along z, up to 1 T Zeeman shift is vanishing and from 1.25 T and above, the line begins to redshift slowly. These results are similar to what we obtained from the uniaxial magnet measurements. For plotting the evolution of energy as a function of applied field for nanowire W-12, as shown in Fig. 4.49, we took its values at the barycenter of the main emission line.
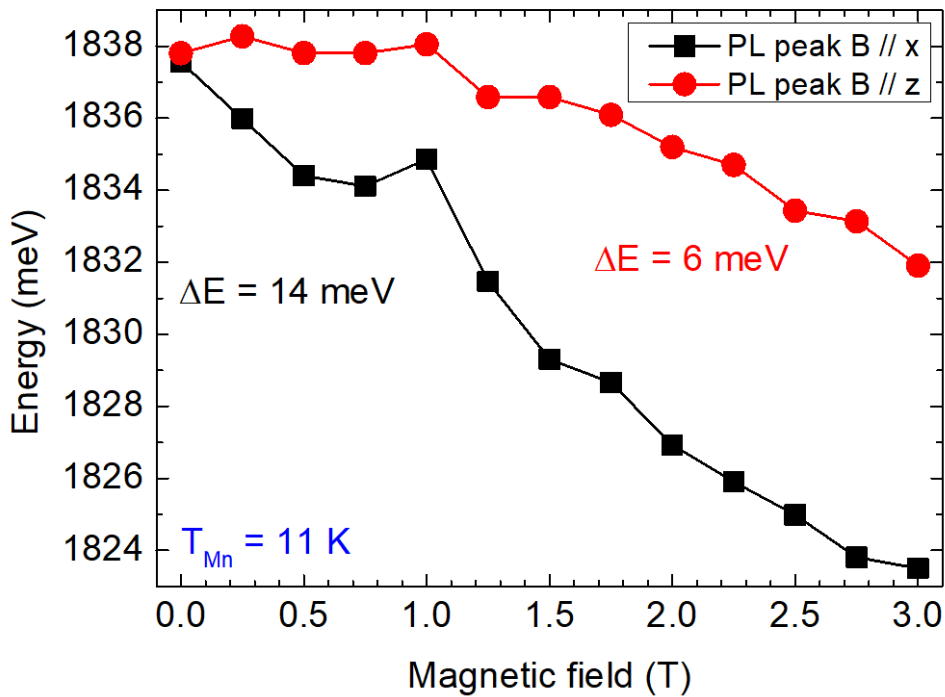
Figure 4.49 – Emission energy position of the CdMnTe quantum dot in nanowire W-12 as a function of the applied magnetic field for both orientations along x and z axis.

For a magnetic field applied perpendicular to the wire axis we observe that the energy begins to shift following a linear behaviour even at small values of field and the Zeeman shift at 3 T is

$\Delta E = 14$ meV. On the contrary, when the field is applied parallel to the wire axis, up to 1 T the Zeeman shift is vanishing. For $B//z$, 3 T the shift is smaller in comparison to that for $B//x$, $\Delta E = 6$ meV. From the shift plot for the field along both axis, we confirm that the evolution of energy is almost identical with that of the nanowires measured in the uniaxial magnet for excitation powers 4 μW along x and 6 μW along z. The vanishing vanishing slope of Zeeman shift for the field applied parallel to the nanowire axis is in good agreement with a light hole magnetic polaron formation.

The greatest advantage of using a vectorial magnet is that we can apply the field in any direction and through that, measure the Zeeman shift anisotropy in the same nanowire quantum dot. Since the nanowire of interest was from the as-grown sample, by changing the magnetic field values along x and z axis, we rotated the magnetic field vector along the zx plane. The field component along the two axis were calculated in order to always keep constant the magnitude of the magnetic field at $\left|\vec{B}\right| = 2$ T. In our convention, $\theta = 0^o$ correspond to $\vec{B}//z$ (parallel to the nanowire axis). In the table below we present the values of magnetic field and the corresponding angle of the field vector.

Table 4.2 – The angle of magnetic field vector of magnitude $\left|\vec{B}\right| = 2$ T and the corresponding values of the two magnetic field components B_z and B_x.

Angle θ (deg.)	$\vec{B}_z$ (T)	$\vec{B}_x$ (T)
0	2	0
22.5	1.85	0.77
45	1.41	1.42
67.5	0.77	1.85
90	0	2
112.5	-0.77	1.85
135	-1.42	1.41
157.5	-1.85	0.77
180	-2	0

The objective initially was to carry out the magneto-optical measurements for a full magnetic field rotation of 360° on zx plane but this was not feasible due to the fact that by lowering the field, we lost the nanowire and due to malfunctioning piezoelectric stage we were not able to retrieve it again.

In Fig. 4.50 a) we present the photoluminescence spectra recorded from the CdMnTe dot emission of nanowire W-12 for different orientations of magnetic field on zx plane. When $B_x = 0$ T and $B_z = 2$ T the Zeeman shift is minimum. As we reduce B_z and we increase B_x, emission shifts fast towards lower energies and when field becomes aligned along x axis the quantum dot emission reaches the lowest energy. As we start to decrease again B_x and increase the magnitude of B_z towards the opposite direction, spectra move at higher energies and when $B_z = -2$ T and $B_x = 0$ T the emission energy is the same to that of the opposite field direction. Through this measurement we can visualize the anisotropy of Zeeman shift as we rotate the angle of magnetic field on zx plane. This is depicted in the polar plot of Fig. 4.50 b) where we present the Zeeman shift as a function of the field angle. The nanowire is oriented parallel to z axis. When the field vanishes along z and becomes maximized along x, the difference in the Zeeman shift is 11.5 meV. As a guide for the eye only and by considering that the Zeeman shift remains unchanged when we switch from B_x to $-B_x$, we have completed by symmetry the polar plot for $0^o \leq \theta \leq 360^o$.

Up to this very point, by analyzing the data obtained from magneto-optical measurements we confirm a light hole ground state in the nanowire quantum dot, characterized by an anisotropic
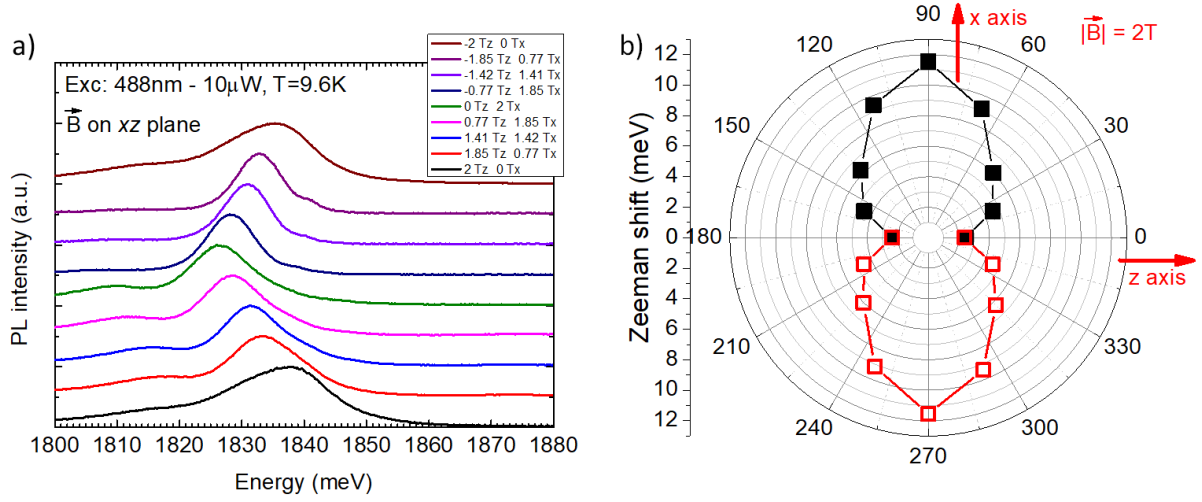
Figure 4.50 – Micro-photoluminescence spectra from the CdMnTe quantum dot in nanowire W-12 for different angles of magnetic field on zx plane a). Zeeman shift of the quantum dot emission as a function of the angle of magnetic field on zx plane b). Black points correspond to the energy position as obtained from the barycenter of the main emission line, while the red points were introduced considering identical Zeeman shift along the two directions of x axis.

Zeeman shift for a field rotated along the plane on which the axis of the nanowire quantum dot lies. Additionally and as revealed by the plateau for low field applied along z axis, we always observe the effect of magnetic polaron formation. In the last section of this chapter we will combine all the knowledge acquired so far from the theoretical study of the nanowire quantum dots, with the results obtained from experimental measurements and we will attempt to fit quantitatively the Zeeman shift by taking into account the formation of magnetic polaron, light hole spin renormalization and reconfinement due to small valence band offset.

4.4.4.3 Quantitative analysis of experimental results

In this section we develop a model, which describes the formation of magnetic polaron and we fit the data obtained experimentally by taking into account the mixing of light hole with split-off. We will also include the effect of hole reconfinement, as discussed in Chapter 3. Through this model, which was originally proposed by David Ferrand, we calculate numerically the photoluminescence spectra for different values of temperature and magnetic field (not only in the linear approximation) and we include the magnetic fluctuations. For the description of our system, we use the $sp-d$ exchange interaction Hamiltonian we described in Chapter 1, Eq. 1.14.

● **Light hole spin renormalization**

The spin matrix for the light holes is given by

$$\vec{\sigma}_h = \begin{pmatrix} \frac{\beta_{SO}}{6} & \frac{\delta_{SO}}{3} \\ \frac{\delta_{SO}}{3} & -\frac{\beta_{SO}}{6} \end{pmatrix} \tag{4.46}$$

where β_{SO} and δ_{SO} are the parameters which determine the strain induced mixing between light hole and split-off, as discussed in the previous chapter. At this point we have to underline that for the light hole states we use the spin matrix obtained from perturbation theory. As a result, spin is a 4×4 matrix on the total angular momentum basis for heavy holes and mixed light hole - split-off states. In our model however, we consider that the separation between heavy

and light holes is very large, consequently spin reduces to a 2×2 matrix. We also remind to the reader that the formalism for developing the spin matrices which take into account the coupling between light hole and split-off is described analytically in Chapter 3, section 3.4.

- **Magnetic polaron formation**

$$\vec{M} = \sum_{i \in QD} g_{Mn} \mu_B \vec{S}_i = M_{sat} \vec{m}(\theta)$$

$$M_{sat} = N_{eff} g_{Mn} \mu_B S_{Mn}, \quad N_{eff} = \int \int \int \rho_{Mn}(\vec{r}) d^3 \vec{r}$$

In the dot: $\quad \rho_{Mn}(\vec{r}) = N_0 x_{eff}$

$$\vec{m} = \frac{<\vec{M}>}{M_{sat}}$$

$$0 \leq \|\vec{m}\| \leq 1$$

$$0 \leq \theta \leq \pi$$

$$0 \leq \phi \leq 2\pi$$
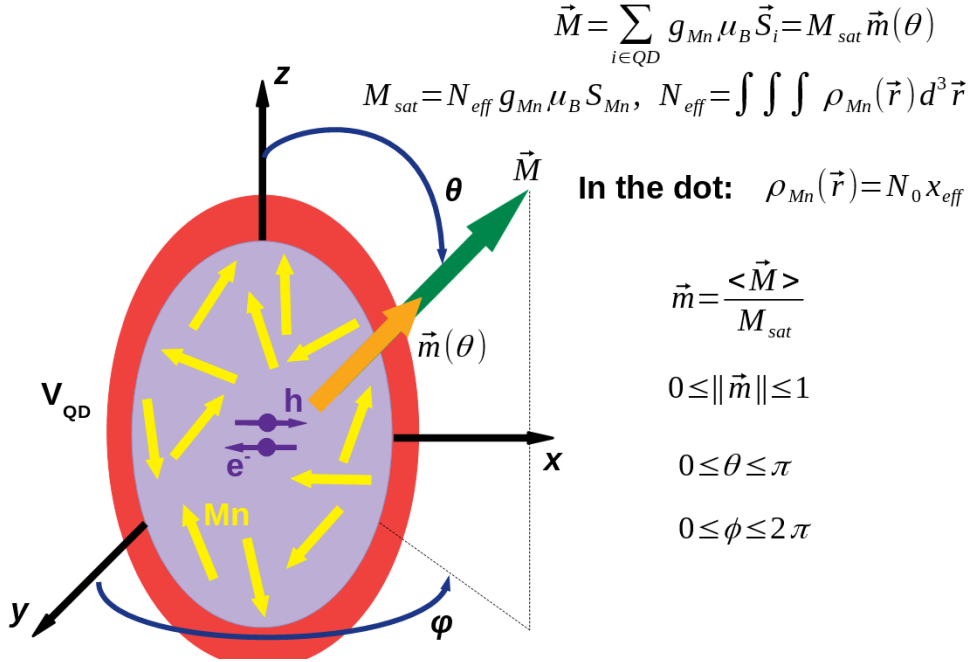
Figure 4.51 – Sketch of an ellipsoidal CdMnTe quantum dot with a photo-generated electron-hole pair (purple arrows) and the Mn spins (yellow arrows).

In Fig. 4.51 we present a sketch of a CdMnTe quantum dot which contains N_{eff} Mn ions with spin $S_{Mn} = 5/2$. The polarization $\vec{M}$ of Mn spins is oriented towards the direction of vector $\vec{m}(\theta)$. The magnetic moment induced by spin polarization of Mn ions is given by

$$\vec{M} = \sum_i g_{Mn} \mu_B \vec{S}_i \tag{4.47}$$

where $g_{Mn} = 2$ the Landé factor and $S_i = 5/2$ the spin of Mn ions inside the dot. In the spherical coordinate system, we can write the expression for the magnetization as

$$\vec{M} = M_{sat} \vec{m}(\theta, \varphi) \tag{4.48}$$

where for an effective concentration of Mn ions, N_{eff}, magnetization at saturation is $M_{sat} = N_{eff} g_{Mn} \mu_B S$ and $0 \leq |\vec{m}| \leq 1$. We consider the approximation that the system is symmetric on xy plane, as a result the dependence on angle φ vanishes.

The most simple way to describe magnetic polarons in heterostructures is through the mean field approximation [103, 104, 105, 106]. The drawback though is that thermal fluctuations are not taken into account, thus it is valid only at very low temperatures. Our objective is to be able to simulate the photoluminescence spectra obtained experimentally for different magnetic fields and temperatures. For this purpose we will introduce from thermodynamics the free energy for the system $F(T, \vec{M})$, as a function of temperature and magnetization. In the absence of carriers which can polarize Mn spins, the probability of having an arbitrary magnetic moment $\vec{M}$ is

$$P(m,\theta) = P(\vec{M}) = Ae^{-\frac{F(T,\vec{M})}{k_B T}}, \qquad 0 \le m \le 1, \qquad 0 \le \theta \le \pi \tag{4.49}$$

where A is a normalizing constant. From the probability calculation we can find all possible orientations of the total magnetic moment $\vec{M}$ for any given value of magnetic field and temperature.

In order to calculate Helmholtz free energy, we begin with the general expression of partition function given by

$$Z = \sum_{m_S = -S}^{S} = e^{\frac{g_S \mu_B B m_S}{k_B T}} \tag{4.50}$$

We assume that inside the quantum dot, N_{eff} paramagnetic spins with $S_{Mn} = -5/2, ..., 5/2$ are introduced through Mn doping. By introducing the Brillouin function argument $\frac{g_{Mn}\mu_B B}{k_B T_{Mn}}$ we calculate the partition function as

$$Z = \frac{\sinh\left(\frac{6\mu_B B}{k_B T_{Mn}}\right)}{\sinh\left(\frac{\mu_B B}{k_B T_{Mn}}\right)} \tag{4.51}$$

From the above expression we calculate the Helmholtz free energy by summing all free energies of N_{eff} independent Mn spins

$$F(T,B) = -N_{eff}k_B T \ln Z = -N_{eff}k_B T_{Mn} \ln \left[\frac{\sinh\left(\frac{6\mu_B B}{k_B T_{Mn}}\right)}{\sinh\left(\frac{\mu_B B}{k_B T_{Mn}}\right)} \right] \tag{4.52}$$

The total magnetic moment inside the dot is given by

$$M(T,B) = -\left(\frac{\partial F(B,T)}{\partial B}\right)_T = N_{eff}g_{Mn}\mu_B S_{Mn} B_{\frac{5}{2}}\left[\frac{g_{Mn}\mu_B B}{k_B T_{Mn}}\right] \tag{4.53}$$

and the magnetic moment at saturation is equal to $M_{sat} = N_{eff}g_{Mn}\mu_B S_{Mn}$. For our calculations, we need to express Helmholtz free energy as a function of temperature and magnetization. In order to switch from magnetic field B to magnetization M we have to apply a Legendre transform as follows

$$\mathcal{L}[F(T,B)] = F^*(T,M) = F(T,B^*) + MB^*, \quad -\frac{\partial F(T,B)}{\partial B}\bigg|_{B=B^*} = M \tag{4.54}$$

from which we calculate B^*

$$B^* = \left(\frac{k_B T_{Mn}}{g_{Mn}S\mu_B}\right) B_{5/2}^{-1}\left(\frac{M}{M_{sat}}\right) \tag{4.55}$$

where $B_{5/2}^{-1}$ the reciprocal Brillouin function. As also shown in [107], Helmholtz free energy of Mn spins, as a function of magnetization is written

$$F_{Mn}(T,M) = -N_{eff}k_B T_{Mn} \ln \left\{ \frac{\sinh\left[\frac{6}{5}B_{5/2}^{-1}\left(\frac{M}{M_{sat}}\right)\right]}{\sinh\left[\frac{1}{5}B_{5/2}^{-1}\left(\frac{M}{M_{sat}}\right)\right]} \right\} +$$
$$N_{eff}k_B T_{Mn}\frac{M}{M_{sat}}B_{5/2}^{-1}\left(\frac{M}{M_{sat}}\right) \tag{4.56}$$

In the above expression only the magnitude M of magnetic moment is taken into account. In a real system of volume V, the free energy depends on the profile of magnetization $\vec{M}(\vec{r})$, but the calculation of the functional $F(V, T, \vec{M}(\vec{r}))$ is non-trivial. For our purpose we will consider a uniform magnetization in the quantum dot.

When we apply an external magnetic field we have also to take into account the Zeeman contribution of Mn. As a result the Helmholtz free energy becomes

$$F_{S_{Mn}}(\vec{M}) = F_{Mn}(\vec{M}) - \vec{M} \cdot \vec{B} = F_{Mn}(\vec{M}) - M_{sat}\vec{m} \cdot \vec{B} \tag{4.57}$$

The next step is to calculate the energies of the photogenerated carriers. To do that we have to diagonalize the Hamiltonian

$$\mathcal{H}_{carriers} = \Delta E_{hh}^{sat}\vec{m} \cdot \vec{\sigma}_h + \Delta E_e^{sat}\vec{m} \cdot \vec{\sigma}_e + E_x \tag{4.58}$$

where ΔE_{hh}^{sat} and ΔE_e^{sat} the giant Zeeman term at saturation for holes and electrons respectively and E_X the exciton recombination energy taken as a constant. The spin of electrons is given by the $\vec{\sigma}_e$ matrix (Pauli matrices) and that of the holes by $\vec{\sigma}_h$ (see Eq. 4.46).

From the eigenvalues of the carrier Hamiltonian $\mathcal{H}_{carrier}$, we calculate the partition function for electron and holes given by

$$
\begin{aligned}
Z_h &= \sum_{j=1}^{2} e^{-E_h(j)/k_B T} \\
Z_e &= \sum_{j=1}^{2} e^{-E_e(j)/k_B T}
\end{aligned}
\tag{4.59}
$$

where the calculated energy levels with the Zeeman splitting and the associated transition probability with the corresponding polarization of light are shown in Fig. 4.52.
In this case we consider a light hole ground state, coupled with split-off, which is separated by a very large energy from heavy hole. In this configuration we can have only 4 transitions in total as we ignore completely any contribution from heavy holes. The electron - light hole recombination, is characterized by both σ and π transitions.

From the partition function of the carriers we calculate the Helmholtz free energy as follows

$$
\begin{aligned}
F_e(\vec{m}) &= -k_B T \ln Z_h \\
F_h(\vec{m}) &= -k_B T \ln Z_e
\end{aligned}
\tag{4.60}
$$

The total Helmholtz free energy is given by the sum of the individual free energy components of the carriers and Mn ions

$$F_{tot}(\vec{M}) = F_{Mn}(\vec{m}) - M_{sat}(\vec{m} \cdot \vec{B}) + E_X + F_e(\vec{m}) + F_h(\vec{m}) \tag{4.61}$$

In order to calculate and plot the photoluminescence spectra, we have to impose that the carriers are in thermal equilibrium. In this case, the level population is

$$P_{i,j}^{eh} = \frac{e^{-\frac{E_h(j)}{k_B T}} e^{-\frac{E_e(i)}{k_B T}}}{Z_h Z_e} \tag{4.62}$$

where $E_h(j)$ and $E_e(i)$ are the calculated confined levels for electrons and holes. Through this
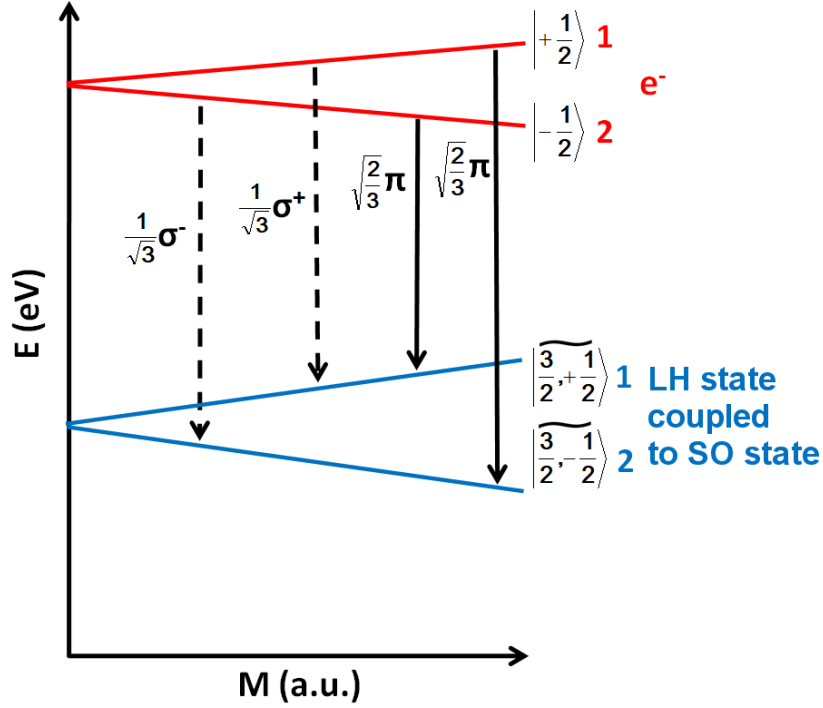
Figure 4.52 – Schematic representation of the Zeeman splitting of the calculated energy levels for the conduction band electrons and valence band light holes, with the corresponding oscillator strength for the allowed transitions between them.

equation, we take into account all possible transitions with a respective weight regardless of the ground state, which in our case is a light hole. By using the level population we can calculate a theoretical photoluminescence spectrum for one specific orientation of magnetic moment $\vec{M}$ through the sum over all calculated levels

$$I_{\vec{M}}(\varepsilon) = \sum_{i,j} f_{i,j}\delta(\varepsilon - E_{i,j})P_{i,j}^{eh} \tag{4.63}$$

where in place of Dirac function $\delta(\varepsilon - E_{i,j})$ we introduce a Gaussian function, the linewidth of which is 1 meV chosen accordingly in order to include the line broadening induced by the spectral diffusion. With $f_{i,j}$ we denote the oscillator strengths between the electron and hole states as shown in Fig. 4.52.

In order to obtain the real spectra however, we have to integrate over all possible orientations of magnetization $\vec{M}$ as follows

$$I(\varepsilon) = \int P_{occ}[\vec{M}]I_{\vec{M}}(\varepsilon)d^3\vec{M} \tag{4.64}$$

where $P_{occ}(\vec{M})$ is the probability of having a magnetization of a certain orientation and it is a functional of the Helmholtz free energy defined as

$$P_{occ}[\vec{M}] = e^{-\frac{F_{tot}(\vec{M})}{k_B T}} \tag{4.65}$$

From the maximum of $I(\varepsilon)$ which gives the simulated photoluminescence spectra of a magnetic dot, we can fit the experimental measurements under different values of magnetic field and temperatures including also the effect of magnetic polaron, as we integrate over all probabilities

of magnetization $\vec{M}$. The applied field for constructing the photoluminescence spectra is from 0 T to 11 T, similar to what we used for the experimental measurements.

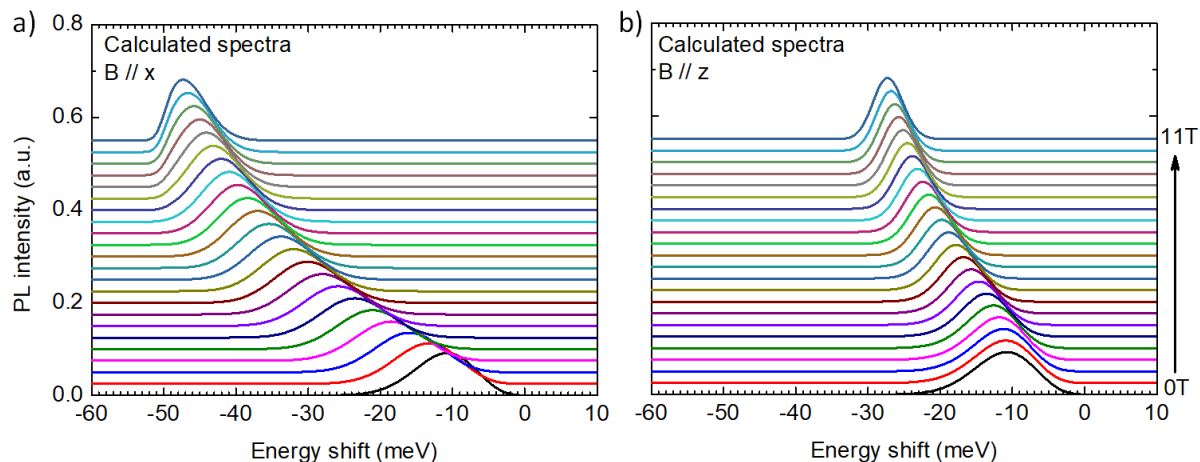Figure 4.53 – Calculated photoluminescence spectra for different values of magnetic field, applied along x a) and z axis b)

In Fig. 4.53 a) we present the calculated photoluminescence spectra for the CdMnTe quantum dot for a magnetic field applied along x and in Fig. 4.53 b) for a field applied along z. As we see in Fig. 4.53, at 0T and for both orientations of magnetic field the shift is not vanishing and this is attributed to the polaron energy, $E_P = 11$ meV.

The parameters for calculating the spectra are the exchange energies for holes and electrons which are $E_{sh} = 88$ meV and $E_{se} = 22$ meV, the spin renormalization factors β_{SO} and δ_{SO} and the effective number of Mn ions N_{eff}. In this calculation, $N_{eff} = 47$. The spin renormalization factors along z and x axis, due to the coupling of light hole with split-off are respectively (Eq. 3.23)

$$\beta_{SO} = 1 - \frac{4\Delta E_{HL}}{\Delta_{SO}}, \quad \delta_{SO} = 1 - \frac{\Delta E_{HL}}{\Delta_{SO}} \tag{4.66}$$

and for the photoluminescence spectra calculation, they take the values $\beta_{SO} = 1.44$ and $\delta_{SO} = 1.11$. These values are in agreement with an heavy hole - light hole splitting $\Delta E_{LH} \approx 110$ meV, confirming a strongly isolated light hole ground state.

In Fig. 4.54 a) we present the Zeeman shift for a field applied perpendicular and parallel to the axis of the two different nanowires (w-10 and W-11 respectively) measured in the uniaxial magnet. Although the nanowires are different, the model fits well the data and confirms a light hole ground state. Same applies for nanowire W-12 from the as-grown sample measured with the vectorial magnet shown in Fig. 4.54 b). The difference between the two fits is the Mn temperature, where there is a difference of 2 K between the two magnets. In both cases for the field applied parallel to the nanowire axis we also fit the vanishing Zeeman shift at small fields which is typical for a light hole magnetic polaron. This is a very important feature of the fitting program, as it can calculate the angle of magnetization as a function of the applied field.

In Fig. 4.55 we present the orientation of Mn magnetic moment as a function of an applied field along z axis. Initially the magnetization due to polarization of Mn ions is oriented parallel to x axis. As the magnetic field increases it begins to rotate and above 1.5 T it is oriented parallel to the applied field. Above this value the Brillouin like evolution of Zeeman shift gets restored.
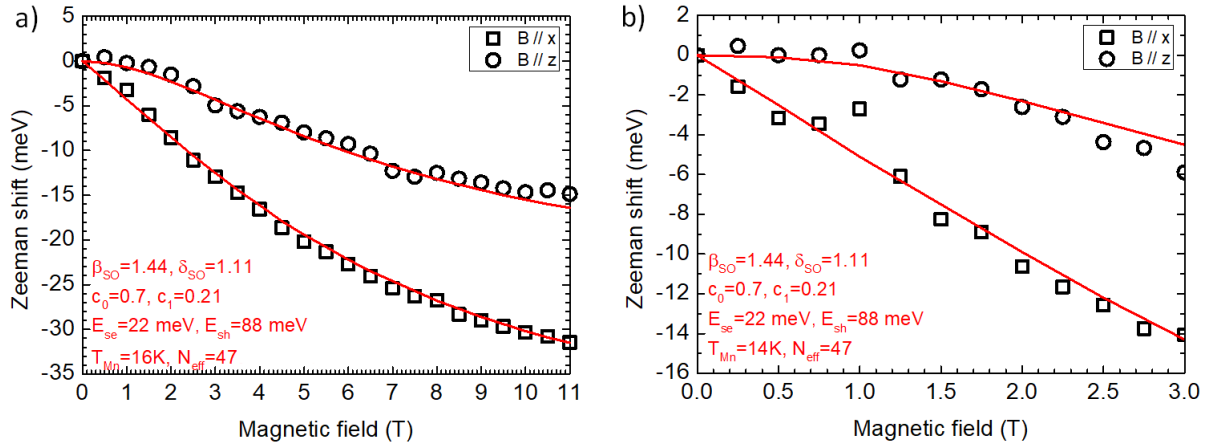
Figure 4.54 – Zeeman shift as measured experimentally and the analytical model fit (red lines), for the two different nanowires - dispersed W-10 and as-grown W-11 - measured in the uniaxial magnet a) and for nanowire W-12 from the as-grown sample in the vectorial magnet b)
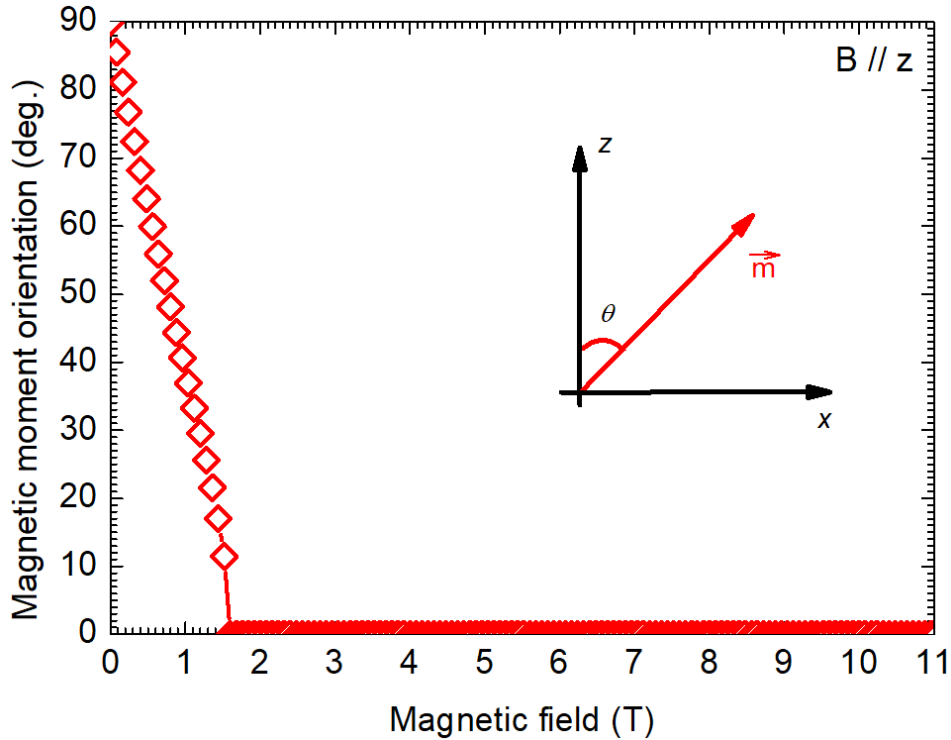
Figure 4.55 – The orientation of Mn ions magnetic moment as a function of an applied magnetic field along z axis.

• Reconfinement effect

In order to fit the data, we had also to introduce the hole reconfinement effect, which we demonstrated in Chapter 3. The increase of magnetic field increases the band offset between the CdMnTe dot and the ZnTe core as it "digs" the confinement potential. This effect can increase the confinement, up to 20% in the quantum dot and this of course influences the Zeeman shift. The reconfinement effect is imposed through c_0 and c_1 terms, as we discussed in Chapter 3.

After fitting the data for the two directions of field along x and z axis, we calculated the

spectra for a rotating field on xz plane, in order to fit the anisotropic Zeeman shift as measured in the vectorial magnet.
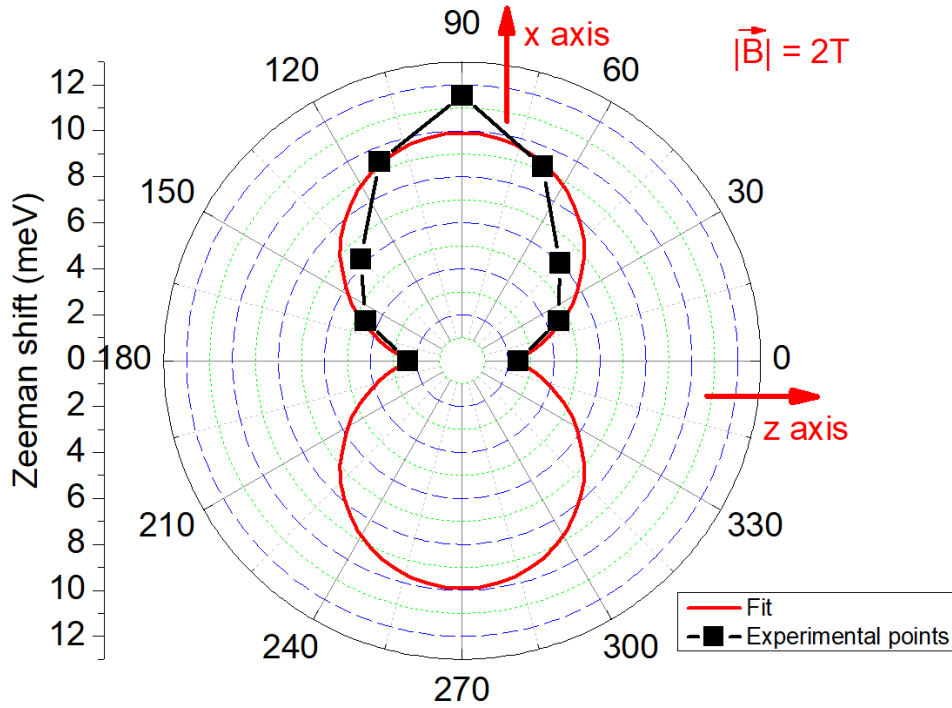
Figure 4.56 – Experimental measurements of the anisotropic Zeeman shift on zx plane obtained from nanowire W-12, superimposed with the fitting values as obtained from the calculated spectra.

In Fig. 4.56 we present the experimental measurements of the anisotropic Zeeman as obtained from a single nanowire on the as-grown sample measured in the vectorial magnet. The fitting parameters are the same as those shown in Fig. 4.54 b) and by extracting the Zeeman shift from the calculated spectra we fit quite well the experimental data.

The last thing we want to confirm is the fitting of energy shift under different temperatures and the characteristic redshift for decreasing temperature which is an indication of the magnetic polaron formation.

For a CdTe quantum dot, we can fit the energy gap using the gap variation formula introduced by Passler [102]

$$E(T) = E(0) - \frac{\alpha \Theta_p}{2} \left\{ \left[1 + \left(\frac{2T}{\Theta_p} \right)^p \right]^{\frac{1}{p}} - 1 \right\} \qquad (4.67)$$

where $\alpha = 0.35$, $\Theta_p = 134$ K and $p = 2.415$. We use this formula because it can fit the gap dependence on temperature more accurately than the empirical formula of Varshni [108] for CdTe quantum dots. These parameters are calculated and taken from the thesis of P. Stepanov [12]

In Fig. 4.57 a) we present the calculated photoluminescence spectra as we increase temperature for the as-grown nanowire W-11, measured in the uniaxial magnet. Unfortunately we didn't manage to carry out temperature dependent measurements in the vectorial magnet due to a malfunctioning piezo-manipulator. The minimum and maximum values of temperature are respectively 5 K and 105 K and the step for each spectrum is 2.5 K. From the spectra we confirm the anticipated redshift. By fitting though the experimental data, as show in Fig. 4.57 b) the 6 meV redshift we observed from 30 K to 10 K is in agreement with the calculated one but

Figure 4.57 – Calculated photoluminescence spectra for different temperatures a). The evolution of emission energy as a function of temperature as measured experimentally on nanowire W-11, superimposed with the fit from the numerical model and the gap variation for a dot without magnetic impurities b).
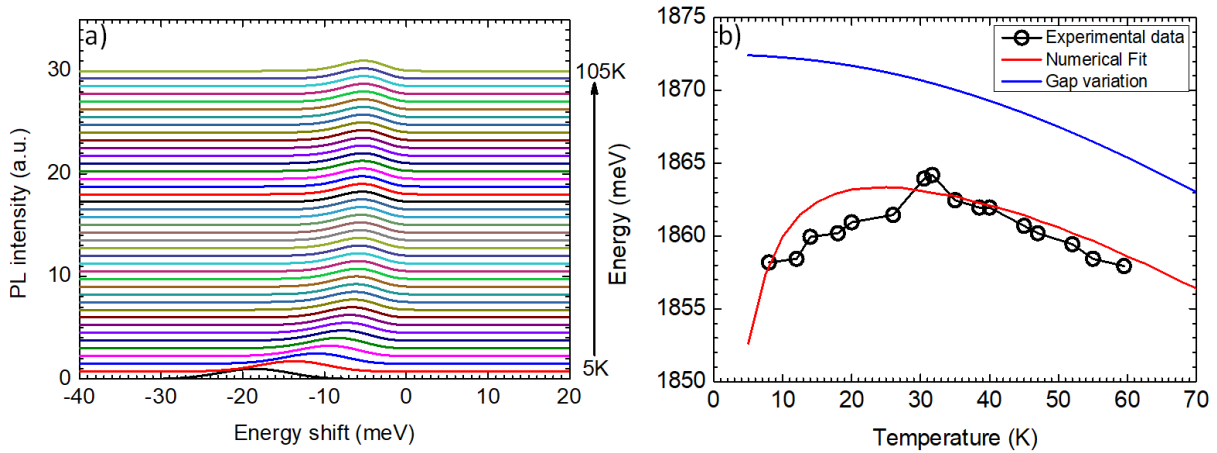
we note some deviations and the measurement will have to be redone when a new piezoelectric stage is available.

4.5 Conclusions

In this chapter we described our attempts and results to stabilize a light hole as a ground state in a semiconductor nanowire quantum dot using three different samples. The first attempt was through a tensile, flat ZnTe quantum dot in a ZnTe - ZnMgTe nanowire. The experimental results are encouraging, as the recorded emission in polarization becomes stronger along the nanowire axis. This suggest the presence of a light hole in the ground state. On the other hand, numerical calculations demonstrate that confinement energy compensates strain, as a result heavy hole and light hole levels remain very close. From theoretical predictions however, we find that by adding more Mg to the shell, we compensate the effect of confinement and promote well isolated light hole states.

In parallel to the attempts of stabilizing a light hole ground state, we attempted to probe a hole spin texture in a strong type II heterostructure consisting of a ZnSe inclusion in a ZnTe nanowire. In that case we expect, that the off-diagonal strain in the ZnTe shell would contribute to the formation of a complex spin structure with skyrmion like characteristics. Unfortunately, we showed that in this structure Se substitutes Te, resulting a ZnSe nanowire with potentially some Te doping.

The final category of samples we studied, were compressive, elongated CdTe and CdMnTe dots in core - shell ZnTe - ZnMgTe nanowires. In particular, the quantum dots doped with Mn ions where surrounded by ZnMgTe in order to restore confinement by increasing the valence band offset. In this case we demonstrated a pure and isolated light hole ground state, while by using the results obtained from numerical calculations we developed a model to fit the experimental data. The characteristic plateau observed by measuring the Zeeman shift for a field applied parallel to the nanowire axis is due to the formation of a light hole magnetic polaron and it depends on Mn concentration. In the Zeeman shift of Fig. 1.14 in Chapter 1, section 1.4 for a CdMnTe-CdMgTe core-shell nanowire, there is no plateau for the field applied along the nanowire axis [33]. This is attributed to the low Mn content (1.5%) used in this work in order to keep the carriers confined in the nanowire core. For the observation of a magnetic polaron, it is required that its formation time is smaller than the exciton lifetime.

Highlights

- **CdTe quantum dots**

Polarization dependent measurements on CdTe quantum dots, indicate the presence of light hole in the ground state. It is important however to remeasure the emission diagram and extract information for the ground state by taking into account the effects of the dielectric screening and environment.

- **Zeeman shift CdMnTe quantum dots**

The measurement of Zeeman shift confirms without ambiguity the presence of light hole and the formation of a magnetic polaron.

- **Very well stabilized light hole**

We fit the experimental data considering a pure light hole ground state. From this model we extract an energy difference between heavy and light holes $\Delta E_{LH} = 110$ meV which is much larger in comparison to few meVs reported in previous samples [59] and in the work of [33] where the heavy hole - light hole splitting was $\Delta_{LH} = 6.5 meV$ and it was attributed to the small valence band offset. This results to lower Zeeman shift anisotropy as the light hole - heavy hole anticrossing becomes stronger.

- **Light hole magnetic polaron**

In this work, a light hole ground state was confirmed for the first time by the measurement of the Zeeman shift anisotropy and by a quantitative fit taking into account the spin renormalization, the field induced reconfinement and the effect of a light hole magnetic polaron formation observed at low temperatures. The magnetic moment induced by the exchange interaction of a light hole exciton and Mn spins is oriented perpendicular to the nanowire axis. The formation of a light hole magnetic polaron is manifested by a characteristic plateau which is associated to the rotation of the magnetic moment.

From the experimental results we didn't directly confirm the renormalization of spin, because the effect is counterbalanced by the field induced reconfinement. In order to confirm the spin enhancement effect, we have to carry out magneto-optical measurements on a structure where there will be Mn everywhere and not only in the dot.

Chapter 5

General conclusions

Addressing a light hole state in a semiconductor heterostructure is of particular interest due to the versatile optical selection rules and spin properties. In this work we investigated the parameters which influence the properties of valence band and we employed different approaches in order to promote a light hole as a ground state. Through a combination of continuum elasticity and 6-band $\vec{k} \cdot \vec{p}$ theory we investigated the influence of quantum dot dimensions, valence band offset and strain environment to the purity of valence band ground state. As a second step, on the same structures, we carried out calculations under an exchange field for the theoretical investigation of Zeeman shift. Experimentally we studied three different categories of nanowire - quantum dots: Compressive CdTe and CdMnTe dots in ZnTe - ZnMgTe core-shell nanowires and tensile ZnTe quantum dots in ZnTe - ZnMgTe core-shell nanowires. In parallel to that we attempted to probe a complex spin texture in a strong type II system comprising of a ZnSe inclusion embedded in a ZnTe nanowire. The main technique we used for the optical characterization of the nanowire quantum dots, was micro-photoluminescence spectroscopy with and without the presence of an external magnetic field. In parallel these heterostructures were studied by EDX and cathodoluminescence spectroscopy. The major results obtained in this work are the following:

- **The influence of quantum dot aspect ratio, strain and valence band offset to the hole ground state:** From the numerical calculations we confirm that for a strong type I quantum dot for $L_{QD}/D_{QD} \geq 1$, the valence band ground state switches from heavy, to light hole. It is attributed to a combined effect of confinement and axial shear strain in the quantum dot. However, when valence band offset is small, as in the case of a CdTe quantum dot in a ZnTe nanowire, confinement becomes weak and the hole envelopes leak outside the dot. This results to a stronger mixing between light and heavy holes near $L_{QD}/D_{QD} = 1$ and light hole is restored as the predominant ground state component only for larger aspect ratios. This is demonstrated by both the integrated presence probability calculation and the oscillator strengths and it agrees with experiments. If the nanowire is passivated by a ZnMgTe shell, this induces additional in-plane compressive strain to the ZnTe nanowire core. For a strong type I system where the holes are confined inside the dot, this additional strain does not have any effect on the switching from heavy to light hole, which takes place for an $L_{QD}/D_{QD} \geq 1$. If however, holes leak outside the dot, the strain induced by the ZnMgTe shell, promotes a heavy hole ground state even for $L_{QD}/D_{QD} > 1$. As the confinement becomes weaker, larger quantum dots aspect ratios are required in order to restore light hole as a ground state. As the valence band offset decreases the numerical calculations show that the critical L_{QD}/D_{QD} ratio required to stabilize a light hole increases (beyond the limit of our calculation for a strong type II).

- **Mixing of light hole with split-off states, renormalization of spin and the effect of field induced reconfinement:** Although separated by almost 1 eV, there is always

a small mixing in the order of 1-2% between split-off states at Γ_7 manifold and Γ_8 hole states. For a heavy hole this mixing does not have any influence on its spin properties. On the contrary, for a light hole ground state, strain and the coupling with split-off states significantly increase the light hole spin projections $< S_x >$ and $< S_z >$. This enhancement is particularly large in strong type I systems. For weak valence band offsets the effect becomes smaller due to envelope leaking in the barrier.

- **Reconfinement effect:** Another observation from these calculations is that spin values increase with increasing exchange field especially when confinement is weak. This effect is directly connected to the split-off presence probability which also increases with the exchange field. By studying the percentage of envelope presence probability inside dots with small valence band offsets, we realized that the exchange field, "digs" the confinement potential thus restoring the presence probability in the quantum dot. In particular, for a weak type I or II band alignment, the envelope presence probability in the dot increases by 15% under magnetic field. These results are of major importance for understanding the Zeeman shift recorded experimentally and quantifying the properties of the valence band ground state of a real nanowire - quantum dot heterostructure.

- **Towards a light hole ground state in a tensile ZnTe quantum dot - a maverick approach:** By reversing the sign of lattice mismatch we can introduce a compressive shear strain along z axis in a flat ZnTe quantum dot surrounded by a ZnMgTe outer shell. We expect that this configuration will promote a light hole as the dominant component of the ground state for $L_{QD}/D_{QD} < 1$. The results from optical measurements, further investigated by numerical calculations, show that the heavy and light hole states are almost degenerate. This results either a heavy hole ground state for small aspect ratios, or a strong mixing between heavy and light holes for a wide range of L_{QD}/D_{QD}. In order to stabilize a light hole in this system, we have to increase the strain in the quantum dot, induced by the surrounding ZnMgTe layer. This of course requires a significant increase of Mg content in ZnMgTe which will potentially have detrimental effects to the integrity and quality of the compound.

- **Probing a complex spin texture in a strong type II system:** Type II band alignment and elastic strain could lead to the formation of spin textured hole states in ZnTe nanowires containing ZnSe inclusions. Up to this point however, such a structure has not been grown, as Se attacks ZnTe, substituting Te, resulting finally to an almost pure ZnSe nanowire. Interestingly though the optical quality of these nanowires is good, as we recorded bright photoluminescence at energies associated to ZnSe emission.

- **An -almost- pure light hole ground state in a compressive Cd(Mn)Te quantum dot:** Considering the small valence band offset between the dot and the core and in order to make sure that indeed the ground state has switched from heavy to light hole we studied experimentally extremely elongated CdTe quantum dots in ZnTe nanowires with $L_{QD}/D_{QD} \approx 9$. The polarization resolved measurements were initially in agreement with a ground state which is not a pure heavy hole. By analyzing the far field emission of a dispersed nanowire we confirmed that the emitted light is strongly polarized and in agreement with a dipole oriented parallel to the nanowire axis which by extent is associated to a π like transition. Of course we could not conclude as regards to the purity of valence band ground state, as we know that the effect of dielectric screening, strongly suppresses any emission from a dipole oriented perpendicular to the nanowire axis, potentially associated to a heavy hole transition. The most rigorous way to investigate and quantify the hole ground state is by measuring the giant Zeeman shift under different magnetic field orientations through magneto-optical micro-photoluminescence. For these

measurements we had to introduce Mn ions in the quantum dots which further decreases the valence offset, leading to a type II band alignment. In order to tackle this issue, the Cd(Mn)Te dots were surrounded by ZnMgTe which increases the valence band offset, restoring a weak type I band alignment and by extent the hole confinement in the dot. By taking into account the mixing of light hole and split-off states (renormalization of light hole spin by δ_{SO} and β_{SO}), the reconfinement effect under magnetic field (c_0 and c_1 parameters) and the formation of a light hole magnetic polaron, we fitted the experimental data assuming a pure light hole ground state strongly decoupled from heavy hole excited states. The fitting parameters are summarized to the table below.

Table 5.1 – Fitting parameters for the nanowire - quantum dots studied experimentally with magneto-optical measurements.

E_{se}	E_{sh}	β_{SO}	δ_{SO}	c_0	c_1	N_{eff}	Δ_{SO}
22 meV	88 meV	1.44	1.11	0.7	0.21	47	1 eV

The difference among the nanowires studied in the uniaxial and vectorial magnet was the Mn temperature T_{Mn}, being respectively 16 K and 14 K.

Future perspectives

- **A vast pool of different configurations to investigate with $\vec{k} \cdot \vec{p}$ numerical calculations:** In this work we investigated numerically the properties of ellipsoidal quantum dots based on the II-VI family of materials. It would be of particular interest to carry out similar calculations for quantum dots of different shapes and random geometries and investigate the effect of local strain anisotropies to the valence band ground state. It is also very interesting to investigate the spin properties of nanowire quantum dots with smaller split-off energy as in InAs where $\Delta_{SO} = 0.39$ eV [109], or InP where $\Delta_{SO} = 0.108$ eV [110]. There is an on-going collaboration with C2N - CNRS in Paris for the investigation of GaAs quantum dots in Ga(As)P nanowires.

  In the simulations carried out in this work, we always calculate separately electron and hole states. A next step is to take into account Coulomb interactions between electrons and holes and investigate excitonic effects. Additionally, as reported in [111] second order piezoelectric effects induced by hydrostatic strain are expected to further affect the properties of valence and conduction band. They have to be taken into account in future calculations. As regards the flat ZnTe quantum dot calculations, it would be very interesting to explore the limit up to which the Mg content in the ZnMgTe barriers, is sufficient to promote a light hole ground state via the elastic strain. Finally we may use the numerical calculations, in order to study the behavior of a hole spin textured state under magnetic field.

- **Further experiments with flat and elongated nanowire quantum dots:** For tensile ZnTe flat dots, measurements with quantum dots having different aspect ratios have to be done. Samples with higher Mg content in the barriers can also be investigated.

  Measurement of the emission diagram resolved in polarization, combined with the modeling of the dielectric screening would be very interesting in order to determine precisely the purity of the hole ground state.

  Concerning type II systems, it would be really interesting to grow a ZnTe shell around a ZnSe nanowire and reveal the presence of a complex hole spin textured state in this core-shell configuration.

Regarding light hole ground states in elongated Cd(Mn)Te quantum dots, the full hole spin anisotropy should be investigated by applying the magnetic field in all directions with a vectorial magnet.

Of course, a systematic investigation of the structural properties (TEM and EDX) of the studied structures must take place in parallel to optical studies, in order to have a clear image about chemical compositions, the crystal quality and the interfaces between the materials. Finally it would be really useful to combine all these different spectroscopic and microscopy techniques on the same nanowire in order to correlate directly its structural properties with the electronic and optical ones.

Appendices

Appendix A

Parameters used for the numerical calculations

Table A.1 – The parameters of ZnTe used for the numerical calculations

Lattice parameter a	6.104 Å	[112]
Elastic constants		
C_{11}	71.6 GPa	[113]
C_{12}	40.7 GPa	[113]
C_{44}	31.2 GPa	[113]
Deformation potentials		
a_c	-4.69 eV	[114]
a_v	0.79 eV	[114]
b_v	-1.3 eV	[114]
d_v	-4.3 eV	[114]
Luttinger Parameters		
γ_1	4.07	[115]
γ_2	0.78	[115]
γ_3	1.59	[115]
Piezoelectric coefficient e_{14}	0.03 C/m^2	[116], [117]
Energy gap E_g	2.391 eV	[72]
Electron effective mass m^*	0.116 m_0	[115]
Spin orbit splitting Δ_{SO}	0.95 eV	[118]
Kane Energy E_P	19.1 eV	[119]
Static dielectric constant ε_0	10.1	[120]

Table A.2 – The parameters of CdTe used for the numerical calculations

Lattice parameter a	6.481 Å	[112]
Elastic constants		
C_{11}	61.5 GPa	[113]
C_{12}	43 GPa	[113]
C_{44}	19.6 GPa	[113]
Deformation potentials		
a_c	-3.0 eV	[121], [122]
a_v	0.55 eV	[121], [122]
b_v	-1.23 eV	[123]
d_v	-5.1 eV	[123]
Luttinger Parameters		
γ_1	4.6	[124], [115]
γ_2	1.6	[124], [115]
γ_3	1.8	[124], [115]
Piezoelectric coefficient e_{14}	0.03 C/m^2	[116], [117]
Energy gap E_g	1.606 eV	[72]
Electron effective mass m^*	0.094 m_0	[124]
Spin orbit splitting Δ_{SO}	0.9 eV	[125]
Kane Energy E_P	20.7 eV	[119]
Static dielectric constant ε_0	10.6	[120]

In this Appendix the parameters used for the numerical calculations for ZnTe and CdTe are listed. For ZnMgTe we used Vegard's law for the calculation of lattice constant and energy gap while for other quantities we performed a linear interpolation between the values of ZnTe and MgTe as a function of Zn content x. For the calculations under magnetic field we used the parameters of CdTe for the quantum dot, since an effective concentration of 4% for Mn is not expected to modify significantly their values.

Appendix B

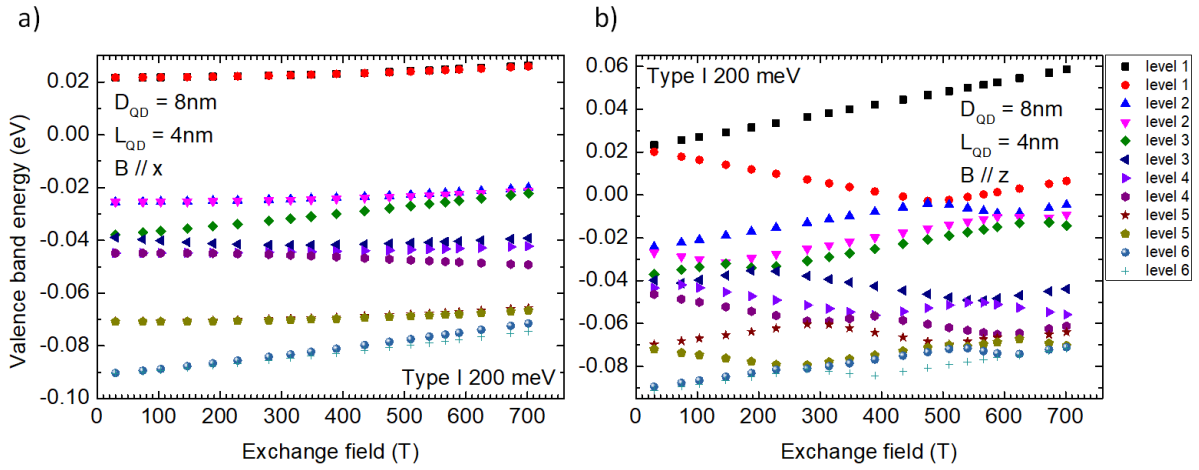# Zeeman shift of all calculated levels for a 200 meV type I quantum dot

a)

b)

Figure B.1 – Zeeman shift of all 6 calculated Kramers doublet for a 200 meV type I flat CdTe quantum dot with $L_{QD}/D_{QD} = 0.5$ in a ZnTe-ZnMgTe core-shell nanowire, as a function of magnetic field applied perpendicular a) and parallel b) to the dot quantization axis

a)

b)

Figure B.2 – Zeeman shift of all 6 calculated Kramers doublet for a 200 meV type I CdTe elongated dot with $L_{QD}/D_{QD} = 2.25$ in a ZnTe-ZnMgTe core-shell nanowire, as a function of magnetic field applied perpendicular a) and parallel b) to the dot quantization axis

Appendix C

Zeeman shift of all calculated levels for a 20 meV type I quantum dot

Figure C.1 – Zeeman shift of all 6 calculated Kramers doublet for a 20 meV weak type I flat CdTe quantum dot with $L_{QD}/D_{QD} = 0.5$ in a ZnTe-ZnMgTe core-shell nanowire, as a function of magnetic field applied perpendicular a) and parallel b) to the dot quantization axis
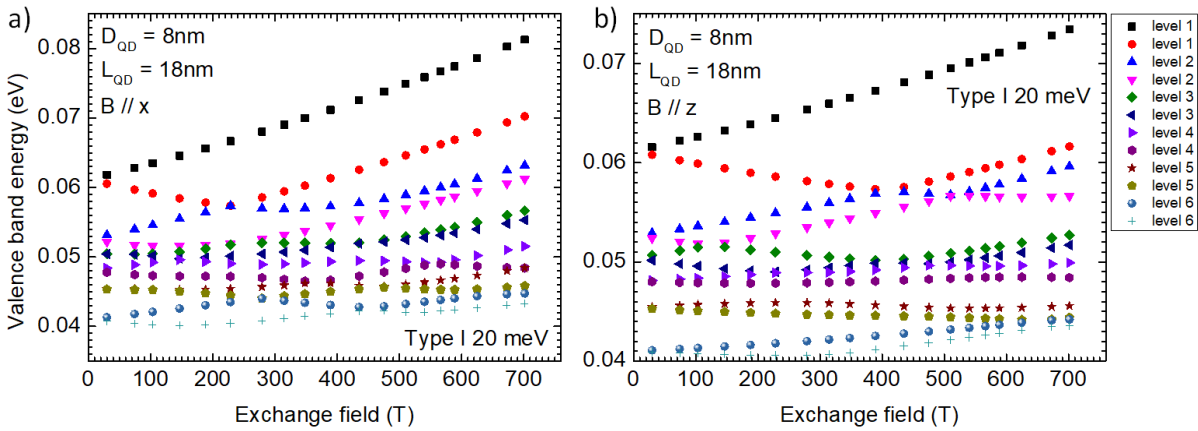
Figure C.2 – Zeeman shift of all 6 calculated Kramers doublet for a 20 meV weak type I CdTe elongated dot with $L_{QD}/D_{QD} = 2.25$ in a ZnTe-ZnMgTe core-shell nanowire, as a function of magnetic field applied perpendicular a) and parallel b) to the dot quantization axis
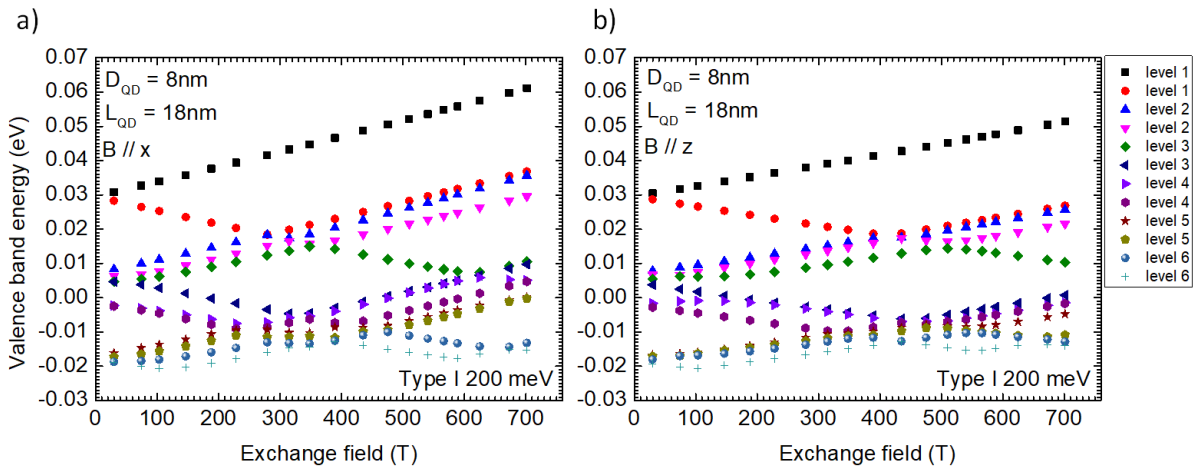
Appendix D

Zeeman shift of all calculated levels for a 20 meV type II quantum dot
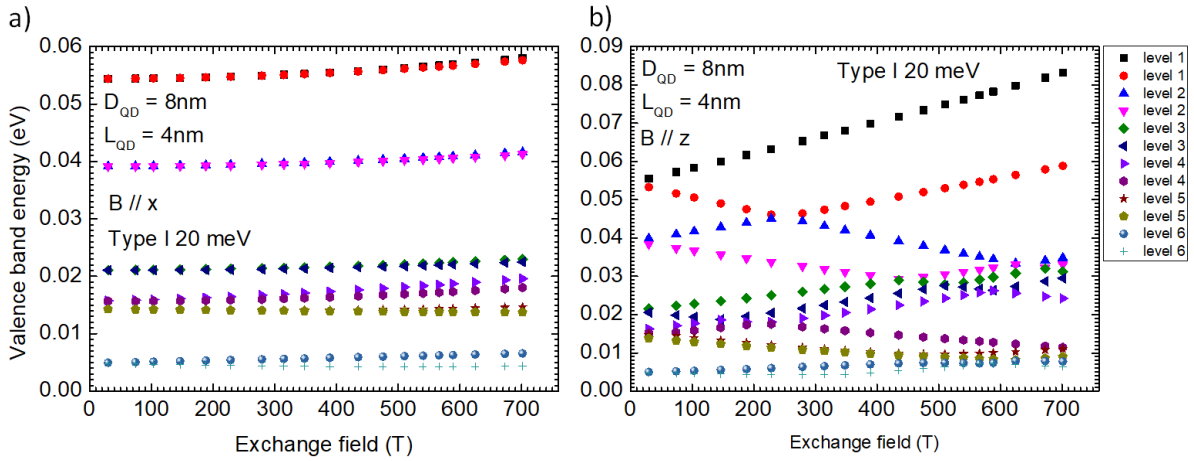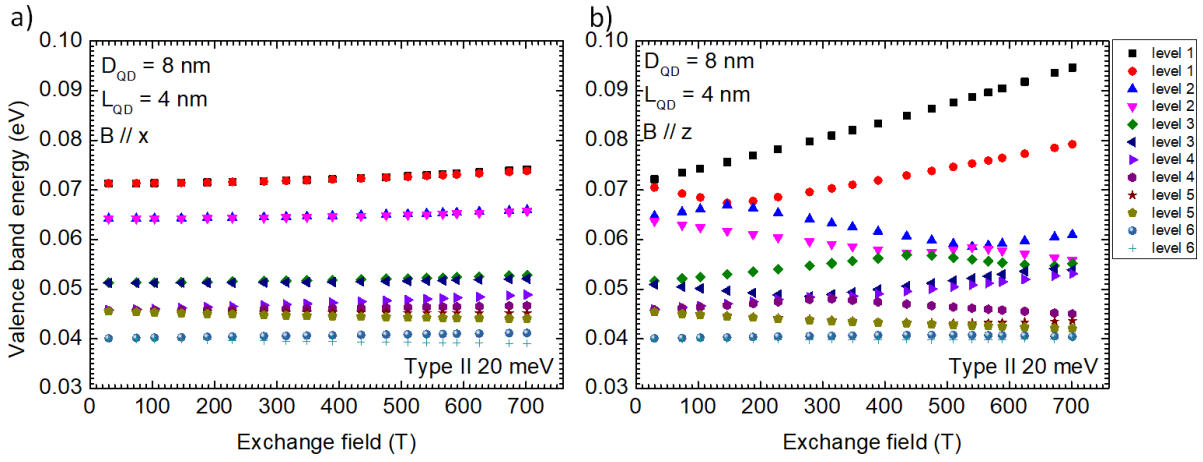

Figure D.1 – Zeeman shift of all 6 calculated Kramers doublet for a 20 meV type II flat CdTe quantum dot with $L_{QD}/D_{QD} = 0.5$ in a ZnTe-ZnMgTe core-shell nanowire, as a function of magnetic field applied perpendicular a) and parallel b) to the dot quantization axis

Figure D.2 – Zeeman shift of all 6 calculated Kramers doublet for a 20 meV type II flat CdTe quantum dot with $L_{QD}/D_{QD} = 1.5$ in a ZnTe-ZnMgTe core-shell nanowire, as a function of magnetic field applied perpendicular a) and parallel b) to the dot quantization axis
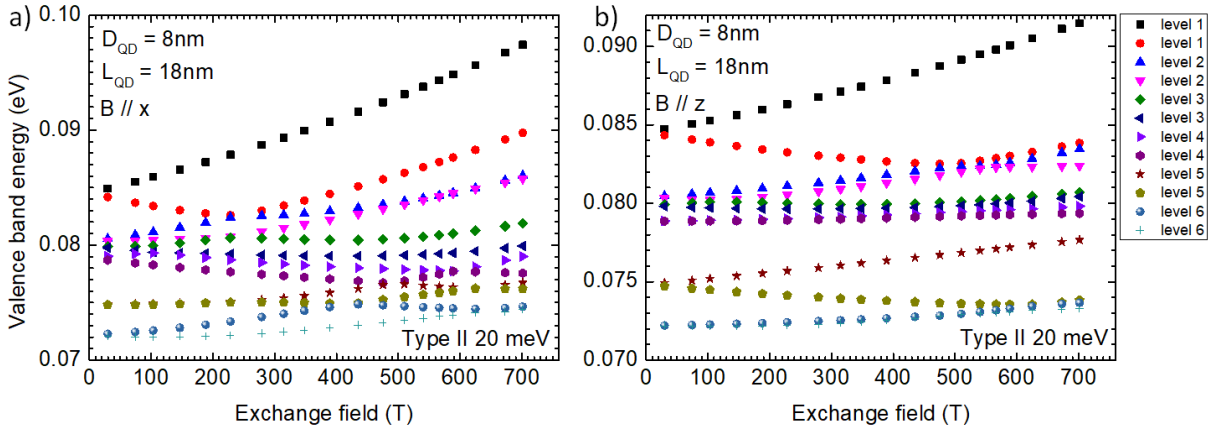
Figure D.3 – Zeeman shift of all 6 calculated Kramers doublet for a 20 meV type II flat CdTe quantum dot with $L_{QD}/D_{QD} = 2.25$ in a ZnTe-ZnMgTe core-shell nanowire, as a function of magnetic field applied perpendicular a) and parallel b) to the dot quantization axis
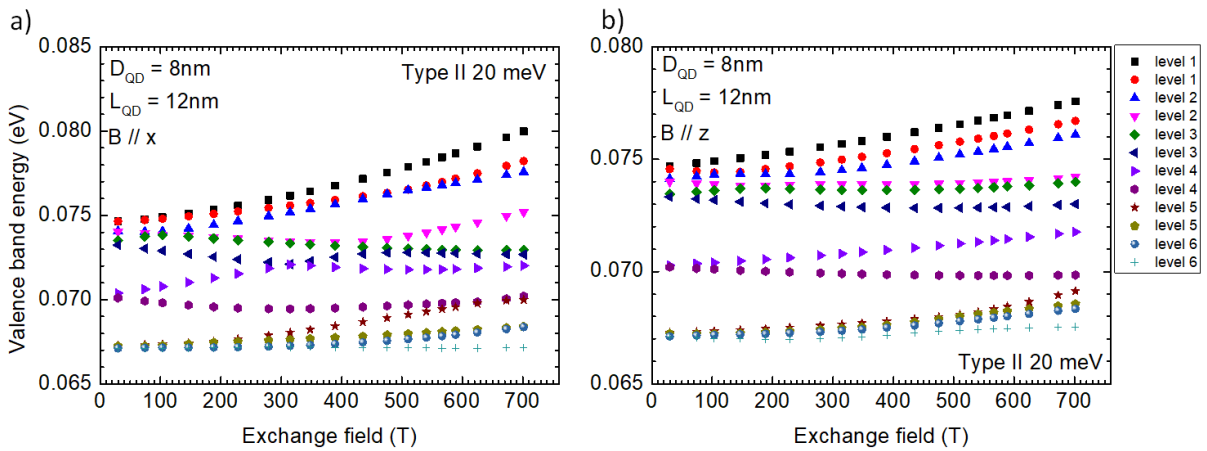
Appendix E

Emission of (II,Mg)Te alloys

The determination of MgTe emission energy is very difficult due to the fact that this compound is unstable in standard conditions. There are numerous works reported in literature where the authors tried to extrapolate it, by studying the emission of $Zn_xMg_{1-x}Te$ and $Cd_xMg_{1-x}Te$ alloys for different Mg content [100, 126, 127, 67]. In order to analyze our data we addressed to all these works as it was necessary to deduce an accurate fit for calculating Mg content for both core - shell ZnTe - ZnMgTe nanowires and the ZnMgTe nanowires containing a ZnTe quantum dot.
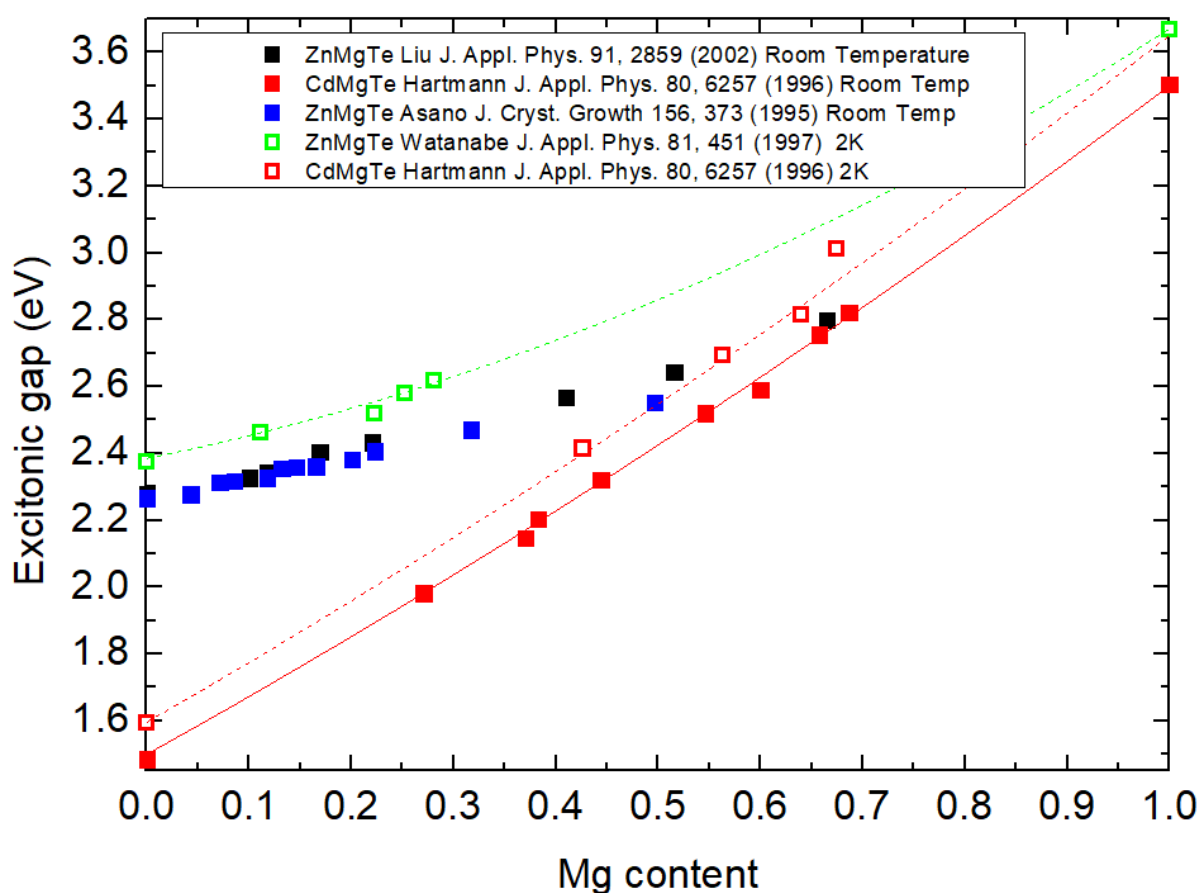
Figure E.1 – Emission of $Zn_xMg_{1-x}Te$ and $Cd_xMg_{1-x}Te$ at low and room temperature for different Mg content

In Fig. E.1 we present the emission for different (II,Mg)Te alloys and the interpolation up to MgTe. The most reliable study for fitting the data is [Watan] which is also in very good

agreement with the study for $Cd_xMg_{1-x}Te$ at room temperature. With the dashed red line the evolution of $Cd_xMg_{1-x}Te$ at low temperature is fitted, which for pure MgTe we retrieve the same emission energy value as for $Zn_xMg_{1-x}Te$.

As regards the measurements for $Zn_xMg_{1-x}Te$ reported in [blue,black] for small Mg content up to 20% it seems that they fit quite well. For a content of 60% Mg however, $Cd_{0.4}Mg_{0.6}Te$ and $Zn_{0.4}Mg_{0.6}Te$ have the same gap at room temperature (black and red squares) which is definitely inconsistent. Consequently the credibility of these results requires further investigation.

Appendix F

Power dependence of CdMnTe quantum dot in W-11
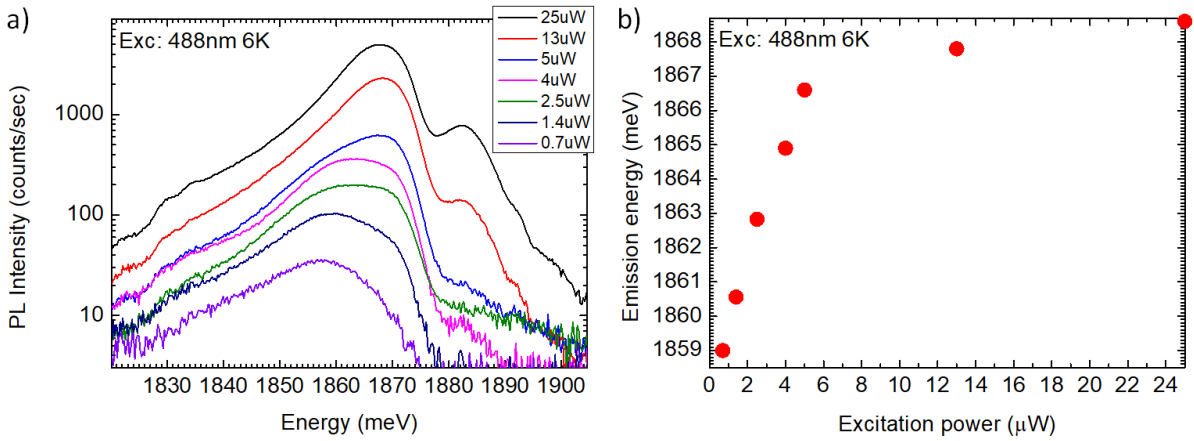
Figure F.1 – Micro-photoluminescence spectra of Cd(Mn)Te dot in nanowire W-11 under different excitation powers a). The energy position as a function of excitation power

In Fig. F.1 a) we present the power dependence of micro-photoluminescence measurements of the Cd(Mn)Te quantum dot in W-11 and in Fig. F.1 b) the energy position as a function of the excitation power. These figures are shown as a confirmation that by decreasing the excitation power we move towards lower energies. At the same they demonstrate the formation of magnetic polaron, as by decreasing the excitation power we also decrease the temperature and this is manifested by a redshift of emission energy. This redshift is attributed to the magnetic moment induced by the polarization of Mn due to $sp - d$ exchange interaction with the spin of the holes.

Bibliography

[1] M. Julliere, "Tunneling Between Ferromagnetic Films," *Physics Letters A*, vol. 54, no. 3, p. 225, 1975.

[2] M. Johnson and R. H. Silsbee, "Spin-injection experiment," *Physical Review B*, vol. 37, pp. 5326–5335, apr 1988.

[3] A. Fert, "Nobel Lecture: Origin, development, and future of spintronics," *Reviews of Modern Physics*, vol. 80, pp. 1517–1530, dec 2008.

[4] S. Datta and B. Das, "Electronic analog of the electro-optic modulator," *Applied Physics Letters*, vol. 56, pp. 665–667, feb 1990.

[5] S. Bounouar, M. Elouneg-Jamroz, M. D. Hertog, C. Morchutt, E. Bellet-Amalric, R. André, C. Bougerol, Y. Genuist, J. P. Poizat, S. Tatarenko, and K. Kheng, "Ultra-fast room temperature single-photon source from nanowire-quantum dots," *Nano Letters*, vol. 12, no. 6, pp. 2977–2981, 2012.

[6] R. M. Stevenson, R. J. Young, P. Atkinson, K. Cooper, D. A. Ritchie, and A. J. Shields, "A semiconductor source of triggered entangled photon pairs," *Nature*, vol. 439, no. 7073, pp. 178–182, 2006.

[7] T. H. Chung, G. Juska, S. T. Moroni, A. Pescaglini, A. Gocalinska, and E. Pelucchi, "Selective carrier injection into patterned arrays of pyramidal quantum dots for entangled photon light-emitting diodes," *Nature Photonics*, vol. 10, no. 12, pp. 782–787, 2016.

[8] R. J. Warburton, "Single spins in self-assembled quantum dots," *Nature Materials*, vol. 12, pp. 483–493, jun 2013.

[9] D. Sleiter and W. F. Brinkman, "Using holes in GaAs as qubits: An estimate of the Rabi frequency in the presence of an external rf field," *Physical Review B - Condensed Matter and Materials Physics*, vol. 74, no. 15, pp. 3–5, 2006.

[10] H. Kosaka, T. Inagaki, Y. Rikitake, H. Imamura, Y. Mitsumori, and K. Edamatsu, "Spin state tomography of optically injected electrons in a semiconductor," *Nature*, vol. 457, no. 7230, pp. 702–705, 2009.

[11] E. Tsitsishvili, "Light-hole exciton spin relaxation in quantum dots," *Physical Review B - Condensed Matter and Materials Physics*, vol. 91, no. 15, pp. 1–8, 2015.

[12] P. Stepanov, *Magneto-optical spectroscopy of semiconductor magnetic quantum dots*. PhD thesis, 2013.

[13] J. Piprek, *Semiconductor Optoelectronic Devices*. Elsevier, 2003.

[14] J. M. Luttinger, "Quantum Theory of Cyclotron Resonance in Semiconductors: General Theory," *Physical Review*, vol. 102, pp. 1030–1041, may 1956.

[15] J. K. Furdyna, "Diluted magnetic semiconductors," *Journal of Applied Physics*, vol. 64, no. 4, pp. 29 – 36, 1988.

[16] B. Späth, J. Fritsche, A. Klein, and W. Jaegermann, "Nitrogen doping of ZnTe and its influence on CdTe/ZnTe interfaces," *Applied Physics Letters*, vol. 90, no. 6, 2007.

[17] J. Calatayud, J. Allègre, H. Mathieu, N. Magnéa, and H. Mariette, "Piezoreflectance in CdTe/(Cd,Zn)Te strained-layer superlattices: Periodicity effect, valence-band offset, and exciton binding energies," *Physical Review B*, vol. 47, no. 15, pp. 9684–9692, 1993.

[18] B. D. Gerardot, D. Brunner, P. A. Dalgarno, P. Öhberg, S. Seidl, M. Kroner, K. Karrai, N. G. Stoltz, P. M. Petroff, and R. J. Warburton, "Optical pumping of a single hole spin in a quantum dot," *Nature*, vol. 451, no. 7177, pp. 441–444, 2008.

[19] K. De Greve, P. L. McMahon, D. Press, T. D. Ladd, D. Bisping, C. Schneider, M. Kamp, L. Worschech, S. Höfling, A. Forchel, and Y. Yamamoto, "Ultrafast coherent control and suppressed nuclear feedback of a single quantum dot hole qubit," *Nature Physics*, vol. 7, no. 11, pp. 872–878, 2011.

[20] D. V. Bulaev and D. Loss, "Spin relaxation and decoherence of holes in quantum dots," *Physical Review Letters*, vol. 95, no. 7, pp. 1–4, 2005.

[21] D. Heiss, S. Schaeck, H. Huebl, M. Bichler, G. Abstreiter, J. J. Finley, D. V. Bulaev, and D. Loss, "Observation of extremely slow hole spin relaxation in self-assembled quantum dots," *Physical Review B - Condensed Matter and Materials Physics*, vol. 76, no. 24, pp. 1–4, 2007.

[22] G. Bester, A. Zunger, and S. Nair, "Pseudopotential calculation of the excitonic fine structure of million-atom self-assembled In(1-x)Ga(x)As/ GaAs quantum dots," *Physical Review B - Condensed Matter and Materials Physics*, vol. 67, no. 16, pp. 3–6, 2003.

[23] Y. H. Huo, B. J. Witek, S. Kumar, J. R. Cardenas, J. X. Zhang, N. Akopian, R. Singh, E. Zallo, R. Grifone, D. Kriegner, R. Trotta, F. Ding, J. Stangl, V. Zwiller, G. Bester, A. Rastelli, and O. G. Schmidt, "A light-hole exciton in a quantum dot," *Nature Physics*, vol. 10, no. 1, pp. 46–51, 2013.

[24] Y. M. Niquet and D. C. Mojica, "Quantum dots and tunnel barriers in InAs InP nanowire heterostructures: Electronic and optical properties," *Physical Review B - Condensed Matter and Materials Physics*, vol. 77, no. 11, pp. 1–12, 2008.

[25] J. D. Eshelby, "The determination of the elastic field of an ellipsoidal inclusion, and related problems," *Proceedings of the Royal Society of London. Series A. Mathematical and Physical Sciences*, vol. 241, pp. 376–396, aug 1957.

[26] M. Zieliński, "Fine structure of light-hole excitons in nanowire quantum dots," *Physical Review B - Condensed Matter and Materials Physics*, vol. 88, no. 11, pp. 1–6, 2013.

[27] M. Jeannin, A. Artioli, P. Rueda-Fonseca, E. Bellet-Amalric, K. Kheng, R. André, S. Tatarenko, J. Cibert, D. Ferrand, and G. Nogues, "Light-hole exciton in nanowire quantum dot," *Physical Review B*, vol. 95, p. 035305, 2017.

[28] J. M. Fatah, T. Piorek, P. Harrison, T. Stirner, and W. E. Hagston, "Numerical simulation of antiferromagnetic spin-pairing effects in diluted magnetic semiconductors and enhanced paramagnetism at interfaces," *Physical Review B*, vol. 49, pp. 10341–10344, apr 1994.

[29] S. Lee, M. Dobrowolska, J. K. Furdyna, and H. Luo, "Magneto-optical study of interwell coupling in double quantum wells using diluted magnetic semiconductors," vol. 54, no. 23, 1996.

[30] J. Gaj, R. Planel, and G. Fishman, "Relation of magneto-optical properties of free excitons to spin alignment of Mn2+ ions in Cd(1-x)Mn(x)Te," *Solid State Communications*, vol. 29, pp. 435–438, feb 1979.

[31] J. A. Gaj, W. Grieshaber, C. Bodin-Deshayes, J. Cibert, G. Feuillet, Y. Merle d'Aubigné, and A. Wasiela, "Magneto-optical study of interface mixing in the CdTe-(Cd,Mn)Te system," *Physical Review B*, vol. 50, pp. 5512–5527, aug 1994.

[32] A. Artioli, *Magnetic polaron in (Cd , Mn) Te quantum dot inserted in ZnTe nanowire.* PhD thesis, 2016.

[33] J. Płachta, E. Grodzicka, A. Kaleta, S. Kret, L. T. Baczewski, A. Pietruczik, M. Wiater, M. Goryca, T. Kazimierczuk, P. Kossacki, G. Karczewski, T. Wojtowicz, and P. Wojnar, "Magnetic field induced mixing of light hole excitonic states in (Cd, Mn)Te/(Cd, Mg)Te core/shell nanowires," *Nanotechnology*, vol. 29, p. 205205, may 2018.

[34] S. Series, *Introduction to the Physics of Diluted Magnetic Semiconductors*, vol. 144 of *Springer Series in Materials Science.* Berlin, Heidelberg: Springer Berlin Heidelberg, 2010.

[35] R. A.Golnik, J. A.Gaj, M.Nawrocki and C. a la Guillaume, ":," *J. Phys. Soc. Jpn. Suppl. A*, vol. 49, p. 819, 1980.

[36] T. Kasuya and A. Yanase, "Anomalous transport phenomena in eu-chalcogenide alloys," *Reviews of Modern Physics*, vol. 40, no. 4, pp. 684–696, 1968.

[37] M. Nawrocki, R. Planel, G. Fishman, and R. Galazka, "Exchange-induced spin-flip raman scattering in a semimagnetic semiconductor," *Physical Review Letters*, vol. 46, no. 11, pp. 735–738, 1981.

[38] T. Dietl and J. Spałek, "Effect of fluctuations of magnetization on the bound magnetic polaron: Comparison with experiment," *Physical Review Letters*, vol. 48, no. 5, pp. 355–358, 1982.

[39] M. Bugajski, P. Becla, P. A. Wolff, D. Heiman, and L. R. Ram-Mohan, "Acceptor-bound magnetic polarons in Cd1-xMnxTe," *Physical Review B*, vol. 38, no. 15, pp. 10512–10516, 1988.

[40] G. Mackh, W. Ossau, D. R. Yakovlev, A. Waag, G. Landwehr, R. Hellmann, and E. O. Göbel, "Localized exciton magnetic polarons in Cd(1-x)Mn(x)Te," *Physical Review B*, vol. 49, no. 15, pp. 10248–10258, 1994.

[41] Y. Sun, S. E. Thompson, and T. Nishida, *Strain Effect in Semiconductors.* Boston, MA: Springer US, 2010.

[42] S. L. Chuang, *Physics of Photonic Devices, 2nd Edition.* John Wiley & Sons, Inc, 2009.

[43] C. Kittel, *Introduction to Solid State physics.* Willey, 8th ed., 2004.

[44] R. Winkler, *Spin–Orbit Coupling Effects in Two-Dimensional Electron and Hole Systems*, vol. 191 of *Springer Tracts in Modern Physics.* Berlin, Heidelberg: Springer Berlin Heidelberg, 2003.

[45] M. Willatzen and L. C. Lew Yan Voon, *The k p Method.* Berlin, Heidelberg: Springer Berlin Heidelberg, 2009.

[46] J. Singh, *Electronic and Optoelectronic Properties of Semiconductor Structures.* Cambridge: Cambridge University Press, 2003.

[47] G. A. Korn and T. M. Korn, "Mathematical handbook for scientists and engineers : definitions, theorems, and formulas for reference and review," pp. xvii, 1130 p., 2000.

[48] P. Harrison and A. Valavanis, *Quantum Wells, Wires and Dots*, vol. 133. Chichester, UK: John Wiley & Sons, Ltd, may 2016.

[49] M. Grundmann, *The Physics of Semiconductors.* Graduate Texts in Physics, Cham: Springer International Publishing, 2016.

[50] G. Fishman, "Semi-conducteurs: les bases de la théorie k.p," 2010.

[51] G. Bastard, *Wave mechanics applied to semiconductor heterostructures.* Les Éditions de Physique, 1988.

[52] J. D. Eshelby, "The elastic field outside an ellipsoidal inclusion," *Proceedings of the Royal Society of London. Series A. Mathematical and Physical Sciences*, vol. 252, pp. 561–569, oct 1959.

[53] D. Ferrand and J. Cibert, "Strain in crystalline core-shell nanowires," *The European Physical Journal Applied Physics*, vol. 67, no. 3, p. 30403, 2014.

[54] M. J. Klein, "On a Degeneracy Theorem of Kramers," *American Journal of Physics*, vol. 20, no. 65, 1952.

[55] B. Späth, J. Fritsche, A. Klein, and W. Jaegermann, "Nitrogen doping of ZnTe and its influence on CdTe/ZnTe interfaces," *Applied Physics Letters*, vol. 90, no. 6, 2007.

[56] J. Calatayud, J. Allègre, H. Mathieu, N. Magnéa, and H. Mariette, "Piezoreflectance in CdTe//(Cd,Zn)Te strained-layer superlattices: Periodicity effect, valence-band offset, and exciton binding energies," *Physical Review B*, vol. 47, pp. 9684–9692, apr 1993.

[57] S.-h. Wei and A. Zunger, "InAsSb/InAs: A type-I or a type-II band alignment," *Physical Review B*, vol. 52, pp. 12039–12044, oct 1995.

[58] K. Moratis, S. L. Tan, S. Germanis, C. Katsidis, M. Androulidaki, K. Tsagaraki, Z. Hatzopoulos, F. Donatini, J. Cibert, Y. M. Niquet, H. Mariette, and N. T. Pelekanos, "Strained GaAs/InGaAs Core-Shell Nanowires for Photovoltaic Applications," *Nanoscale Research Letters*, vol. 11, no. 1, pp. 0–6, 2016.

[59] A. Artioli, P. Rueda-fonseca, K. Moratis, J.-f. Motte, F. Donatini, M. I. D. Hertog, E. Robin, R. André, Y.-m. Niquet, E. Bellet-amalric, A. Artioli, P. Rueda-fonseca, K. Moratis, J.-f. Motte, and F. Donatini, "Probing the light hole / heavy hole switching with correlated magneto-optical spectroscopy and chemical analysis on a single quantum dot," *Nanotechnology*, 2019.

[60] S. P. Robert Triboulet, *CdTe and Related Compounds; Physics, Defects, Hetero- and Nano-structures, Crystal Growth, Surfaces and Applications.* Elsevier, 2010.

[61] T. Nakaoka, T. Saito, J. Tatebayashi, and Y. Arakawa, "Size, shape, and strain dependence of the g factor in self-assembled In(Ga)As quantum dots," *Physical Review B - Condensed Matter and Materials Physics*, vol. 70, no. 23, pp. 1–8, 2004.

[62] C. Hamaguchi, *Basic Semiconductor Physics*. Graduate Texts in Physics, Cham: Springer International Publishing, 2017.

[63] B. &. H. GmbH, "The bh TCSPC Technique," 2019.

[64] R. H. BROWN and R. Q. TWISS, "Correlation between Photons in two Coherent Beams of Light," *Nature*, vol. 177, pp. 27–29, jan 1956.

[65] A. Artioli, P. Rueda-Fonseca, P. Stepanov, E. Bellet-Amalric, M. Den Hertog, C. Bougerol, Y. Genuist, F. Donatini, R. André, G. Nogues, K. Kheng, S. Tatarenko, D. Ferrand, and J. Cibert, "Optical properties of single ZnTe nanowires grown at low temperature," *Applied Physics Letters*, vol. 103, no. 22, 2013.

[66] P. Wojnar, E. Janik, L. T. Baczewski, S. Kret, E. Dynowska, T. Wojciechowski, J. Suffczyński, J. Papierska, P. Kossacki, G. Karczewski, J. Kossut, and T. Wojtowicz, "Giant spin splitting in optically active ZnMnTe/ZnMgTe core/shell nanowires," *Nano Letters*, vol. 12, no. 7, pp. 3404–3409, 2012.

[67] K. Watanabe, M. T. Litz, M. Korn, W. Ossau, A. Waag, G. Landwehr, and U. Schüssler, "Optical properties of ZnTe/Zn1-xMgxSeyTe1-y quantum wells and epilayers grown by molecular beam epitaxy," *Journal of Applied Physics*, vol. 81, no. 1, pp. 451–455, 1997.

[68] A. Spinelli and A. Lacaita, "Physics and numerical simulation of single photon avalanche diodes," *IEEE Transactions on Electron Devices*, vol. 44, no. 11, pp. 1931–1943, 1997.

[69] C. Kurtsiefer, P. Zarda, S. Mayer, and H. Weinfurter, "The breakdown flash of silicon avalanche photodiodes-back door for eavesdropper attacks?," *Journal of Modern Optics*, vol. 48, pp. 2039–2047, nov 2001.

[70] A. N. Bogdanov and U. B. Rößler, "Chiral symmetry breaking in magnetic thin films and multilayers," *Physical Review Letters*, vol. 87, no. 3, pp. 37203–1–37203–4, 2001.

[71] M. Finazzi, M. Savoini, A. R. Khorsand, A. Tsukamoto, A. Itoh, L. Duò, A. Kirilyuk, T. Rasing, and M. Ezawa, "Laser-induced magnetic nanostructures with tunable topological properties," *Physical Review Letters*, vol. 110, no. 17, pp. 1–5, 2013.

[72] C. G. Van de Walle and J. Neugebauer, "Universal alignment of hydrogen levels in semiconductors, insulators and solutions," *Nature*, vol. 423, pp. 626–628, jun 2003.

[73] J. Bang, J. Park, J. H. Lee, N. Won, J. Nam, J. Lim, B. Y. Chang, H. J. Lee, B. Chon, J. Shin, J. B. Park, J. H. Choi, K. Cho, S. M. Park, T. Joo, and S. Kim, "ZnTe/ZnSe (Core/Shell) Type-II Quantum Dots: Their Optical and Photovoltaic Properties," *Chemistry of Materials*, vol. 22, pp. 233–240, jan 2010.

[74] S. O. Ferreira, H. Sitter, W. Faschinger, R. Krump, and G. Brunthaler, "Type I-type II band offset transition of the ZnMgSeZnTe system," *Journal of Crystal Growth*, vol. 146, no. 1-4, pp. 418–421, 1995.

[75] W. Y. Liang and A. D. Yoffe, "Luminescence in hexagonal zinc selenide crystals," *The Philosophical Magazine: A Journal of Theoretical Experimental and Applied Physics*, vol. 16, pp. 1153–1166, dec 1967.

[76] I. L. Kuskovsky, C. Tian, G. F. Neumark, J. E. Spanier, I. P. Herman, W. C. Lin, S. P. Guo, and M. C. Tamargo, "Optical properties of δ-doped ZnSe:Te grown by molecular beam epitaxy: The role of tellurium," *Physical Review B - Condensed Matter and Materials Physics*, vol. 63, no. 15, pp. 1–8, 2001.

[77] V. T. Fauske, J. Huh, G. Divitini, D. L. Dheeraj, A. M. Munshi, C. Ducati, H. Weman, B.-o. Fimland, and A. T. J. van Helvoort, "In Situ Heat-Induced Replacement of GaAs Nanowires by Au," *Nano Letters*, vol. 16, pp. 3051–3057, may 2016.

[78] F. Rossella, V. Piazza, M. Rocci, D. Ercolani, L. Sorba, F. Beltram, and S. Roddaro, "GHz Electroluminescence Modulation in Nanoscale Subwavelength Emitters," *Nano Letters*, vol. 16, pp. 5521–5527, sep 2016.

[79] Y.-l. Chueh, A. C. Ford, J. C. Ho, Z. A. Jacobson, Z. Fan, C.-y. Chen, L.-j. Chou, and A. Javey, "Formation and Characterization of Ni x InAs/InAs Nanowire Heterostructures by Solid Source Reaction," *Nano Letters*, vol. 8, pp. 4528–4533, dec 2008.

[80] K. Seo, N. Bagkar, S.-i. Kim, J. In, H. Yoon, Y. Jo, and B. Kim, "Diffusion-Driven Crystal Structure Transformation: Synthesis of Heusler Alloy Fe 3 Si Nanowires," *Nano Letters*, vol. 10, pp. 3643–3647, sep 2010.

[81] Y. Chen, Y.-c. Lin, X. Zhong, H.-c. Cheng, X. Duan, and Y. Huang, "Kinetic Manipulation of Silicide Phase Formation in Si Nanowire Templates," *Nano Letters*, vol. 13, pp. 3703–3708, aug 2013.

[82] H. Liu, G. She, L. Mu, and W. Shi, "Temperature-dependent structure and phase variation of nickel silicide nanowire arrays prepared by in situ silicidation," *Materials Research Bulletin*, vol. 47, pp. 3991–3994, dec 2012.

[83] W. I. Park, H. S. Kim, S. Y. Jang, J. Park, S. Y. Bae, M. Jung, H. Lee, and J. Kim, "Transformation of ZnTe nanowires to CdTe nanowires through the formation of ZnCdTe–CdTe core–shell structure by vapor transport," *Journal of Materials Chemistry*, vol. 18, no. 8, p. 875, 2008.

[84] K. KOLASINSKI, "Catalytic growth of nanowires: Vapor–liquid–solid, vapor–solid–solid, solution–liquid–solid and solid–liquid–solid growth," *Current Opinion in Solid State and Materials Science*, vol. 10, pp. 182–191, jun 2006.

[85] M. Orrù, E. Robin, M. Den Hertog, K. Moratis, Y. Genuist, R. André, D. Ferrand, J. Cibert, and E. Bellet-Amalric, "Nanowire growth and sublimation: CdTe quantum dots in ZnTe nanowires," *Physical Review Materials*, vol. 2, p. 043404, apr 2018.

[86] P. Rueda-Fonseca, E. Bellet-Amalric, R. Vigliaturo, M. den Hertog, Y. Genuist, R. André, E. Robin, A. Artioli, P. Stepanov, D. Ferrand, K. Kheng, S. Tatarenko, and J. Cibert, "Structure and Morphology in Diffusion-Driven Growth of Nanowires: The Case of ZnTe," *Nano Letters*, vol. 14, pp. 1877–1883, apr 2014.

[87] G. Sallen, A. Tribu, T. Aichele, R. André, L. Besombes, C. Bougerol, M. Richard, S. Tatarenko, K. Kheng, and J.-P. Poizat, "Subnanosecond spectral diffusion measurement using photon correlation," *Nature Photonics*, vol. 4, pp. 696–699, oct 2010.

[88] D. Williams, A. Andreev, and E. O'Reilly, "Self-consistent calculations of exciton, biexciton and charged exciton energies in InGaN/GaN quantum dots," *Superlattices and Microstructures*, vol. 36, pp. 791–798, oct 2004.

[89] P. Wojnar, E. Janik, L. T. Baczewski, S. Kret, G. Karczewski, T. Wojtowicz, M. Goryca, T. Kazimierczuk, and P. Kossacki, "Growth and optical properties of CdTe quantum dots in ZnTe nanowires," *Applied Physics Letters*, vol. 99, p. 113109, sep 2011.

[90] S. Moehl, *Etude des propriétés optiques de boîtes quantiques semiconductrices II-VI pour leur application à l'émission à un photon à haute température To cite this version : HAL Id : tel-00010332 e Joseph Fourier – Grenoble I Discipline : Physique Etude des propr.* PhD thesis, 2005.

[91] M. J. Stevens, R. H. Hadfield, R. E. Schwall, S. W. Nam, and R. P. Mirin, "Time-correlated single-photon counting with superconducting single-photon detectors," in *Advanced Photon Counting Techniques* (W. Becker, ed.), vol. 6372, p. 63720U, oct 2006.

[92] L. Besombes, *Spectroscopie optique de boîtes quantiques uniques de semiconducteurs II-VI.* PhD thesis, 2001.

[93] B. Patton, W. Langbein, and U. Woggon, "Trion, biexciton, and exciton dynamics in single self-assembled CdSe quantum dots," *Physical Review B*, vol. 68, p. 125316, sep 2003.

[94] G. Bacher, R. Weigand, J. Seufert, V. D. Kulakovskii, N. A. Gippius, A. Forchel, K. Leonardi, D. Hommel, K. Leonardi, and D. Hommel, "Biexciton versus exciton lifetime in a single semiconductor quantum dot," *Physical Review Letters*, vol. 83, no. 21, pp. 4417–4420, 1999.

[95] G. Sęk, A. Musiał, P. Podemski, and J. Misiewicz, "On the applicability of a few level rate equation model to the determination of exciton versus biexciton kinetics in quasi-zero-dimensional structures," *Journal of Applied Physics*, vol. 108, p. 033507, aug 2010.

[96] L. Besombes, K. Kheng, L. Marsal, and H. Mariette, "Few-particle effects in single CdTe quantum dots," *Physical Review B*, vol. 65, p. 121314, mar 2002.

[97] T. Cremel, *Vers une source de photons uniques opérationnelle à base de nanofils semiconducteurs.* PhD thesis, 2016.

[98] J. Wang, "Highly Polarized Photoluminescence and Photodetection from Single Indium Phosphide Nanowires," *Science*, vol. 293, pp. 1455–1457, aug 2001.

[99] D. J. Griffiths, *Introduction to Electrodynamics.* Cambridge University Press, 4 ed., 2017.

[100] X. Liu, U. Bindley, Y. Sasaki, and J. K. Furdyna, "Optical properties of epitaxial ZnMnTe and ZnMgTe films for a wide range of alloy compositions," *Journal of Applied Physics*, vol. 91, pp. 2859–2865, mar 2002.

[101] G. Bacher, A. A. Maksimov, H. Schömig, V. D. Kulakovskii, M. K. Welsch, A. Forchel, P. S. Dorozhkin, A. V. Chernenko, S. Lee, M. Dobrowolska, and J. K. Furdyna, "Monitoring Statistical Magnetic Fluctuations on the Nanometer Scale," *Physical Review Letters*, vol. 89, p. 127201, aug 2002.

[102] R. Pässler, "Parameter sets due to fittings of the temperature dependencies of fundamental bandgaps in semiconductors," *Physica Status Solidi (B) Basic Research*, vol. 216, no. 2, pp. 975–1007, 1999.

[103] P. Wojnar, J. Suffczyński, K. Kowalik, A. Golnik, G. Karczewski, and J. Kossut, "Microluminescence from Cd(1-x)Mn(x)Te magnetic quantum dots containing only a few Mn ions," *Physical Review B*, vol. 75, p. 155301, apr 2007.

[104] A. A. Maksimov, G. Bacher, A. McDonald, V. D. Kulakovskii, A. Forchel, C. R. Becker, G. Landwehr, and L. W. Molenkamp, "Magnetic polarons in a single diluted magnetic semiconductor quantum dot," *Physical Review B*, vol. 62, pp. R7767–R7770, sep 2000.

[105] D. R. Yakovlev, G. Mackh, B. Kuhn-Heinrich, W. Ossau, A. Waag, G. Landwehr, R. Hellmann, and E. O. Göbel, "Exciton magnetic polarons in short-period CdTe/Cd(1-x)Mn(x)Te superlattices," *Physical Review B*, vol. 52, pp. 12033–12038, oct 1995.

[106] K. V. Kavokin, I. A. Merkulov, D. R. Yakovlev, W. Ossau, and G. Landwehr, "Exciton localization in semimagnetic semiconductors probed by magnetic polarons," *Physical Review B*, vol. 60, pp. 16499–16505, dec 1999.

[107] R. Oszwałdowski, P. Stano, A. G. Petukhov, and I. Žutić, "Spin ordering in magnetic quantum dots: From core-halo to Wigner molecules," *Physical Review B*, vol. 86, p. 201408, nov 2012.

[108] Y. P. Varshni, "Temperature dependence of the energy gap in semiconductors," *Physica*, vol. 34, no. 1, pp. 149–154, 1967.

[109] I. Vurgaftman, J. R. Meyer, and L. R. Ram-Mohan, "Band parameters for III–V compound semiconductors and their alloys," *Journal of Applied Physics*, vol. 89, pp. 5815–5875, jun 2001.

[110] J. Camassel, P. Merle, L. Bayo, and H. Mathieu, "Deformation potentials of the fundamental exciton spectrum of InP," *Physical Review B*, vol. 22, pp. 2020–2024, aug 1980.

[111] G. Bester, X. Wu, D. Vanderbilt, and A. Zunger, "Importance of Second-Order Piezoelectric Effects in Zinc-Blende Semiconductors," *Physical Review Letters*, vol. 96, p. 187602, may 2006.

[112] J. Furdyna and J. Kossut, "A simple lattice-matching guide for superlattices and heterostructures of tetrahedrally-bonded semiconductors," *Superlattices and Microstructures*, vol. 2, pp. 89–96, jan 1986.

[113] D. Berlincourt, H. Jaffe, and L. R. Shiozawa, "Electroelastic properties of the sulfides, selenides, and tellurides of zinc and cadmium," *Physical Review*, vol. 129, no. 3, pp. 1009–1017, 1963.

[114] W. Wardzyński, W. Giriat, H. Szymczak, and R. Kowalczyk, "Stress-induced splitting of excitons due to exchange interaction in zinc telluride," *Physica Status Solidi (b)*, vol. 49, pp. 71–83, jan 1972.

[115] C. Neumann, A. Nöthe, and N. O. Lipari, "Two-photon magnetoabsorption of ZnTe, CdTe, and GaAs," *Physical Review B*, vol. 37, pp. 922–932, jan 1988.

[116] R. M. Martin, "Piezoelectricity," *Physical Review B*, vol. 5, pp. 1607–1613, feb 1972.

[117] R. André, *Effet piezo-electrique dans les puits quantiques CdTe/CdMnTe et CdTe/CdZnTe Régis*. PhD thesis, 2003.

[118] W. Martienssen and H. Warlimont, eds., *Springer Handbook of Condensed Matter and Materials Data*. Springer Berlin Heidelberg, 2005.

[119] S. Z. Karazhanov, "Ab initio Studies of the Band Parameters of III–V and II–VI Zinc-Blende Semiconductors," *Semiconductors*, vol. 39, no. 2, p. 161, 2005.

[120] Landolt-Börnstein, "Zinc telluride (ZnTe) dielectric constants," in *II-VI and I-VII Compounds; Semimagnetic Compounds*, vol. d, pp. 1–5, Berlin/Heidelberg: Springer-Verlag.

[121] M. Zigone, H. Roux-Buisson, H. Tuffigo, N. Magnea, and H. Mariette, "Pressure dependence of photoluminescence in CdTe/Cd 1-x Zn x Te strained-layer heterostructures," *Semiconductor Science and Technology*, vol. 6, pp. 454–460, jun 1991.

[122] L. S. Dang, J. Cibert, Y. Gobil, K. Saminadayar, and S. Tatarenko, "Optical study of residual strains in CdTe and ZnTe layers grown by molecular beam epitaxy on GaAs," *Applied Physics Letters*, vol. 55, pp. 235–237, jul 1989.

[123] L. S. Dang, J. Cibert, Y. Gobil, K. Saminadayar, and S. Tatarenko, "Optical study of residual strains in CdTe and ZnTe layers grown by molecular beam epitaxy on GaAs," *Applied Physics Letters*, vol. 55, no. 3, pp. 235–237, 1989.

[124] L. S. Dang, G. Neu, and R. Romestain, "Optical detection of cyclotron resonance of electron and holes in CdTe," *Solid State Communications*, vol. 44, pp. 1187–1190, nov 1982.

[125] S. Adachi, *Handbook on Physical Properties of Semiconductors, II-VI Compound Semiconductors*, vol. 3. 2004.

[126] J. M. Hartmann, J. Cibert, F. Kany, H. Mariette, M. Charleux, P. Alleysson, R. Langer, and G. Feuillet, "CdTe/MgTe heterostructures: Growth by atomic layer epitaxy and determination of MgTe parameters," *Journal of Applied Physics*, vol. 80, no. 11, pp. 6257–6265, 1996.

[127] T. Asano, K. Funato, F. Nakamura, and A. Ishibashi, "Epitaxial growth of ZnMgTe and double heterostructure of ZnTe ZnMgTe on GaAs substrate by metalorganic chemical vapor deposition," *Journal of Crystal Growth*, vol. 156, no. 4, pp. 373–376, 1995.